UNIVERSIDADE Đ
COIMBRA

Luis Felipe Falda de Ulhoa Coelho

Phase-II Tracking in ATLAS and search for $ttHH$ production using Run 2 and Run 3 LHC Data

Tese no âmbito do Doutoramento em Física, Física Nuclear e de Partículas orientada pelo Professor José Ricardo Morais Silva Gonçalo e Doutora Noemi Calace e apresentada ao Departamento de Física da Faculdade de Ciências e Tecnologia da Universidade de Coimbra.

Julho de 2025

FCTUC FACULDADE DE CIÊNCIAS
E TECNOLOGIA
UNIVERSIDADE DE COIMBRA

Luis Felipe Falda de Ulhoa Coelho

Phase-II Tracking in ATLAS and search for $t\bar{t}HH$ production using Run-2 and Run-3 LHC Data

Doctoral Thesis on Nuclear and Particle Physics

Supervisors:
José Ricardo Morais Silva Gonçalo
Noemi Calace

July, 2025

Abstract

Following the discovery of the Higgs boson, the precise measurement of its properties and their consistency with Standard Model (SM) predictions remains a central goal of the physics program at the Large Hadron Collider (LHC). While current measurements align with the SM predictions, unanswered questions suggest the potential for new physics beyond the SM (BSM). The first part of this thesis presents the first ATLAS search for Higgs boson pair production (HH) associated with top quarks ($t\bar{t}HH$), a rare process that provides direct access to BSM physics through the quartic top-Higgs coupling, offering unique opportunities to probe the Higgs sector of the SM and the electroweak symmetry breaking (EWSB) mechanism. This thesis establishes observed (expected) 95% confidence level upper limits on the SM $t\bar{t}HH$ production cross-sections of 30.8 (24.6) times the SM in leptonic final states, using the full Run 2 and partial Run 3 datasets, corresponding to integrated luminosities of 140 and 59 fb^{-1}, respectively. No significant excess in data above the SM expectations is seen. Additionally, the results are interpreted within the framework of Effective Field Theories by establishing limits on the top-Higgs quartic interaction.

The second part of this dissertation also discusses the experimental challenges and opportunities presented by the High-Luminosity LHC (HL-LHC). The increased luminosity will enable precision measurements of the Higgs self-coupling and provide enhanced sensitivity to BSM physics. Key detector upgrades, such as the Inner Tracker (ITk) and improved b-jet tagging, photon reconstruction, and tau identification, are crucial for maximising the sensitivity of HH searches, including $t\bar{t}HH$. This thesis describes ongoing efforts to address the computational challenges of Phase-II tracking at the HL-LHC. The expected Phase-II ITk tracking physics and computational performance is evaluated. It details improvements in the A Common Tracking Software (ACTS) framework, focusing on the implementation and optimization of the ITk seeding algorithm. Finally, the current expected tracking performance of the ACTS algorithms are presented together with a discussion on CPU optimisation.

Resumo

Após a descoberta do bóson de Higgs, a medição precisa de suas propriedades e a verificação de sua consistência com as previsões do Modelo Padrão (SM) continuam sendo um objetivo central do programa de física do Large Hadron Collider (LHC). Embora as medições atuais estejam alinhadas com as previsões do SM, questões ainda não respondidas sugerem a possibilidade de nova física além do SM (BSM). A primeira parte desta tese apresenta a primeira busca da ATLAS pela produção em pares do bóson de Higgs (HH) associada a quarks top ($t\bar{t}HH$), um processo raro que fornece acesso direto à física BSM por meio do acoplamento quártico top-Higgs, oferecendo oportunidades únicas para explorar o setor de Higgs do SM e o mecanismo de quebra espontânea da simetria eletrofraca (EWSB). Esta tese estabelece limites superiores observados (esperados) ao nível de 95% de confiança para a secção-eficaz de produção de $t\bar{t}HH$ no SM de 30.8 (24.6) vezes o valor previsto pelo SM em estados finais leptônicos, utilizando os conjuntos de dados completos do Run 2 e uma parte do Run 3, correspondendo a luminosidades integradas de 140 e 59 fb^{-1}, respectivamente. Nenhum excesso significativo nos dados acima das expectativas do SM foi observado. Além disso, os resultados são interpretados no contexto das Teorias Efetivas de Campo, estabelecendo limites para a interação quártica top-Higgs.

A segunda parte desta dissertação também discute os desafios experimentais e as oportunidades apresentadas pelo High-Luminosity LHC (HL-LHC). O aumento da luminosidade permitirá medições de precisão do autoacoplamento de Higgs e proporcionará maior sensibilidade à física BSM. Atualizações importantes no detector, como o Inner Tracker (ITk) e melhorias na identificação de jatos b, reconstrução de fótons e identificação de taus, são cruciais para maximizar a sensibilidade das buscas por HH, incluindo $t\bar{t}HH$. Esta tese descreve os esforços em andamento para enfrentar os desafios computacionais da reconstrução da trajetória das particulas na Fase II do HL-LHC. O desempenho esperado da reconstrução em termos de física e computação na Fase II é avaliado. São detalhadas melhorias no software A Common Tracking Software (ACTS), com foco na implementação e otimização do algoritmo de seeding do ITk. Finalmente, o desempenho atual esperado dos algoritmos de reconstrução do ACTS é apresentado, juntamente com uma discussão sobre otimização de CPU.

Personal Contributions

The ATLAS Collaboration consists of a diverse team of over 3000 scientists who contribute to various aspects of the experiment, including detector operation, data analysis, and software development. The work presented in this thesis is the result of collective efforts.

The author's individual contributions are briefly summarised below.

Contributions to the First $t\bar{t}HH$ ATLAS Search

The author played a central and fundamental role in initiating and co-coordinating the first $t\bar{t}HH$ ATLAS search as analysis contact, leading a team that expanded from three to over twenty collaborators, targeting multiple final states (1L, OS2L, ML, and $b\bar{b}\gamma\gamma$).

The author has been involved in every stage of the analysis, from its inception to completion, including early R&D projective studies that motivated the analysis. The author was the primary analyser of the 1L and OS2L final states and contributed significantly to the following aspects:

- Development and implementation of the analysis framework and workflow.
- Leading $t\bar{t}$ + jets background modelling and analysis strategy, including:
    - $t\bar{t}+\geq 3b$ studies (Section 5.6);
    - Data-driven modelling approaches (Section 5.6);
    - Event categorization (Section 5.6.2);
    - Trigger strategy and pre-selection optimizations (Sections 5.3 and 5.4).
- Conducting MVA studies, including:
    - Training the BDT for event classification using high-level variables from HH pairing (Section 5.8),
    - Investigating novel attention-based transformer architectures (Section 5.8).
- Implementation of the b-jet pairing algorithm for Higgs candidate reconstruction in the MVA training (Section 5.5).
- Ntuple production and signal/background sample generation for the latest ATLAS release (Section 5.2).
- Leading statistical analysis efforts, including:
    - Correlation studies between Run 2 and Run 3;

  - Sensitivity estimation and combination studies between all $t\bar{t}HH$ final states (Section 6.5).
- Contribution to the documentation, including the internal analysis note for collaboration review.
- Conducting R&D studies in the fully hadronic final state.

The search is well advanced, with a publication planned for 2025. The author remains crucial to finalizing results, addressing collaboration review feedback, and ensuring readiness for publication. This work has been presented in multiple internal meetings and workshops.

Contributions to Track Reconstruction for Phase-II

The author has contributed to ATLAS Phase-II Inner Tracker (ITk) reconstruction using A Common Tracking Software (ACTS), with significant efforts in:

- Implementation of the ITk seeding algorithm for Phase-II track reconstruction within ACTS (Chapter 9).
- Deployment of the ACTS seeding algorithm within the ATLAS software framework (Chapter 9).
- Validation of the physics performance of the ACTS seeding algorithm, achieving identical results to the legacy counterpart (Section 9.3).
- Implementation of the algorithmic and configuration optimisations to improve execution time and validating CPU optimizations in both ACTS stand-alone and the ATLAS software (Section 9.4).
- Integration and validation of the Fast Tracking configuration for seeding in ACTS.
- Contribution to Phase-II expected performance validation (Chapter 8), including:
  - Technical efficiency results;
  - Seeding performance studies.
- Contribution as a core developer of the ACTS framework, including enhancing core software, developing new algorithmic strategies, and reviewing code.
- Investigation of new approaches to track reconstruction, such as:
  - Integration and optimisation of the ITk configuration within orthogonal seeding;
  - Implementation of machine-learning-driven optimizations of seeding parameters.
- Contribution as a key contact for ACTS seeding routines, supporting clients from collaborations such as sPHENIX, EPIC, ALICE, and NA62.
- Documentation of the seeding algorithm in ACTS documentation [1] and ATLAS Athena code to enhance accessibility.
- Identification and correction of a bug in the ATLAS code related to seeding efficiency evaluation.
- Validation of the ITk cluster sizes.

The validation of Phase-II tracking performance contributed to the publication of Ref. [2] submitted, accepted and published in the Journal of Instrumentation (JINST). The author's work on ACTS track-finding algorithms was presented at the Connecting the Dots 2023 conference, several workshops, and internal meetings. A corresponding conference note is publicly available in Ref. [3]. Contributions to the ATLAS Tracking Combined Performance group are expected to lead to multiple publications related to ACTS integration for Phase-II track reconstruction.

Contributions to the $t\bar{t}H$ CP Analysis

The author contributed to studying the CP nature of the top-Higgs Yukawa coupling in $t\bar{t}H$ and tH events with $H \to b\bar{b}$ decays. This work, which led to the publication of Ref. [4], involved:

- Statistical analysis;
- Background pulls and correlation studies;
- $t\bar{t}H$ and tH signal parameterization.

This work was not included in this thesis.

Contributions to the $HH \to b\bar{b}\gamma\gamma$ Analysis

The author contributed to the search for Higgs boson pair production in the $HH \to b\bar{b}\gamma\gamma$ final state using the full Run 2 and partial Run 3 datasets. Their specific contributions include:

- Implementing the post-processing framework;
- Providing minor contributions to b-tagging studies;
- Debugging and troubleshooting aspects of the analysis workflow.

The search is well advanced, with a publication planned for 2025. This work was not included in this thesis.

Acknowledgments

Along this PhD journey, I have had the privilege of learning from, collaborating with, and being inspired by remarkable people. To them, my deepest gratitude:

To my advisor, Ricardo Gonçalo, for giving me the opportunity to join the ATLAS group at the University of Coimbra. Thank you for your support, for giving me the freedom to pursue my interests, and for always being available for discussions despite your tight schedule.

To Noemi Calace for being the best co-advisor I could ask for. For always thinking on what was best for me, trusting me, given me endless support and advice, and being incredibly available and involved, even while raising two young kids and handling all aspects of tracking, including being tracking CP convener. I am truly grateful to you.

To Valentina Cairo, for being like a third advisor to me. Thank you for always being available, for your encouragement and guidance. I also thank her, along with Marco Valente as HH conveners, for their dedication in di-Higgs searches, and for transmitting so much enthusiasm to everyone involved.

To Andreas Salzburger, Armin Nairz, Markus Elsing, Michael Duehrssen and the EP-ADP group. I am very thankful for the financial support that allowed me to be at CERN during my PhD—especially for covering almost six extra months beyond my contract. Also for the opportunities to attend conferences, workshops and a summer school.

I would also like to thank LIP, Laboratory of Instrumentation and Experimental Particle Physics, for the financial support during my PhD, conferences and workshops.

To the tracking people and ACTS group, thank you for creating such a cooperative and healthy work environment. Apart from those I already mentioned, I would like to thank Carlo Varni, Paul Gessinger, Felix Russo, Andreas Stefl, Stephen Swatman, Tomohiro Yamazaki, Alexander Pfleger, Benjamin Huth, Corentin Allaire, Robert Langenberg, Attila Krasznahorkay, Alexis Vallier, PF Butti, Gabriel Facini, Florencia Castillo, Beomki Yeo, Roberta Arnaldi.

To Djamel Boumediene and Lorenzo Santi for sharing with me the coordination of the $t\bar{t}HH$ analysis. Thank you for being so knowledgeable, reasonable and kind.

To all the people who contributed to the $t\bar{t}HH$ analysis in different ways, especially Hui-Chi Lin, Doga Elitez, Giovanni Rupnik, Adrien Auriol, Meng-Ju Tsai, Renske Wierda, Arthur Lafarge, Andjela Besir, Giulia Di Gregorio and Kevin Nelson. I would also like to thank Alexander Held, Martina Ojeda, Simonetta Gentile, Jelena Jovicevic and Nedaa Alexandra Asbah for contributing with their expertise to interesting

analysis-related discussions, specially $t\bar{t}$ + jets background modelling.

To the editorial board members of the $t\bar{t}HH$ search, Tamara Vázquez Schröeder, Francesco Armando Di Bello, and Laura Pereira Sánchez, thank you for reviewing the analysis, for being so positive, and for giving such practical and useful suggestions.

To the HH framework contacts, especially Thomas Strebler and Georges Aad, for always being extremely helpful, clear, and proactive.

To the developers of FastFrames and TRExFitter for developing very useful and practical codes, especially Tomas Dado, for also being super prompt and helpful.

To Dominik Duda, for always being prompt with all samples derivation requests.

To Arely Cortes Gonzalez, Paolo Francavilla, and Elizabeth Brost for being very supportive and knowledgeable as HIGP/HDBS conveners.

To the other HH analysis contacts for the partial Run 3 analysis who have been very inspiring, specially Fábio Alves, Petar Bokan and Sébastien Rettie.

To my colleges from LIP, Ana Luísa Carvalho and Emanuel Gouveia, who have been great sources of information even after leaving ATLAS.

To other friends that I met at CERN who have not been mentioned yet: Spyros Merianos, Benedikt Gocke, and Laura Winkler.

To my Taiwanese friends, Guilherme Telo Catumba and Parsly, for showing me Taiwan and for the exciting discussions.

To my friends from BIF, Pedro Flávio, Mike, Maria, Joaquim, Diego, Felipe, Henrique...

To my family and to Heloisa—for your endless support, and for making every step of this journey richer and more meaningful.

"*Nada hay absoluto, todo se cambia, todo se mueve, todo revoluciona, todo vuela y se va.*"
FRIDA KAHLO

Aos meus avós, Manlio e Elisabetha

Contents

Introduction

Following the discovery of the Higgs boson [5, 6], one of the primary objectives of the Large Hadron Collider (LHC) has been to precisely measure its properties and confirm their consistency with the predictions of the Standard Model (SM). While current Higgs boson measurements align with SM predictions at the existing level of precision, several unanswered questions hint at the existence of new physics beyond the SM (BSM). The Higgs boson remains a critical tool in this search for BSM physics, particularly through its role in probing the Electroweak Symmetry Breaking mechanism (EWSB) [7–12].

While experimental results from ATLAS and CMS have extensively explored the region around the Higgs potential minimum, there are no experimental constrains on the shape of this potential. The shape can be probed through measurements of the Higgs boson self-coupling. Accessing the self-coupling experimentally is possible via the simultaneous production of two Higgs bosons (HH), a rare process with a production rate approximately 1000 times lower than single Higgs boson production. Higgs boson pair production can occur via gluon-gluon fusion (ggF), vector boson fusion (VBF), or associated production with top quarks ($t\bar{t}HH$) or vector bosons (VHH). Deviations in Higgs boson couplings due to BSM effects could enhance the HH production rate by more than an order of magnitude, making it an important area of study.

Due to their higher cross sections, ggF and VBF production modes have received more attention in HH searches to date. However, $t\bar{t}HH$ may also play a crucial role in probing the Higgs and top sectors, despite its smaller cross-section. This process may uniquely complement existing HH searches due to the direct access to the quartic top-Higgs coupling ($c_{t\bar{t}HH}$), which is not predicted by the SM and is only indirectly constrained with ggF and VBF. Effective field theories offer a model-independent framework for exploring this coupling, making $t\bar{t}HH$ measurements a powerful production mode for BSM physics exploration.

This thesis is structured in three major parts: Part I introduces the SM of elementary particle physics, the LHC and the ATLAS experiment. Part II of this thesis presents the first search for Higgs boson pair production associated with top quarks conducted by ATLAS. The search investigates $t\bar{t}HH$ production in multiple final states, categorized by the decay modes of the HH system and the top quark pair. The analysis establishes observed and expected limits on the SM $t\bar{t}HH$ production cross-sections using the ATLAS full Run 2 and partial Run 3 datasets, corresponding to an integrated luminosity of 140 and 59 fb^{-1}, respectively.

Due to the small cross-section and overwhelming backgrounds in HH production modes, the current LHC Run 3 is only expected to be sensitive to potential BSM enhancements. Achieving sensitivity to the SM self-coupling will require the increased luminosity of the High-Luminosity LHC (HL-LHC) [13–15]. The HL-LHC is projected to deliver approximately 10 times the data of Run 3 by 2040, significantly improving the precision of SM measurements and enhancing the potential for BSM discoveries. By probing the trilinear Higgs self-coupling and studying HH production, the HL-LHC will place meaningful constraints on the Higgs potential and improve our understanding of the EWSB mechanism. Moreover, it will enable the observation of rare phenomena and improve the accuracy of measurements that could reveal signs of BSM physics.

However, the HL-LHC environment will also present substantial experimental challenges. The ATLAS detector must be upgraded to handle up to 200 simultaneous proton-proton collisions per bunch crossing and the associated high radiation doses. For instance, the Inner Tracker (ITk) detector will replace the current Inner Detector and is designed to maintain or exceed its performance in far more demanding conditions. The ITk upgrade may greatly benefit di-Higgs searches: its improved pseudorapidity range will be essential for processes that involve forward jets in its final state. In addition, expected improvements in the tagging of b-jets, photon reconstruction and tau identification will benefit the most important HH decay modes, such as $HH \to b\bar{b}b\bar{b}$, $HH \to b\bar{b}\tau^+\tau^-$, $HH \to b\bar{b}\gamma\gamma$. The $t\bar{t}HH$ production mode will benefit significantly from improvements in b-tagging in view of the high b-jet multiplicity of its final state.

Significant advances in reconstruction algorithms will also be required. The additional hits and track density will make pattern recognition and track-finding computationally intensive, driving the need for more efficient and scalable software. To address these challenges, ATLAS is adopting the A Common Tracking Software (ACTS) framework [16, 17], which builds on the ATLAS tracking algorithms and is optimized for modern computing architectures and multi-threaded event processing. By improving CPU efficiency and maintaining high physics performance, ACTS will ensure that ATLAS achieves its physics goals during the Phase-II upgrade.

Part III of this thesis describes the current state of the art and the ongoing efforts for Phase-II upgrade of the ATLAS track reconstruction. A particular focus is given on the development and optimization of the ITk seeding algorithm with ACTS. The current improvements in tracking software and tracking performance are shown.

Part I

Theory and the ATLAS Experiment

"See that the imagination of nature is far, far greater than the imagination of man."
Richard Feynman

1

The Standard Model of Elementary Particle Physics

Contents

This chapter details my understanding of the Standard Model (SM) of Particle Physics. It begins with an overview of the particle content of the theory in Section 1.1.1 and the underlying group structure that governs it. The SM Lagrangian density, which describes the theory and the fundamental interactions between each particle, is discussed in Section 1.1.2. Given that this thesis focuses on di-Higgs production, particular emphasis is placed on the Higgs mechanism of Electroweak Symmetry Breaking in Section 1.1.3, explaining how particles acquire mass through interaction with the Higgs field in Section 1.1.4. The LHC production and decay modes of the Higgs boson, along with other experimental aspects of Higgs analysis, are presented in Sections 1.2.1 and 1.2.2. The discovery of the Higgs boson and its measured properties are described in Section 1.2.3. Finally, Section 3 covers the current state of di-Higgs searches.

1.1 The Most Beautiful Theory

1.1.1 Particle Content

The SM is a gauge field theory that explains the interactions of elementary particles through three of the four known fundamental forces: electromagnetic, weak nuclear, and strong nuclear forces. It does not encompass the gravitational force, which is described by Einstein's general relativity, since quantising the canonical formulation of general relativity remains an unresolved challenge in modern physics. Furthermore, the gravitational force between individual particles is extremely weak and can be disregarded in SM calculations.

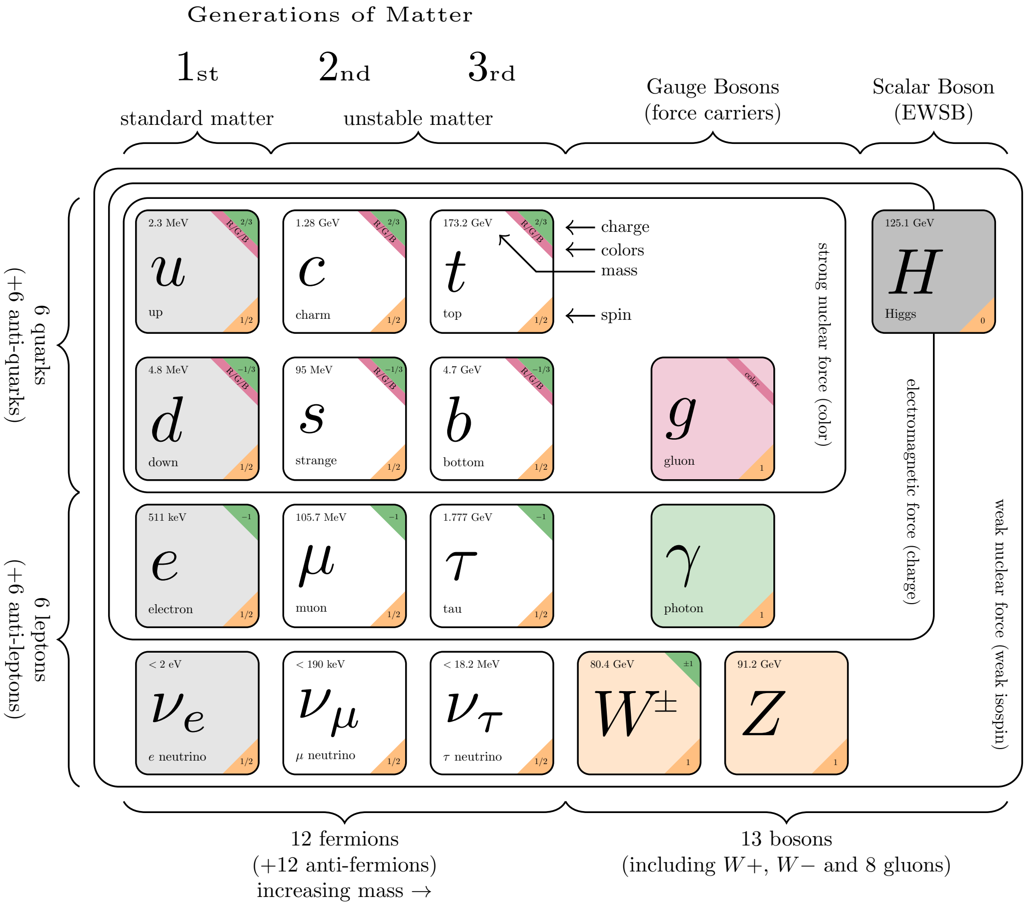

Figure 1.1: Particles and interactions of the SM. The diagram shows the three generations of fermions (quarks and leptons), the gauge vector bosons (gluons, photon, $W^{\pm}$, and Z), and the scalar Higgs boson. The masses are displayed in the left upper corner of each box, the electric and colour charge are displayed in the right upper corner and the spin in the right lower corner. Image adapted from [18].

In the SM, fundamental particles are classified as either fermions or bosons. Fermions, which are spin-1/2 particles following Fermi-Dirac statistics. All matter in the universe is made up of fermions. Bosons, with integer spins, follow Bose-Einstein statistics. Among these, the gauge bosons, which are spin-1 particles, serve as force carriers, mediating interactions between matter particles (i.e. the fermions). The properties (mass, electric charge, colour charge, spin) of all particles described by the SM are summarised in Figure 1.1.

There are two types of elementary fermions in the SM, Quarks and leptons, that come in six flavours each and are organised into three families. Each family consists of two quarks and two leptons, making up a total of 12 fermions in the SM. Each fermion has a corresponding antiparticle with the same mass and spin as their corresponding fermions but have opposite charge and other quantum numbers, such as baryon number or lepton number.

Quarks carry one of three colour charges in Quantum Chromodynamics (QCD)—red, green, or blue—and a fractional electric charge in Quantum Electrodynamics (QED). The six flavours of quarks are named up (u), down (d), charm (c), strange (s), top (t), and bottom (b). As illustrated in Figure 1.1, quarks in the top row have an electric charge of $q = {}^{2}\!/_{3}|e|$[1], while those in the bottom row have a charge of $q = {}^{-1}\!/_{3}|e|$. Due to colour confinement coloured objects, such as quarks, are always bound together to form colour-neutral particles called hadrons and cannot exist as free particles. Hadrons come in two types based on their quark composition. Baryons, which have half-integer spin, are composed of three quarks. Mesons, on the other hand, consist of a quark-antiquark pair and possess either integer or zero spin.

Leptons, which carry no colour charge, are divided into electrically charged leptons and their electrically neutral neutrino counterparts: The electrically charged leptons include the electron (e), muon (μ), and tau (τ), each with an electric charge of $q = -|e|$. Their neutrino counterparts are the electron neutrino (ν_e), muon neutrino (ν_μ), and tau neutrino (ν_τ).

Fermions interact through the exchange of gauge bosons, each mediating a specific interaction. The photon (γ), which is electrically neutral and massless, mediates the electromagnetic interaction and couples with all electrically charged particles, including charged leptons, quarks, and charged gauge bosons. This interaction is described by Quantum Electrodynamics.

The gluon (g) exists in eight distinct states and mediates the strong nuclear force, interacting with all particles that carry colour charge, such as quarks and other gluons. Since gluons themselves carry colour charge, they not only mediate but also participate in the strong interaction, adding complexity to Quantum Chromodynamics, the theory describing strong interactions. This makes Quantum Chromodynamics mathematically more complex than Quantum Electrodynamics.

The W^+, W^-, and Z bosons are the mediators of the weak nuclear force, which involves all quarks and leptons. Weak interactions come in two forms: charged interactions, mediated by the W^+ and W^- bosons, and neutral interactions, mediated by the Z boson. The W^+ and W^- bosons have a mass of 80.369 ± 0.013 GeV[19] and electric charges of $q = +|e|$ and $q = -|e|$, respectively. The Z boson is electrically neutral with a mass of 91.188 ± 0.002 GeV[19]. The significant masses of these bosons explain for the extremely short range of the weak force, roughly 0.1% of a proton's diameter. The weak interaction uniquely changes quark flavour and violates charge-parity (CP) symmetry.

Beyond quarks, leptons, and gauge bosons, the SM requires one electrically neutral scalar boson (spin-0) to make the theory renormalizable. This particle, known as the Higgs boson, has a mass of 125 GeV. The Higgs field, whose excitations produce the

---

[1] e represents the elementary charge, which is the magnitude of the electric charge of a single proton, approximately 1.602×10^{-19} C.

Higgs boson, is crucial for the Brout-Englert-Higgs (BEH) mechanism [7–12]. This mechanism explains how the weak interaction gauge bosons (W^+, W^-, and Z) acquire mass through a process known as Electroweak Symmetry Breaking (discussed in Section 1.1.3). This field has a non-zero vacuum expectation value, which means that it permeates all of space and gives mass to elementary particles through their interactions with the field. The mass depends on the strength of their interaction, i.e. coupling, with the Higgs field.

1.1.2 The Lagrangian of the Standard Model

In quantum field theory, each particle is represented as an excitation in a quantum field defined across all spacetime. The dynamics of these fields are governed by a Lorentz invariant Lagrangian density, $\hat{\mathcal{L}}$, ensuring that the physical laws remain consistent across all reference frames. Furthermore, the SM is a local gauge theory, meaning that $\hat{\mathcal{L}}$ remains invariant under specific local gauge transformations[2].

The fundamental gauge symmetry that forms the basis of the SM is represented by $SU(3)_C \otimes SU(2)_L \otimes U(1)_Y$. This includes $SU(3)_C$, the colour symmetry groups that describes QCD and strong interactions; $SU(2)_L$, describing the weak isospin interactions among left-handed fermions; and $U(1)_Y$, which governs the weak hypercharge interactions that vary between left- and right-handed fermions. The combination of $SU(2)_L \bigotimes U(1)_Y$ is referred to as the Glashow-Weinberg-Salam theory of electroweak interactions, representing the unification of weak and electromagnetic interactions.

Noether's theorem [20] states that each differentiable symmetry generated from local actions is linked to a corresponding conserved current and charge. In the SM, the conserved charges such as the colour charge, weak isospin (I), and weak hypercharge ($Y = 2(Q - I_3)$), where Q denotes the electric charge and I_3 represents the projection of the weak isospin along the z-axis, are associated with their respective symmetry groups.

The $SU(3)_C$ group, which is non-abelian, meaning its group generators do not commute, includes a coupling constant g_s and eight Hermitian gauge fields[3] represented by $G^i_\mu(i = 1,...,8)$—the gluon fields. Similarly, the non-abelian $SU(2)_L$ group possesses a coupling constant g and three gauge fields $W^i_\mu(i = 1,2,3)$. Conversely, the $U(1)_Y$ group is abelian, includes a coupling constant g', and one gauge field B_μ.

The combined $SU(2)_L \otimes U(1)_Y$ symmetry undergoes spontaneous symmetry breaking due to the Higgs mechanism, as discussed in Section 1.1.3. This process leads to the mixing of the W^i_μ and B_μ gauge fields, resulting in the two charged $W^\pm$ and the neutral Z bosons of the weak interactions, and the photon γ of the electromagnetic interactions. The Z and $W^\pm$ bosons acquire mass through this mechanism.

The SM Lagrangian density is defined as a sum of several distinct terms that rep-

---

[2] Local gauge transformations refers to a kind of symmetry transformation in which the field values are changed but the described physical phenomena remain the same. This invariance ensures that the theory's predictions are consistent and independent of arbitrary choices made during calculations.

[3] Hermitian gauge field refers to fields whose corresponding gauge bosons can be described by Hermitian operators, which is one that is equal to its own conjugate tranpose.

resent different aspects of particle interactions:

$$\hat{\mathcal{L}}_{SM} = \hat{\mathcal{L}}_g + \hat{\mathcal{L}}_f + \hat{\mathcal{L}}_H + \hat{\mathcal{L}}_Y. \tag{1.1}$$

The initial term, the gauge term, represents the interactions within the gauge fields and is expressed as:

$$\hat{\mathcal{L}}_g = -\frac{1}{4}\hat{G}^i_{\mu\nu}\hat{G}^{\mu\nu i} - \frac{1}{4}\hat{W}^i_{\mu\nu}\hat{W}^{\mu\nu i} - \frac{1}{4}\hat{B}_{\mu\nu}\hat{B}^{\mu\nu}, \tag{1.2}$$

where the field strengths (described previously) for $SU(3)_C$, $SU(2)_L$, and $U(1)_Y$ groups are given by:

$$\hat{G}^i_{\mu\nu} = \partial_\mu \hat{G}^i_\nu - \partial_\nu \hat{G}^i_\mu - g_s f_{ijk}\hat{G}^j_\mu \hat{G}^k_\nu \quad i,j,k = 1,...,8 \tag{1.3}$$

$$\hat{W}^i_{\mu\nu} = \partial_\mu \hat{W}^i_\nu - \partial_\nu \hat{W}^i_\mu - g\epsilon_{ijk}\hat{W}^j_\mu \hat{W}^k_\nu \quad i,j,k = 1,2,3 \tag{1.4}$$

$$\hat{B}_{\mu\nu} = \partial_\mu \hat{B}_\nu - \partial_\nu \hat{B}_\mu. \tag{1.5}$$

The structure constants f_{ijk} for $SU(3)_C$ and ϵ_{ijk} for $SU(2)_L$, that govern the third terms of equations (1.3) and (1.4), enable the possibility of self-interactions among the gauge fields. This is a direct result of the non-Abelian nature of these groups. In contrast, the Abelian $U(1)_Y$ group does not allow self-interactions, reflecting the fact that photons do not carry electric charge.

Table 1.1: Q, I_3 and Y quantum numbers of all Standard Model fermions.

Fermions	Q	I_3	Y
q_{mL}	$\begin{pmatrix} 2/3 \\ -1/3 \end{pmatrix}$	$\begin{pmatrix} 1/2 \\ -1/2 \end{pmatrix}$	$\begin{pmatrix} 1/3 \\ 1/3 \end{pmatrix}$
u_{mR}, d_{mR}	$2/3, -1/3$	$0, 0$	$4/3, -2/3$
l_{mL}	$\begin{pmatrix} 0 \\ -1 \end{pmatrix}$	$\begin{pmatrix} 1/2 \\ -1/2 \end{pmatrix}$	$\begin{pmatrix} -1 \\ -1 \end{pmatrix}$
e_{mR}	-1	0	-2

The second term of the Lagrangian in equation (1.1) represents the fermion fields and their interactions with gauge fields, described as follows:

$$\hat{\mathcal{L}}_f = \bar{q}_{mL} i\gamma^\mu D_\mu q_{mL} + \bar{l}_{mL} i\gamma^\mu D_\mu l_{mL} + \bar{u}_{mR} i\gamma^\mu D_\mu u_{mR} \tag{1.6}$$

$$+ \bar{d}_{mR} i\gamma^\mu D_\mu d_{mR} + \bar{e}_{mR} i\gamma^\mu D_\mu e_{mR} + \bar{\nu}_{mR} i\gamma^\mu D_\mu \nu_{mR}, \tag{1.7}$$

where $m = 1, 2, 3$ represents the index of the family, L and R indicate the left and right chirality of the fermions, respectively, and $\hat{D}\mu$ is the gauge covariant derivative. Left-handed fermions form weak isodoublets, while right-handed ones are weak isosinglets:

$$q_{mL} = \begin{pmatrix} u \\ d \end{pmatrix}_L, \begin{pmatrix} c \\ s \end{pmatrix}_L, \begin{pmatrix} t \\ b \end{pmatrix}_L \qquad l_{mL} = \begin{pmatrix} \nu_e \\ e^- \end{pmatrix}_L, \begin{pmatrix} \nu_\mu \\ \mu^- \end{pmatrix}_L, \begin{pmatrix} \nu_\tau \\ \tau^- \end{pmatrix}_L \tag{1.8}$$

$$u_{mR} = u_R,\ c_R,\ t_R \qquad \nu_{mR} = \nu_{eR},\ \nu_{\mu R},\ \nu_{\tau R} \tag{1.9}$$

$$d_{mR} = d_R,\ s_R,\ b_R \qquad e_{mR} = e^-_R,\ \mu^-_R,\ \tau^-_R. \tag{1.10}$$

The fermions' quantum numbers, Q, I_3, and Y, are summarised in Table 1.1. The covariant derivatives applied to each fermion fields are as follows:

$$\hat{D}_\mu \hat{q}_{mL} = \left(\partial_\mu + \frac{ig_s}{2}\lambda_\alpha \hat{G}^\alpha_\mu + \frac{ig}{2}\tau_\beta \hat{W}^\beta_\mu + \frac{ig'}{6}\hat{B}_\mu\right)\hat{q}_{mL} \tag{1.11}$$

$$\hat{D}_\mu \hat{l}_{mL} = \left(\partial_\mu + \frac{ig}{2}\tau_\beta \hat{W}^\beta_\mu - \frac{ig'}{2}\hat{B}_\mu\right)\hat{l}_{mL} \tag{1.12}$$

$$\hat{D}_\mu \hat{u}_{mR} = \left(\partial_\mu + \frac{ig_s}{2}\lambda_\alpha \hat{G}^\alpha_\mu + \frac{2ig'}{3}\hat{B}_\mu\right)\hat{u}_{mR} \tag{1.13}$$

$$\hat{D}_\mu \hat{d}_{mR} = \left(\partial_\mu + \frac{ig_s}{2}\lambda_\alpha \hat{G}^\alpha_\mu - \frac{ig'}{3}\hat{B}_\mu\right)\hat{d}_{mR} \tag{1.14}$$

$$\hat{D}_\mu \hat{\nu}_{mR} = \partial_\mu \hat{\nu}_{mR} \tag{1.15}$$

$$\hat{D}_\mu \hat{e}_{mR} = \left(\partial_\mu - ig'\hat{B}_\mu\right)\hat{e}_{mR}, \tag{1.16}$$

using Gell-Mann matrices $\lambda^\alpha(\alpha = 1,...,8)$ and Pauli matrices $\tau^\beta(\beta = 1,2,3)$. As the right-handed fermions are isosinglets under $SU(2)_L$, they do not interact with weak fields ($\tau_\beta \hat{W}^\beta_\mu$), and thus, the $W^\pm$ gauge bosons only couple to left-handed fermions, as seen in equations (1.11 - 1.16). Moreover, quarks are colour triplets[4] under $SU(3)_C$ transformation, participating in the strong interactions ($\lambda_\alpha \hat{G}^\alpha_\mu$ are 3×3 matrices in colour space), while leptons, as colour singlets, do not engage in strong interactions.

Another outcome of the left-handed fermions being $SU(2)_L$ doublets and the right-handed fermions being singlets is that the SM Lagrangian cannot include explicit mass terms for the fermions, such as $(-m_f\bar{\psi}\psi)$. This is because these terms mix left- and right-handed components, violating isospin symmetry. Similarly, mass terms for gauge bosons, like $(-m^2_W W^i_\mu W^{\mu i})$, are also not gauge invariant. The following sections will elaborate on the mechanisms that allows the addition of mass terms for both gauge bosons and fermions within a renormalizable gauge theory. The Higgs ($\hat{\mathcal{L}}_H$) and Yukawa ($\hat{\mathcal{L}}_Y$) terms in the Lagrangian will be discussed later.

1.1.3 BEH Mechanism and Electroweak Symmetry Breaking

At this point, the Lagrangian does not include mass terms, meaning all fermions and gauge fields are massless. While gluons and photons are indeed massless in nature,

---

[4] The colour indices are not shown in the equations for simplicity.

electroweak vector bosons have been proven to be massive [26, 27]. Adding mass terms directly for the weak bosons or fermions would violate the local $SU(2)_L \otimes U(1)_Y$ gauge invariance, which is essential for ensuring the renormalizability of the theory. These mass terms can be introduced in the theory without breaking gauge invariance by the BEH mechanism. This is accomplished by incorporating an $SU(2)_L$ Higgs doublet with weak isospin $I = {}^1\!/_2$ and hypercharge $Y = 1$:

$$\hat{\phi} = \begin{pmatrix} \hat{\phi}^+ \\ \hat{\phi}^0 \end{pmatrix} = \frac{1}{\sqrt{2}} \begin{pmatrix} \hat{\phi}_1 + i\hat{\phi}_2 \\ \hat{\phi}_3 + i\hat{\phi}_4. \end{pmatrix} \tag{1.17}$$

The Lagrangian for the Higgs field is given by

$$\hat{\mathcal{L}}_H = \left(\hat{D}_\mu \hat{\phi}\right)^\dagger \left(\hat{D}^\mu \hat{\phi}\right) - \hat{V}(\hat{\phi}^\dagger \hat{\phi}), \tag{1.18}$$

where $\hat{V}(\hat{\phi}^\dagger \hat{\phi})$ is the Higgs potential and the gauge covariant derivative applied to the Higgs field, $\hat{\phi}$, is given by

$$\hat{D}_\mu \hat{\phi} = \left(\partial_\mu + \frac{ig}{2} \vec{\tau} \cdot \hat{\vec{W}}_\mu + \frac{ig'}{2} \hat{B}_\mu\right) \hat{\phi}. \tag{1.19}$$

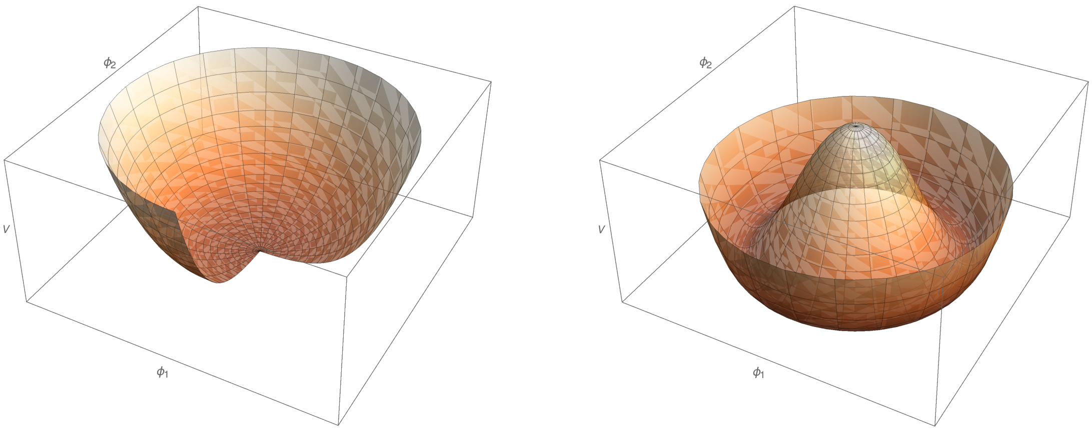

(a) **(b)**

Figure 1.2: Shape of Higgs potential represented for $\mu^2 > 0$ (a), where the potential has a single unique minimum located at the center, and for $\mu^2 < 0$ (b), where the potential has a set of minima arranged on a circle. By choosing a specific point on this circle of minima and defining it as the ground state, there is no more symmetry, which is said to be spontaneously broken.

The Lagrangian $\hat{\mathcal{L}}_H$ remains invariant under $SU(2)_L \otimes U(1)_Y$ transformations. The Higgs potential, written in the most general and renormalizable form consistent with this gauge invariance, is given by:

$$\hat{V}(\hat{\phi}^\dagger \hat{\phi}) = \mu^2 \hat{\phi}^\dagger \hat{\phi} + \lambda \left(\hat{\phi}^\dagger \hat{\phi}\right)^2. \tag{1.20}$$

The first term of the expression represents a mass term, while the second term is a self-interaction term. For the potential $\hat{V}(\hat{\phi}^\dagger\hat{\phi})$ to be bounded from below, λ must be positive. The shape of the potential depends on the value of μ^2. When μ^2 is positive ($\mu^2 > 0$), the potential describes a scalar field with mass μ, and the vacuum state[5] is unique, corresponding to $\langle 0|\,\hat{\phi}\,|0\rangle = 0$, as shown in Figure 1.2a. In this case, the $SU(2)_L \otimes U(1)_Y$ symmetry remains unbroken at the minimum.

If μ^2 is negative ($\mu^2 < 0$), the potential reaches its minimum for

$$\langle 0|\,\hat{\phi}^\dagger\hat{\phi}\,|0\rangle = \frac{1}{2}\,\langle 0|\left(\hat{\phi}_1^2 + \hat{\phi}_2^2 + \hat{\phi}_3^2 + \hat{\phi}_4^2\right)|0\rangle = -\frac{\mu^2}{2\lambda}. \tag{1.21}$$

As illustrated in Figure 1.2b, this results in a degenerate ground state with an infinite set of minima arranged on a circle. Selecting a specific value from the circle as the ground state leads to symmetry breaking. The chosen vacuum does not retain the original symmetry of the Lagrangian, this process is referred to as spontaneously symmetry breaking. For instance, if we choose $\langle 0|\,\hat{\phi}_i\,|0\rangle = 0$ for $i = 1, 2, 4$ and $\langle 0|\,\hat{\phi}_3\,|0\rangle = \sqrt{-\mu^2/\lambda}$, the vacuum expectation value will be given by:

$$\langle 0|\,\hat{\phi}\,|0\rangle = \frac{1}{\sqrt{2}}\begin{pmatrix} 0 \\ v \end{pmatrix} \quad \text{with} \quad \langle 0|\,\hat{\phi}_3\,|0\rangle \equiv v = \sqrt{\frac{-\mu^2}{\lambda}}. \tag{1.22}$$

To determine the particle spectrum (i.e. the excitations of the field), the fields must be expanded around their values at the minimum. Oscillations around equation (1.22) can be parametrized as:

$$\hat{\phi}(x) = \frac{1}{\sqrt{2}}\exp\left(-i\vec{\tau}\cdot\hat{\vec{\theta}}(x)/v\right)\begin{pmatrix} 0 \\ v + \hat{H}(x) \end{pmatrix}, \tag{1.23}$$

where $\tau_i (i = 1,2,3)$ are referred to as the Pauli matrices.

The three $\hat{\theta}(x)$ fields can be removed via an appropriate gauge transformation $\hat{\phi} \to \hat{\phi}' = \exp\left(i\vec{\tau}\cdot\hat{\vec{\theta}}(x)/v\right)\hat{\phi}$. This rotates the field $\hat{\phi}$ into the form:

$$\hat{\phi}'(x) = \frac{1}{\sqrt{2}}\begin{pmatrix} 0 \\ v + \hat{H}(x) \end{pmatrix}. \tag{1.24}$$

After this rotation, of the four scalar fields, only the Hermitian scalar field $\hat{H}(x)$ remains, while the three $\hat{\theta}(x)$ fields vanished. The $\hat{H}(x)$ field is interpreted as the physical Higgs boson. This gauge choice, represented by equation (1.24), is known as the unitary gauge.

The $\hat{\theta}(x)$ fields are referred to as Goldstone bosons. According to Goldstone's theorem [28], when a continuous symmetry is spontaneously broken, a massless scalar spinless particle, known as a Goldstone boson, appears. For a local gauge symmetry, Goldstone bosons disappear from the spectrum and the massless gauge boson associated

---

[5] The vacuum state is the configuration in which the energy of the field is minimal.

with the broken symmetry will acquire mass and a third[6] polarisation state (i.e. the longitudinal polarisation state). This is known as the BEH mechanism.

Each spontaneously broken symmetry corresponds to one massless Goldstone boson. In cases of broken non-Abelian symmetries, the associated massless gauge fields gain mass, while those respecting the symmetries do not. If the $SU(2)_L \otimes U(1)_Y$ symmetry were fully broken, four Goldstone modes would be expected. However, the chosen vacuum of equation (1.22) conserves electric charge $Q = (I_3 + {}^{Y}\!/_{2})$, maintaining invariance under $U(1)_Q$ transformations. Consequently, since the $U(1)_Q$ symmetry of electromagnetism is conserved, the photon remains massless. Thus, only three of the original four degrees of freedom from the Higgs doublet become Goldstone bosons, contributing to the longitudinal polarisation states of the W^+, W^-, and Z bosons and making them massive. The remaining degree of freedom manifests as a scalar particle, the Higgs boson.

By substituting equation (1.24) into equation (1.18) and defining the $\hat{W}^{\pm}_{\mu}$, $\hat{Z}_{\mu}$ and $\hat{A}_{\mu}$ fields as follows:

$$\hat{W}^{\pm}_{\mu} = \frac{1}{\sqrt{2}}\left(\hat{W}^{1}_{\mu} \mp i\hat{W}^{2}_{\mu}\right) \tag{1.25}$$

$$\hat{Z}_{\mu} = \cos\theta_W \hat{W}^{3}_{\mu} - \sin\theta_W \hat{B}_{\mu} \tag{1.26}$$

$$\hat{A}_{\mu} = \sin\theta_W \hat{W}^{3}_{\mu} + \cos\theta_W \hat{B}_{\mu}, \tag{1.27}$$

with the weak mixing angle (also refereed to as Weinberg angle) θ_W defined by:

$$\sin\theta_W = \frac{g'}{\sqrt{g^2 + g'^2}} \qquad \cos\theta_W = \frac{g}{\sqrt{g^2 + g'^2}}, \tag{1.28}$$

the full Electroweak Symmetry Breaking Lagrangian becomes:

$$\hat{\mathcal{L}}_H = \frac{1}{2}\partial_\mu \hat{H} \partial^\mu \hat{H} + \left[m_W^2 \hat{W}^{+\mu}\hat{W}^{-}_{\mu} + \frac{m_Z^2}{2}\hat{Z}^{\mu}\hat{Z}_{\mu}\right]\left(1 + \frac{\hat{H}}{v}\right)^2 - \hat{V}(\hat{H}), \tag{1.29}$$

where the potential is:

$$\hat{V}(\hat{H}) = \frac{1}{2}m_H^2 \hat{H}^2 + \sqrt{\frac{\lambda}{2}}m_H \hat{H}^3 + \frac{\lambda}{4}\hat{H}^4 - \frac{m_H^4}{16\lambda} \quad \text{with} \quad m_H = \sqrt{2\mu^2}. \tag{1.30}$$

As expected, the second term in equation (1.29) now incorporates the mass terms for the $W^{\pm}$ and Z boson fields, while the photon remains massless. The (tree-level) masses are given by:

$$m_W = \frac{gv}{2}; \quad m_Z = \frac{\sqrt{g^2 + g'^2}v}{2}; \quad m_A = 0 \tag{1.31}$$

leading to the relation:

$$\frac{m_W}{m_Z} = \cos\theta_W \tag{1.32}$$

---

[6] A massless vector particle only has two transverse polarisation degrees of freedom.

Thus, θ_W describes the mixing between the electromagnetic and weak forces and connects the two forces in the unified electroweak theory. $\sin^2\theta_W$ can be experimentally measured through, for example, forward-backward asymmetry in Z decays and used to calculate the mass ratio between the W and Z bosons.

Interaction terms between the vector bosons and the Higgs boson (e.g., ZZH, W^+W^-H, $ZZHH$, and W^+W^-HH) are also included in equation (1.29). The first term in equation (1.30) is the (tree-level) mass term for the Higgs boson, expressed as $m_H = \sqrt{2\mu^2} = \sqrt{2\lambda}v$. The value of m_H cannot be determined by the theory alone, as it depends on the coupling constant λ, which is a free parameter. The potential also includes terms for Higgs self-interactions involving three and four Higgs bosons. The couplings are illustrated in Figure 1.3.

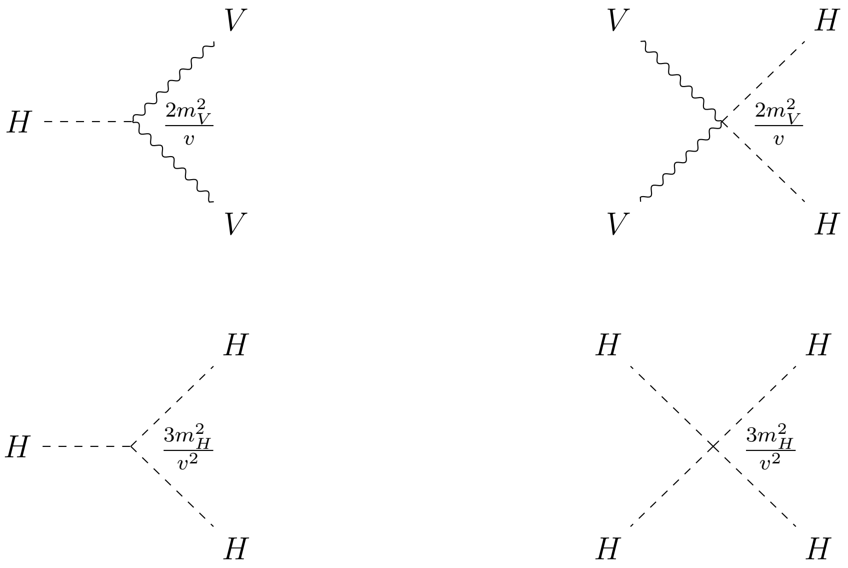

Figure 1.3: Feynman diagrams of the couplings for interactions between the Higgs boson and the weak bosons ($V \equiv W^\pm, Z$), as well as for Higgs self-interactions. The couplings are shown at each vertex.

1.1.4 Fermion Masses and Yukawa Couplings

The Lagrangian can include an SU(2)-invariant interaction between the fermions and the Higgs doublet. These interactions, known as Yukawa couplings, generate mass terms for the fermions after spontaneous symmetry breaking. The Yukawa Lagrangian is expressed as:

$$\hat{\mathcal{L}}_Y = -y_e \bar{l}_{mL} \hat{\phi} e_{mR} - y_d \bar{q}_{mL} \hat{\phi} d_{mR} - y_u \bar{q}_{mL} \hat{\phi}_C u_{mR} + h.c., \tag{1.33}$$

where $h.c.$ denotes the Hermitian conjugate of the preceding terms, $\hat{\phi}_C = i\tau_2\hat{\phi}^\dagger$ is the charge-conjugate of $\hat{\phi}$, and y_f are arbitrary couplings.

By substituting equation (1.24) into the Yukawa Lagrangian, we get:

$$\hat{\mathcal{L}}_Y = \frac{-1}{\sqrt{2}}(v+H)\left(y_e\bar{e}_{mL}e_{mR} + y_d\bar{d}_{mL}d_{mR} + y_u\bar{u}_{mL}u_{mR}\right) + h.c. \tag{1.34}$$

$$= -m_e\bar{e}_m e_m - m_d\bar{d}_m d_m - m_u\bar{u}_m u_m - \frac{m_e}{v}\bar{e}_m e_m H - \frac{m_d}{v}\bar{d}_m d_m H - \frac{m_u}{v}\bar{u}_m u_m H, \tag{1.35}$$

where the second line is derived using $\bar{\psi}_L\psi_R + \bar{\psi}_R\psi_L = \bar{\psi}\psi$ and defining $m_e = y_e\frac{v}{\sqrt{2}}$, $m_d = y_d\frac{v}{\sqrt{2}}$, and $m_u = y_u\frac{v}{\sqrt{2}}$. The fermions, except for neutrinos, acquire mass through their interaction with the Higgs boson after spontaneous symmetry breaking. Since the SM does not include a right-handed neutrino state (ν_R), neutrinos remain massless. However, neutrino masses can be incorporated into the SM using Majorana terms [29].

The last three terms in equation (1.35) describe the interactions between the fermions and the Higgs boson, as illustrated in Figure 1.4. These interactions are proportional to the fermion masses so the Higgs boson couples most strongly to the heaviest fermions. The couplings are free parameters of the theory and must be experimentally determined.

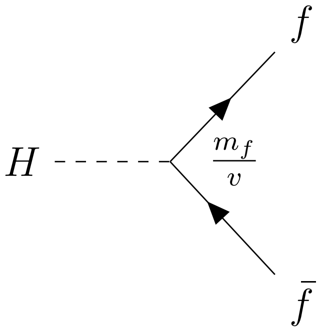

Figure 1.4: Feynman diagram of the Higgs boson coupling to massive fermions.

1.2 The Higgs Boson

The Higgs boson is unique in the SM as the only elementary scalar particle. It is associated with the Higgs field and is predicted to be neutral and CP-even (denoted as $J^{PC} = 0^{++}$). The Higgs boson couples to both bosons and fermions with coupling strengths proportional to their masses. Consequently, Higgs production and decay are primarily influenced by interactions with heavy particles, such as the third generation of fermions and the weak vector bosons. However, the Higgs boson does not couple directly to massless gauge bosons like photons and gluons. These interactions occur through higher-order processes involving loops of heavy quarks (mainly top and bottom quarks, due to their significant masses) or $W^{\pm}$ bosons in the case of photons. The mass of the Higgs boson, m_H, is a free parameter within the theory. Once the mass is specified, the couplings, production rates, and decay widths of the Higgs boson can be precisely calculated.

1.2.1 Higgs Boson Production Modes at the LHC

The primary Higgs boson production modes in proton-proton collisions at the LHC, ordered by cross section from highest to lowest, are: gluon-gluon fusion (ggF), vector boson fusion (VBF), vector boson-associated production or “Higgsstrahlung” (VH), and Higgs associated production with $t\bar{t}$ and $b\bar{b}$ (qqH). Each of these production modes is described below. Figure 1.5 illustrates Feynman diagrams for these production modes. The theoretical cross sections for each mode are listed in Table 1.2 and shown as a function of the center-of-mass energy $\sqrt{s}$ for $m_H = 125$ GeV in Figure 1.6.

Gluon-gluon fusion: The ggF process is the dominant production mode for the Higgs boson at the LHC center-of-mass energy, contributing approximately 87% of the total Higgs cross section. This process, shown in Figure 1.5 (a), is primarily mediated by a loop of virtual heavy quarks (mostly top or bottom), and its high contribution is due to the abundance of gluons in proton collisions. Lighter quarks contributions in the loop are suppressed proportionally to m_q^2.

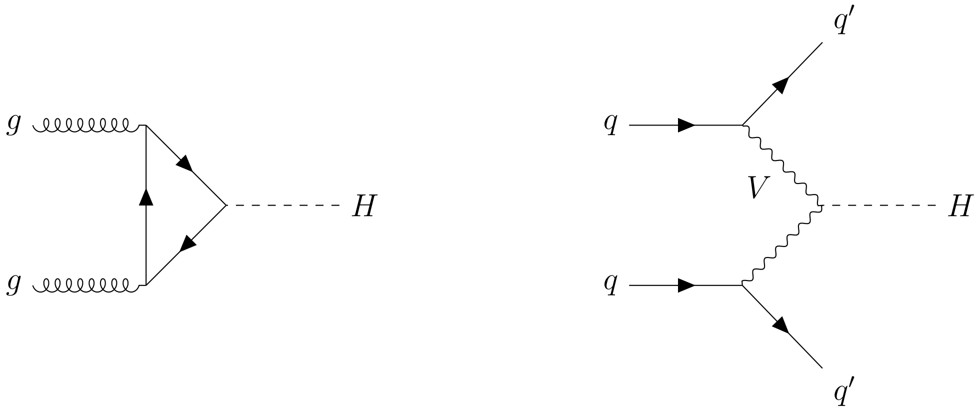

(a) Gluon fusion ($pp \to H$).

(b) Vector boson fusion ($pp \to qqH$).

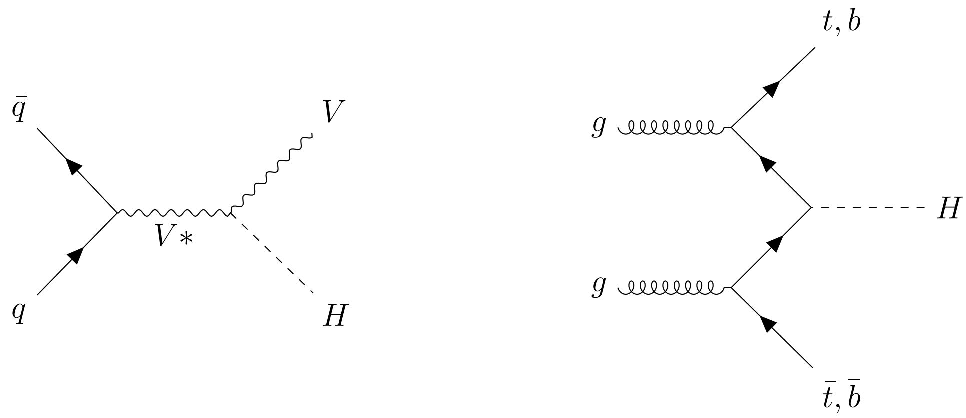

(c) Vector boson associated production ($pp \to VH$).

(d) Heavy quarks associated production ($pp \to t\bar{t}$ ($b\bar{b}$)H).

Figure 1.5: The dominant production modes for the Higgs boson at the LHC, represented by Feynman diagrams.

Vector boson fusion: The second most probable production mode is VBF, where the Higgs is produced via $W^{\pm}$ or Z bosons originating from two initial state quarks as shown in Figure 1.5 (b). These quarks scatter into the final state, forming two hard jets in the forward and backward regions, which serve as a characteristic signature for identifying this process in analysis. If the vector boson is a $W^{\pm}$, the flavour of the quarks will change. This mode accounts for about 7% of the total Higgs cross section.

Vector boson-associated production: The VH process involves a quark and an antiquark interacting to form an off-shell vector boson that radiates a Higgs boson along with an on-shell vector boson as shown in Figure 1.5 (c). The final state vector boson subsequently decays into leptons or hadrons. ZH production can also occur through a gluon-induced initial state. The presence of the vector boson in the final state helps in event identification and in reducing background contributions.

Quark-associated production: The qqH production mode, contributing the least, involves producing one Higgs boson and two heavy quarks from a pair of gluons or a quark-antiquark pair (it can be produced both by gluon- or quark-induced interactions) as shown in Figure 1.5 (d). Although the $t\bar{t}H$ channel has the lowest cross-section at the LHC, it is an experimentally important channel as it provides direct access to the Higgs Yukawa coupling to top quarks, allowing for the study of the Higgs coupling to fermions, as well as probing new physics or the CP nature of the Higgs boson.

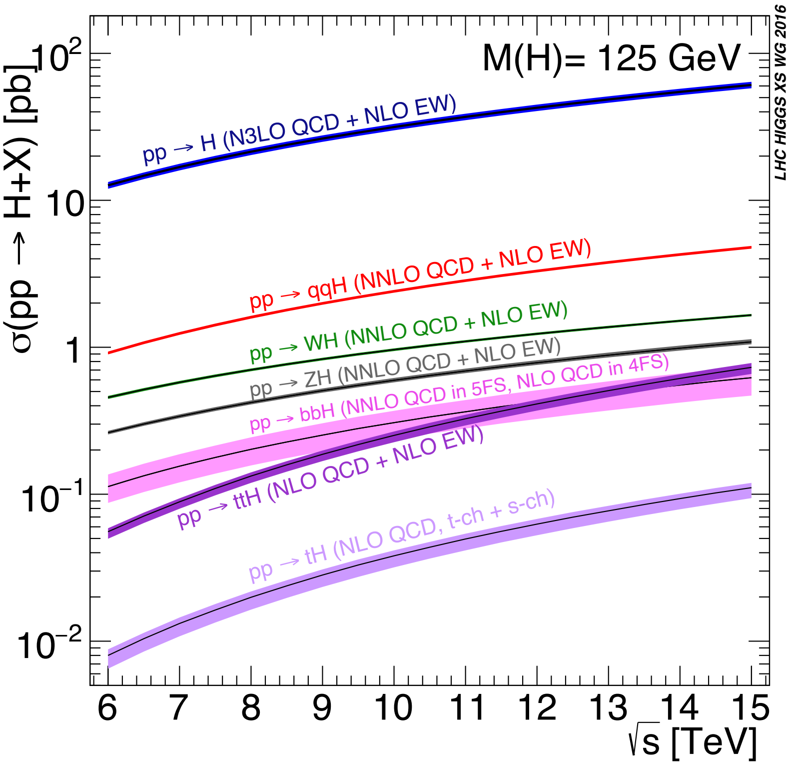

Figure 1.6: Production cross sections for the various Higgs modes as a function of the center-of-mass-energies $\sqrt{s}$ of proton-proton collisions for a Higgs mass of $m_H = 125$ GeV. The theoretical uncertainties are indicated as bands [30].

Table 1.2: Production cross-sections of SM Higgs boson assuming $m_H = 125.09$ GeV in pp collisions at center-of-mass energies of $\sqrt{s} = 13$ and 14 TeV. The fraction f of the total cross-section is presented along with the expected number of events N, assuming integrated luminosities of 147 and 350 fb^{-1} for Run 2 and Run 3, respectively [30].

	$\sqrt{s} = 13$ TeV			$\sqrt{s} = 14$ TeV		
	σ (pb)	f (%)	N	σ (pb)	f (%)	N
ggF	$48.51^{+7.8\%}_{-9.9\%}$	87.137	$7.13 \cdot 10^6$	$54.60^{+7.8\%}_{-9.9\%}$	87.091	$1.91 \cdot 10^7$
VBF	$3.922^{+2.3\%}_{-2.0\%}$	7.045	$5.77 \cdot 10^5$	$4.442^{+2.3\%}_{-2.0\%}$	7.085	$1.55 \cdot 10^6$
WH	$1.370^{+2.4\%}_{-2.6\%}$	2.461	$2.01 \cdot 10^5$	$1.510^{+2.3\%}_{-2.6\%}$	2.409	$5.28 \cdot 10^5$
ZH	$0.882^{+5.4\%}_{-4.6\%}$	1.584	$1.30 \cdot 10^5$	$0.983^{+5.4\%}_{-4.8\%}$	1.568	$3.44 \cdot 10^5$
ttH	$0.498^{+9.4\%}_{-12.8\%}$	0.895	$7.32 \cdot 10^4$	$0.603^{+9.6\%}_{-12.8\%}$	0.962	$2.11 \cdot 10^5$
bbH	$0.486^{+20.1\%}_{-23.9\%}$	0.873	$7.14 \cdot 10^4$	$0.552^{+20.1\%}_{-24.1\%}$	0.88	$1.93 \cdot 10^5$
tH	$0.0028^{+4.6\%}_{-4.0\%}$	0.005	$4.12 \cdot 10^2$	$0.0032^{+4.5\%}_{-3.9\%}$	0.005	$1.12 \cdot 10^3$

1.2.2 Higgs Boson Decay Channels

The Higgs boson has a very short lifetime and, if kinematically allowed ($m_H > 2m_{V,f}$), predominantly decays into pairs of weak vector bosons or fermions ($H \to V\bar{V}, f\bar{f}$). However, since $m_H < 2m_t$, an on-shell Higgs cannot decay into pairs of top quarks despite the large Yukawa coupling. Therefore, the decay into bottom quark pairs is the one with the highest branching fraction. When decaying into $W^\pm$ or Z boson pairs, one of the bosons must be off-shell for the decay to be possible. Additionally, the Higgs can decay into pairs of massless gauge bosons via loops of massive particles. The main decay modes are $H \to b\bar{b}$ and $H \to WW^*$, followed by $H \to gg$, $H \to \tau^+\tau^-$, $H \to c\bar{c}$, $H \to ZZ^*$, $H \to \gamma\gamma$, $H \to Z\gamma$, and $H \to \mu^+\mu^-$.

The branching ratio of any individual decay channel is calculated as the ratio of the partial width[7] to the total width, which is the sum of all possible partial widths:

$$BR(H \to XX) = \frac{\Gamma(H \to XX)}{\sum_i \Gamma(H \to X_i X_i)}. \tag{1.36}$$

Figure 1.7 shows the branching ratios of these decay channels as a function of the Higgs mass. Table 1.3 provides the branching ratios for a Higgs boson with mass of 125.09 GeV.

The sensitivity of one search channel depends on more than just the branching ratios. It is also influenced by the production cross section, the resolution of the reconstructed mass, the trigger and selection efficiency, and the background levels in the final state. For a Higgs boson with $m_H = 125$ GeV, the decay channels $H \to \gamma\gamma$ and $H \to ZZ^* \to 4\ell$ offer the best reconstructed mass resolution because photons and leptons can be measured very precisely. The primary background contribution of $H \to \gamma\gamma$ comes from continuum photon pair production, which is effectively distinguished

---

[7] The decay width or partial width of a channel is a measure of the probability of a certain decay mode happening. It depends on the lifetime of the particle and the decay rate.

from the signal since the energy and momentum of the photons are measured with high precision. Despite the lower branching ratios of channels involving photons and leptons, these can often show good or even better significance in Higgs searches.

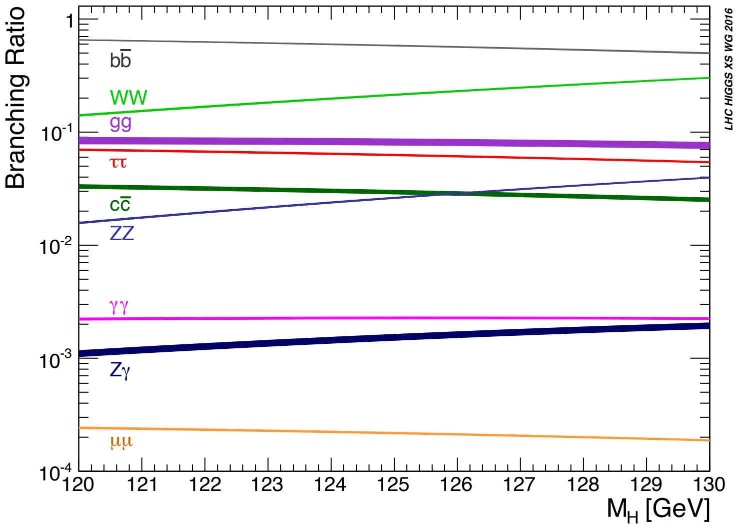

Figure 1.7: Branching fractions and uncertainty bands for various Higgs boson decays represented as a function of the Higgs mass [30].

Table 1.3: Branching fractions and total relative uncertainties for a SM Higgs boson with $m_H = 125.09$ GeV. The Higgs total width is represented at the bottom of the table [30].

Decay channel	Branching ratio (%)	
$H \to b\bar{b}$	58.09	$^{+2.14\%}_{-2.18\%}$
$H \to WW^*$	21.52	$^{+2.64\%}_{-2.6\%}$
$H \to gg$	8.18	$^{+8.21\%}_{-8.15\%}$
$H \to \tau^+\tau^-$	6.256	$^{+2.77\%}_{-2.74\%}$
$H \to c\bar{c}$	2.884	$^{+7.75\%}_{-3.41\%}$
$H \to ZZ^*$	2.641	$^{+2.62\%}_{-2.59\%}$
$H \to \gamma\gamma$	0.227	$^{+3.27\%}_{-3.33\%}$
$H \to Z\gamma$	0.1541	$^{+7.26\%}_{-7.37\%}$
$H \to \mu^+\mu^-$	0.02171	$^{+2.8\%}_{-2.86\%}$
$\Gamma_H = 4.100 \cdot 10^{-3}\,^{+2.32\%}_{-2.31\%}$ GeV		

Although the $H \to b\bar{b}$ and $H \to WW^*$ channels have large branching ratios, their reconstructed mass resolutions are lower. The $H \to b\bar{b}$ channel suffers from the presence of significant QCD background, and the resolution for b-jets is significantly worse compared to leptons and photons. The $H \to WW^*$ channel includes either jets or neutrinos in the final state; neutrinos cannot be directly detected and must be reconstructed from missing energy. The decay into a pair of charm quarks ($H \to c\bar{c}$) has a low branching ratio and faces significant contamination from QCD processes like $g \to c\bar{c}$. Additionally, tagging hadronic jets from charm quarks is experimentally challenging. The decay into a pair of muons ($H \to \mu^+\mu^-$) has a very low branching ratio but can be important since it allows for the measurement of the Higgs couplings to the second generation of fermions at the LHC.

1.2.3 Discovery and Properties of the Higgs Boson and Beyond

The ATLAS [5] and CMS [6] collaborations announced the discovery of a particle with a mass around 125 GeV, consistent with the Higgs boson, on July 4, 2012. This discovery marked the culmination of a nearly half-century-long search due to the difficulty in identifying the Higgs boson, whose mass is dependent on the Higgs self-coupling coefficient λ (see section 1.1.3). Since λ is not determined by theory or any other observable, experiments had to be designed to search for the Higgs boson across a wide mass range rather than a specific value.

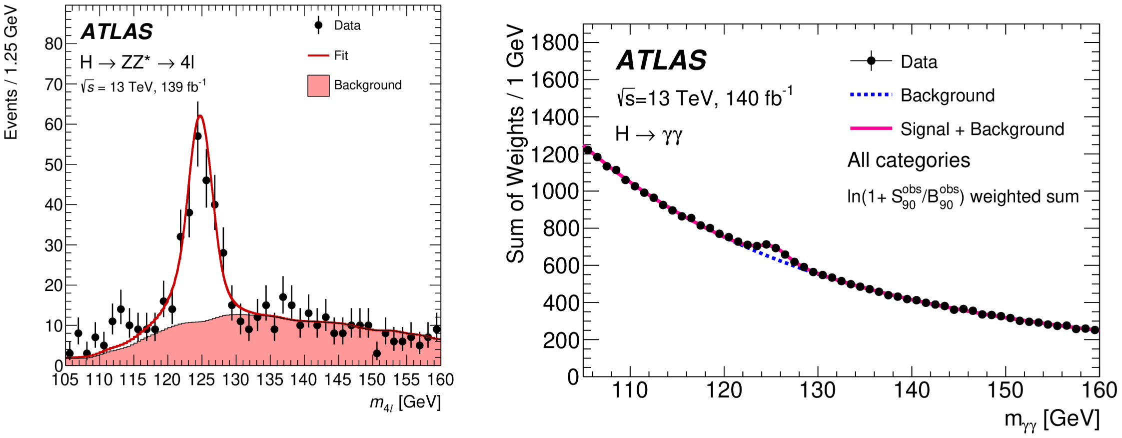

(a) **(b)**

Figure 1.8: Four-lepton (a) and diphoton (b) system invariant mass distributions overlaid with fit results and background expectations [31, 32].

The discovery of the Higgs boson marked a new era in particle physics, prompting extensive studies of its properties to test the consistency of the new particle with the SM predictions. The primary focus of Higgs research has been to obtain precise measurements of its fundamental parameters—such as mass, decay width, and coupling constants—to further validate the SM and search for potential deviations.

The most recent combined measurement conducted by ATLAS and CMS of the Higgs boson mass using data from the $H \to ZZ^* \to 4\ell$ and $H \to \gamma\gamma$ decay channels, obtained with the full LHC Run 1 and Run 2 datasets at a center-of-mass energy of 7, 8 and 13 TeV, has determined the Higgs boson mass to be [33]:

$$m_H = 125.11 \pm 0.09\,(\text{stat}) \pm 0.06\,(\text{syst})\,\text{GeV} \tag{1.37}$$

This corresponds to a total uncertainty of 0.11 GeV, achieving a remarkable precision of 0.09%. This measurement involved a combined fit to the four-lepton and diphoton invariant mass spectra shown in Figure 1.8. Figure 1.9 presents a summary of individual and combined Higgs boson mass measurements from the two decay channels. The ATLAS Collaboration's efforts to understanding detector performance and developing advanced analysis techniques has played a crucial role in improving the precision of these measurements.

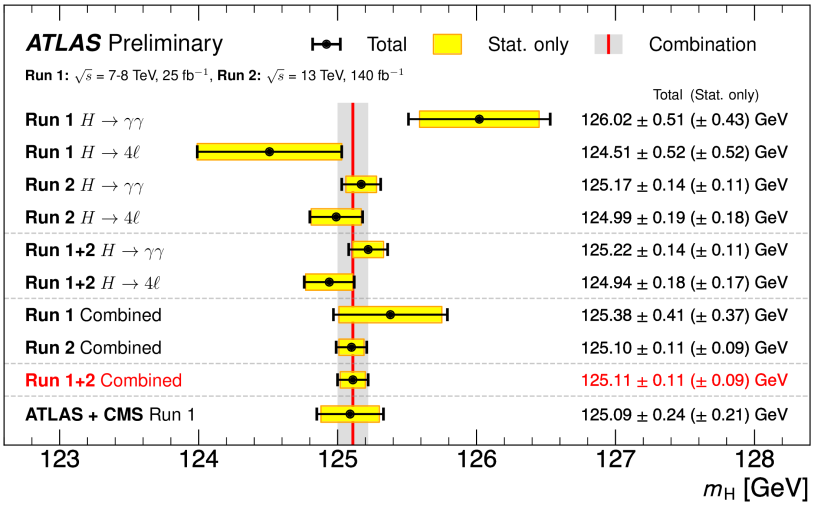

Figure 1.9: Higgs boson mass measurements from the individual $H \to \gamma\gamma$ and $H \to ZZ^* \to 4\ell$ channels, along with their combined result. These results are compared with the ATLAS+CMS Run 1 mass combination. The uncertainty bars on each data point indicate the total uncertainty, while the shaded bands represent the statistical component [33].

With the mass determined, SM predictions for production cross-sections and decay branching ratios can be precisely tested. The signal strength parameter μ is used to compare expected and observed Higgs boson yields:

$$\mu = \mu_i \times \mu^f = \frac{\sigma_i \times BR^f}{(\sigma_i \times BR^f)_{SM}}, \tag{1.38}$$

where σ_i is the cross-section of production mode i, and BR^f is the branching ratio for decay channel f. As these quantities cannot be measured separately, only the product $\mu_i \times \mu^f$ is extracted experimentally. The most recent measurement of the global Higgs signal strength by the ATLAS collaboration is given by [34]:

$$\mu = 1.06 \pm 0.03\,(\text{stat.}) \pm 0.03\,(\text{exp.}) \pm 0.04\,(\text{sig. th.}) \pm 0.02\,(\text{bkg. th.}), \tag{1.39}$$

where the total uncertainty is decomposed into four components: statistical uncertainties, experimental systematic uncertainties, and theory uncertainties on signal and background modelling. The value is consistent with SM expectations.

To explore possible deviations from SM predictions, the Higgs couplings are analysed using the kappa framework [35]:

$$(\sigma \cdot BR)\,(i \to H \to f) = \sigma_{SM}\,(i \to H) \cdot BR_{SM}\,(H \to f) \cdot \frac{\kappa_i^2 \kappa_f^2}{\kappa_H^2}, \tag{1.40}$$

where $\kappa_j = 1$ represents SM predictions, with $j = i, f$ for the initial and final states of the process. κ_H represents the scale factor for the Higgs boson total width. The expected Higgs couplings can be tested by combining data from multiple channels.

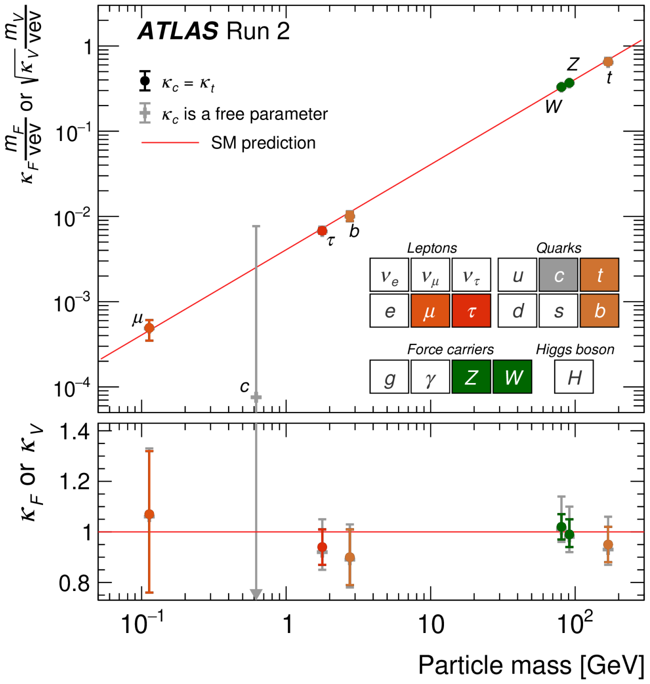

Figure 1.10: Higgs boson reduced coupling strength modifiers to fermions and vector bosons and their uncertainties measured by ATLAS as a function of particle mass [36].

As discussed in Sections 1.1.3 and 1.1.4, the SM predicts a linear relation between fermion couplings to the Higgs boson and fermion masses, as well as a quadratic dependence of vector boson couplings on their masses. The reduced couplings used in the parameterization are defined as $y_f = \kappa_f \frac{m_f}{v}$ for fermions and $y_V = \sqrt{\kappa_V} \frac{m_V}{v}$ for vector bosons. Figure 1.10 presents a summary of the best-fit Higgs boson coupling measurements and their uncertainties from ATLAS, demonstrating a pattern in agreement with SM expectations.

Additionally, it is crucial to determine the Higgs boson's spin (J), charge conjugation (C), and parity (P). In the SM, the Higgs is predicted as a CP-even scalar ($J^{PC} = 0^{++}$). ATLAS and CMS have searched for CP-odd contributions in Higgs boson couplings to gauge bosons, with results aligning with CP-even expectations [37–40]. Since bosonic couplings alone may not fully reveal CP properties, Higgs-fermion interactions provide an alternative approach. Probing Yukawa couplings is essential to understanding the Higgs sector and possible CP violation, which could contribute to explaining baryogenesis.

It remains an open question whether this is the only Higgs boson or part of a larger Higgs sector, as proposed by theories like supersymmetry. While some models predicting additional Higgs bosons have already been ruled out, others require more data for thorough exploration. Furthermore, a complete understanding of the Higgs sector requires exploring the shape of the Higgs potential. Higgs pair production (HH) provides a direct probe of the Higgs self-coupling, which is crucial for testing the electroweak symmetry breaking mechanism. These aspects will be discussed in detail in Chapter 3.

2

ATLAS Experiment at the Large Hadron Collider

Contents

To test the theory and its predictions in high-energy physics (HEP) analysis, advanced particle accelerators and multi-purpose detectors are needed to produce high-energy collisions at high rates, as well as efficiently detect, identify and reconstruct various particles resulting from these collisions. This chapter provides an overview of the Large Hadron Collider and its upcoming High-Luminosity upgrade. It also describes the ATLAS detector, including its components and the trigger and data acquisition systems.

2.1 Large Hadron Collider

The Large Hadron Collider (LHC) [41] is the world's most powerful superconducting hadron accelerator and collider. It is located at CERN (the European Organisation for Nuclear Research) between 45 and 170 meters below the France-Switzerland border near Geneva and it lies in a 26.7-kilometre tunnel that previously hosted the Large Electron-Positron Collider (LEP) [42]. The LHC was constructed to test and explore new energy frontiers and address some of the unanswered and most fundamental questions in particle physics.

The LHC has been originally designed to collide beams of protons at a center-of-mass energy of 14 TeV and achieve a luminosity of 10^{34} cm^{-2}s^{-1}. It is capable of colliding heavy ions, particularly lead (Pb) nuclei, at an energy of 2.8 TeV per nucleon with a peak luminosity of 10^{27} cm^{-2}s^{-1}. During the first operational period of the LHC, known as Run 1, which spanned from 2011 to 2012, *pp* collisions were delivered at center-of-mass energies of 7 TeV and 8 TeV. The LHC underwent a shutdown in 2013 and 2014 for consolidation activities. Following this, Run 2 started in 2015 and continued until the end of 2018, with *pp* collisions occurring at an increased center-of-mass energy of 13 TeV. In Run 2, the LHC's instantaneous luminosity was increased to up to twice its design luminosity. Run 3 began in 2022 and is expected to continue until the end of 2026. Operating at a center-of-mass energy of 13.6 TeV, Run 3 is projected to double the dataset size collected in previous runs. The dataset used in this thesis includes data from both Run 2 and partial data from Run 3 (from 2022 and 2023).

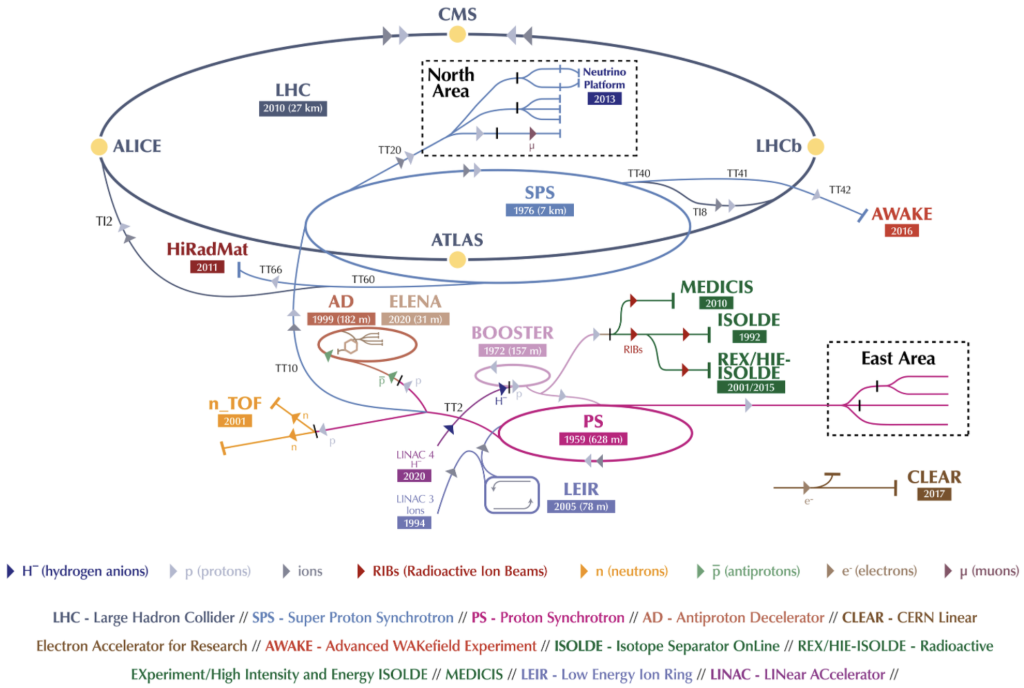

Figure 2.1: CERN Accelerator Complex for Run 3 configuration [43].

To achieve the required energies, particles pass through multiple stages of acceleration, as illustrated in Figure 2.1. The process begins with the injection of negative hydrogen ions (hydrogen atoms with an extra electron) into the Linac4 linear accelerator. Linac4 accelerates these ions to an energy of 160 MeV. The ion source for Linac4 starts with a container of hydrogen gas, similar to the setup used in the previous Linac2 accelerator, and produces ions by heating the gas into a plasma using high-frequency waves. In Linac4, radio-frequency cavities generate alternating electric fields that accelerate the ions. As the ions move through a sequence of cylindrical conductors, these conductors alternately carry positive and negative charges. The conductors behind the ions push them forward, while the ones ahead pull them, causing the ions to accelerate. Quadrupole magnets ensure that the ions remain focused in a narrow beam as they travel through the accelerator. The negative hydrogen ions are pulsed through Linac4 for intervals of 400 microseconds.

After passing through Linac4, the ions enter the Proton Synchrotron Booster (PSB), where they are stripped of their electrons, leaving only protons. These protons are then accelerated to an energy of 2 GeV before being injected into the Proton Synchrotron (PS). With a circumference of 628 meters, the PS further boosts the protons' energy to 26 GeV. The protons are then transferred to the Super Proton Synchrotron (SPS), which has a nearly 7 km circumference, where they are accelerated to 450 GeV. Finally, the proton beam is split and directed to the Large Hadron Collider (LHC), where the protons travel in opposite directions in two separate beam pipes and are accelerated to their final energy.

2.1.1 The LHC Luminosity

Inside the LHC, each beam consisted of up to 2808 bunches during Run 2 and up to 2748 bunches during Run 3 until August 2024, with each bunch containing approximately 10^{11} protons with a spacing interval of 25 ns between bunches. These bunches collide at four designated interaction points, in each of these points it is located one of the four detectors of the LHC, each dedicated to an specific study: A Toroidal LHC ApparatuS (ATLAS) [44] and Compact Muon Solenoid (CMS) [45] detectors are designed for general-purpose studies. A Large Ion Collider Experiment (ALICE) detector is intended to study quark-gluon plasma in Pb-Pb and p-Pb collisions. Finally, LHC-beauty (LHCb) detector is designed to explore the physics of the bottom quarks.

Luminosity is an important concept of high energy physics, it indicates a collider's ability to produce a certain number of interactions and evaluate the performance of the collider. For a specific process i, the number of events N_i is determined by the product of the process's production cross section σ_i and the time integral of the instantaneous luminosity $\mathcal{L}(t)$:

$$N_i = \sigma_i \int \mathcal{L}(t)\ dt. \tag{2.1}$$

The number of events is proportional to the probability of a certain final state to be produced and may vary with energy in different ways.

The integrated luminosity is defined as the time integral of the instantaneous luminosity. For bunched beams, the instantaneous luminosity itself can be expressed as a function of the geometrical characteristics of the colliding bunches and the machine

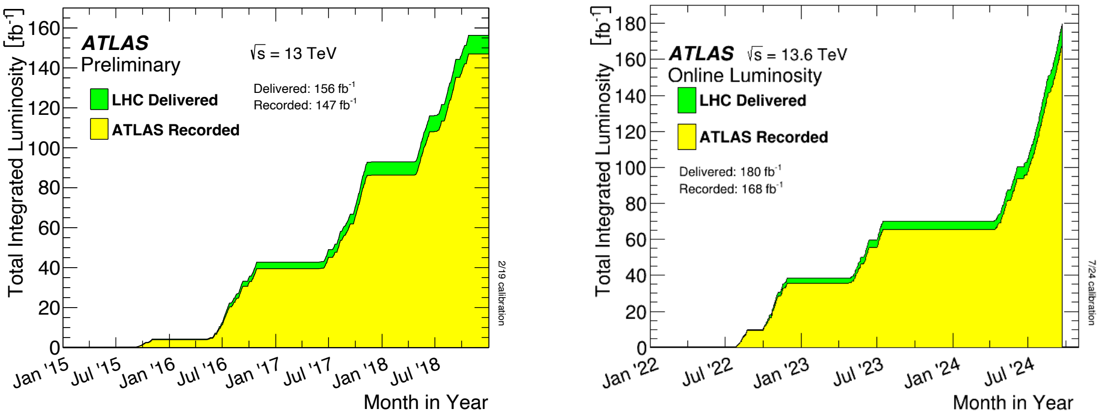

(a) **(b)**

Figure 2.2: Total integrated luminosity delivered to ATLAS (green) and recorded by ATLAS (yellow) as a function of time during stable beams for pp collisions at 13 TeV center-of-mass energy during LHC Run 2 [46] (a) and Run 3 [47] (b).

parameters as:

$$\mathcal{L} = \frac{N_p^2 n_b f_{rev}}{4\pi\sigma_x\sigma_y} F, \tag{2.2}$$

where N_p is the number of protons per bunch, n_b is the number of bunches per revolution injected into the LHC, f_{rev} is the revolution frequency of the beam (approximately 11 kHz at the LHC), σ_x and σ_y are the beam transverse dimensions, and F is the geometric luminosity reduction factor. The factor F accounts for minor corrections due to collisions with a transverse offset or crossing angle between beams at the interaction point; it is defined as:

$$F = \frac{1}{\sqrt{1 + \left(\frac{\theta_c \sigma_z}{2\sigma^*}\right)^2}}, \tag{2.3}$$

where θ_c is the full crossing angle at the interaction point, σ_z is the RMS of the bunch length, and σ^* is the RMS of the transverse beam size at the interaction point.

The detectors operation begins only once the beams circulating the beam pipe are stabilised, leading to a difference between the total luminosity delivered by the LHC and the amount recorded by each detector. The total integrated luminosity delivered by the LHC and recorded by ATLAS during Run 2 and partial Run 3 is shown in Figure 2.2. The primary operation parameters of the LHC for each data-taking period up to the end of Run 2 are summarised in Table 2.1.

Increasing the luminosity at the LHC leads to a higher number of collisions per bunch crossing, which in turn raises the probability of observing rare processes. However, this also results in a higher density of protons, producing a non-negligible number of simultaneous pp interactions during a single bunch crossing. These additional collisions are superimposed to the interesting physics process and overlap with the primary event (the so-called hard-scatter interaction), they are referred to as pile-up.

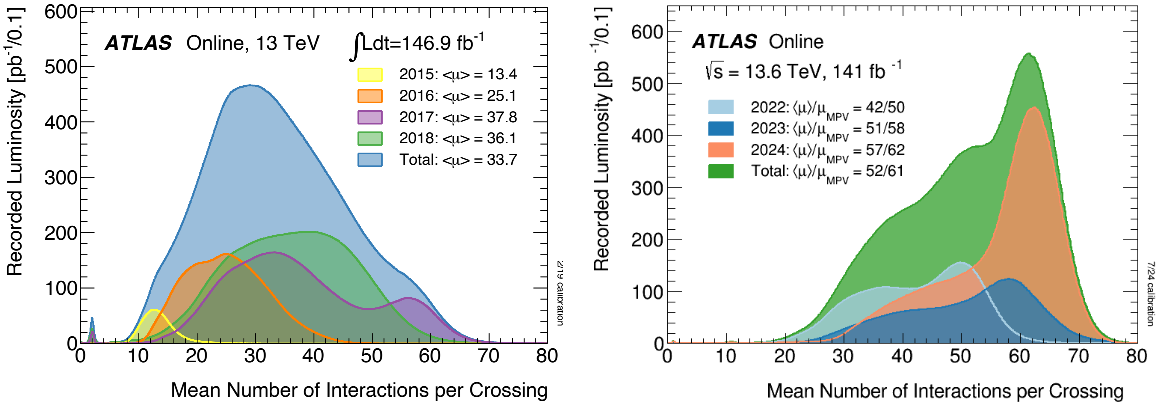

(a) **(b)**

Figure 2.3: Luminosity-weighted distribution of the mean number of interactions per crossing for the 13 TeV data collected by the ATLAS experiment from 2015 to 2018 [46] (a) and 13.6 TeV data from 2022 to 2024 [47] (b). The yearly-averaged pile-up, $\langle \mu \rangle$, per year is indicated.

Table 2.1: LHC running parameters for pp collisions during operation in Run 1 (2010 - 2012), Run 2 (2015 - 2018) and partial Run 3 (2022 - up to today), shown together with the design parameters [46, 47, 49–54]. For 2024 the values are reported up to August of that year.

	Run 1			Run 2				Run 3			
Parameter	2010	2011	2012	2015	2016	2017	2018	2022	2023	2024	Design
Beam energy (TeV)	3.5	3.5	4.0	6.5	6.5	6.5	6.5	6.8	6.8	6.8	7.0
Max peak luminosity (10^{34} cm^{-2}s^{-1})	0.021	0.35	0.77	0.5	1.3	1.6	1.9	2.39	2.24	2.33	1.0
Total integrated luminosity ($1fb^{-1}$)	0.048	5.5	22.8	4.0	38.5	50.2	63.4	39.7	31.8	110.5	-
Number of Interactions per Crossing		9.1	20.7	13.4	25.1	37.8	36.1	42.5	50.9	57	24

The expected number of *in-time*[1] pile-up collisions in a single bunch crossing, μ, is given by:

$$\mu = \frac{\sigma_{\text{inelastic}} \mathcal{L}}{f_{\text{rev}}} \tag{2.4}$$

where $\sigma_{\text{inelastic}}$ denotes the inelastic pp interaction cross-section, $\mathcal{L}$ is the instantaneous luminosity and f_{rev} is the revolution frequency.

As the instantaneous luminosity increases, so does the pile-up, posing a significant challenge to physics analyses. Figure 2.3 displays the distribution of pile-up for the data collected by the ATLAS experiment during LHC Run 2 and partial Run 3. During the Run 2 period, the average number of interactions per bunch crossing, $\langle \mu \rangle$, varied between 13.4 and 37.8, while for partial Run 3 varied between 42.5 and 57. The high granularity of the detectors allows for the isolation of the interaction of interest from the *in-time* pile-up by distinguishing between different interaction vertices and their associated particles. In addition, with a high bunch crossing frequency, interactions

---

[1] In-time pile-up is defined as the additional pp collisions occurring in the same bunch-crossing as the collision of interest.

from adjacent bunch crossings may contaminate the signal in detector systems with integration times significantly longer than the 25 ns bunch spacing. These will be recorded as part of the same event and are known as *out-of-time* pile-up.

2.2 ATLAS Detector

The ATLAS detector [44] is one of the two general-purpose detectors at the LHC (together with CMS), situated at Interaction Point 1, in a cavern 100 meters underground. This cylindrical detector measures 44 meters in length and 25 meters in height, making it the largest detector at the LHC. ATLAS is composed of several distinct subsystems arranged concentrically in layers around the interaction point at the centre of the detector. These subsystems are designed to measure the momentum, trajectory, and energy of particles, enabling the identification of each particle. A large toroid magnet system bends the trajectories of charged particles, allowing for precise momentum measurements.

The layout of the ATLAS detector is represented in Figure 2.4. Each layer is specialised in precisely identifying and measuring specific properties of particles that emerge from the interaction point. The innermost sub-detector, known as the Inner Detector (ID), serves as the tracking system, responsible for reconstructing the trajectories of charged particles and identifying interaction vertices. This is surrounded by a solenoid magnet system, which generates a 2 T solenoidal magnetic field. Surrounding the magnet system are the electromagnetic and hadronic calorimeters (ECAL and HCAL), designed to measure electromagnetic and hadronic showers, respectively. The outermost layer, the Muon Spectrometer (MS), is necessary for a complete reconstruction of muons.

The major components of the ATLAS detector and the ATLAS coordinate system are detailed in the following sections. Table 2.2 provides a summary of the design pseudorapidity coverage and sub-detector resolution for each component of the ATLAS detector.

Table 2.2: The original design performance goals for each component of the ATLAS detector [44]. The units for p_T and E are given in GeV, and the $\oplus$ symbol denotes a sum in quadrature.

Detector component	Required resolution	η coverage	
		Measurement	Trigger
Tracking	$\sigma_{p_T}/p_T = 0.05\% p_T \oplus 1\%$	± 2.5	
EM calorimetry	$\sigma_E/E = 10\%/\sqrt{E} \oplus 0.7\%$	± 3.2	± 2.5
Hadronic calorimetry (jets)			
barrel and end-cap	$\sigma_E/E = 50\%/\sqrt{E} \oplus 3\%$	± 3.2	± 3.2
forward	$\sigma_E/E = 100\%/\sqrt{E} \oplus 10\%$	$3.1 < \lvert\eta\rvert < 4.9$	$3.1 < \lvert\eta\rvert < 4.9$
Muon spectrometer	$\sigma_{p_T}/p_T = 10\%$ at $p_T = 1$ TeV	± 2.7	$3.1 < \lvert\eta\rvert < 4.9$

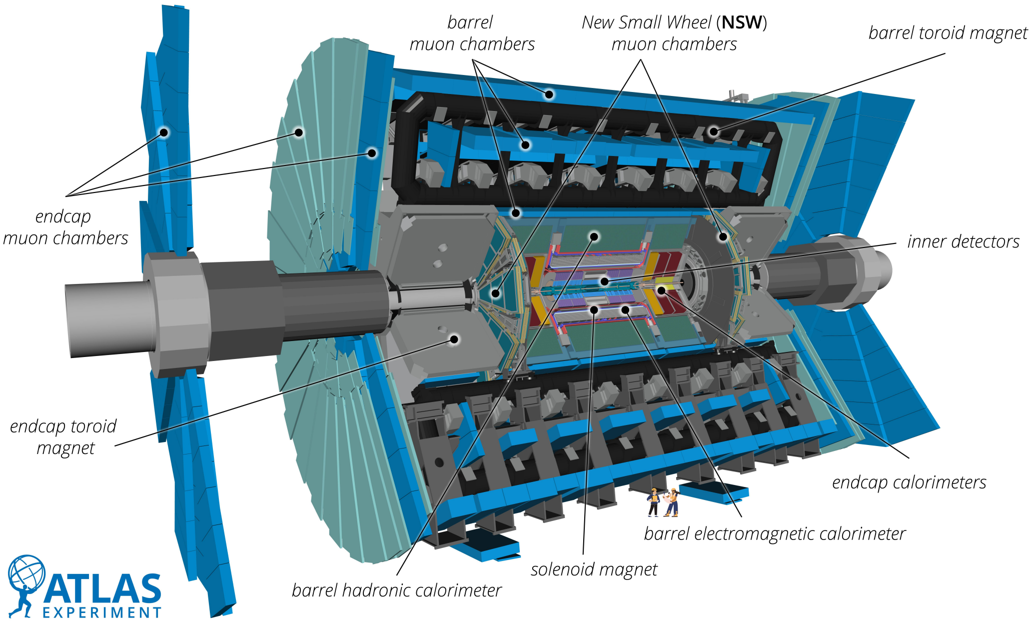

Figure 2.4: Cutaway view of the Run 3 ATLAS detector layout. The different sub-detectors are shown in the figure [56].

2.2.1 ATLAS Coordinate system

ATLAS utilises a right-handed coordinate system, originating at the nominal interaction point at the detector's center. The z-axis is aligned with the beam line direction, while the $x-y$ plane is oriented transversely to it, with the x-axis directed towards the centre of the LHC ring and the y-axis directed upwards. The $x-y$ plane is referred to as the transverse plane. Figure 2.5a shows a representation of the ATLAS right-handed coordinate system.

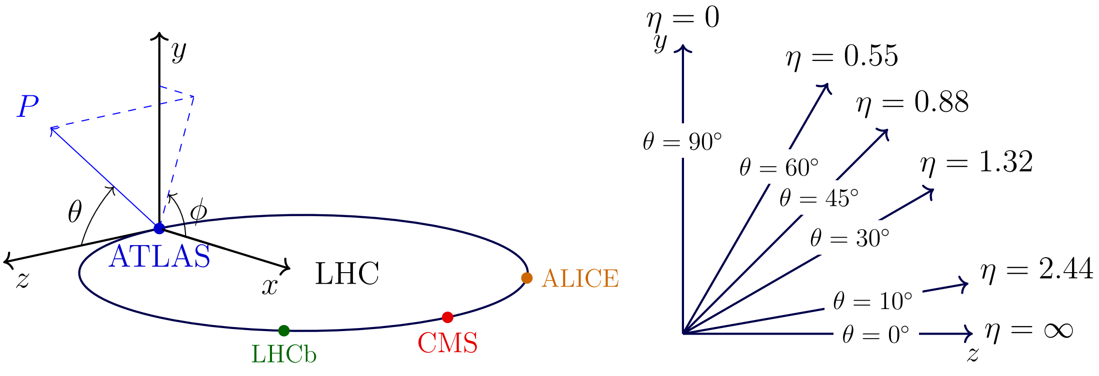

(a) **(b)**

Figure 2.5: Schematic representation of the coordinate system used by the ATLAS detector (a) and values of pseudorapidity η for various values of polar angle θ (b). Images taken and adapted from [57].

In the transverse plane, cylindrical coordinates are used, where ϕ $(-\pi < \phi < \pi)$

represents the azimuthal angle around the z-axis, and r is the radius extending outward from the detector. To describe the angle of a particle relative to the beam direction, pseudorapidity η is preferred over the polar angle θ $(0 < \theta < \pi)$ because rapidity differences (Δy) remain Lorentz invariant under boosts along the z-axis. Figure 2.5b shows a representation of η for different values of the polar angle θ. As shown in the figure, a particle has $\eta = 0$ if it travels perpendicular to the beam pipe ($\theta = 90°$). While its pseudorapidity tends towards infinity ($|\eta| \to \infty$) if it is travelling parallel to the beam pipe ($\theta = 0°$ or $\theta = 180°$). Pseudorapidity is defined as:

$$\eta = \ln\left(\frac{|\vec{p}| + p_L}{|\vec{p}| - p_L}\right) = -\ln\left(\tan\frac{\theta}{2}\right), \tag{2.5}$$

where $\vec{p}$ and p_L are the momentum and longitudinal momentum of the particle, respectively. In the limit of a massless particle, the pseudorapidity is equivalent to the rapidity, which is defined as:

$$y = \frac{1}{2}\log\left(\frac{E + p_z}{E - p_z}\right) \tag{2.6}$$

The angular distance between two particles in the pseudorapidity-azimuthal plane can be defined based on their η and θ distance as:

$$\Delta R = \sqrt{\Delta\phi^2 + \Delta\eta^2} \tag{2.7}$$

The momentum of an object in Cartesian coordinates is expressed as $\mathbf{p} = (p_x, p_y, p_z)$, where p_x, p_y, and p_z are the momentum components in the x, y, and z axis, respectively. The particle's transverse momentum p_T is defined as:

$$p_T = \sqrt{p_x^2 + p_y^2} = |\vec{p}|\sin\theta \tag{2.8}$$

2.2.2 Inner Detector

The Inner Detector (ID) [58–61] serves as the tracking system at the core of the ATLAS detector, positioned closest to the beam pipe. It is essential for reconstructing the trajectories of charged particles that transverse the material of the detector and determining their momenta. The ID offers excellent coverage up to $|\eta| < 2.5$ and full azimuthal coverage (ϕ) for transverse momenta ranging from 0.4 GeV to several TeV. The detector provides a resolution of $\sigma_{p_T}/p_T = 0.05\% \times p_T \oplus 1\%$ in the plane perpendicular to the beam axis and a transverse impact parameter resolution of approximately 10 μm for high-momentum particles in the central η region. Additionally, the ID accurately reconstruct primary vertices, distinguishing hard-scatter vertices from pile-up vertices, and identifying secondary vertices, such as those from B-hadrons and photon conversions.

As charged particles pass through the ID, they ionise the sensitive detector's material layers. These ionisation signals are recorded by the electronics, enabling the reconstruction of the particles' trajectories. The ID consists of three main sub-detectors: the Pixel Detector [62], the Semiconductor Tracker (SCT) [63], and the Transition

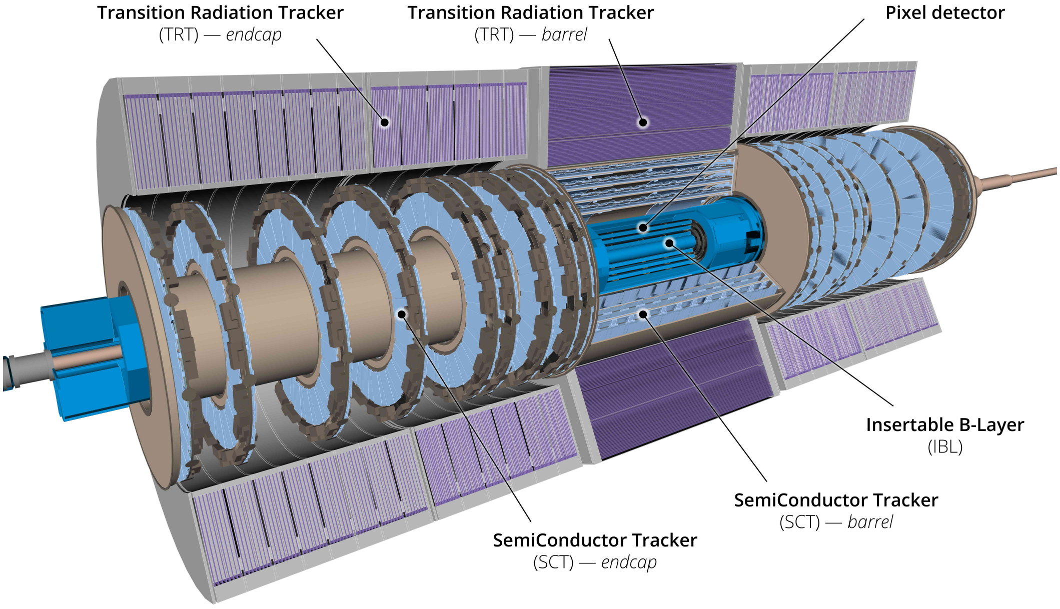

Figure 2.6: Cutaway display of the Run 3 ATLAS Inner Detector layout. The different barrel and end-cap sub-layers are represented in the figure. At the innermost radii, it features a silicon pixel detector, followed by a silicon microstrip detector (SCT), and a straw-tube detector (TRT), which provides continuous tracking and particle identification through transition radiation [56].

Radiation Tracker (TRT) [64]. Figure 2.6 illustrates the layout of the ID and its sub-detectors. Each of its sub-detectors has a barrel region, arranged in concentric cylinders around the beam direction, and an end-cap region, arranged in disks perpendicular to the beam axis. The entire ID is immersed in a 2 T magnetic field, generated by a superconducting solenoid (Section 2.2.5), which spans a length of 5.3 meters and a diameter of 2.5 meters. This magnetic field bends the paths of charged particles, enabling the measurement of their charge and momenta. Each component of the ID detector will be described in more details below.

2.2.2.1 Pixel Detector

The Pixel Detector is the innermost component of the ID, so it is exposed to the highest amount of particle flow and requires large granularity. It consists of 1,744 silicon pixel modules arranged in three concentric barrel layers covering $|\eta| < 1.5$ and two end-caps with three disks each covering $1.5 < |\eta| < 2.5$. Each module contains 47,232 pixels, with dimensions of 50×400 μm^2, providing a spatial hit resolution of 14 μm in the (r,ϕ) plane and 115 μm along the z-axis.

During the first long shutdown of the LHC in May 2014, the Insertable B-layer (IBL) [65] was added to the Pixel Detector, introducing an additional fourth pixel layer closer to the beam pipe, as shown in Figure 2.7. Positioned at a radius of 3.3 cm with respect to the interaction point, the IBL was intended to enhance track and vertex reconstruction precision for the increasing luminosity conditions of Run 2. The IBL's

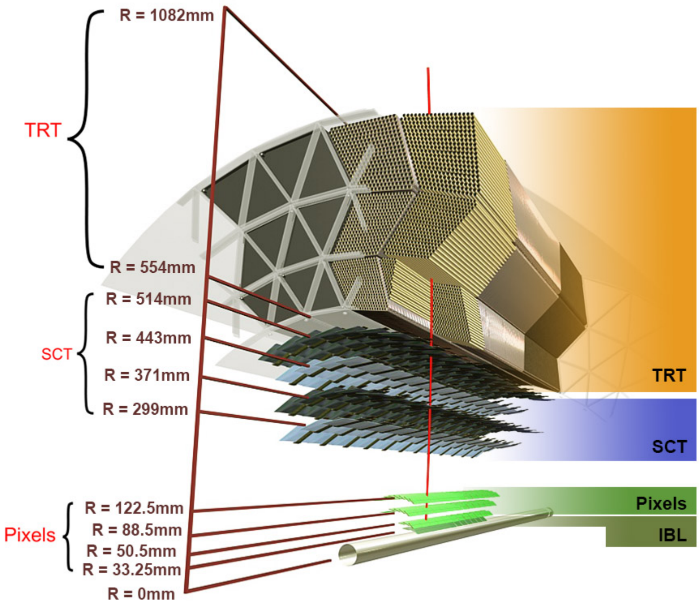

Figure 2.7: Detailed cutaway view of the Inner Detector. The Insertable B-layer can be seen in more details together with the other ID layers as a function of the radial distance to the interaction point [65].

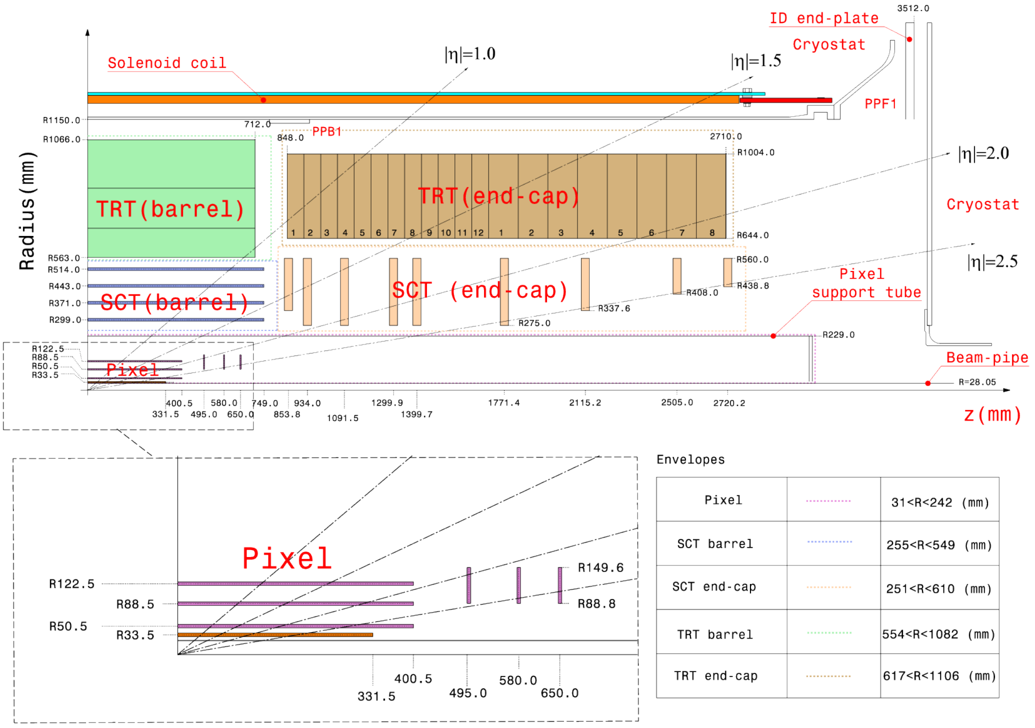

Pixel	┈	31<R<242 (mm)
SCT barrel	┈	255<R<549 (mm)
SCT end-cap	┈	251<R<610 (mm)
TRT barrel	┈	554<R<1082 (mm)
TRT end-cap	┈	617<R<1106 (mm)

Figure 2.8: The r-z cross-sectional view illustrates a quadrant of the ATLAS inner detector. The upper section displays the complete inner detector, while the bottom-left section provides an enlarged view focusing on the pixel detector area. The Insertable B-Layer is highlighted in red in the bottom-left section [66].

finer granularity and proximity to the interaction point improve the Pixel Detector's transverse and longitudinal impact parameter resolution by over 40% [67], leading to better b-tagging performance. With the inclusion of the IBL, the Pixel Detector now provides at least four precise hit measurements for reconstructing particle tracks from the collision point.

2.2.2.2 Semiconductor Tracker

The SCT, located outside the Pixel Detector, consists of 4,088 modules of stereo silicon-strip sensors arranged in four concentric barrel layers covering $|\eta| < 1.4$ and two end-caps with nine disks each covering $1.4 < |\eta| < 2.5$. The sensors consist of two layers of 6 cm long silicon strips, angled at 40 mrad to measure both r and ϕ. Each barrel or disk generates two strip measurements that are combined to create space-points. The SCT is designed to provide at least eight precision measurements (four space-points) for particle tracking.

The SCT offers a transverse resolution of 17 μm and a longitudinal resolution of 580 μm. Silicon strips are used instead of silicon pixels due to the lower expected particle density in the SCT region compared to the Pixel Detector, which helps maintain spatial resolution while limiting the number of readout channels. The SCT's high granularity significantly contributes to the resolution of impact parameters, momenta, and the vertex z-position of the tracks. Due to their proximity to the beam pipe, the Pixel and SCT detectors are exposed to high radiation doses, leading to performance degradation over time. Consequently, a complete replacement of the ID is planned for the Phase-II Upgrade, which will be discussed in Section 2.3.

2.2.2.3 Transition Radiation Tracker

The TRT is the outermost sub-detector in the ID. It consists of 298,304 proportional drift tubes, or straws, each with a diameter of 4 mm. In the barrel region, the straws are aligned parallel to the beam axis, while in the end-cap regions, they are arranged radially in wheel-like structures. The tubes are filled with a gas mixture of 70% xenon, 27% carbon dioxide, and 3% oxygen. An node with 31 m diameter cylinder of tungsten wire is placed in the centre of each tube. The anode is grounded and linked to the front-end electronics, while the inner surface of the tube, which acts as the cathode, is coated with gold and maintained at a potential of -1.5 kV. Each tube functions as a proportional drift chamber. When charged particles pass through the drift tubes, they ionise the gas molecules within the straw, releasing free electrons and creating positive ions. These electrons accelerate toward the anode due to the electric field, generating detectable signals proportional to the energy deposited by the particle. This helps distinguish between particle types, such as electrons from heavier charged hadrons.

Transition radiation is emitted by relativistic particles when they cross the boundary between materials with different permittivity values. Electrons emit more transition radiation compared to pions, and this difference is detected by the TRT, helping in the discrimination between electrons and pions.

The barrel section of the TRT provides (r, z) position information, while the end-caps offer (z, ϕ) information. A passing particle typically interacts with around 36

TRT tubes providing approximately 36 hits per track. Although the precision of the TRT hits is lower than that of the silicon detectors, the higher number of hits contributes to better momentum resolution. While the silicon trackers must be cooled to a temperature between -5° C and -10° C, the TRTs operate at room temperature.

2.2.3 Electromagnetic and Hadronic Calorimeters

The ATLAS calorimeter system is crucial for precisely measuring the energy deposition of hadronic and electromagnetic showers [44]. Most of the particles that leave the ID are supposed to be stopped by the calorimeter system, with the exception of muons and neutrinos. This system is divided into two primary detectors: the Electromagnetic Calorimeter (ECAL) and the Hadronic Calorimeter (HCAL). The ECAL covers the region $|\eta| < 3.2$ and is responsible for measuring the energy of electrons and photons, while the HCAL extends the coverage to $|\eta| < 4.9$ and measures the energy from hadronic showers (jets). The configuration of the ATLAS calorimeter system is shown in Figure 2.9.

In the ECAL, electrons and photons primarily generate electromagnetic showers through high-energy processes like bremsstrahlung and electron-positron pair production, as well as through ionisation at lower energies. On the other hand, hadrons initiate hadronic showers in the HCAL, which are generally more complex and spread out compared to electromagnetic showers. The energy of the initial particle is determined by summing up the energy deposits within the active layers of the calorimeter. For accurate energy measurements, it is essential that hadronic showers are fully contained within the calorimeter, minimising any potential energy loss. Both ECAL and HCAL are sampling calorimeters, meaning they are constructed from alternating layers of absorber material, which induces particle showers, and active material, which provides the signals. Figures 2.10a and 2.10b illustrate the different modules within the ATLAS calorimeter system, which will be described in more details below.

The relative energy resolution of a calorimeter system is typically expressed by the equation:

$$\frac{\sigma_E}{E} = \frac{S}{\sqrt{E}} \oplus \frac{N}{E} \oplus C, \tag{2.9}$$

where the stochastic term, S, reflects the intrinsic fluctuations in the number of particles produced during shower evolution. The term N accounts for pile-up noise and noise from the readout electronics, which is independent of the deposited energy. The constant term, C, addresses systematic effects such as detector mis-calibration and the presence of inactive material within the detector. At low energies, the pile-up noise limits the resolution, while at high energies, the two first terms tend to zero and the constant term becomes the limiting factor.

2.2.3.1 Electromagnetic Calorimeters

The ECAL is divided into three sections: a barrel region ($|\eta| < 1.475$) and two end-cap regions ($1.375 < |\eta| < 3.2$). The barrel consists of two identical half-barrels separated by a small central gap, while each end-cap is divided into two coaxial wheels: an outer wheel covering the range $1.375 < |\eta| < 2.5$ and an inner wheel extending

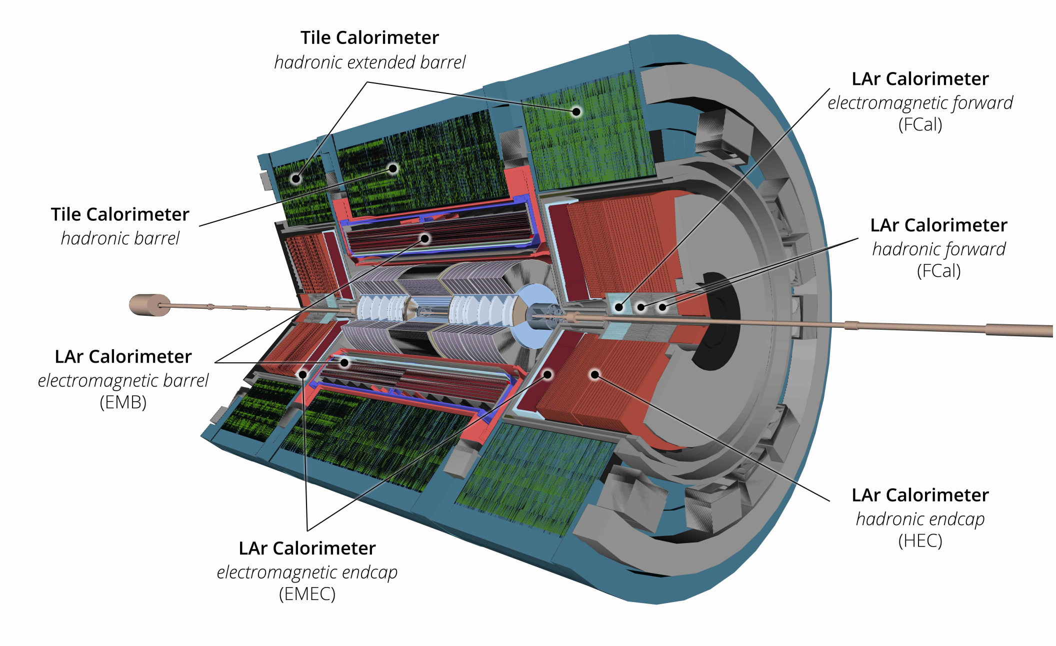

Figure 2.9: Cutaway diagram of the Run 3 ATLAS calorimeter system layout, illustrating the barrel and end-cap regions of the Electromagnetic and Hadronic Calorimeters. The Tile Calorimeter is part of the hadronic calorimeter, consisting of steel plates and plastic scintillating tiles, while the LAr Calorimeter (Liquid Argon) is used for both electromagnetic and hadronic calorimetry [56].

coverage up to $|\eta| = 3.2$.

The ECAL uses lead plates as the absorber material, interleaved with accordion-shaped Kapton electrodes immersed in Liquid Argon (LAr), which serves as the active material. LAr is chosen for its linear response, high ionisation yield, and stability, as well as its resistance to radiation damage, making it ideal for use near the interaction point and in forward regions. The signal detection electronics are arranged in up to three longitudinal sampling layers with granularity varying from (0.003×0.1) to (0.05×0.025) in $(\Delta\eta \times \Delta\phi)$. The ECAL has a total thickness of more than 22 radiation lengths[2] (X_0) in the barrel region and more than 24 X_0 in the end-caps, ensuring efficient absorption of electron and photon showers up to several TeV.

In the region dedicated to precision physics $(|\eta| < 2.5)$, the ECAL is segmented into four longitudinal layers, which are three active layers (EM1, EM2, EM3) and one presampler layer. In the region $|| < 1.8$, the presampler is employed to account for the energy lost by electrons and photons before reaching the main calorimeter. This presampler comprises an active liquid argon (LAr) layer, with a thickness of 1.1 cm in the barrel region and 0.5 cm in the end-cap region. The first active layer, EM1, with a thickness of $4.2X_0$ and a granularity of 0.003×0.1, is optimised for precise position measurements and improved particle identification (improving discrimination between neutral pions and photons); EM2, the thickest layer at $16X_0$, has a granularity of 0.025×0.025 to collect the bulk of the energy deposition; and EM3, with a thickness

---

[2] Radiation length is defined as the mean distance over which the particle loses $1/e$ of its energy and is used to characterise the evolution of an electromagnetic shower in a certain material.

of $2.0X_0$ and a granularity of 0.05×0.025, captures the energy at the tail of the shower.

2.2.3.2 Hadronic Calorimeters

The HCAL consists of the Tile Calorimeter (TileCAL), the LAr Hadronic End-Cap Calorimeter (HEC), and the LAr Forward Calorimeter (FCAL). TileCAL is situated directly outside the ECAL, covering the region $|\eta| < 1.7$, and uses steel as the absorber material with scintillating tiles as the active material. The HEC extends the coverage to $|\eta| < 3.2$ and is composed of two independent wheels in each end-cap, positioned directly behind the ECAL end-caps. These wheels consist of parallel copper absorber plates interleaved with 8.5 mm LAr gaps serving as the active medium. The FCAL is briefly described in the next subsection.

Unlike electromagnetic showers, which are characterised by radiation length X_0, hadronic showers are characterised by interaction length λ_I[3]. The HCAL is designed with a total thickness exceeding 11 λ_I to effectively contain hadronic showers. Each cell in the calorimeter has a granularity of (0.1×0.1) in $(\Delta\eta \times \Delta\phi)$.

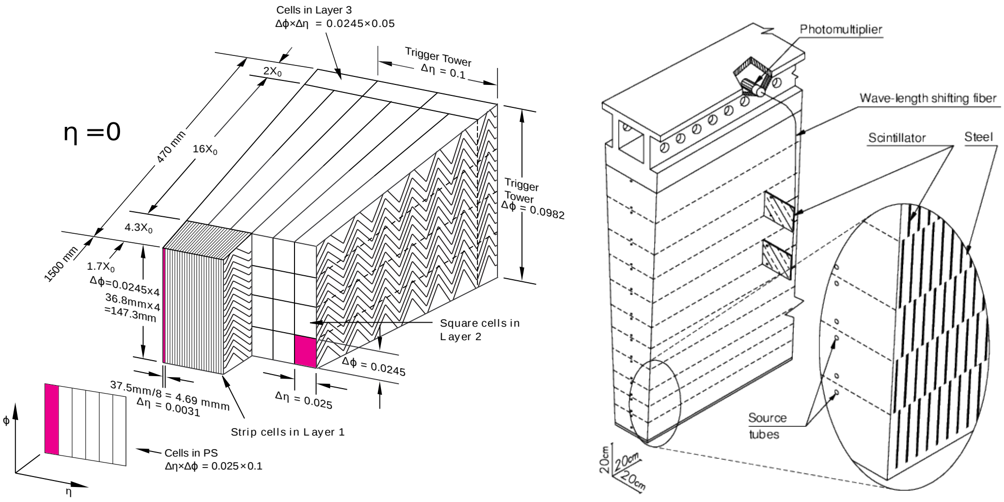

(a) **(b)**

Figure 2.10: Schematics representation of the various modules of the ATLAS calorimeters: the Electromagnetic Calorimeter [68] (a) and the Hadronic Calorimeter [69] (b).

2.2.3.3 Forward Calorimeters

In addition to the calorimeter sub-detectors described above, ATLAS also covers the forward region with $3.1 < |\eta| < 4.9$ with the forward calorimeter (FCAL), which is a combination of an electromagnetic and hadronic calorimeter system. The FCAL is a sampling calorimeter composed of three modules in each end-cap. The innermost module uses copper as the absorber and is optimised for electromagnetic detection, while the other two modules use tungsten as the absorber, optimised for hadronic

---

[3] Interaction length is defined as the average distance a hadron travels before its energy is reduced by $1/e$

showers. The FCAL is designed with a high-density material structure to manage the high particle flux in this region and has a depth of approximately 10 λ_I.

2.2.4 Muon Spectrometer

The Muon Spectrometer (MS), positioned around the calorimeter system, is the outermost and largest sub-detector of the ATLAS experiment. It is specifically designed for identifying and measuring the momenta of muons, the only charged particles expected to traverse the calorimeters. The MS extends to a radius of up to 11 meters and covers a pseudorapidity range of $|\eta| < 2.7$. Muon tracking within the MS relies on the deflection of muons in the presence of a magnetic field generated by toroidal magnets. These magnets consist of a barrel toroid providing a 1 T magnetic field in the $|\eta| < 1.4$ region and end-cap toroids producing a 0.5 T field in the $1.6 < |\eta| < 2.7$ region. In the transition region, $1.4 < |\eta| < 1.6$, the magnetic field is a combination of the fields generated by both the barrel and end-cap toroids.

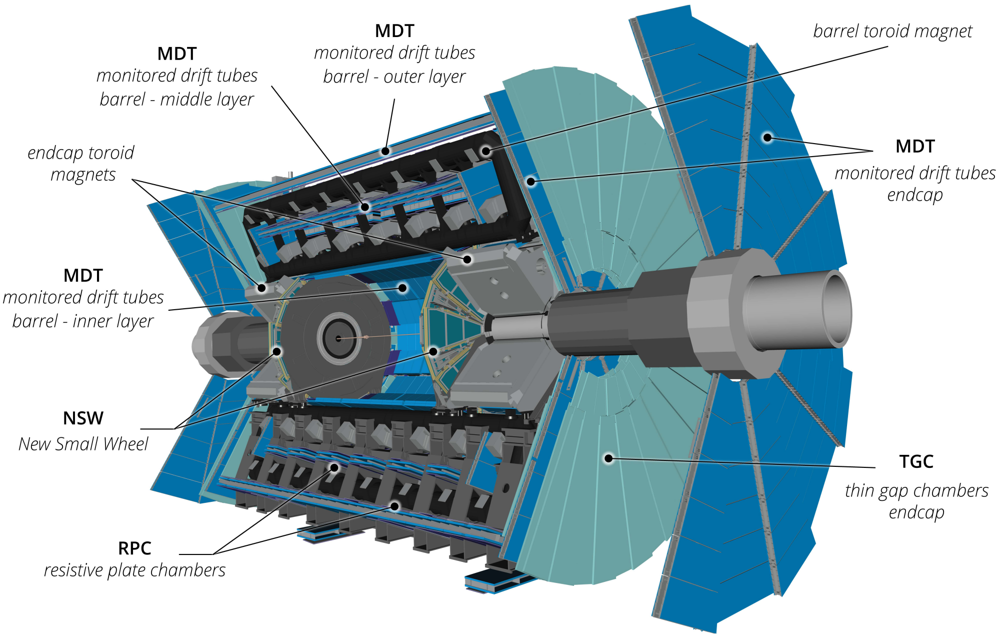

Figure 2.11: Cut-away view of the Run 3 ATLAS muon system layout. The muon system is built around an air-core toroidal magnet system. The main muon detector components upgraded for Run 3 (e.g., the NSW) are visible [56].

The MS is composed of four types of muon chambers: two in the central barrel region and two in the forward region of the detector. Each region includes a chamber system dedicated to precise momentum measurements and another designed for fast response times with less granularity, which is used primarily for ATLAS trigger system. The muon chambers include the Monitored Drift Tubes (MDT), Cathode Strip Chambers (CSC), Thin Gap Chambers (TGC), and Resistive Plate Chambers (RPC). The layout of the Muon Spectrometer is shown in Figure 2.11.

The MDT provide precise measurements of the momentum in the pseudorapidity range $|\eta| < 2.7$, with exception of the innermost end-cap layer where its coverage extents only up to $|\eta| < 2$. In this region the CSC are used instead, due to their higher rate capability and time resolution. The two fast trigger chambers TGC and RPC are used to complement the tracking, the RPC in the barrel region ($|\eta| < 1.05$) and the TGC in the end-cap ($1.05 < |\eta| < 2.4$). These trigger chambers are capable of generating track information within a few tens of nanoseconds after the passage of the particle, as well as bunch-crossing identification.

The MS can operate independently from other sub-detectors, enabling it to perform stand-alone measurements. This is essential for fast event triggering and redundancy removal in pattern recognition. The MS is optimised to deliver high transverse momentum resolution for muons, along with excellent charge identification across a wide momentum range, from 3 GeV to 3 TeV. At lower energies, the resolution is further improved and the overall performance of the MS is significantly enhanced by integrating track information from the ID with MS measurements.

2.2.4.1 New Small Wheels

The New Small Wheels (NSW) [56, 70, 71] are part of the Phase-I upgrade to the ATLAS detector, designed to enhance the precision and efficiency of muon detection. These two large, wheel-shaped detectors are positioned on opposite ends of the ATLAS experimental cavern, replacing the first end-cap station from Run 2's muon MS system. Installed in 2021, the NSW improves the trigger capabilities, particularly for events involving muons, in preparation for the HL-LHC era (Section 2.3.2).

The NSW employs two advanced gaseous detector technologies: Micromegas (MM) and small-strip Thin Gap Chambers (sTGC). Both of these technologies provide robust tracking and triggering functionalities, designed to cope with the increased collision rates. Each NSW contains eight layers of Micromegas and eight layers of sTGC, covering a total active area exceeding 2500 m^2. The NSW detectors have spatial resolutions of less than 100 m per detection plane. This allows the NSW detectors to provide the muon trigger system with reconstructed track segments of high angular precision (less than 1 mrad), enabling clear identification of whether triggered muons originate from the collision point. The Micromegas detectors have a very fine strip pitch, less than 0.5 mm, whereas the sTGCs has a strip pitch of 3.2 mm. The combination of MM and sTGC provides a fast and precise performance that can meet the demands of both Run 3 and the future upgrades and is essential for both online triggering and offline tracking.

2.2.5 Magnet System

The ATLAS magnet system consists of a central solenoid [72] and a toroidal magnet system [73, 74], each producing a magnetic field in different sub-systems: the central solenoid provides a longitudinal magnetic field for the ID, while the toroidal magnets generate the magnetic field for the MS. This design allows ATLAS to achieve pseudorapidity coverage up to $|\eta| < 3$ while ensuring that the magnetic field remains zero within the calorimeters. This is important since the presence of a magnetic field in the calorimeters would decrease their performance. Liquid helium at 4.5 K is used to cool down all superconducting magnets. A schematic layout of the ATLAS magnet system is shown in Figure 2.12.

The central solenoid [72] is a superconducting magnet situated between the ID and the ECAL. It measures 5.8 m in length, with an inner diameter of 2.46 m and an outer diameter of 2.56 m. The solenoid generates an axial magnetic field of 2 T at the centre of the ID. This magnetic field is carefully optimised to minimise interactions with particles traversing the solenoid and be as transparent as possible. The strong and uniform magnetic field causes high-energy particles to bend in the ϕ direction, allowing for precise momentum measurements within the acceptance of the tracking system. Additionally, low momentum particles (below a few hundred MeV) are likely to loop repeatedly in the magnetic field, making them unlikely to be detected. The finite dimensions of the solenoid, makes the magnetic field strength to decrease as the distance from the interaction point increases along the z-axis.

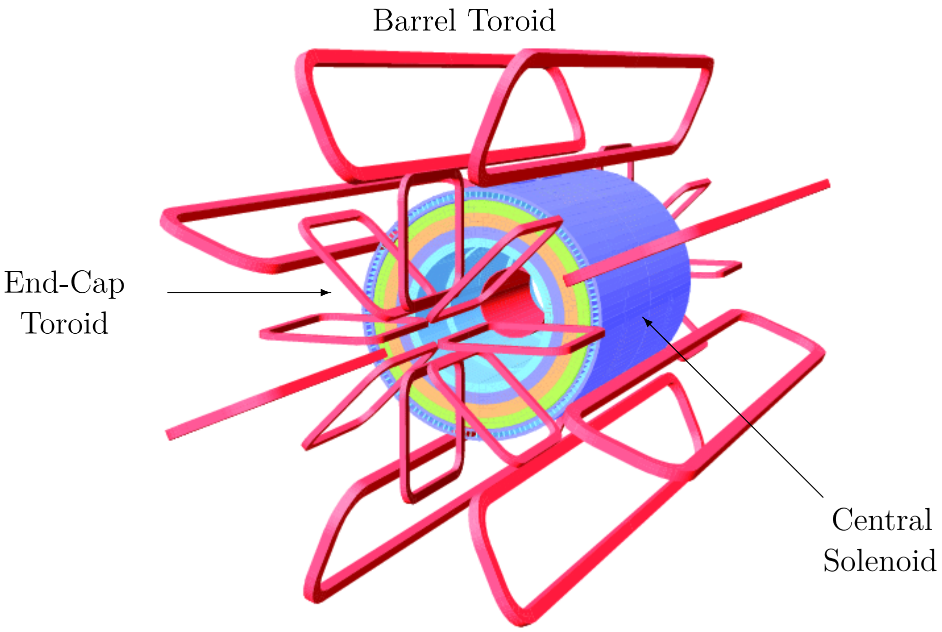

Figure 2.12: Schematic representation of the ATLAS magnet system. The figure illustrates the barrel toroid, the two end-cap toroids and the central solenoid. The central solenoid lies inside the calorimeter volume [44].

The toroidal magnet system [73, 74] is located around the HCAL and inside the MS. It provides complete angular coverage using three large air-core toroids: a barrel toroid and two end-cap toroids. The system generates a magnetic field of 1 T in the barrel region and 0.5 T in the end-cap region in the MS region. Each toroid consists of eight air-core superconducting coils. The barrel toroid system measures 25.3 m in length, with an inner diameter of 9.4 m and an outer diameter of 20.1 m. The end-cap toroids are 5 m deep, with an inner diameter of 1.6 m and an outer diameter of 10.7 m.

The barrel toroid generates magnetic bending in the pseudorapidity range $|\eta| < 1.4$, while the end-cap toroids cover the range $1.6 < |\eta| < 2.7$. Magnetic field present in the region between $1.4 < |\eta| < 1.6$, known as the transition region, is produced from the combined fields of both the barrel and end-cap toroids.

2.2.6 Trigger and Data Acquisition System

Given the immense data produced by the LHC, which results in roughly 10^9 proton collisions per second, it is impractical to record all the generated information. With a design bunch-crossing frequency of about 40 MHz and the ATLAS detector capable of writing events to permanent storage at a rate of only about 1 kHz, a highly selective two-level triggering system is essential. This system must efficiently identify and record events with significant physics signatures, such as high-p_T leptons, photons, jets, or substantial missing transverse momentum, while discarding events involving low-momentum parton interactions. The Trigger and Data Acquisition system (TDAQ) [75–77] is responsible for this real-time event selection, effectively filtering out less relevant events and reducing the massive data volume to a manageable size. The ATLAS TDAQ system, illustrated in Figure 2.13, consists of a hardware-based first-level trigger (L1) and a software-based high-level trigger (HLT).

The L1 trigger processes a subset of information from the calorimeters and the MS to make an initial event selection. Due to the large number of channels and the associated long readout time, data from the ID is not considered at this stage. The trigger identifies specific detector coordinates in η and ϕ, where objects are detected, marking these as regions of interest (RoI). The coordinates, event type, and energy details are stored in the RoI data, which is subsequently used by the HLT. The L1 trigger makes a decision within less than 2.5 μs after the bunch crossing, reducing the input event rate from approximately 40 MHz to around 100 kHz. If an event is accepted by the L1 trigger, the event information is read out from the detectors' pipeline memories and stored in read-out buffers before it is further processed by the HLT.

In the HLT, data from the RoIs and the full event are processed using fast, offline-like reconstruction and selection algorithms. This processing leverages high-granularity calorimeter information, tracking data from the ID, and precision measurements from the MS. The enhanced granularity and additional information allow for refined threshold cuts and improved particle identification based on more accurate energy deposition and track reconstruction information. Additionally, the HLT applies object calibration and alignment corrections. The event rate is reduced from the L1 input of 100 kHz to about 1 kHz, with the HLT processing each event in an average of 0.2 s. Events selected by the HLT are then stored to be used in analysis.

A series of trigger chains are used to configure the trigger system, which define the sequence of reconstruction and selection steps from L1 to HLT. Trigger rates can be adjusted by modifying the selection criteria and thresholds applied to detected objects. To keep the maximum HLT output rate at 1.5 kHz, trigger thresholds may be increased, or triggers may be pre-scaled by a factor N, meaning that only one out of every N events meeting the selection criteria is accepted for readout. This pre-scaling determines the fraction of events retained out of those that would have passed the trigger requirements.

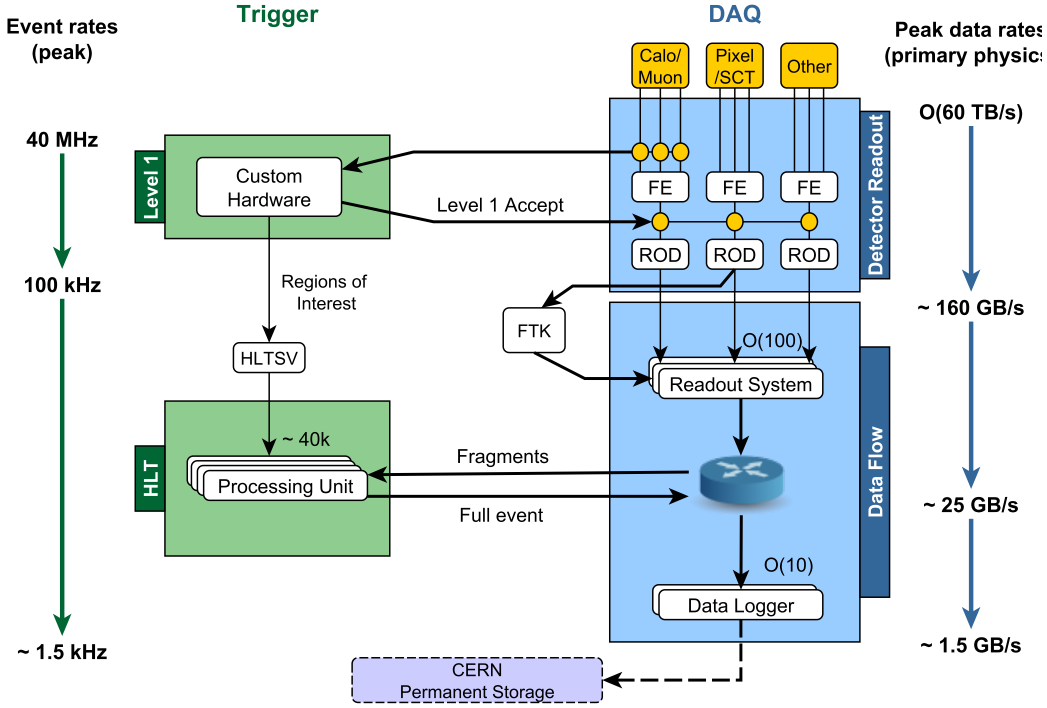

Figure 2.13: ATLAS Trigger and Data Acquisition system flow in Run 2. the figure shows the expected peak rates and bandwidths through each component [78].

2.3 Phased Upgrade for High-Luminosity

After about sixteen years of operation period, the LHC has performed exceptionally well to date and has already undergone a series of upgrades. ATLAS has outlined a phased upgrade plan for the detector to enhance its capability to handle higher instantaneous luminosity and deal with degradation of their components because of the accumulated radiation damage [79].

Phase-I of this plan, which prepared ATLAS for Run 3, has already been completed and its upgrades were discussed intrinsically in this chapter. Notable upgrades include the installation of the New Small Wheel forward muon detector (Section 2.2.4.1) and improvements to the trigger and data acquisition system, particularly increasing trigger granularity in depth and η through updates to the calorimeter electronics. The upgrade now continues with Phase-II [80], which focuses on preparing ATLAS for the High-Luminosity LHC era, as detailed in below.

The current Run 3 campaign plans to double the total integrated luminosity achieved by Runs 1 and 2 combined, targeting an instantaneous luminosity of about $L = 3 \times 10^{34}\,\text{cm}^{-2}\,\text{s}^{-1}$ and approximately 350 fb^{-1} of integrated luminosity, with more than 80 simultaneous collisions per bunch crossing and a 25 ns bunch spacing. Now the phased plan continues with Phase-II [80], which targets the HL-LHC era (detailed in Section 2.3.2).

2.3.1 High-Luminosity Large Hadron Collider

The High-Luminosity Large Hadron Collider (HL-LHC) [13–15] project represents a significant upgrade to the current LHC, aiming to enhance its performance and increase its potential for new physics discoveries. Scheduled to start in 2029, the HL-LHC intends to boost the instantaneous luminosity by at least a factor of five beyond the original design value. This increase in luminosity will enable the HL-LHC to collect a dataset approximately ten times larger than what is anticipated for LHC baseline programme. The timeline for the LHC baseline programme and the HL-LHC upgrade, is shown in Figure 2.14.

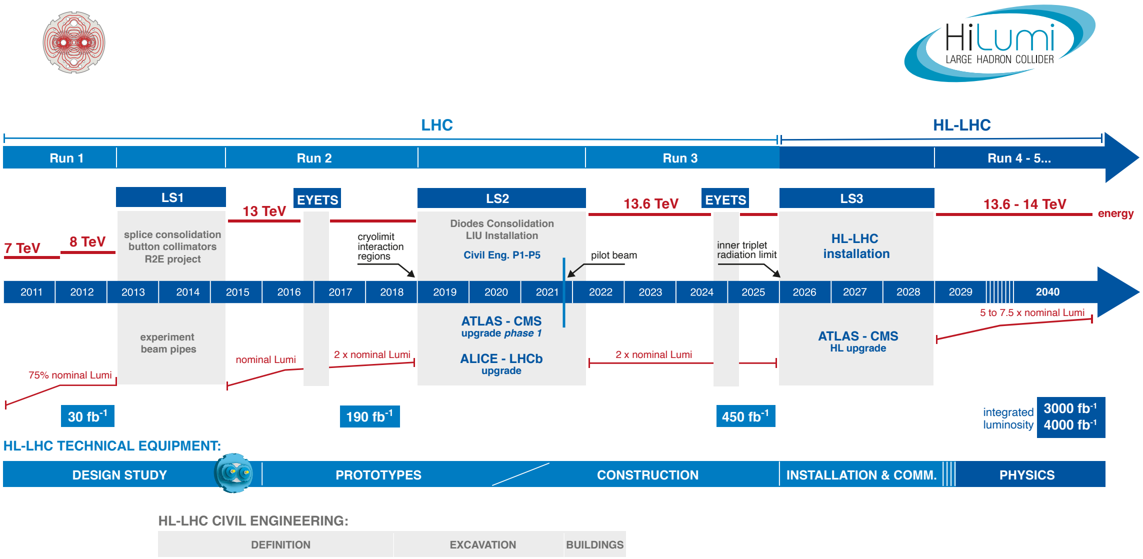

Figure 2.14: LHC plan for the next decade and beyond showing the energy of the collisions and the luminosity. After the third long shutdown (LS3) the machine will be in the High Luminosity configuration [13, 81].

By the time the HL-LHC begins operation, the ATLAS experiment will have gathered a dataset corresponding to an integrated luminosity of more than 300 fb^{-1}. Over an estimated 10-year operating period, the HL-LHC is expected to deliver an integrated luminosity of 3000 fb^{-1}, achieving an instantaneous luminosity of 7.5×10^{34} cm^{-2}s^{-1} and exceeding 300 fb^{-1} per year. Collisions are expected to occur at a center-of-mass energy of $\sqrt{s} = 14$ TeV, with a pile-up environment of 140-200 simultaneous events and a bunch spacing of 25 ns.

The increase in luminosity will result in more collisions per bunch crossing, thereby increasing the amount of collected data. This will significantly increase the experimental precision of SM measurements, provide access to rare processes not previously observed, and improve critical measurements for exploring BSM physics. For instance, the precision in measuring the Higgs boson's coupling to SM particles is expected to improve to the point where new physics effects could be seen. Moreover, as discussed in Section 3.4.3 the HL-LHC will probe Higgs pair production, enabling the study of the Higgs trilinear self-coupling, which will offer insights into the Higgs potential and the Electroweak Symmetry Breaking (EWSB) mechanism.

2.3.2 Phase-II Upgrade

After Run 3, during the LS3, ATLAS will embark on the Phase-II upgrade programme to prepare for the HL-LHC. The LHC will require upgrades or even replacement of many detector components to deal with the severe radiation doses and high particle production rates, in order to maintain the excellent performance and reach the project expectations. Key elements of the Phase-II upgrade include changes in both tracking and trigger systems, as well as further upgrades of detector components and software.

A new subsystem, the High Granularity Timing Detector (HGTD), will enhance track-vertex association in the forward region ($2.4 < |\eta| < 4.0$) by integrating timing measurements into the tracking. It will be composed of Low-Gain Avalanche Detectors (LGAD) with a time resolution of about 30 ps. The two HGTD disks will be placed between the Inner Tracker (ITk) (described in Section 7.1) and the calorimeter end-caps and will also be used for online and offline luminosity measurements.

Additionally, the Phase-I TDAQ upgrade [82] was designed to efficiently select and record events of interest at instantaneous luminosities that are up to twice that of the nominal LHC design luminosity with up to 80 proton-proton collisions per beam crossing, while maintaining trigger thresholds close to those used in Run 1. The TDAQ system will feature a new single-level hardware trigger, known as Level-0, which receives inputs from both the calorimeter (L0Calo) and the muon system (L0Muon). The result of the Level-0 trigger decision is transmitted to all detectors and trigger processors at the rate 1 MHz (as opposed to 100 kHz in the LHC period) with the latency of 10 s. The current calorimeter trigger processors will be supplemented with new hardware that can execute more sophisticated, offline-like algorithms to improve background rejection. An event filter system will select events using a farm of commodity processors alongside a custom Hardware Tracking for Trigger (HTT) co-processor, which helps to reduce the overall CPU load.

The readout electronics of both the LAr and Tile calorimeters will be upgraded due to their limited radiation tolerance and the inability of their on-detector front-end electronics to handle the higher trigger rates and latencies expected during Phase-II to support the redesign of TDAQ system [83]. The hardware-based tracking performed by the upgraded trigger system will also profit from the extended coverage of the planned ITk.

Finally, the current ID will be entirely replaced with a completely new all-silicon tracker, ITk, that offers extended rapidity coverage. The ITk will be composed of pixel layers for optimal tracking near the interaction point with higher granularity for pileup and fake rejection, as well as a strip system to ensure accuracy at larger radii. The ITk detector will be detailed in Chapter 7, together with its performance requirements and motivation. The track reconstruction of charged particles will also become a greater computational challenge, motivating the development of more efficient algorithms. Part of this thesis focuses on tracking software development for the ITk detector as part of the ATLAS Phase-II Upgrade. In Chapter 9, some upgrades related to the tracking of charged particles will be discussed, along with a motivation for the proposed improvements. One of these upgrades is related to the adoption of the ACTS tracking software (Section 9.1) in the current ATLAS software.

Part II

The First ATLAS Search for $t\bar{t}HH$ Production

“If you truly love nature, you will find beauty everywhere.”
Vincent Van Gogh

3

From Higgs Pair Production to $t\bar{t}HH$ and Beyond

Contents

The study of Higgs boson pair production, or di-Higgs (HH) production, is essential for probing the fundamental properties of the Higgs boson and understanding the shape of the Higgs potential, particularly the trilinear Higgs self-couplings. Since the discovery of the Higgs boson in 2012 (Section 1.2.3), significant efforts have been made to measure its interactions and couplings with other particles, but the self-interactions have not been measured to date. The self-coupling is critical for confirming the dynamics of the Higgs potential and Electroweak Symmetry Breaking (described in Section 1.1.3), providing a unique window to study potential BSM effects.

The current chapter describes the motivation for di-Higgs searches in Section 3.1, followed by a review of Higgs pair production at the LHC in Section 3.2.1. Section 3.4 describes the state of the art of HH analysis highlighting both resonant and non-resonant HH searches for Run 2, along with prospects for the HL-LHC. Section 3.5 describes the top-quark phenomenology at the LHC and, finally, Section 3.6 concludes with a motivation for the $t\bar{t}HH$ search.

3.1 Motivation for HH Searches

As introduced in Chapter 1, after Electroweak Symmetry Breaking (EWSB) [7–12] the Higgs potential is given by

$$V_H = \frac{1}{2}m_H^2 H^2 + \lambda_{HHH}H^3 + \lambda_{HHHH}H^4, \tag{3.1}$$

where m_H is the Higgs boson mass and λ_{HHH} and λ_{HHHH} are the trilinear and quartic Higgs self-couplings, respectively. The trilinear and quartic couplings are predicted, according to the SM, to be $\lambda_{HHH}^{SM} = \frac{m_H^2}{2v}$ and $\lambda_{HHHH}^{SM} = \frac{m_H^2}{8v^2}$, where v is the vacuum expectation value (vev) of the Higgs field. This value is given by $v = 2M_W/g = (\sqrt{2}G_F)^{-1/2} \approx 246.22\,\text{GeV}$, where M_W is the mass of the W boson, G_F the reduced Fermi constant, and g the weak isospin coupling. After the measurement of Higgs mass m_H all the free parameter of the SM were known. However, BSM effects may allow for corrections to the trilinear and quartic couplings, as well as higher order terms in the EWSB potential.

In order to determine the exact structure of the potential, it is necessary to measure the self-coupling of the Higgs boson directly. A promising probe to directly access the trilinear Higgs coupling is the production of a pair of Higgs bosons. This is an extremely rare process that has not been observed before and whose expected production rate is approximately 1000 times smaller than that of a single Higgs boson. Because of its small effective cross-section and overwhelming background, the current Run 3 of the LHC is expected to be sensitive probably only to possible enhancements of the self-coupling. The SM value of the coupling is expected to be accessed before the end of Run 4 after the Phase-II upgrade. The quartic coupling and the complete understanding of the shape of the potential will probably require an even longer time scale, beyond the reach of the HL-LHC, but may be possible with future colliders.

3.2 Higgs Pairs at the LHC

3.2.1 Higgs Pair Production Modes at the LHC

The dominant processes for the production of Higgs boson pairs in pp collisions at the LHC at $\sqrt{s} = 13$ and 13.6 TeV are similar to the ones presented in Section 1.2.1 for single Higgs production but with the addition of a second radiated on-shell Higgs. In order of decreasing effective cross section, these are: gluon-gluon fusion (ggF), vector boson fusion (VBF), and associated production with top quarks ($t\bar{t}HH$) or vector bosons (VHH). Figures 3.1 and 3.2 show examples of leading-order (LO) Feynman diagrams for ggF and VBF production modes, respectively. The theoretical cross-section for each production mode is shown in Figure 3.3 as a function of the LHC center-of-mass energy $\sqrt{s}$ for $m_H = 125$ GeV. Different Feynman diagrams contribute to the production mechanisms, and some do not necessarily include any Higgs self-coupling. The diagrams also largely interfere with each other, and deviations from the SM couplings lead to significant changes in the predicted kinematic distributions.

In the case of ggF, the process is mediated by top quark loops (due to its larger mass) and a smaller contribution from bottom quark loops. The box diagram in Figure 3.1a destructively interferes with the triangular one in Figure 3.1b, which includes the Higgs self-coupling. The interference effect can be seen in the distribution of the invariant mass of the Higgs pair from Figure 3.4 as well as in the individual contribution of each diagram, accounting for a reduction of about 50% compared to the box-only diagram.

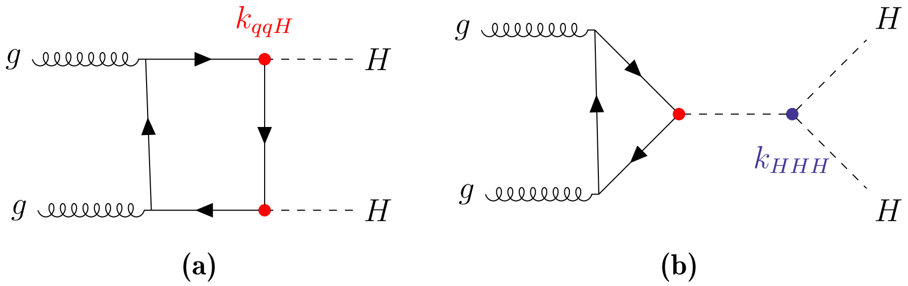

Figure 3.1: Feynman diagrams at LO of gluon-gluon fusion production mode for pairs of Higgs bosons at the LHC.

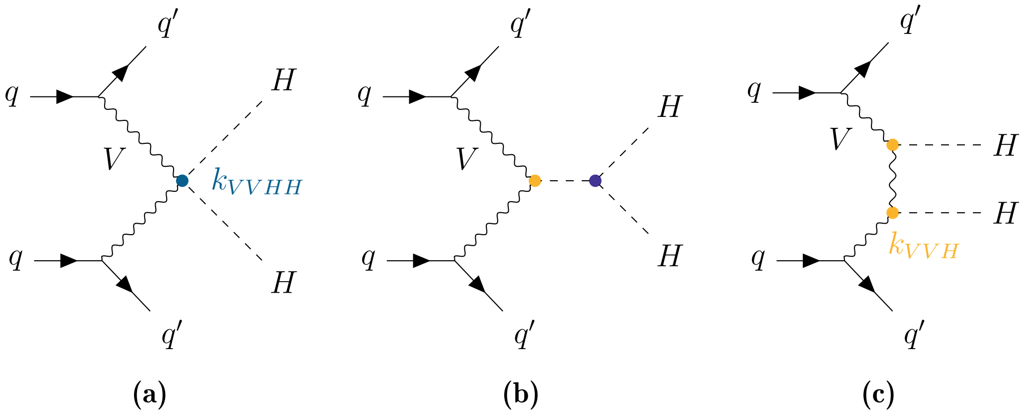

Figure 3.2: Feynman diagrams at LO of the vector boson fusion production mode for pairs of Higgs bosons at the LHC.

The VBF process involves the radiation of two Higgs from the exchange of virtual W or Z bosons from the interaction of two quarks in the initial state, which will scatter to the final state and form two jets. It may also include diagrams involving the trilinear coupling (Figure 3.2b), in which a single off-shell Higgs boson splits into a Higgs pair. The VBF is the second largest production mechanism, but can be surpassed by $t\bar{t}HH$ for large values of center-of-mass energy. In addition to the Higgs self-coupling (HHH), the VBF process also involves the Higgs-boson-vector-boson coupling (VVH) and quartic Higgs-boson-vector-boson coupling ($VVHH$).

The inclusive ggF, VBF and $t\bar{t}HH$ cross-sections for Higgs boson pair production are reported in Table 3.1 for different centre-of-mass energies and the most accurate theoretical precision recommended by ATLAS to date.

Modifications of the EWSB potential in Equation 3.1 are predicted by BSM theories. Some BSM anomalies in the Higgs boson couplings and/or interactions could affect the

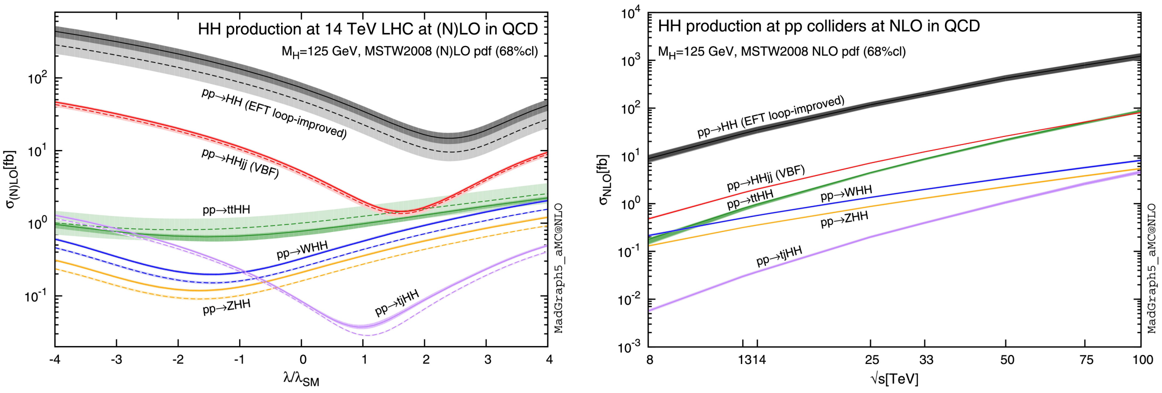

(a) **(b)**

Figure 3.3: Total cross sections for HH production models at LO and next-to-leading order (NLO) in QCD, shown as a function of the self-coupling (a) and as a function of the center-of-mass energy (b). The dashed lines and light-coloured bands represent LO results, while the solid lines and dark-coloured bands correspond to NLO results [84, 85].

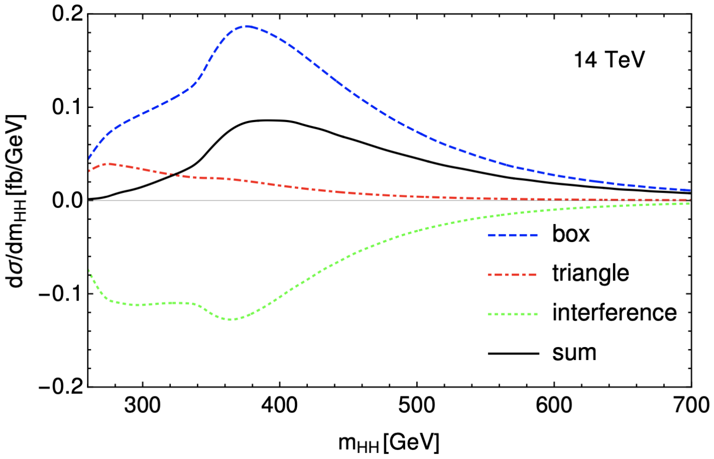

Figure 3.4: Higgs pair invariant mass distribution at LO for the different contributions to the ggF production mode and their strong destructive interference effect [85].

production rate of Higgs boson pairs, which could be increased by more than an order of magnitude and even be observed with the current LHC luminosity.

3.2.2 Higgs Pair Decay Modes

The main HH decay channels and their branching ratios are represented in Figure 3.5. At the LHC, the most sensitive HH final states are usually the ones that provide a good trade-off between large branching ratio and clean final state. For example, when one Higgs decays to a final state containing photons or leptons, that provide a clean and precise signature, and the other Higgs decays to bottom quarks to maximize the total branching fraction. The most promising channels for the HH searches are $HH \to b\bar{b}b\bar{b}$, $HH \to b\bar{b}\gamma\gamma$ and $HH \to b\bar{b}\tau^+\tau^-$.

Table 3.1: Cross-sections in fb for the three main HH production modes at different center-of-mass energies with their relative uncertainties and QCD order of the calculation. The first uncertainty is the scale uncertainty, while the second represents the PDF + α_s uncertainty. The Higgs boson mass of $m_H = 125$ GeV is assumed in the calculations. The ggF cross-sections are calculated using the FT approximation in which the real radiation matrix elements contain the full top quark mass dependence, while the virtual part is calculated at NLO [86–90].

$\sigma_{\text{prod.}}$ (fb)	$\sqrt{s} = 13$ TeV	$\sqrt{s} = 13.6$ TeV	$\sqrt{s} = 14$ TeV	Theoretical precision
ggF	$30.77^{+2.2\%}_{-5.0\%} \pm 2.3\%$	$34.13^{+2.1\%}_{-4.9\%} \pm 2.3\%$	$36.37^{+2.1\%}_{-4.9\%} \pm 2.2\%$	NNLO $\text{FT}_{\text{approx}}$
VBF	$1.687^{+0.05\%}_{-0.04\%} \pm 2.7\%$	$1.874^{+0.05\%}_{-0.03\%} \pm 2.7\%$	$2.005^{+0.05\%}_{-0.03\%} \pm 2.7\%$	N3LO QCD + NLO EW
$t\bar{t}HH$	$0.756^{+4.3\%}_{-15.0\%} \pm 3.4\%$	$0.860^{+4.2\%}_{-14.0\%} \pm 3.3\%$	$0.934^{+3.9\%}_{-13.6\%} \pm 3.2\%$	NLO QCD

The $HH \to b\bar{b}b\bar{b}$ final state benefits from the largest branching fraction (around 33.9%) of HH production. However, it suffers from the presence of an overwhelming multijet background. The $HH \to b\bar{b}\gamma\gamma$ decay channel has a low branching fraction of around 0.3%, but the final state can be fully reconstructed and can be easily distinguished from the background, due to the excellent trigger and reconstruction efficiency of photons, and excellent invariant mass resolution. The $HH \to b\bar{b}\tau^+\tau^-$ channel presents a more significant branching fraction (around 7.3%) when compared to the $HH \to b\bar{b}\gamma\gamma$, and a smaller background when compared to the $HH \to b\bar{b}b\bar{b}$ channel. This channel is a good compromise between rate and background contamination, and yields the most stringent limits to date on HH production from an ATLAS search using an individual channel [91].

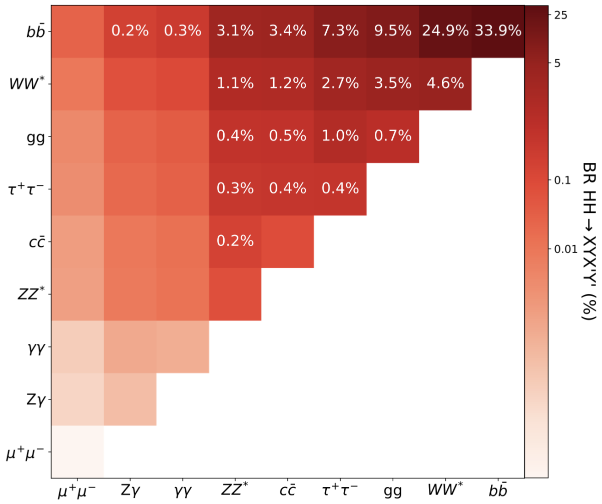

Figure 3.5: Branching ratios of a selected group of decay modes of Higgs pairs evaluated for the SM Higgs boson with $m_H = 125.09$ GeV [85].

3.3 Effective Field Theory Interpretations

If new physics exists at a high energy scale such that the new particles cannot be directly observed at current collider energies, their effects can still manifest as small corrections at lower energies. These corrections may lead to observable deviations from SM expectations. Effective Field Theories (EFTs) provide a general way to parameterise deviations from the SM and explore possible extensions without considering any specific new physics model. Two widely used EFT models are the Standard Model Effective Field Theory (SMEFT) and the Higgs Effective Field Theory (HEFT). These frameworks allow for the exploration of new physics in the HH sector that might modify the Higgs potential or introduce new interactions that affect the HH production cross-sections and branching ratios.

3.3.1 Standard Model Effective Field Theory

In SMEFT [92], the SM is extended by including higher-dimensional operators that represent the effects of BSM physics. To capture the impact of new particles and interactions occurring at energy scales beyond the reach of current experiments, these effects are parameterised in terms of the known SM fields. The expansion of the SM Lagrangian, suppressed by powers of the new physics scale Λ, is given by:

$$\mathcal{L}_{\text{SMEFT}} = \mathcal{L}_{\text{SM}} + \sum_i \frac{C_i^{(6)}}{\Lambda^2} \mathcal{O}_i^{(6)} + \sum_i \frac{C_i^{(8)}}{\Lambda^4} \mathcal{O}_i^{(8)} + \ldots \tag{3.2}$$

where $\mathcal{L}_{\text{SM}}$ is the SM Lagrangian, and $\mathcal{O}_i^{(n)}$ are higher-dimensional operators with free parameters C_i, known as Wilson coefficients, that describe the unknown physics at scale Λ. The value of Λ is also a free parameter, typically set to 1 TeV. All Wilson coefficients are set to zero in the SM. The leading effects of interest come from dimension-6 operators, as they can modify interactions such as Higgs couplings, gauge boson interactions, and fermion interactions. Dimension-5 operators are not considered because they violate lepton number conservation, while dimension-7 operators violate the conservation of the difference between baryon and lepton numbers. Dimension-8 operators are suppressed by higher powers of Λ and are assumed to have negligible effects.

3.3.2 Higgs Effective Field Theory

In the HEFT framework [93–96], the Lagrangian is determined according to the description of chiral perturbation theory, with the low-energy dynamics of electroweak symmetry breaking described using a non-linear realisation of $SU(2)_L \times U(1)_Y$ where the Higgs field is treated as a singlet. In this approach, anomalous Higgs boson couplings are expected to play a leading source of new physics within the electroweak sector. Unlike in SMEFT, these couplings are defined to separately account for interactions with a single Higgs boson and Higgs boson pairs, making HEFT more suitable for simplified interpretations of HH production.

The relevant terms for HH production of the HEFT Lagrangian[1] are given by [93]:

$$\mathcal{L}_{\text{HEFT}} = -\frac{m_t}{v}\left(c_{tth}h + c_{tthh}\frac{h^2}{v}\right)\bar{t}t - c_{hhh}\frac{m_h^2}{2v}h^3 + \frac{\alpha_s}{8\pi v}\left(c_{ggh}h + c_{gghh}\frac{h^2}{v}\right)G^{\mu\nu}G_{\mu\nu} \quad (3.3)$$

with α_s the strong coupling constant to the gluons. The Wilson coefficients c_{hhh}, c_{tth}, c_{ggh}, c_{gghh}, and c_{tthh} represent the coupling modifiers for the Higgs boson self-coupling, the top-quark Yukawa coupling, as well as the ggH, $ggHH$ and $ttHH$ vertices, respectively. The HEFT Lagrangian reduces to the SM Lagrangian when the Wilson coefficients take the following values: $c_{hhh} = c_{tth} = 1$ and $c_{ggh} = c_{gghh} = c_{tthh} = 0$.

The HH production is the most promising process for measuring the Higgs self-coupling, as it provides direct access to c_{hhh} at tree level. Additionally, the HH process uniquely allows for probing the two other Wilson coefficients, c_{gghh} and c_{tthh}. Single Higgs processes, on the other hand, offer better sensitivity to the remaining two coefficients, c_{ggh} and c_{tth}. The $t\bar{t}HH$ production can give direct sensitivity to the c_{tthh} coupling, as will be described in Section 3.6.

3.4 Searches for Higgs Pair Production

This section presents the status of ATLAS searches for di-Higgs production. The searches conducted so far by ATLAS and CMS at the LHC cover distinct decay channels and target SM process and also some BSM scenarios with enhanced Higgs pair production. To date, no searches have achieved sufficient statistical significance to report the measurement of this process in the SM, nor have they found a significant deviation from the expected SM values. These searches led to upper limits on the effective cross-section of HH production and Higgs self-coupling in the SM and values of the BSM parameters.

3.4.1 Resonant and Non-resonant HH Searches

The searches for HH production conducted by the ATLAS and CMS experiments are usually divided into resonant and non-resonant searches. Resonant searches are performed considering that a new massive intermediate particle is produced, which subsequently decays to pairs of Higgs bosons, creating a distinct peak in the Higgs boson pair invariant mass. For a new heavy particle to decay to pairs of Higgs bosons, it must be either a scalar (spin-0) itself or a massive spin-2 particle to preserve the total angular momentum along the decay axis. Several models of new physics that account for extended Higgs sectors, e.g. minimal-super-symmetric models (MSSM) and two-Higgs doublet model (2HDM), predict the existence of multiple Higgs bosons; some are neutral and can mix with the observed 125 GeV Higgs boson. As an example, the 2HDM contains additional CP even and odd scalars that are good candidates for these resonances. The analysis can also be model-independent, searching for enhancements to the HH production through the presence of a generic scalar particle.

Non-resonant searches look for evidence of HH production, aim to measure the

---

[1] Also referred to as non-linear chiral EW Lagrangian.

trilinear Higgs boson self-coupling, and eventually unveil potential deviations of the production cross-section from the SM predictions. In this case, new physics contributions can be described in an EFT framework adding BSM terms, assuming that the contributing new particles are significantly heavier than the scales assessed experimentally.

3.4.2 Full Run 2 HH Combination

Six analyses searching for HH production decaying into the $b\bar{b}\tau^+\tau^-$, $b\bar{b}\gamma\gamma$, $b\bar{b}b\bar{b}$, multilepton and $b\bar{b}ll+E_T^{\text{miss}}$ final states using full Run-2 dataset of up to 140 fb^{-1} at a center-of-mass energy $\sqrt{s} = 13$ TeV were combined [91] for ggF and VBF non-resonant production, achieving an observed (expected) limit on the HH production rate of 2.9 (2.4) times the SM expectation at 95% CL. The ratio $k_\lambda = \lambda_{HHH}/\lambda_{HHH}^{SM}$ of the Higgs boson self-coupling to its SM value, as well as the quartic $HHVV$ coupling modifier $k_{2V} = \lambda_{HHVV}/\lambda_{HHVV}^{SM}$ were constrained individually. The observed (expected) 95% CL intervals are $-1.2 < k_\lambda < 7.2$ ($-1.6 < k_\lambda < 7.2$) for the self-coupling and $0.6 < k_{2V} < 1.5$ ($0.4 < k_{2V} < 1.6$) for the $HHVV$ coupling. Figure 3.6a shows the individual and combined limits, along with its associated uncertainty bands on the HH SM signal strength. Figure 3.6b shows the 95% CL contours in the (k_{2V}, k_λ) plane for the individual decay channels and their combination.

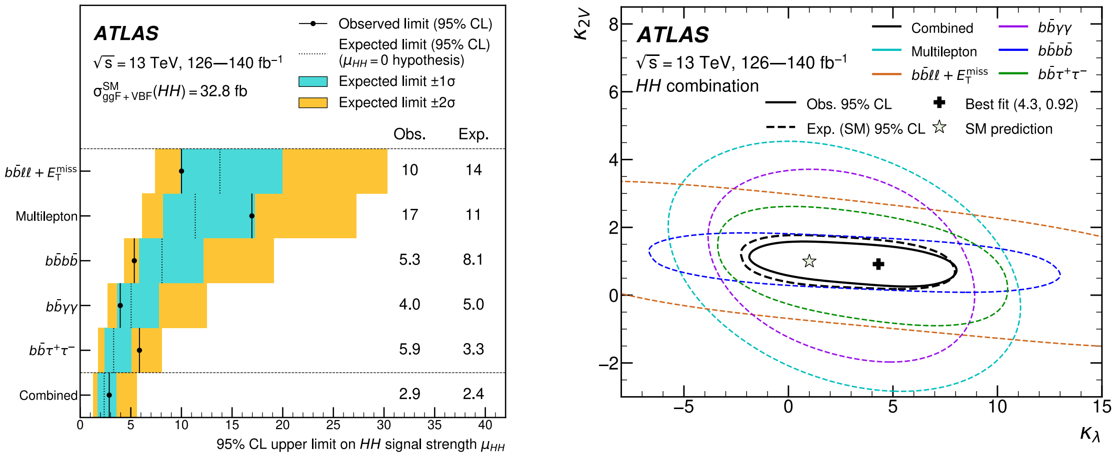

(a)

(b)

Figure 3.6: (a) The observed and expected 95% CL upper limits on the signal strength for inclusive ggF and VBF non-resonant HH production for various decay channels, as well as their statistical combination. A Higgs boson mass of $m_H = 125$ GeV is assumed for the predicted SM cross-section and the σ bands are calculated under the assumption of no HH production, profiling all nuisance parameters to the observed data. (b) The expected 95% CL intervals in the (k_{2V}, k_λ). Dashed lines are used for the individual decay channels and their combination, while the solid black line shows the observed contour from the combined results. The SM prediction is shown with a star, while the combined best-fit value is indicated with a cross [91].

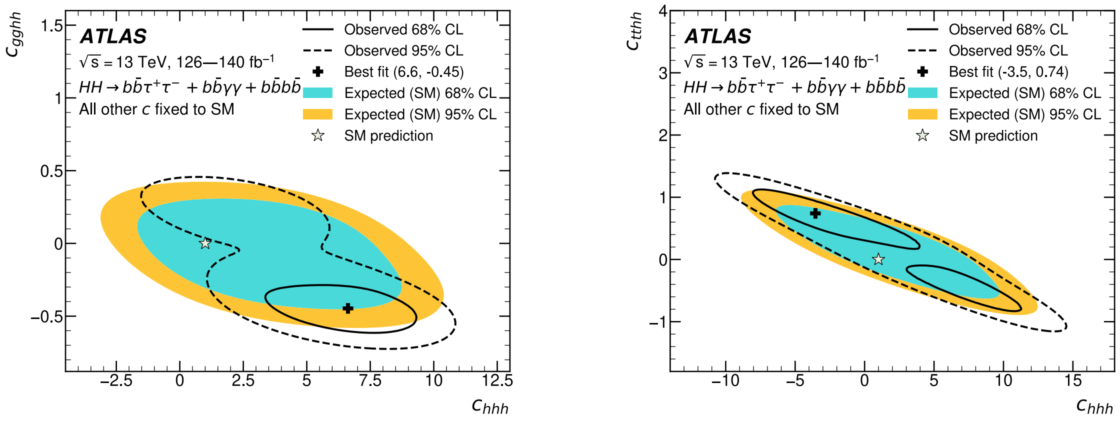

(a) **(b)**

Figure 3.7: Two-dimensional test-statistic expected and observed contours at 68% CL and 95% CL displayed for the c_{gghh}–c_{hhh} (a) and c_{tthh}–c_{hhh} (b) coefficient spaces within the HEFT framework, where c_{tthh}, c_{gghh}, and c_{hhh} are individually fixed to their SM values. The expected SM contours are represented by the inner and outer shaded regions, while the observed are represented by dashed and solid lines. The SM prediction is marked by a star, while the best-fit value is indicated by a cross [91].

In addition, exclusion contours are also set in the framework of HEFT model. A combination is performed for the HEFT interpretation the three most sensitive ggF HH decay channels, $b\bar{b}\tau^+\tau^-$, $b\bar{b}\gamma\gamma$ and $b\bar{b}b\bar{b}$. One-dimensional constraints are evaluated separately for c_{gghh} and c_{tthh} coefficients while maintaining all other coefficients fixed to the SM values. The observed (expected) 95% CL combined intervals on c_{gghh} are $-0.38 < c_{gghh} < 0.49$ ($-0.36 < c_{gghh} < 0.36$) assuming $c_{gghh} = 0$ for the SM. While the observed (expected) 95% CL combined intervals on c_{tthh} are $-0.19 < c_{tthh} < 0.70$ ($-0.27 < c_{tthh} < 0.66$) assuming $c_{tthh} = 0$ for the SM. The two-dimensional test-statistic contours on the (c_{gghh}, c_{hhh}) and (c_{tthh}, c_{hhh}) coefficient spaces are shown in Figure 3.7. The top-quark associated HH production can be a good candidate for providing higher sensitivity on the c_{tthh} coefficient as will be discussed in Section 3.6.

3.4.3 Prospects of HH Production with the HL-LHC

The previous combined results provide the highest sensitivity yet to the Higgs self-coupling strength and on the HH production cross-section. The results mark a significant milestone in the study of HH production using Run 2 data, with a sensitivity that is significantly higher than what was previously expected with this dataset. Not only the enlarged dataset, but also the improved analysis techniques and reconstruction of the physical objects were particularly important factors in achieving this large increase in HH sensitivity compared to previous results and Run-2 projections. Nevertheless, the measurement of the Higgs self-coupling, which is one of the priorities of the high-luminosity program, is expected to remain a major challenge during HL-LHC, motivating the study of new techniques.

A recent perspective study of HH production from ATLAS [97] for the HL-LHC was performed in 2022 using a statistical combination of the $b\bar{b}b\bar{b}$, $b\bar{b}\gamma\gamma$ and $b\bar{b}\tau^+\tau^-$ searches using partial Run 2 dataset. The combination was extrapolated assuming 3000 fb^{-1} of pp collisions at a centre-of-mass energy of $\sqrt{s} = 14$ TeV in the ATLAS detector at the HL-LHC.

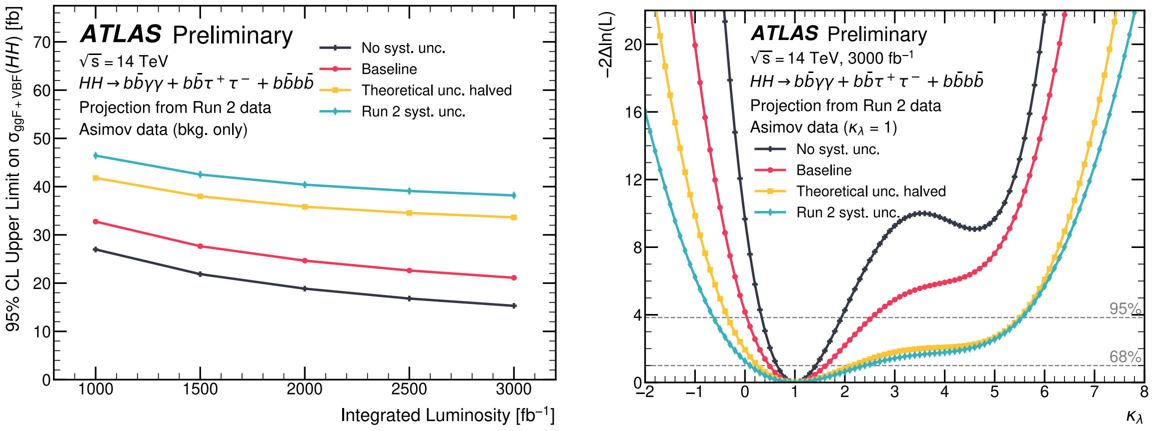

(a) **(b)**

Figure 3.8: (a) Expected 95% CL upper limits on the signal cross-section for SM HH production, combining the $b\bar{b}\gamma\gamma$, $b\bar{b}\tau^+\tau^-$ and $b\bar{b}b\bar{b}$ channels projected for integrated luminosities up to 3000 fb^{-1} at $\sqrt{s} = 14$ TeV at the HL-LHC. (b) Projected negative log-profile-likelihood as a function of κ_λ, evaluated on an Asimov dataset assuming the SM value $\kappa_\lambda = 1$. The combination of $b\bar{b}\gamma\gamma$, $b\bar{b}\tau^+\tau^-$ and $b\bar{b}b\bar{b}$ channels at 3000 fb^{-1} and $\sqrt{s} = 14$ TeV is shown, with the four uncertainty scenarios applied. The 68% and 95% confidence intervals are determined by the intersections of the profile likelihood curve with the dashed horizontal lines [97].

Four extrapolation scenarios were considered: one scenario where only statistical uncertainties are included, with no systematic uncertainties; one scenario called baseline scenario that assumes reduced systematic uncertainties; one scenario that includes Run 2 experimental uncertainties but assumes that theoretical uncertainties related to Higgs boson pair production signals are reduced to 50%; and one scenario in which the systematic uncertainties remain the same as for the Run 2 analysis. For each scenario, a profile-likelihood fit is applied based on a background-only Asimov dataset. Figure 3.8a shows the upper limits on the HH production cross-section as a function of the luminosity. Figure 3.8b shows the projected negative log-profile-likelihood as a function of κ_λ at 3000 fb^{-1}.

The combined analysis projects a significance for the HH production of 3.4σ in the baseline scenario, increasing to 4.9σ when systematic uncertainties are excluded. κ_λ is constrained in the 1σ CL to the range $0.5 < \kappa_\lambda < 1.6$. In the coming years, further enhancements in offline reconstruction, analysis techniques and improved detector are expected and will determine the outcomes for the discovery of non-resonant HH production.

3.5 Top-quark Physics at the LHC

The top quark is an important component of the SM, classified as part of the weak-isospin doublet alongside the bottom quark. The theoretical prediction of the top and bottom quarks, was proposed in 1973 to address the observed CP violation in kaon decay [98]. Its discovery occurred in 1995 at the Tevatron collider by the CDF and D0 experiments [99, 100].

Due to its unique characteristics, the top quark plays a crucial role in precision measurements of the SM, significantly influencing loop contributions to observables at lower energy scales. Since its discovery, various properties of the top quark have been measured, including its mass, couplings to vector bosons and the Higgs boson, and spin correlation in top-antitop ($t\bar{t}$) production. The top quark is the heaviest particle in the SM, with a mass of $172.57 \pm 0.29\,\mathrm{GeV}$ [19]. This means that the top quark also possesses the strongest Yukawa coupling to the Higgs boson, approximately equal to unity, as expressed by the equation $y_t = \frac{\sqrt{2}m_t}{v} \approx 1$. This strong coupling suggests that the top quark may play a significant role in the EWSB mechanism. It is also the reason why ggF through a top-quark loop is the leading H and HH production mode at LHC. Additionally, it has an extremely short lifetime, approximately 0.5×10^{-24} s [19], and decays before hadronization occurs, so no top-flavoured hadrons are formed. This allows for the study of a bare quark that behaves like a free particle, which transmits its spin information directly to its decay products.

Table 3.2: Measured branching ratios for the top-quark decays [19].

Decay channel ($t \to Wb$)	Branching ratio (%)
$t \to e\nu_e b$	11.1 ± 0.3
$t \to \mu\nu_\mu b$	11.4 ± 0.2
$t \to \tau\nu_\tau b$	10.7 ± 0.5
$t \to q\bar{q}b$	66.5 ± 1.4

Table 3.3: Predicted cross-section, in fb, for $t\bar{t}$ production at different center-of-mass energies with relative uncertainty and QCD order of the calculation. The first uncertainty is the scale uncertainty, while the second represents the PDF + α_s uncertainty. The top-quark mass of $m_t = 172.5$ GeV is assumed in the calculations [101].

$\sigma_{\text{prod.}}$ (fb)	$\sqrt{s} = 13$ TeV	$\sqrt{s} = 13.6$ TeV	$\sqrt{s} = 14$ TeV
$t\bar{t}$	$833.9^{+20.5\%}_{-30.0\%} \pm 21.0\%$	$923.6^{+22.6\%}_{-33.4\%} \pm 22.8\%$	$985.7^{+24.1\%}_{-35.7\%} \pm 24.1\%$

The top quark primarily decays into a real W boson and a bottom quark, with a branching ratio of approximately 95.7% [19]. The bottom quark subsequently hadronizes, and the W boson can either decay hadronically into a quark-antiquark pair or leptonically into a charged lepton and a neutrino. Table 3.2 summarises the branching fractions for different top quark decay modes.

At the LHC, top quarks are predominantly produced in pairs via the processes $q\bar{q} \to t\bar{t}$ and $gg \to t\bar{t}$, with ggF accounting for about 90% of top-quark pair production at $\sqrt{s} = 13\,\text{TeV}$. Predictions for the total production cross-section of top quarks are available up to next-to-next-to-leading order (NNLO), including next-to-next-to-leading-log (NNLL) resummation of soft gluons [19]. The top-quark pair production cross-section is approximately six orders of magnitude larger than the $t\bar{t}HH$ production cross-section, which is the focus of this thesis and will be described in the next section. The $t\bar{t}$ cross-section is shown in Table 3.3 for various center-of-mass energies.

In processes that include top-antitop production, such as $t\bar{t}$, $t\bar{t}V$and $t\bar{t}VV$, three distinct decay channels are expected based on how the W bosons from the two top quarks decay:

- **All-hadronic channel:** Both W bosons decay into quark-antiquark pairs, giving this channel the highest branching fraction (about 46%). However, it is not very distinguishable from the large QCD multijet background due to the high number of jets in the final state.
- **Dilepton channel:** Here, both W bosons decay into leptons. While this channel has the lowest branching ratio (about 9%) and is harder to reconstruct due to the presence of two neutrinos, it is easier to distinguish from background because of the two isolated leptons.
- **Single-lepton (or lepton + jets) channel:** One W boson decays leptonically and the other hadronically. This channel has a relatively clean signature, with only one lepton and one neutrino in the final state. Its branching ratio is about 30%, excluding decays to τ leptons, which are treated separately due to their subsequent decays into hadrons or other leptons.

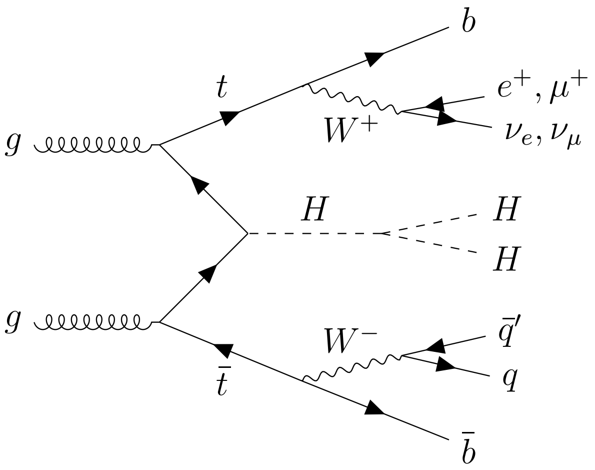

Figure 3.9: Tree-level Feynman diagram for the $t\bar{t}HH$ single-lepton channel, including the subsequent top-quarks decays.

Figure 3.9 shows an example Feynman diagram for $t\bar{t}HH$ production in the single-lepton top-quark decay channel. A more detailed description of the possible $t\bar{t}HH$ final states will be give in Section 5.1.

3.6 Top Associated HH Production and Beyond

The study of HH production through the $t\bar{t}HH$ mode at colliders could provide valuable insights into the fundamental properties of the Higgs and top physics. The SM production cross section of $t\bar{t}HH$ process computed at next-to-leading order (NLO) QCD is $0.756^{+4.3\%}_{-15.0\%} \pm 3.4\%$ fb at $\sqrt{s} = 13$ TeV and $0.860^{+4.2\%}_{-14.0\%} \pm 3.3\%$ fb at $\sqrt{s} = 13.6$ TeV, as reported in Table 3.1. Due to the higher cross sections of ggF and VBF, these processes have received more attention in HH searches from ATLAS and CMS to date. This thesis presents the first ATLAS search for $t\bar{t}HH$, which, despite its smaller cross-section, may play a crucial role in measuring the Higgs self-coupling and constraining new physics, as will be explained below.

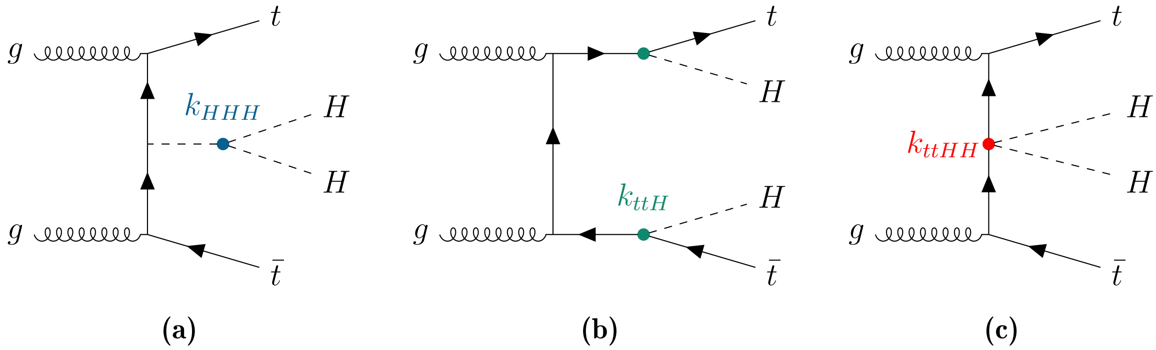

Figure 3.10: Examples of Feynman diagrams for the non-resonant $t\bar{t}HH$ production at leading order in QCD. Three different physical sub-processes are represented with their couplings of interest: the Higgs trilinear self-coupling (a), where the Higgs pair is produced via an off-shell Higgs boson mediator, the top-Higgs Yukawa vertex (b) and the top-Higgs quartic interaction or double Higgs Yukawa vertex (c) arising in EFT models.

For example, the destructive interference between Feynman diagrams with and without the Higgs self-coupling in ggF and VBF processes may lead to minimal HH production cross-sections around $k_\lambda = 2$ [84] (Figure 3.3a). This interference may significantly affect the analysis sensitivity at the HL-LHC [102]. In contrast, the relevant interference in $t\bar{t}HH$ production is constructive, making the $t\bar{t}HH$ mode interesting to study as it can complement observational constraints where ggF and VBF searches lack sensitivity.

Additionally, the $t\bar{t}HH$ cross-section increases faster than the ggF cross-section as the LHC beam energy increases (Figure 3.3b). The difference in their cross-sections reduces significantly at 100 TeV, where $t\bar{t}HH$ even surpasses the VBF production cross-section. This suggests that $t\bar{t}HH$ measurements may gain more sensitivity at future hadron colliders, such as the Future Circular Collider (FCC), compared to ggF and VBF.

Apart from complementing the current HH searches, measuring $t\bar{t}HH$ will also enable more extensive new physics searches in the top and Higgs sectors. The additional radiated Higgs boson provides a richer dependence on new physics than in $t\bar{t}H$ [103–105]. The non-resonant $t\bar{t}HH$ production can probe the quartic Higgs self-coupling

(c_{ttHH}), which is not predicted by the SM. As discussed in Section 3.3, EFTs can be used to agnostically model the quartic coupling. Figure 3.10 illustrates the tree-level Feynman diagrams for this process. The diagram in Figure 3.10a depends on the trilinear Higgs self-coupling, with the HH pair radiated from an off-shell Higgs boson. The diagram in Figure 3.10b provides access to the top-Higgs Yukawa vertex. Additionally, the diagram in Figure 3.10c includes the anomalous quartic interaction, which can be used to constrain new physics.

The $t\bar{t}HH$ contact interaction can also appear in BSM models, such as Composite Higgs Models (CHM), and in supersymmetry. In CHM, an extended top sector typically interacts with the Higgs boson. When the heavy degrees of freedom are integrated out at the cut-off scale of strong dynamics, a $t\bar{t}HH$ contact interaction is generated. This interaction could contribute to the non-resonant production at tree level, affecting its signal rate at the LHC [106–109].

Additionally, CHM may also contribute to resonant processes since the model predicts vector-like top partners with a charge of $q = {}^{2}/{}_{3}|e|$. These top partners are heavy fermions that can decay through channels like tH, where a top quark and a Higgs boson are produced and can be pair produced leading to a final state with the same signature as $t\bar{t}HH$. The resonant search for $t\bar{t}HH$ can provide direct access into the composite Higgs sector and the interactions involving heavy top partners.

Resonant $t\bar{t}HH$ production can also emerge from models such as the Two Higgs Doublet Model (2HDM) of type II, which includes extensions like the Minimal Supersymmetric Standard Model (MSSM). In these models, a heavy CP-even Higgs boson can be produced in association with a pair of top quarks. The heavy Higgs boson decays into two lighter Higgs bosons, leading to a $t\bar{t}HH$ final state.

Finally, $t\bar{t}HH$ provides access to the top-quark Yukawa coupling and, as in $t\bar{t}H$ production, these interactions can provide insights on the charge-parity (CP) properties of the Higgs boson, which are directly related to its role in electroweak symmetry breaking and could explain the observed matter-antimatter asymmetry during baryogenesis.

This makes the $t\bar{t}HH$ channel particularly useful for probing both the SM and BSM theories, where the extended Higgs sector plays a central role in new physics searches.

4

Reconstruction and Identification of Physics Objects

Contents

After the reconstruction of tracks from the particle hits left in the tracking system, as described in Section 8.1, the events need to be reconstructed into physical objects (electrons, muons or jets) so the momentum, the vertex and tracks of each particle, as well as the physical processes, can be determined. The low-level objects such as tracks and calorimeter clusters are then combined into higher-level objects. Both the data and the MC samples need to be reconstructed for the analysis.

In this chapter, the reconstruction and definition of the physics objects are described. The objects considered in this work are electrons, muons, jets, b-jets and missing transverse energy. These are the are the possible final state objects present in the $t\bar{t}HH$ analysis described in this dissertation.

4.1 Reconstruction and Identification of Tracks

Track reconstruction is a fundamental task in HEP experiments, that consists of the estimation of the parameters describing the trajectories of charged particles and the properties of these charged particles when traversing some form of sensitive detector. Usually the particles are embedded in a static magnetic field so their momentum and charge can be determined. A more detailed description of the ATLAS tracking algorithm is presented in Section 8.1. The current section provides a brief description of the ID tracking and the quality identification requirements used in the analysis presented in this thesis.

The ID track reconstruction [110–112] begins with a pre-processing stage, where signals from adjacent channels in the Pixel and SCT sub-detectors are combined into clusters. These clusters are interpreted as the energy deposits left by incident charged particles. Subsequently, pairs of one-dimensional SCT clusters on either side of a sensor module, or individual pixel clusters, are transformed into three-dimensional space-points (SP). The position uncertainties of these SPs are determined by the geometry of the detector and the pitch of the sensors. For SCT SPs, the missing second coordinate is derived from the stereo angle between the strips on both sides of the sensor module. ID tracks must meet specific quality criteria, categorised as either *loose* or *tight*, to filter out tracks originating from very low-energy particles and to eliminate fake tracks caused by noise or combinatorial effects.

The *loose* requirement represents the track quality requirements applied during reconstruction, where the track must satisfy the following conditions: transverse momentum (p_{T}) greater than 500 MeV, pseudorapidity ($|\eta|$) less than 2.5, at least 8 silicon hits, no shared hits, no more than two holes[1] in the Pixel and SCT detectors, and no more than one hole in the Pixel detector. The minimum transverse momentum is dictated by the track's curvature in the magnetic field, while the pseudorapidity range is constrained by the geometry of the instrumented detector. The *tight* requirement aims at keeping high efficiency for prompt/primary tracks while significantly reducing fakes. More stringent conditions are applied: in addition to meeting the *loose* criteria, they must have 9 or more silicon hits in the barrel region, $|\eta| < 1.65$, or 11 or more silicon hits in the end-cap region, $|\eta| > 1.65$. Furthermore, they require at least one hit in one of the two innermost pixel layers and no holes are allowed in the pixel detector.

---

[1] Holes refer to layers within the tracking system that the track passes through without registering any hits.

4.2 Reconstructed Leptons

In ATLAS analysis, the term *leptons* can be commonly used to refer to long lived charged leptons, i.e. electrons and muons only. Since τ-leptons have a short life-time and decay before interacting with the detector material only its decay products can be detected. The analysis presented in this thesis only considers the leptonic decays of the τ-leptons and does not use reconstructed τ objects. Therefore, the reconstruction of τ objects is not covered in this chapter. The reconstruction and identification of electrons and muons will be discussed in Sections 4.2.1 and 4.2.2. Neutrinos do not leave any signal in the detector and their missing energy contribution will also be treated separately in Section 4.4. From now on, the term lepton will be used to refer only to reconstructed electrons and muons. In this work, leptons play an important role in the classification of the different final states of the analysis as will be discussed in Section 5.1.

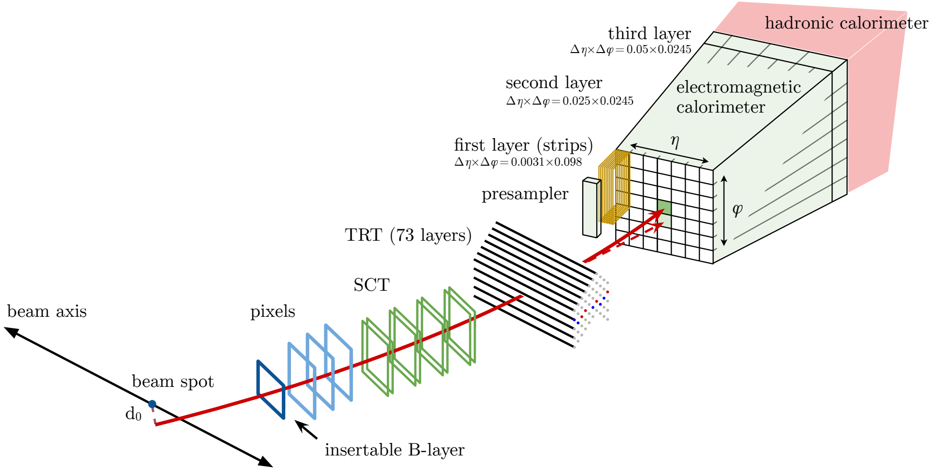

Figure 4.1: Illustration of the path of an electron interacting with the layers of the ATLAS detector. Low-level objects, such as a track and energy deposits in the calorimeter, are combined to identify and reconstruct the electron [113].

4.2.1 Reconstructed Electrons

As electrons traverse the ATLAS detector, they leave a track in the ID and deposit most of their energy in the ECAL. In the ECAL, electrons interact with the dense material via electromagnetic processes, primarily bremsstrahlung and pair production. These interactions result in a cascade of secondary particles, or electromagnetic showers, which forms localised energy clusters. Electromagnetic showers are initiated by electrons and photons. This leads to a collimated object that is typically reconstructed within the same EM cluster. Electron reconstruction [113, 114] is achieved by associating these energy clusters in the ECAL with charged-particle tracks identified in the ID. Close matching of these tracks to the energy clusters in the $\eta \times \phi$ space is required.

The electron reconstruction begins with the formation of calorimeter cell clusters, known as topo-clusters. The $\eta \times \phi$ space of the ECAL is divided into a grid of 200 $\times$

256 elements, known as towers, each with a size of $\Delta\eta \times \Delta\phi = 0.025 \times 0.025$. A sliding-window algorithm [115] is then applied to identify clusters of towers, known as seed clusters, which must have a minimum transverse energy of 2.5 GeV. Then, tracks are extrapolated into the volume of the ECAL and associated to the seed clusters using a fitting procedure based on an optimised Gaussian-Sum Filter[2]. The track perigee point and the cluster-barycenter must be within 0.05 in $|\Delta\eta|$ and the azimuthal separation must satisfy one of two alternative criteria: $-0.20 < \Delta\phi < 0.05$ or $-0.10 < \Delta\phi_{\mathrm{res}} < 0.05$. The values $\Delta\phi$ and $\Delta\phi_{\mathrm{res}}$ are calculated using the formula $-q \times (\phi_{\mathrm{cluster}} - \phi_{\mathrm{track}})$, where q represents the electric charge of the particle, and for $\Delta\phi_{\mathrm{res}}$ the momentum of the track is re-scaled to the energy of the cluster.

If a seed cluster has no associated tracks, it is identified as a photon candidate. When multiple tracks are matched to a seed cluster, one track is selected as the primary track. If this primary track is also matched to a secondary vertex and has no pixel hits, the object is classified as a photon that has converted into an e^+e^- pair. An electron candidate is identified when the topo-cluster matches an ID track that is not associated with a conversion vertex. Once this match is established, the track is re-fitted to account for any bremsstrahlung energy loss, ensuring a more accurate reconstruction of the electron trajectory and energy.

The primary vertex of the hard scattering event needs to be consistent with the track associated with the electron candidate and the transverse impact parameter (d_0) of the electron candidates must satisfy $|d_0/\sigma_{d_0}| < 5$, where σ_{d_0} represents the estimated uncertainty of d_0. Additionally, the longitudinal impact parameter (z_0) must satisfy $|z_0 \sin\theta| < 0.5$.

The components involved in the reconstruction and identification of an electron are illustrated in Figure 4.1. In this work, all electron candidates are required to have $p_{\mathrm{T}} > 10$ GeV with $|\eta| < 2.47$. Electron candidates in the region $1.37 < |\eta| < 1.52$, known as the LAr crack region, are rejected to reduce the contribution from non-prompt and fake electrons.

4.2.1.1 Electron Identification

An identification algorithm is then applied to assess whether the electron candidates are prompt electrons or fake reconstructed electrons, this includes hadronic jets, electrons from photon conversion, and electrons from semileptonic decays of heavy-flavour hadrons. The algorithm uses a likelihood (LH) discriminant [116], which combines various variables associated with the electron cluster and track measurements to differentiate between true electrons and background-like objects. The LH discriminant uses as input measurements from the ID and calorimeter systems and variables combined with information from both systems.

The LH-based electron identification offers improved background rejection compared to previous cut-based method. Three main identification working points (WPs) are defined for physics analysis based on different efficiencies for background rejections,

---

[2] The Gaussian-Sum Filter method is an extension of the Kalman filter designed to handle the non-linear effects associated with bremsstrahlung. In the GSF approach, experimental noise is modelled using a sum of Gaussian functions.

usually referred to as Loose, Medium, and Tight, with increasing background rejection power but lower signal acceptance. For the definition of the various WPs, different selection thresholds are applied to each LH input variable when defining the LH discriminant. Figure 4.2 shows the identification efficiencies of various WPs as a function of the electron's transverse energy (E_{T}) and pseudorapidity for $Z \to ee$ events. The identification efficiency for each WP is calculated as the ratio of the number of electrons passing a specific identification selection to the total number of electrons with a matching track that meets the track quality requirements using both data and simulated samples. There is a noticeable drop in efficiency when moving from the barrel region ($|\eta| < 1.2$) to the end-caps and for lower transverse energy. For the different physics analyses to correct for efficiency differences between data and MC simulation, associated data-to-simulation ratios, known as scale factors, are applied during analysis stage as multiplicative factors to the MC simulation event weight.

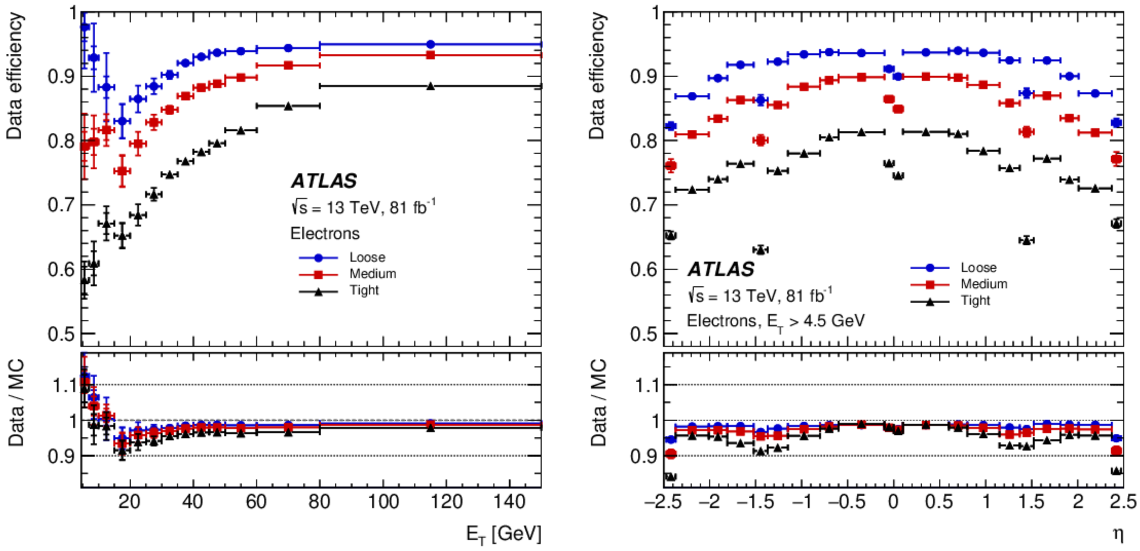

(a) (b)

Figure 4.2: The electron identification efficiency in $Z \to ee$ events is as a function of (E_{T}) (a) and η (b) for Loose, Medium, and Tight selection criteria. These efficiencies are calculated by applying ratios of data-to-simulation efficiency, derived from $J/\psi \to ee$ and $Z \to ee$ events, to the $Z \to ee$ simulation. The total uncertainties combine statistical and systematic errors in the data-to-simulation efficiency ratio [117].

4.2.1.2 Electron Charge Identification

The electric charge of an electron is inferred from the curvature of its track as reconstructed in the ID. However, misidentification of the electron charge can occur due to two main reasons. First, high-momentum electrons exhibit very subtle track curvature, which can result in misidentification of the charge during the reconstruction. Second, when electrons interact with the material of the detector and undergo bremsstrahlung, they produce photons that may convert into e^+e^- pairs through photon conversion, resulting in three electrons in the final state and producing a spread-out cluster in the

ECAL. Multiple tracks can be reconstructed from the hits produced in the ID by the prompt and the subsequently produced electrons. If the best-matching track among all the tracks assigned to the electron candidate, is the one from an electron with opposite charge to the prompt one, the incorrect charge will be assigned. This issue is not as much relevant for muons, thanks to the lower occurrence of bremsstrahlung and the precise charge determination offered by the combination of the ID and MS measurements.

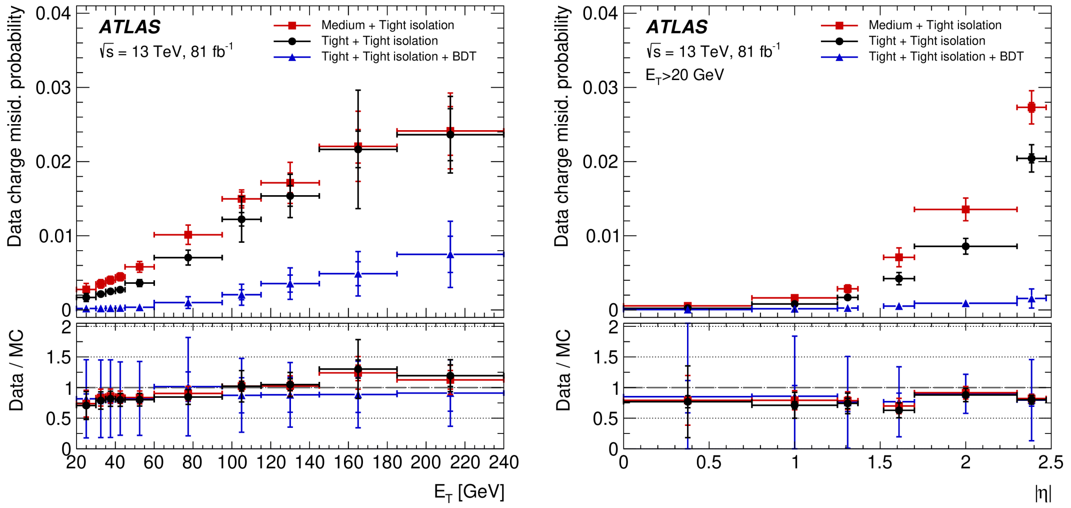

(a) **(b)**

Figure 4.3: The charge misidentification probabilities as a function of E_{T} (a) and $|\eta|$ (b). The electron energies have been corrected for energy losses due to interactions with detector material, which represent the primary cause of charge misidentification. The inner error bars indicate statistical uncertainties, while the total uncertainties combine both statistical and systematic components [117].

The events with charge-misidentified electrons are often referred to as charge misassigned electrons (QmisID) and can contaminate analysis regions. To mitigate this background, a Multivariate Analysis (MVA) discriminant based on Boosted Decision Trees (BDT) is employed. This tool, known as the Electron Charge ID Selector (ECIDS), is trained using the TMVA toolkit [118] with data from $Z \to ee$ events. The training uses variables from the ID and the ECAL as input. Using data instead of MC simulations, which were used in the previous version of the BDT [113, 117], helps to reduce efficiency losses caused by mismodeling of input variables. For electrons passing the Tight WPs, the BDT achieves a 98% efficiency in $Z \to ee$ events. The charge misidentification probabilities, both with and without the BDT selection, are shown in Figure 4.3.

4.2.2 Reconstructed Muons

Muon reconstruction is performed by matching track segments or complete tracks identified in the MS with tracks reconstructed in the ID [119]. Initially, tracks are reconstructed separately in both the ID and MS. The hits from both the ID and MS sub-detectors are used in a global refit to obtain the combined track. The reconstruction process typically begins in the MS, where a search is conducted for hit patterns within each muon chamber to form segments. These segments are then fitted together across different layers to generate track candidates. Then the track candidates are extrapolated inwards to match with an ID track. This is referred as an *outside-in* approach for pattern recognition. During this global fit, MS hits may be added or excluded to improve the fit quality.

The transverse impact parameter of muon candidates must satisfy $|d_0/\sigma_{d_0}| < 3$ and the longitudinal impact parameter must satisfy $|z_0 \sin\theta| < 0.5$. In this work, all muons are required to have $p_T > 10\,\mathrm{GeV}$ and $|\eta| < 2.7$.

4.2.2.1 Muon Identification

Similar to electrons, muon identification criteria are applied to suppress non-prompt muons, such as those arising from the decays of charged hadrons like pions and kaons. These non-prompt muons often originate from a secondary vertex and exhibit a distinctive topology in the reconstructed track, making them identifiable through the poor fit quality of the global fit and the discrepancy between the momentum measurements in the ID and the MS.

Unlike electron identification, muon identification relies on a cut-based analysis. The key variables used in this process include:

- the $\frac{q}{p}$ significance, defined as the absolute value of the difference between the charge-to-momentum ratios measured in the ID and MS, divided by the sum in quadrature of the corresponding uncertainties:

$$\frac{q}{p}\text{significance} = \frac{\left|\frac{q}{p_{\mathrm{T}}^{ID}} - \frac{q}{p_{\mathrm{T}}^{MS}}\right|}{\sqrt{\sigma^2_{p_{\mathrm{T}}^{ID}} + \sigma^2_{p_{\mathrm{T}}^{MS}}}}; \tag{4.1}$$

- ρ', which is the absolute value of the difference between the transverse momentum measurements in the ID and MS, normalised by the momentum of the combined track:

$$\rho' = \frac{\left|p_{\mathrm{T}}^{ID} - p_{\mathrm{T}}^{MS}\right|}{p_{\mathrm{T}}^{CB}}; \tag{4.2}$$

- the χ^2 of the global track fit, the number of hits in the ID and MS.

Several identification WPs are defined with varying levels of background rejection efficiency. The three major WPs used in physics analyses are Loose, Medium, and Tight. The Loose WP, optimised for multi-lepton analyses, prioritises reconstruction efficiency over purity. The Tight WP, on the other hand, maximises the purity of prompt muons while reducing non-prompt muon background. The Medium WP gives a good trade off between efficiency and purity, minimising systematic uncertainties, and is the default selection for muons in ATLAS. Figure 4.4 illustrates the muon reconstruction efficiency for various identification WPs, measured in $J/\psi \to \mu\mu$ events. To correct for efficiency differences between data and MC simulations, associated scale factors for both identification and isolation are applied as multiplicative factors to the

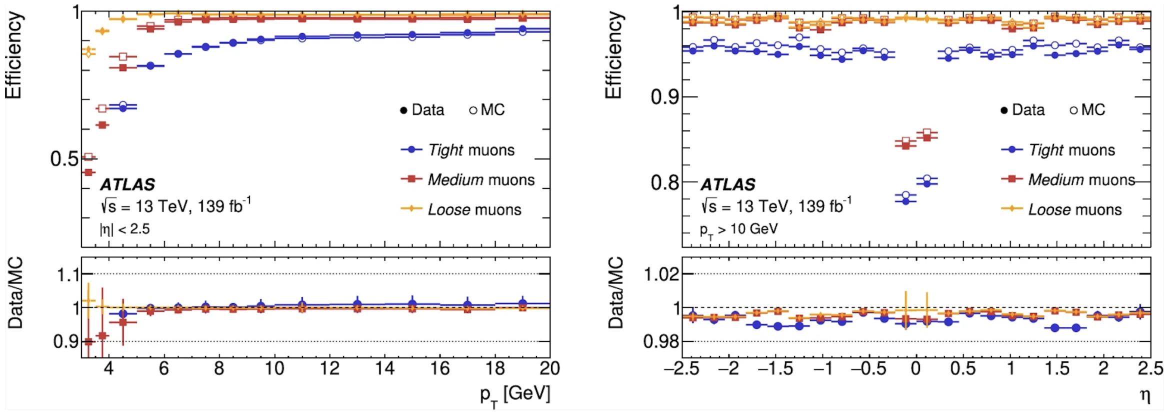

Figure 4.4: Muon reconstruction and identification efficiencies are presented for the Loose, Medium, and Tight selection criteria measured in $J/\psi \to \mu\mu$ events as a function of E_{T} (a) and η (b). Predicted efficiencies are shown with open markers, while filled markers represent the measurement from collision data. The statistical uncertainty is smaller than the marker size and is not displayed. The bottom panel of each plot shows the ratio of measured to predicted efficiencies, including statistical and systematic uncertainties [120].

MC event weights during the analysis stage.

4.2.3 Lepton Isolation

In addition to identification quality requirements, isolation criteria are also applied to measure the detector activity around leptons. Prompt leptons typically exhibit minimal activity (both in the calorimeter and in the ID) in the area surrounding the candidate object. A set of variables is used to quantify the amount of activity in the vicinity of the candidate object. For both electrons and muons, track-based and calorimeter-based isolation variables are used. These variables are determined by summing the transverse energies of calorimeter clusters or the transverse momenta of tracks within a cone of variable radius ΔR centred around the lepton candidate's direction, while excluding the candidate itself from the calculation. The cone size is p_{T}-dependent to improve identification of boosted objects and is defined as:

$$\Delta R = \min\left(\frac{10}{p_{\mathrm{T}}[\mathrm{GeV}]}, \Delta R_{\mathrm{max}}\right) \tag{4.3}$$

where ΔR_{max} is a given maximum cone size. Final isolation cuts are applied to the calculated variables to define lepton isolation WPs. Isolation scale factors, determined as the ratio of data to simulation in $Z \to \ell^+\ell^-$ events, are used in the analysis stage to correct for the isolation efficiency in MC samples. These are generally close to unity with uncertainties mostly at the per-mille level for $p_{\mathrm{T}} > 10$ GeV.

4.3 Hadronic Jets

Because of QCD colour confinement, the final-state partons produced in collisions hadronize when interacting with the material of the detector, resulting in collimated sprays of hadrons known as jets. Jets are typically reconstructed by clustering energy deposits in the calorimeters, forming what are referred to as topological clusters, or topo-clusters. The energy, direction, shape and different substructure variables of the jets can be used to determine the original partons that produced the jet.

Track information from the ID can be combined with topo-clusters as complementary information to create *particle-flow* jets [121]. The calorimeter energy deposits from charged hadrons are replaced by the measurements from the ID to complement the calorimeter's energy measurements for neutral hadrons. This approach benefits from good energy resolution of charged particles obtained from the ID, enhancing the overall jet reconstruction accuracy.

4.3.1 Jet Reconstruction

The main jet clustering algorithm is based on the anti-k_t algorithm [122, 123] that uses topo-clusters as inputs. The anti-k_t algorithm starts by calculating a symmetric distance d_{ij} between pairs of constituents i and j given by

$$d_{ij} = \min(p_{T,i}^{2k}, p_{T,j}^{2k}) \cdot \Delta R_{ij}^2 \tag{4.4}$$

$$d_{iB} = p_{T,i}^{2k} \cdot R^2, \tag{4.5}$$

where ΔR_{ij} is the angular distance between the two topo-cluster objects, $p_{T,i}$ is the transverse momentum of the i-th object and R is the radius parameter that determines the size of the jet cone. k is a parameter that defines the type of algorithm. For the anti-k_t algorithm, $k = -1$. While $k = 0$ and $k = 1$ corresponds to the inclusive Cambridge/Aachen and k_t algorithm [124], respectively. Figures 4.5a and 4.5b show the p_{T} distribution of energy of calorimeter topological clusters and the active area of topo-clusters build using the anti-k_t algorithm in the $\phi - y$ plane for a radius parameter of $R = 1.0$.

The clustering process for each object i begins by calculating the distances d_{iB} (between object i and the beam) and all distances d_{ij} between object i and each other object j. The algorithm then identifies the smallest distance. If the smallest distance is d_{ij}, objects i and j are merged into a single new object. If the smallest distance is d_{iB}, object i is considered a jet and is removed from the list of objects. This process is repeated with the updated list of objects until no objects remain. After the clustering is complete, the jet's four-momentum is obtained by summing the four-momenta of all the topo-clusters that make up the jet.

For a symmetric two-body decay of a massive particle, the angular separation between the two decay prodcuts can be expressed as

$$\Delta R \approx \frac{2m}{p_{\mathrm{T}}} \tag{4.6}$$

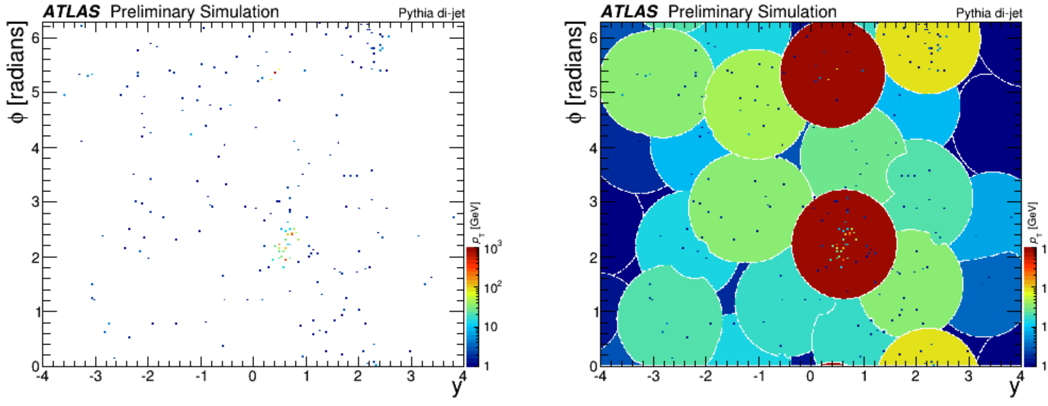

(a) **(b)**

Figure 4.5: (a) The distribution of calorimeter topological cluster energy in the $\phi - y$ plane. (b) The anti-k_t jets active area for a radius parameter of $R = 1.0$ reconstructed from topological clusters. The colours of the plots indicate the p_T of the reconstructed jets and clusters. Energetic jets originating from the hard scatter process (in red) display a circular shape. Both plots are based on MC simulation of a di-jet event.

where m and p_T are the mass and transverse momentum of the decaying parent particle. In the boosted regime, where the parent particle has a high transverse momentum, the separation between its decay products becomes smaller, allowing them to be included within a single jet, known as a large-R jet. A larger radius parameter can be used to reconstruct all the decay products of the original particle as a single jet rather than as separate, individual jets.

There are two commonly used jet definitions based on the radius parameter R used by ATLAS: jets with a small radius parameter, usually $R = 0.4$, are referred to as small-R jets, while those with larger values, usually $R = 1.0$, are called large-R jets. In the search presented in this thesis, only small-R jets are reconstructed using the particle-flow technique with the anti-k_t algorithm and a radius parameter of $R = 0.4$.

4.3.2 Small-R Jet Calibration

After jets are reconstructed using the anti-k_t algorithm, the jet energy scale (JES) needs to be calibrated to match the energy response of the true particles as close as possible. Corrections are applied to restore the JES to that of truth jets reconstructed at the particle-level. The ATLAS JES calibration scheme [125] is shown in Figure 4.6 and proceeds in multiple steps that use both simulation and data-driven techniques to correct the jet four-momentum.

The first step, known as the *origin correction*, involves recalculating the four-momentum of jets to point to the hard-scatter primary vertex instead of the centre of the detector, while maintaining the jet's energy constant. This enhances η resolution of the jets, which is evaluated by comparing the reconstructed jets to the truth jets in MC simulations.

Following the origin correction, the next step is the pile-up correction, which is divided into two steps: the *jet area-based pile-up correction* [122] and the *residual pile-*

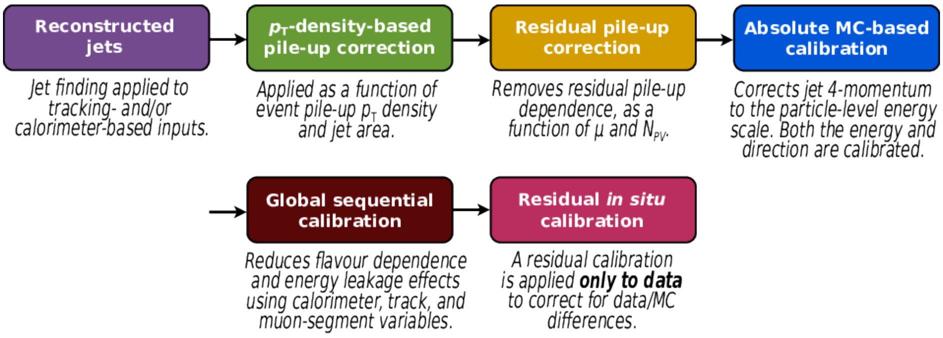

Figure 4.6: Steps for ATLAS jet energy scale calibration applied to the jet four-momentum [126].

up correction. These corrections aim to remove the excess energy introduced by in-time and out-of-time pile-up.

The area-based method subtracts the per-event pile-up contribution from the transverse momentum (p_{T}) of each jet based on its area (A). The pile-up contribution is obtained from the median p_{T} density ρ of jets in the η–ϕ plane using MC simulations. The central, lower-occupancy regions of the calorimeter, are used for the derivation of ρ and may not fully represent the pile-up contribution in the forward region of the calorimeter or in the high-occupancy core of high-p_{T} jets. Therefore, some dependence of the jet p_{T} on the amount of pile-up may remain even after this correction, requiring an additional residual correction.

The residual contribution depends on the number of primary vertices (N_{PV}) and the average number of interactions per bunch crossing (μ). These dependencies are described by the parameters α and β, which are obtained from linear fits to the difference between the reconstructed jet transverse momentum and the truth-jet transverse momentum. The final corrected jet transverse momentum ($p_{\mathrm{T}}^{\mathrm{corr}}$) is calculated by taking the initially measured transverse momentum ($p_{\mathrm{T}}^{\mathrm{reco}}$) and subtracting the pile-up contribution:

$$p_{\mathrm{T}}^{\mathrm{corr}} = p_{\mathrm{T}}^{\mathrm{reco}} - \rho \cdot A - \alpha \cdot (N_{PV} - 1) - \beta \cdot \mu. \tag{4.7}$$

Figure 4.7 shows the dependence of the area-based and residual corrections on N_{PV} and μ as a function of $|\eta|$.

The next step, known as the *absolute JES calibration*, corrects the reconstructed jet's four-momentum to match the particle-level energy scale. Both energy and direction are calibrated. This step corrects biases in the jet's η reconstruction, which can occur due to transitions between different calorimeter technologies and changes in calorimeter granularity.

Even after previous calibrations, residual dependencies of the JES on the jet's longitudinal and transverse characteristics can still be observed. These dependencies arise because the calorimeter response and jet reconstruction are sensitive to variations in the jet's particle composition and the distribution of energy within the jet. For instance, jets initiated by quarks often contain hadrons with a higher fraction of the jet's p_{T}, which penetrate deeper into the calorimeter. In contrast, jets initiated by gluons typi-

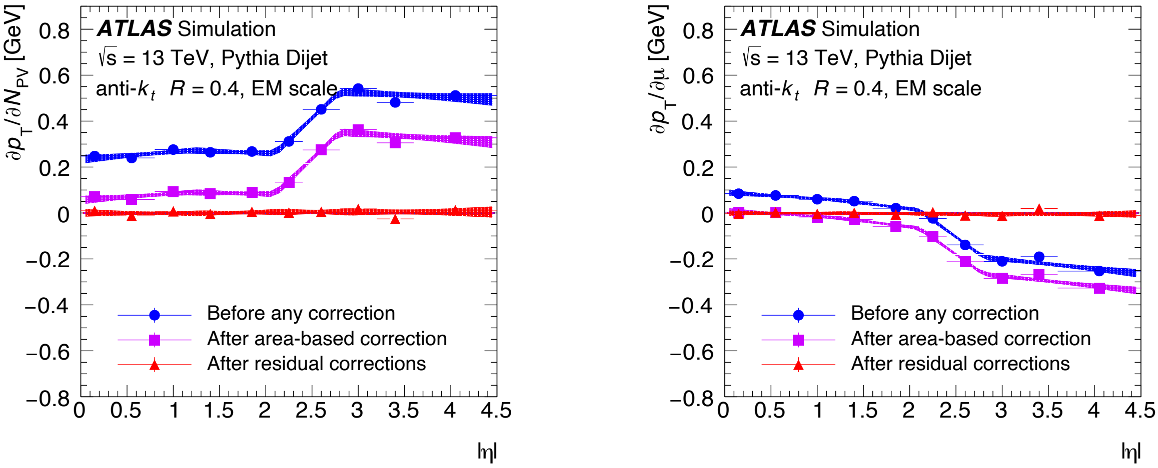

Figure 4.7: EM-scale anti-k_t jet p_T dependence on (a) in-time pile-up (N_{PV} averaged over μ) and (b) out-of-time pile-up (μ averaged over N_{PV}) as a function of $|\eta|$ for $p_\mathrm{T}^\mathrm{true} =$ 25 GeV. The dependence is plotted in $|\eta|$ bins before pile-up corrections, after the area-based correction, and after the residual correction. The shaded bands represent the 68% confidence intervals of the linear fits in four $|\eta|$ regions [127].

cally have more particles with softer p_T, resulting in a lower calorimeter response and a broader transverse profile. To address these differences, a global sequential calibration is applied. This calibration reduces flavour dependence and energy leakage effects by using observables from the calorimeter, Muon Spectrometer and track information.

Finally, a residual in-situ calibration is performed to account for discrepancies between the jet response in data and MC simulation. These discrepancies can arise from imperfect modelling of the detector response, detector material, hard scatter events, underlying events, pile-up, jet formation, and electromagnetic and hadronic interactions with the detector. The differences between data and simulation are quantified by comparing the jet's p_T against other well-measured reference objects, such as photons, Z bosons, and calibrated jets.

4.3.3 Flavour Tagging

Flavour tagging involves determining the flavour of parton responsible for producing a specific jet, and it is an important component in most ATLAS physics analyses. Jets produced by the hadronization of a b quark, known as b-jets, can be distinguished from other jets by exploiting the unique properties of b-hadrons. These properties include their relatively high mass (around 5 GeV), extended lifetime (approximately 1.5 ps), and high decay multiplicity, typically involving around five charged particles. These characteristics result in distinct topologies that can be utilised in multivariate techniques to differentiate b-jets from those originating from light-flavour hadrons. For example, due to their longer lifetime, b-hadrons tend to travel a greater distance within the inner detector, creating a displaced secondary vertex as shown in Figure 4.8. The ATLAS approach to flavour tagging is divided into two steps: first, low-level algorithms are used to reconstruct key features of heavy-flavour jets, and then these outputs are input into multivariate classifiers to improve the performance.

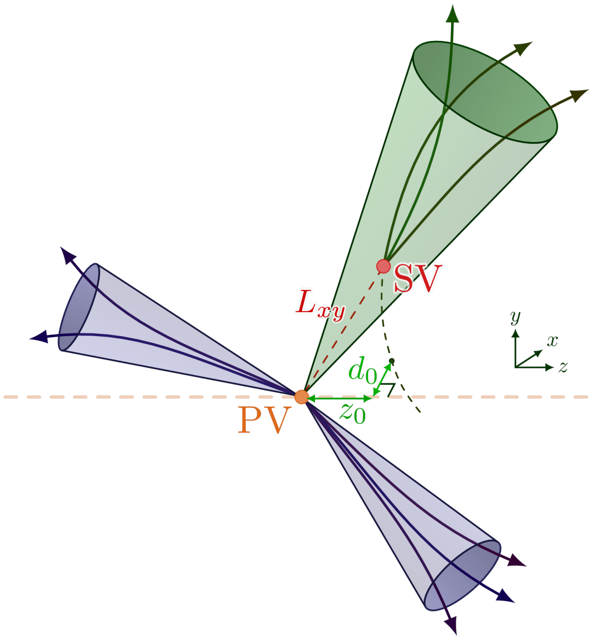

Figure 4.8: Illustration of a jet containing a secondary vertex (SV), reconstructed from displaced tracks with large decay length (L_{xy}) from the primary vertex (PV), characteristic of the decay of a heavy long-lived particle such as a b-hadron [128].

4.3.3.1 Low-level Taggers

Low-level algorithms for flavour tagging can be categorized into three main groups: those utilizing the large impact parameters of tracks from heavy-flavour jets, those explicitly reconstructing displaced vertices, and those using information from muons produced in heavy-flavour decays.

Impact parameter-based algorithms like IP2D and IP3D use the transverse and longitudinal impact parameters to create discriminant variables calculated as a per-track of the log-likelihood ratio of the probability density functions for the b- and light-jet hypothesis [129]. The RNNIP [130] algorithm improves on this by employing recurrent neural networks (RNN) to capture sequential dependencies among tracks within a jet, enhancing the ability to identify b-jets. The log-likelihood ratios defined for the IP2D and IP3D algorithms as well as the transverse and longitudinal impact parameters, the fraction of transverse momentum carried by the track relative to the jet and the angular distance between the track and the jet axis are used as input to the RNN.

For secondary vertex reconstruction, two primary algorithms are typically used in ATLAS: SV1 [131], which identifies a single displaced vertex within a jet using the Single Secondary Vertex Finder algorithm. In cases where a b-jet contains decay vertices from both b- and c-hadrons, SV1 either merges these vertices into one, if they are close together, or selects the vertex with the highest track multiplicity, if they are farther apart. The second algorithm, JetFitter [132], employs a Kalman filter to trace the b-hadron's flight path, enabling the identification of both primary and secondary vertices. It is also capable of reconstructing vertices that are associated with a single track by utilising the jet axis.

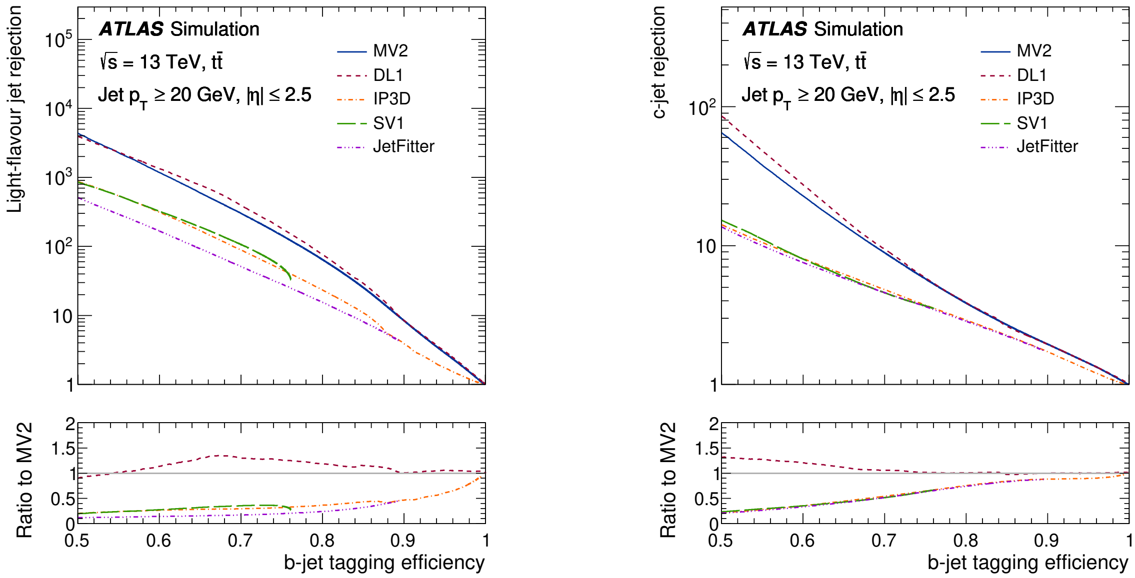

Figure 4.9: The rejection rates of (a) light-flavour jets and (b) c-jets are plotted against the b-jet tagging efficiency for the IP3D, SV1, JetFitter, MV2, and DL1 b-tagging algorithms, evaluated on baseline $t\bar{t}$ events [133].

Additionally, the Soft Muon Tagger algorithm [129] exploits the presence of muons in b-jets, which are more frequent in jets originated from b quarks with respect to c- or light-jets due to the significant semileptonic decay branching ratio of b-hadrons. This algorithm combines the muon's transverse momentum, its angular distance from the jet axis, and other track quality metrics in a multivariate approach to improve b-jet identification.

4.3.3.2 High-level Taggers

Each of the low-level algorithms previously discussed takes a unique yet complementary approach to b-tagging. To enhance overall b-tagging performance, their outputs are combined using a high-level b-tagging algorithm. ATLAS extensively used two such high-level taggers: MV2, which is based on boosted decision trees, and DL1, which relies on a deep neural network [129].

These high-level taggers take the outputs from the individual low-level b-tagging algorithms as inputs and generate output multidimensional predictions for the likelihoods of a jet being a b-jet, c-jet, or light-flavoured jet (p_b, p_c, p_u). These probabilities are then combined into a single discriminating variable defined as:

$$D(f_c) = \log\left(\frac{p_b}{f_c \cdot p_c + (1 - f_c) \cdot p_u}\right), \tag{4.8}$$

where f_c is a free parameter that represents the fraction of c-jets. This fraction is used to weigh the flavour importance, improving the performance for either c-jet or light-jet rejection without a complete retraining.

The standard MV2 algorithm uses input variables computed by the IP2D, IP3D, SV1, and JetFitter algorithms, along with the kinematic properties of the jets. Because many physics analyses are constrained by the ability to reject c-jets, the training composition of MV2 has evolved to increase c-jet rejection while maintaining similar light-jet rejection, with the current c-jet fraction set to 7%.

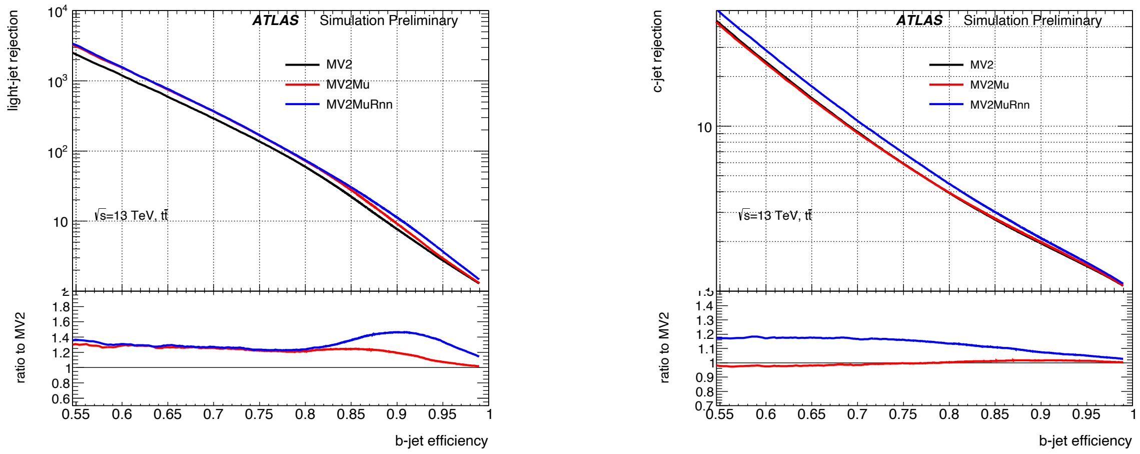

Figure 4.10: Light-flavour and c-jet rejection are shown as a function of b-jet efficiency for MV2 (black line), MV2Mu (red line), and MV2MuRnn (blue line). These algorithms were evaluated on $t\bar{t}$ events. The ratio at the bottom of the figure represents the performance of MV2Mu and MV2MuRnn relative to MV2 [129].

The DL1d tagger was the first baseline tagger for Run 3, incorporating the same input variables used in MV2, as well as c-tagging variables from JetFitter and flavour probabilities from the RNNIP algorithm. In comparison, the DL1d tagger differed from Run 2 DL1r primarily by using the Deep Sets-based tagger (DIPS) [134] instead of the Recurrent Neural Network-based RNNIP.

Heavy-flavour tagging algorithms are trained and optimised using MC simulations. Their performance in actual data often deviates from MC predictions due to imperfect modelling of detector effects. Therefore, the probability of correctly tagging a true b-, c-, or light-jet must be calibrated using collision data. These performance differences are quantified through scale factors, calculated as the ratio of efficiencies between data and MC simulations, which are then applied as event-level weights in physics analyses. Figures 4.9 and 4.10 compare the performance of various low- and high-level tagging algorithms and inputs discussed in this chapter.

4.3.3.3 GNN-based Taggers

In this analysis, jet identification originating from a b-hadron is achieved using a cutting-edge multivariate algorithm called GN2. GN2 represents a significant advancement and is now the main ATLAS flavour tagging algorithm for Run 3 data analysis. Unlike previous approaches, GN2 is a single, unified model that replaces both high- and low-level algorithms. It builds on GN1 [135], an earlier research and development version, by incorporating several key improvements. Specifically, GN2 replaces the Graph Attention Network [136] used in GN1 with Transformer Neural Networks [137, 138], along with other architectural enhancements and significantly more training data. Figure 4.11 compares the novel tagging approach from GN1 and GN2 algorithms against the previous approach used by ATLAS analysis.

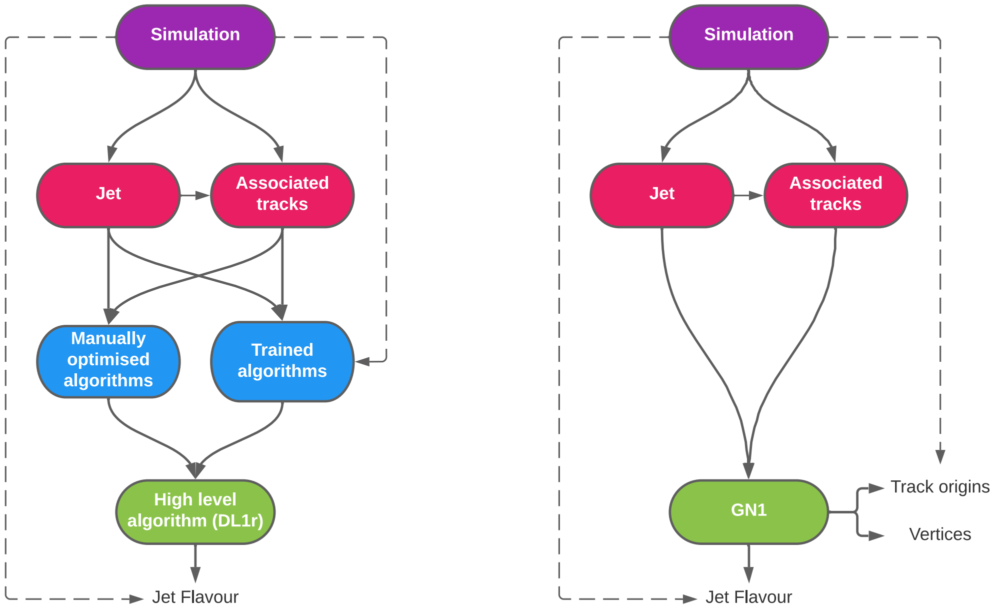

Figure 4.11: Comparison between the Run 2 flavour tagging approach using a combination of high- and low-level algorithms (left) and the new GN1 (or GN2) approach (right). In the previous method, low-level algorithms (indicated in blue) provide inputs to a high-level algorithm (such as DL1r). In contrast, the GN1 approach uses additional truth information from simulations as auxiliary training targets to perform the tagging task. Solid lines represent reconstructed information, while dashed lines represent truth information [135].

The GN2 algorithm predicts jet flavour by directly using low-level variables as inputs, such as individual track parameters, their associated uncertainties, and the jet's p_{T} and η. The transformer is trained with two auxiliary tasks to support to the primary goal of jet flavour identification.

The first auxiliary task determines track-pair vertex compatibility, which checks if two tracks in a pair originated from the same spatial point. This eliminates the need for a dedicated secondary vertexing algorithm. The second auxiliary objective predicts the underlying physics process for each track within the jet, identifying whether it originates from a b-hadron, c-hadron, light-flavour quark, pile-up, or is a fake track. This integrated approach results in a algorithm that shows a higher performance and that can be easily re-optimised in response to updates in the detector or reconstruction algorithms, or for other specific use cases.

The inputs include basic jet kinematics, as well as parameters from the reconstructed tracks and constituent hits. The jet's feature vectors are combined with the features of up to 40 associated tracks. The combined vectors are first passed through

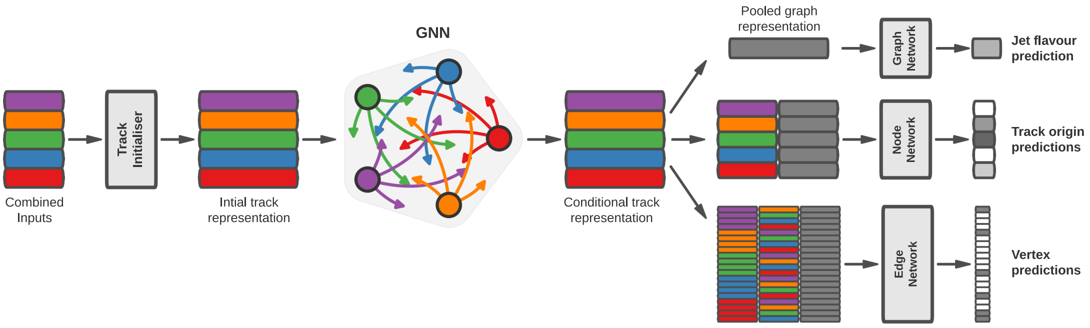

Figure 4.12: The GN1 network architecture. It begins by feeding inputs into a per-track initialisation network, which generates an initial latent representation for each track. These representations are then used to populate the node features in a fully connected graph network. After processing through the graph network, the final node representations are utilised to predict jet flavour, track origins, and track-pair vertex compatibility [135]. The GN2 architecture replaces the GNN used in GN1 with Transformer Neural Networks.

a per-track initialisation network, consisting of a single hidden layer and an output layer with 256 units. This is followed by a four-layer transformer encoder with eight attention heads. After the transformer encoder, the track representations are projected down to a 128-dimensional space. A global jet representation is then derived using attention pooling. This pooled jet representation, along with the output track embeddings, serves as input for three task-specific networks. For jet classification, only the pooled jet representation is used. In contrast, the track origin classification task processes each track embedding individually, and the track-pair compatibility task considers the embeddings of each track pair. In both cases, the global jet representation is also input into the task-specific networks. Each of these networks consists of three hidden layers with sizes of 128, 64, and 32, respectively, and ReLU activation is applied throughout the model. An example of the architecture of GNN-based tagger is shown in Figure 4.12.

As with the previous high-level algorithms, operating working points for GN2 can be selected to correspond to b-tagging efficiencies of 60%, 70%, 77%, 85% or 90%. To utilise the full b-tagging information of an event, each jet is assigned a pseudo-continuous b-tagging score. This score determines whether the jet passes each of the b-tagging operating points. In this work, information of multiple b-tagging WPs were used.

4.3.4 *b*-jet corrections

The jet calibrations described in Section 4.3.2 primarily focus on corrections for light-quark and gluon-initiated jets. As a result, they systematically underestimate the energy of jets initiated by heavy flavoured quarks. Two dedicated additional corrections [139] to the jet energy scale are applied to b-jets to account for two main effects:

1. The decays of b-hadrons have a higher fraction of leptons in their final state

compared to light hadrons, with approximately 10% of all b-hadron decays resulting in a soft muon within the jet. When the b-hadron decays semi-leptonically ($W \to \mu\nu_\mu$) in the cascade this affects the jet energy reconstruction as neutrinos escape the detector without depositing energy in the calorimeter and the neutrino energy is not accounted in the jet reconstruction. Additionally, the energy of muons produced through W-decays is only partially included for in the jet's energy estimate because the muon is not stopped in the calorimeter.

2. The b-jet fragmentation is wider in the $\eta - \phi$ plane than that of corresponding light-jets, resulting in fewer final state hadrons from the b-quark fragmentation being included in jet clustering reconstruction, this is referred as the *out-of-cone* effect.

To correct for these effects and account for the underestimation of the b-jet p_{T}, a harmonised two-step process is applied. Starting with the μ-in-jet and following with the p_{T}-reco correction. A brief description of both corrections is provided below. These calibrations result in a improved invariant-mass resolution of a resonance decaying into two bottom quarks.

4.3.4.1 μ-in-jet p_{T} correction

To account for the missing muon energy, a search for a muon within the jet is conducted. The muons is searched for within a variable radius cone from the jet axis defined as

$$\Delta R(\mu, \mathrm{jet}) < \min\left(0.4, 0.04 + \frac{10}{p_{\mathrm{T}}^{\mu}}\right), \tag{4.9}$$

where p_{T}^{μ} is the muon transverse momentum. The min function selects the smallest of its arguments, ensuring that the muon is not added from a distance greater than the jet clustering distance parameter. This approach accounts for the increasingly collimated decay products of more energetic jets.

If a muon identified at the loose working point with $p_{\mathrm{T}} > 4$ GeV and $|\eta| < 2.5$ is found within this ΔR cone, its four-momentum vector is added to that of the jet. This is done to add the muon reconstructed inside the jet back to the jet. If multiple muons meet these criteria, only the muon closest to the jet axis is used. Additionally, the expected energy that the muon lost in the calorimeter is subtracted from the jet energy estimate to avoid double-counting, as this contribution is already included in the jet's initial energy measurement.

4.3.4.2 p_{T}-reco correction

This second step accounts for the missing neutrino energy and out-of-cone effects that the previous calibrations don't capture. The residual difference is accounted in simulations between the reconstructed-jet p_{T} and the corresponding truth-jet p_{T}. A correction scale factor is derived in $t\bar{t}$ events to correct the reconstructed p_{T} of the b-jets in logarithmic bins of the truth jet p_{T}. The mean of the ratio between the p_{T} of reconstructed jet and truth p_{T} jet (matched with $\Delta R < 0.3$) is filled in bins of reconstructed log jet p_{T}. Since the correction is larger for b-jets decaying semi-leptonically, these correction factors are derived separately for b-jets with and without a muon.

Figure 4.13 illustrates the improvement achieved in this analysis by applying both b-jet corrections in $t\bar{t}HH$ Higgs mass resolution resolution.

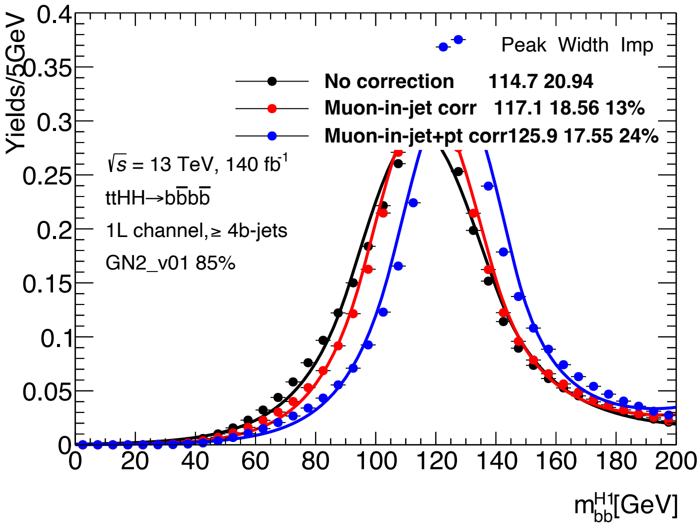

Figure 4.13: Comparisons of m_{bb}^{H1} distribution in the $t\bar{t}HH$ semileptonic channel before the b-jet corrections (black), after μ-in-jet correction (red) and after the μ-in-jet and b-jet corrections (blue). These distributions are fitted using Bukin function, and the peak value, the peak width (i.e. the mass resolution) and the relative improvements on the resolution are shown in the legend.

4.4 Missing Transverse Energy

Since protons at the LHC collide along the beam axis and possess only longitudinal momentum, the total transverse momentum (p_{T}) of the particles after the collision must sum to zero in order to conserve energy and momentum. The neutrinos do not interact with any part of the detector, leaving the detector volume without being observed. This results in an imbalance in the measured total transverse momentum. The neutrinos are inferred only from this missing contribution in the transverse plane, referred to as missing transverse energy ($E_{\mathrm{T}}^{\mathrm{miss}}$), calculated as the magnitude of the negative vector sum of the p_{T} of all selected reconstructed objects [140].

$$E_{x(y)}^{\mathrm{miss}} = E_{x(y)}^{\mathrm{miss},e} + E_{x(y)}^{\mathrm{miss},\mu} + E_{x(y)}^{\mathrm{miss},\tau} + E_{x(y)}^{\mathrm{miss},\gamma} + E_{x(y)}^{\mathrm{miss},jets} + E_{x(y)}^{\mathrm{miss},soft}, \tag{4.10}$$

where $E_{x(y)}^{\mathrm{miss}}$ represents the x (y) component of the MET. Each term corresponds to the negative sum of the energy of objects such as electrons (e), muons (μ), tau leptons (τ), photons (γ), and jets, projected onto the x (y) axis. The final term, known as the soft term, accounts for contributions from objects not associated with any selected object, including inner detector tracks or calorimeter signals.

The magnitude of the $E_{\mathrm{T}}^{\mathrm{miss}}$ and the azimuthal angle ϕ^{miss} can be determined using the following equations:

$$E_{\mathrm{T}}^{\mathrm{miss}} = \sqrt{(E_x^{\mathrm{miss}})^2 + (E_y^{\mathrm{miss}})^2} \tag{4.11}$$

$$\phi^{\mathrm{miss}} = \arctan\left(\frac{E_y^{\mathrm{miss}}}{E_x^{\mathrm{miss}}}\right). \tag{4.12}$$

The missing transverse momentum can also be calculated using only tracks from the inner detector, referred to as $E_{\mathrm{T,trk}}^{\mathrm{miss}}$. This metric offers a more robust estimate of the missing transverse momentum, with reduced sensitivity to pile-up effects. However, since $E_{\mathrm{T,trk}}^{\mathrm{miss}}$ relies solely on tracks left by charged particles, it does not account for neutral particles or those outside the coverage of the inner detector.

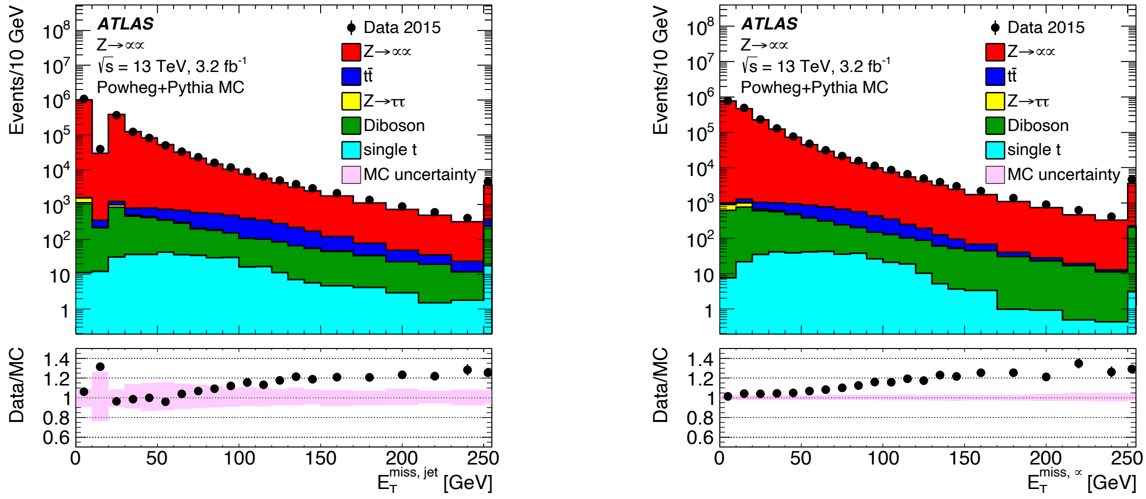

Figure 4.14: Data/MC agreement for the jet (a) and the muon term (b) of $E_{\mathrm{T}}^{\mathrm{miss}}$ for an inclusive sample of $Z \to \mu\mu$ events in data. The shaded areas represent the total uncertainty from MC events, including the combined statistical and systematic uncertainties for each term [141].

The performance of $E_{\mathrm{T}}^{\mathrm{miss}}$ reconstruction is evaluated by comparing a set of $E_{\mathrm{T}}^{\mathrm{miss}}$-related observables between data and MC simulations, using the same final-state, object selection, and event selection criteria. These comparisons are used to derive systematic uncertainties in the $E_{\mathrm{T}}^{\mathrm{miss}}$ response and resolution [140].

The performance of $E_{\mathrm{T}}^{\mathrm{miss}}$ is obtained by comparing two scenarios: one without genuine $E_{\mathrm{T}}^{\mathrm{miss}}$, such as in $Z \to \mu\mu$ events, and one with genuine $E_{\mathrm{T}}^{\mathrm{miss}}$, such as in $W \to e\nu$ events. The $E_{\mathrm{T}}^{\mathrm{miss}}$ individual contributions from jets and muons for these two final states are shown in Figure 4.14. In the $Z \to \mu\mu$ sample, the agreement between data and MC simulations is within 20% for $E_{\mathrm{T}}^{\mathrm{miss}} < 120$ GeV, with significant discrepancies only observed at high $E_{\mathrm{T}}^{\mathrm{miss}}$ values, primarily due to mismodeling in $t\bar{t}$ events. In the $W \to e\nu$ sample, which includes genuine $E_{\mathrm{T}}^{\mathrm{miss}}$, the data and MC simulations show a 20% agreement across the entire missing transverse momentum range.

The width of the distribution of the differences between the measured $E_{x(y)}^{\mathrm{miss}}$ and the true missing transverse momentum vector $E_{x(y)}^{\mathrm{miss,\ true}}$ is used to determine the reso-

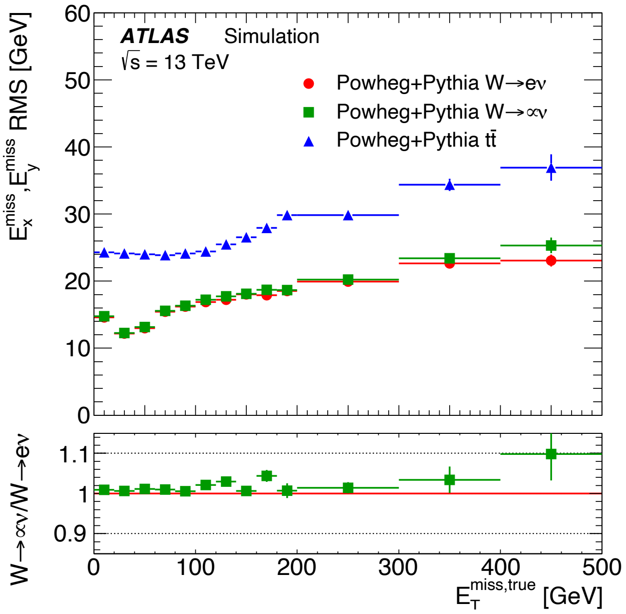

Figure 4.15: The missing energy resolution as a function of the true missing transverse momentum for $W \to e\nu$, $W \to \mu\nu$, and $t\bar{t}$ events [141].

lution of $E_{\mathrm{T}}^{\mathrm{miss}}$. This resolution is quantified as the root mean square (RMS) of these differences. Dedicated MC simulation samples, such as $W \to e\nu$, $W \to \mu\nu$, and $t\bar{t}$ events are used. The $E_{\mathrm{T}}^{\mathrm{miss}}$ resolution as a function of $E_{\mathrm{T}}^{\mathrm{miss}}$ is shown in Figure 4.15. The resolution is found to be similar for the $W \to e\nu$ and $W \to \mu\nu$ final states but is poorer in the $t\bar{t}$ final states. This reduced resolution in $t\bar{t}$ events is primarily due to the presence of at least four jets with relatively low p_{T}, and this topology is more susceptible to fluctuations caused by pile-up.

As the uncertainties related to the hard terms are already included in the systematic uncertainties of the other physics objects, the uncertainties in $E_{\mathrm{T}}^{\mathrm{miss}}$ are primarily associated with the soft terms. These uncertainties are derived from the propagation of energy scale and resolution uncertainties of the soft terms by comparing data to MC simulations of events without genuine $E_{\mathrm{T}}^{\mathrm{miss}}$, such as $Z \to \mu\mu$ events. The maximum discrepancy between data and MC simulations is around 10% at high $E_{\mathrm{T}}^{\mathrm{miss}}$ values.

4.5 Overlap Removal

An overlap removal algorithm is applied to all reconstructed objects to prevent multiple objects from being reconstructed from the same detector information, ensuring that single final state objects are not double-counted as different objects. In this analysis, overlaps between leptons and small-R jets are resolved through a step-by-step procedure, using only the loose object definitions. The algorithm used to address these ambiguities follows the standard overlap removal procedure outlined in Ref. [142]. Table 4.1 shows the overlap removal procedure applied in this thesis.

Lepton duplications are resolved by using track information. An Electron that shares an ID track with another reconstructed electron is removed based on the trans-

Reject	Against	Criteria
Electron	Electron	Shared track, $p_{T,1} < p_{T,2}$
Muon	Electron	Is calorimeter-tagged Muon and shared ID track
Electron	Muon	Shared ID track
Jet	Electron	$\Delta R < 0.2$
Electron	Jet	$\Delta R < 0.4$
Jet	Muon	Number of tracks < 3 and (ghost-associated or $\Delta R < 0.2$)
Muon	Jet	$\Delta R < \min(0.4, 0.04 + \frac{10\text{ GeV}}{p_{\mathrm{T}}(\mu)})$
Photon	Lepton	$\Delta R < 0.4$
Photon	Jet	$\Delta R < 0.4$

Table 4.1: Overlap removal procedure that compares two types of objects at a time and checks for geometric overlap, applied from the top to bottom for the objects reconstructed in the analyses of this thesis. One object or the other is removed, depending on a pre-defined criteria.

verse momentum, the one with the highest p_{T} is kept. Any calorimeter-tagged muon that shares a track with an electron is removed. If the muon is not calorimeter-tagged and is found to share a track with a electron, the electron is removed.

To avoid double-counting electron energy deposits in jet reconstruction, any jet within $\Delta R = 0.2$ of a selected electron is removed. This is necessary because energy deposits in the electromagnetic calorimeter are always included in jet reconstruction, regardless of the electron reconstruction outcome. If the nearest surviving jet is within $\Delta R = 0.4$ of the electron, the electron is discarded, as it is likely to originate from the semi-leptonic decays of heavy-flavour hadrons.

For muons, those within $\Delta R < 0.4$ of the nearest jet are removed, as they are considered products of semi-leptonic heavy-flavour hadron decays. However, if the muon is found within $\Delta R < 0.2$ of a jet and the jet has fewer than three associated tracks, the muon is retained, and the jet is removed instead. This exception accounts for cases where the low track multiplicity may result from radiation effects from the muon, preventing inefficiency for high-energy muons that undergo significant energy loss in the calorimeter. Additionally, any jet with fewer than three associated tracks that has an ID muon track ghost-associated[3] with it is also removed.

Finally, if any photon is found within a $\Delta R = 0.4$ of an electron, a muon or a jet, the photon is removed.

---

[3] Ghost-association refers to a jet matching technique that treats each MC simulated particle as a ghost particle, which means that they have infinitesimal amount of p_{T}, only retaining the direction information of the jets and ensuring that jet reconstruction is not altered by the ghosts [122].

5

Strategy for Non-resonant $t\bar{t}HH$ Search Using Run 2 and partial Run 3 Data

Contents

This chapter presents a summary of the first search for HH production associated with top-quarks conducted by ATLAS. The search uses pp collision data from the full

Run 2 and partial Run 3 datasets, corresponding to a center-of-mass energy of $\sqrt{s} = 13$ and 13.6 TeV and integrated luminosity of 140 and 59 fb^{-1} collected by the ATLAS detector during the years 2015 to 2023.

This chapter outlines the analysis strategy, starting with an overview of the analysis in Section 5.1 and a description of the datasets and MC simulations used in Section 5.2. The subsequent sections cover the trigger selections in Section 5.3, object reconstruction, and event pre-selection in Section 5.4. The reconstruction of Higgs boson candidates is discussed in Section 5.5, and the background modelling is discussed separately for different final states in Section 5.6 and 5.7. Multivariate techniques applied are described in Section 5.8. Finally, the systematic uncertainties are discussed in Section 5.9.

5.1 Analysis Overview

Since the $t\bar{t}HH$ production cross-section is expected to be small in the SM (Table 3.1) and in order to benefit from an increased signal acceptance, the analysis presented in this dissertation searches for $t\bar{t}HH$ production targeting various decay modes of the HH system. Events are selected if they contain multiple jets along with at least one charged lepton (electron or muon). The events are categorised into four final states based on the number specific objects present in the events. The final states are referred to as 1L, OS2L and ML final states and will be detailed bellow.

The 1L and OS2L final states, containing one lepton or two oppositely charged leptons, respectively, mainly target the $HH \to b\bar{b}b\bar{b}$ mode. These states account for a large fraction of $t\bar{t}HH$ decays, capturing almost 20% of all produced $t\bar{t}HH$ events. However, it suffers from a large irreducible background, predominantly composed of $t\bar{t}$ production with additional jets ($t\bar{t}$ + jets). The $t\bar{t}HH(HH \to b\bar{b}b\bar{b})$ topology is characterised by high jet and b-jet multiplicities and high overall energy. This can be quantified by the scalar sum of the transverse momenta of objects in the event (H_{T}), which tends to have a large value for these final states.

The ML final state targets all components of the HH decay modes (excluding $HH \to b\bar{b}b\bar{b}$) which are characterised by two charged leptons (exclusively electrons or muons) of the same electric charge or more than two leptons. The same-sign (SS) leptons are mainly present when one lepton originates from a top quark and the other from a Higgs boson. This allows one Higgs to still decay to $b\bar{b}$ (or other modes), preserving a higher branching fraction. This final state captures almost 7% of all produced $t\bar{t}HH$ events and contains a low level of background contamination.

Figures 5.1 and 5.2 show the contributions of the different decay modes of the Higgs boson pair to possible analysis final states after applying preselection requirements on the number of b-jets, leptons and lepton charge. For clarity, the figures are presented separately, as the acceptance of the ML channels is comparatively lower.

This chapter discusses the common as well as specific elements and strategies for the $t\bar{t}HH$ final states used in the analyses. The differences between the channels are always mentioned throughout this chapter. The 1L and OS2L channels largely share the same strategy because they target a similar phase-space. The orthogonality between

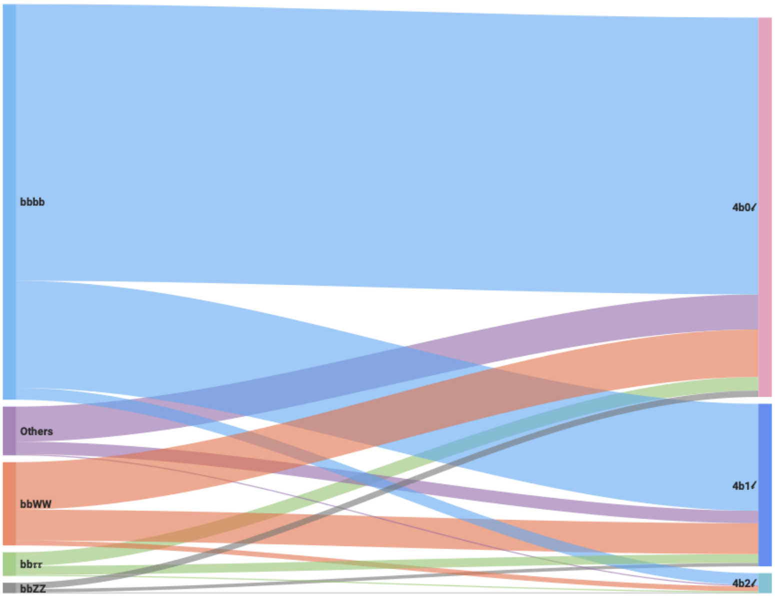

Figure 5.1: Schematic representation of the number of $t\bar{t}HH$ signal events from various HH decay modes on the left and their acceptance into different selections requirements on the number of b-jets, leptons and lepton charge. The y-axis represents the relative number of events.

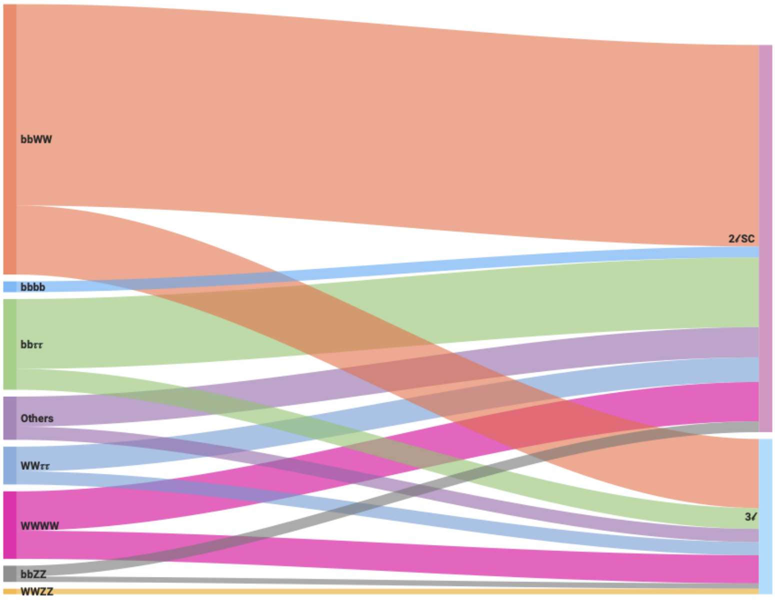

Figure 5.2: Schematic representation of the number of $t\bar{t}HH$ signal events from various HH decay modes on the left and their acceptance into different selections requirements on the number of b-jets, leptons and lepton charge. The y-axis represents the relative number of events.

all four channels is always guaranteed by the trigger and pre-selections applied. The search presented in this thesis establishes observed (expected) limits on the SM $t\bar{t}HH$ production cross-sections.

5.2 Data and Monte Carlo Samples

This section gives a description of the dataset and all MC samples used in this analysis addressing each process individually and the technical aspects about the respective event generators.

Dataset

This thesis uses the full Run 2 dataset of pp collisions collected from 2015 to 2018 by the ATLAS detector, corresponding to an integrated luminosity of 140.1 fb^{-1}. The uncertainty on the combined dataset was reduced from 1.7% to 0.83% [143]. Additionally, partial Run 3 dataset collected during 2022 and 2023 is also used, corresponding to an integrated luminosity of 59 fb^{-1}. The uncertainty of the combined luminosity is 2.0%. Standard data taking quality requirements are applied, such as stable LHC beams and fully operational ATLAS detector conditions.

Monte Carlo Samples

The simulation of pp collisions is crucial for nearly all experimental analyses. These simulated events are generated by MC event generators, which employ numerical techniques to provide a detailed simulation of the underlying physics of particle collisions. The collision process is broken down into several stages, each occurring at different energy scales, ranging from very short distances to the larger scales of hadron formation and decays. These steps can be divided into the matrix element (ME), parton showering (PS), hadronization, underlying event (UE) and detector response simulation.

At short distances, the constituent partons within the incoming protons interact, producing a few energetic outgoing partons, leptons, or gauge bosons. The probability density function for a specific process is determined by the square of the ME. Within the available phase-space, the ME describes the partonic cross-section using perturbative QCD. In this search, the ME of the different processes were calculated at different theoretical precision using MadGraph or MadGraph5_aMC@NLO [144], PowhegBox [145–148] and Sherpa [149]. Different parton distribution function (PDF) sets can be used to describe the probability of finding and interacting with specific partons inside a proton during a collision. For this analysis, the samples are generated using the NNPDF [150] sets, as outlined in Section 5.1. For all processes involving top quarks, a top-quark mass of $m_{\text{top}} = 172.5\,\text{GeV}$ is used. For all processes involving Higgs bosons, the Higgs mass is assumed to be 125 GeV.

When colour-charged particles scatter, they emit QCD radiation in the form of gluons. Since the partons involved in both the initial and final states of the hard process carry colour charge, they radiate gluons. These gluons, in turn, can radiate further gluons or produce quark-antiquark pairs, giving rise to cascading emissions of partons called PS. As the PS progresses to lower energy scales, perturbative methods break down, and it becomes necessary to apply hadronization models. At these energy scales, the partons begin to combine into colour-neutral hadrons. Hadronisation models are used to describe the confinement of partons into hadrons, many of which are initially produced in excited states. These excited hadrons eventually decay into stable particles. Besides the primary hard process, additional parton interactions can occur between the initial proton constituents. These secondary interactions contribute to what is called the UE, which can interfere with the hard process simulation. The UE is modelled using phenomenological approaches, with parameters tuned based on experimental observations.

PS generators are designed to describe the collinear and soft emissions of the radioactive process that occurs after the primary interaction. To prevent double counting in the multi-jet phase space, PS algorithms are integrated with the ME through jet matching and merging techniques. In this search, Pythia8 [151] and Herwig7 [152, 153] are used for the simulation of PS and hadronization in combination with ME generators such as MadGraph5_aMC@NLO and PowhegBox. In some cases, Sherpa is employed to handle both ME and PS calculations. PS generators rely on several free parameters to model PS, hadronization, and UE. These parameters are tuned to experimental data using observables sensitive to these effects. The ATLAS experiment provides a standalone tune for Pythia8, called "A14" tune, with different PDF sets [154]. Default tunes are also available from Herwig and Sherpa. The Higgs boson decays are managed by the PS generator, while the MadSpin package [155, 156] is used for decays at LO of the top-quarks, Z bosons, and W bosons produced with MadGraph5_aMC@NLO ME preserving all spin correlations.

Once PS, hadronization, and the decay of most unstable particles have been simulated, an additional step is performed to simulate the detector response, providing a more realistic representation of what would be observed by the detector. In this analysis, two simulation approaches were utilised: full ATLAS detector simulation (FS) [157] relying on Geant4 [158] and fast simulation (AF3). The full simulation fully simulates particle interactions with the detector material, the electronic response of each detector component, and the algorithms used for identifying and reconstructing various physics objects. The faster simulation uses parameterised models for the electromagnetic and hadronic calorimeter shower shapes [159]. Both simulations are expected to give similar modelling.

A summary of the generators used for each process for Run 2 and Run 3 samples is presented in Table 5.1, together with the ME order, PDF and PS tune.

- Signal $t\bar{t}HH$ samples

The $t\bar{t}HH(HH \rightarrow b\bar{b}b\bar{b})$ signal samples are produced separately for each top decay channel: full hadronic, single-lepton and dilepton. Each sample is simulated using MadGraph v3.3.1 at LO and Pythia8 (v.308) is used for PS and hadronization. The normalisation of the SM process is set to the SM $t\bar{t}HH$ cross-section, $\sigma_{ttHH} = 0.756$ fb^{-1} for Run 2 (13 TeV) and $\sigma_{ttHH} = 0.860$ fb^{-1} for Run 3 (13.6 TeV), calculated at NLO QCD [90], times the $HH \rightarrow b\bar{b}b\bar{b}$ branching ratio (0.582^2 [19]) and the branching fraction of each top decay channel, based on the W decays (67.41% and 10.86% [19] for hadronic and leptonic decays, respectively). The $t\bar{t}HH(HH \rightarrow b\bar{b}b\bar{b})$ branching fraction in the full hadronic, single-lepton and dilepton channels are, respectively:

$$BR_{ttHH}^{all-had.} = 0.6741^2 \times 0.582^2 = 0.153919 \tag{5.1}$$

$$BR_{ttHH}^{single-lep.} = 0.6741 \times (0.1086 \times 3) \times 2 \times 0.582^2 = 0.148782 \tag{5.2}$$

$$BR_{ttHH}^{dilep.} = (0.1086 \times 3)^2 \times 0.582^2 = 0.0359541 \tag{5.3}$$

To consider the contributions of all ML signal decays orthogonal to the previous $t\bar{t}HH$ signal samples, samples were also produced using MadGraph v3.3.1 at LO and Pythia8 (v.308) requesting all HH decays other than $HH \to b\bar{b}b\bar{b}$. A two-lepton filter following by a same-sign ML filter is applied to have either a same-sign di-lepton pair or multi-lepton final states. This guarantees that the sample will cover all non-hadronic component of HH decays and be orthogonal to the $t\bar{t}HH(HH \to b\bar{b}b\bar{b})$ samples.

- $t\bar{t}$ (5FS)

The nominal production of $t\bar{t}$ events is modelled using the Powheg [145–148] v2 generator at NLO in the strong coupling constant α_s, with the NNPDF3.0 NLO [150] PDF set. The h_{damp} parameter[1] set to 1.5 m_{top} [160]. The functional form of the renormalisation and factorisation scales is set to the default scale of $\sqrt{m_{\text{top}}^2 + p_{\text{T}}^2}$. The events are interfaced with Pythia8.230 [151] using the A14 tuned parameters [154] and the NNPDF2.3 LO PDF set. The $t\bar{t}$ sample is normalised to $\sigma(\text{t})_{\text{NNLO+NNLL}} = 832 \pm 51\,\text{fb}^{-1}$, which is the cross-section prediction at next-to-next-to-leading order (NNLO) in QCD including the re-summation of next-to-next-to-leading logarithmic (NNLL) soft-gluon terms calculated using Top++ 2.0 [161–167].

These samples are generated in the 5-flavour scheme (5FS), where b-quarks are considered massless, and used as the nominal prediction for $t\bar{t}$ + jets in all the final states of this analysis.

To evaluate theoretical uncertainties in the modelling of $t\bar{t}$ production, dedicated variations are considered. The impact of the matrix-element and parton-shower NLO matching is assessed through variations of the $p_{\text{T}}^{\text{hard}}$ parameter. Uncertainties associated with the radiation in the matrix element–parton shower matching are evaluated through variations of the h_{damp} parameter in the PowhegGenerator. Additionally, an alternative shower and hadronization model is probed by interfacing the same NLO matrix element with Herwig7.04 [152, 153], referred to as the PhH7 variation. These variations are used to assess the associated modelling uncertainties across all final states considered in this analysis.

- $t\bar{t}b\bar{b}$ (4FS)

The nominal production of top-quarks pairs with additional jets represents the main background source for the 1L and OS2L final states. In these final states, the 4-flavour scheme (4FS) samples, with massive b-quarks, are used to account for shape

---

[1] The h_{damp} parameter controls the transverse momentum p_T of the first additional emission beyond the leading-order Feynman diagram in the PS and therefore regulates the high-p_T emission against which the $t\bar{t}$ system recoils.

and acceptance variation uncertainties of the nominal 5FS samples to model the $t\bar{t} + \geq 1b$ background.

The production of $t\bar{t} + \geq 1b$ is modelled using a dedicated MC simulation for the top-quark pair production in association with a b-quark pair, $t\bar{t}b\bar{b}$ [168]. The predictions are calculated using the PowhegBox-Res framework at NLO with massive b-quarks [169], $m_b = 4.75$ GeV, with the NNPDF3.0NLO PDF sets. The PowhegBox internal parameter h_{damp} is set to $H_T/2$, being H_T the scalar sum of all transverse momenta over leptons and jets. The renormalisation scale is set to half the geometric average of the transverse mass of top- and b-quarks defined as $\sqrt[4]{\Pi_{i=t,\bar{t},b,\bar{b}} E_{T,i}}$, where $E_{T,i}$ refers to the transverse energy and i to the top or bottom quarks. The factorisation scale is related to the average of the transverse mass of the outgoing partons in the ME calculation and is defined as $\frac{1}{2}[\Pi_{i=t,\bar{t},b,\bar{b},j} E_{T,i}]$. The PowhegBox internal parameter h_{bzd}, which controls the fraction of events produced in singular and finite regions, is set to 5. These choice of scales follow the latest recommendations from the LHC Higgs WG, described in detail in [168]. The PowhegBox ME calculation is matched to Pythia8 with the A14 tuned parameters [154] for the PS and hadronisation modelling. This sample is used as systematic uncertainties for $t\bar{t} + \geq 1b$ component in the 1L and OS2L final states of this search.

- Single-top

Single-top tW associated production is modelled using the Powheg [146–148, 170] v2 generator at NLO in QCD in the 5FS with the NNPDF3.0 NLO [150] PDF set. The diagram removal scheme [171] was employed to handle the interference with $t\bar{t}$ production [160].

Single-top $t(q)b$ production is separated into $s-$ and $t-$ channels. The t-channel is modelled using the Powheg [146–148, 172] v2 generator at NLO in QCD in the 4FS with the NNPDF3.0 NLO4f [150] PDF set. The s-channel production is modelled using the Powheg [146–148, 173] v2 generator at NLO in QCD in the 5FS with the NNPDF3.0 NLO [150] PDF set.

For all single-top processes, the events are interfaced with Pythia8.230 for Run 2 (Pythia8.308 for Run 3) [151] using the A14 tune [154] and the NNPDF2.3 LO PDF.

- tWZ + jets

The tWZ events are generated at NLO using MadGraph5_aMC@NLO v2.3.3 for Run 2 (v3.5.1 for Run 3) [174] generator with the NNPDF3.0 NLO [150] PDF set, interfaced with Pythia8.212 for Run 2 (Pythia8.309 for Run 3) [151] using the A14 tune [154] and the NNPDF2.3 LO [175] PDF set.

- Rare $t + X$ and $t\bar{t} + X$

The production of tZ is modelled using the MadGraph5_aMC@NLO generator at LO with $H_{\text{T}}/6$ scale and PDF `NNPDF3.0NLOnf4`.

The production of Run 2 $t\bar{t}WW$ are modelled using the MadGraph5_aMC@NLO generator at LO interfaced with Pythia8 using the A14 tune. The contribution from

$t\bar{t}WW$ has been normalised to the NLO QCD theoretical cross-section [174]. The production of Run 3 $t\bar{t}WW$ and all $t\bar{t}WZ$, $t\bar{t}WH$, $t\bar{t}ZZ$ are modelled using MadGraph generator at LO with PDF `NNPDF3.0nlo`.

All $t+X$ and $t\bar{t}+X$ samples are interfaced with Pythia8 using the A14 tune.

- $t\bar{t}t\bar{t}$

MadGraph5_aMC@NLO v3.5.3 [174] generator is used to model the nominal production of $t\bar{t}t\bar{t}$ events, which provides MEs at NLO in the strong coupling constant $\alpha_s$with the `NNPDF3.0nlo` [150] parton distribution function. The functional form of the renormalization and factorisation scales are set to $0.25\times\sum_i\sqrt{m_i^2+p_{T,i}^2}$, where the sum runs over all the particles generated from the ME calculation, following Ref. [176]. Top quarks are decayed at LO using MadSpin [177, 178] to preserve all spin correlations. The events are interfaced with Pythia8.230 for Run 2 (Pythia8.310 for Run 3) [151] for the PS and hadronization, using the A14 set of tuned parameters [154] and the NNPDF23LO [150] PDF set. The decays of bottom and charm hadrons are simulated using the EvtGen v1.6.0 program [179].

To evaluate the impact of the PS and hadronization model an additional sample is also produced at NLO replacing the PS of the nominal samples to Herwig7.04 [152, 153]. The H7UE set of tuned parameters [153] and the MMHT2014LO PDF set [180] are used for this sample.

An additional $t\bar{t}t\bar{t}$ sample is also produced at NLO using the Sherpa v2.2.11 [149] generator with the NNPDF3.0 NNLO [150] PDF set to account for the generator uncertainty. The functional form of the renormalisation and factorisation scales are set to $\mu_r=\mu_f=H_\mathrm{T}/2$. The Sherpa v2.2.11 sample can include the EW contribution from $\mathcal{O}(\alpha_S^3\alpha)+\mathcal{O}(\alpha_S^2\alpha^2)+\mathcal{O}(\alpha_S^4\alpha)$ (LO2+LO3+NLO2) diagram through the EW weights in the additive scheme. Based on studies from [176], different EW contributions tend to cancel each other and only part of the EW NLO2 terms are included. So the EW contribution is not considered in the nominal fit setup. The EW systematics will be tested in a separated test.

For all the $t\bar{t}t\bar{t}$ samples, the ATLAS detector response is simulated using AF3.

- $t\bar{t}t$

The production of $t\bar{t}t$ is modelled using the MadGraph5_aMC@NLO generator at LO in QCD interfaced with Pythia8 using the A14 tune in the 5FS. The scale used is the default dynamic choice in MadGraph5_aMC@NLO (the transverse mass of the $2\to 2$ system resulting of a k_t clustering). The 5FS is used instead of the 4FS in order to prevent any LO interference between ttt and $t\bar{t}t\bar{t}$ that is currently unknown how to handle. The $t\bar{t}t$ production includes $t\bar{t}tW$ and $t\bar{t}tq$ processes, which are separated into two samples for Run 3. $t\bar{t}tW$ and $t\bar{t}tq$ are normalised to the cross section of 1.02 fb and 0.65 fb at 13 TeV, respectively, computed at NLO.

- $t\bar{t}W$

The production of nominal $t\bar{t}W$ events is modelled in QCD using the Sherpa v2.2.10 for Run 2 (Sherpa v2.2.14) [149] generator with the NNPDF3.0 NNLO [150] PDF set with up to one extra parton at NLO and up to 2 extra partons included at LO. The additional partons are matched and merged with the Sherpa PS based on Catani-Seymour dipole factorisation [181] using the MEPS@NLO prescription [182–185] with a merging scale of 30 GeV. The virtual QCD correction for MEs at NLO accuracy are provided by the OpenLoops 2 [186–188] library. The electroweak contribution from $\mathcal{O}(\alpha^3)+\mathcal{O}(\alpha_S^2\alpha^2)$ (LO3+NLO2) diagrams is included in this sample via two alternative sets of event weights.

The production of $t\bar{t}W$ variation with only electroweak (EW) corrections from $\mathcal{O}(\alpha_S\alpha^3)$ (NLO3) diagrams is modelled at LO using the same generator and PDF set as in the QCD-only production.

- $t\bar{t}Z$

The production of nominal $t\bar{t}Z$ events uses MadGraph5_aMC@NLO v2.8.1 for Run 2 (v3.4.2 for Run 3) [174] generator at NLO with the `NNPDF3.0nlo` [150] PDF set. The events are interfaced with Pythia8.244 for Run 2 (Pythia8.8.309 for Run 3) [151] using the A14 tune [154] and the NNPDF2.3LO [150] PDF set. The ATLAS detector response is simulated using FS.

In order to account for the generator uncertainty, an alternative sample is generated with the Sherpa v2.2.11 generator at NLO with the NNPDF3.0 NNLO PDF set.

- $t\bar{t}H$

The production of nominal $t\bar{t}H$ events is modelled using the PowhegBox [145–148] generator at NLO with the NNPDF3.0NLO [150] PDF set for Run 2, and PDF4LHC21 PDF set [189] for Run 3. The events are interfaced with Pythia8.230 and Pythia8.308 for Run 2 and Run 3 [151], respectively, using the A14 tune [154] and NNPDF2.3LO [150] PDF set.

To evaluate the impact of the PS and hadronization model an additional sample is also produced at NLO replacing the PS of the nominal samples to Herwig7.2.3 for Run 2 (Herwig7.2.3p2 for Run 3) [152, 153]. Note that the NNPDF3.0 NLO PDF set is used for the Run 3 sample.

The ATLAS detector response is simulated using FS for the nominal sample and AF3 for the alternative samples.

- V + jets

The production of V+jets is simulated with the Sherpa v2.2.11 [149] generator using NLO-accurate MEs for up to two jets, and LO-accurate MEs for up to four jets calculated with the Comix [190] and OpenLoops [186, 187] libraries. They are matched with the Sherpa PS [181] using the MEPS@NLO prescription [182–185] using the set of tuned parameters developed by the Sherpa authors. The NNPDF3.0 NNLO set of PDFs [150] is used and the samples are normalised to a NNLO prediction [191].

- VV + jets

Samples of diboson final states (VV) are simulated with the Sherpa v2.2.14 [149] generator. The fully leptonic final states and semileptonic final states, where one boson decays leptonically and the other hadronically, are simulated using MEs at NLO accuracy in QCD for up to one additional parton emission and at LO accuracy for up to three additional parton emissions. Samples for the loop-induced processes $gg \to VV$ are generated using LO-accurate MEs for up to one additional parton emission for both cases of fully leptonic and semileptonic final states. The ME calculations are matched and merged with the Sherpa PS based on Catani-Seymour dipole factorisation [181, 190] using the MEPS@NLO prescription [182–185]. The virtual QCD correction are provided by the OpenLoops library [186, 187]. The NNPDF3.0 NNLO set of PDFs is used [150], along with the dedicated set of tuned parton-shower parameters developed by the Sherpa authors.

- VVV + jets

The production of triboson (VVV) events is simulated with the Sherpa v2.2.2 for Run 2 (v2.2.14 for Run 3) [149] generator using factorised gauge boson decays. MEs, accurate at NLO for the inclusive process and at LO for up to two additional parton emissions, are matched and merged with the Sherpa PS based on Catani-Seymour dipole factorisation [181, 190] using the MEPS@NLO prescription [182–185]. The virtual QCD correction for MEs at NLO accuracy are provided by the OpenLoops library [186, 187].

- VH

The WH and ZH processes were generated using the PowhegBox generator and NNPDF3.0 AZNLO PDF set, interfaced by Pythia8.230 with the A14 tune and NNPDF2.3 LO PDF set. They are normalised to the theoretical cross sections calculated at NNLO in QCD and NLO electroweak accuracy.

5.3 Trigger Selections

In the 1L, OS2L and ML channels, the events are recorded using a combination of the loosest unprescaled single-lepton triggers. These events must either pass triggers with the lowest transverse momentum threshold combined with a lepton isolation requirement or pass triggers with higher thresholds that have looser identification criteria and no isolation requirement. The p_T thresholds, along with the identification and isolation criteria, vary for the lepton flavours and each data-taking period. An event is selected if it passes any of the single-lepton triggers. For muons, the lowest single-lepton trigger p_T threshold is 20 GeV for the 2015 data, 26 GeV for the 2016–2018 period and 24 GeV for 2022-2023. For electrons, the lowest single-lepton p_T thresholds are 24 GeV for 2015 and 26 GeV for 2016–2023. Table 5.2 shows a list of the different single-lepton triggers used for each data taking period. A matching between online objects firing the trigger and the offline reconstructed object is required. Dilepton triggers were also tested and found to have no significant impact on the acceptance.

Process	ME generator	ME order	ME PDF	PS	Tune
di-Higgs boson					
$t\bar{t}HH$	MadGraph v3.3.1	LO	`NNPDF2.3lo`	Pythia8	A14
$t\bar{t}$ and single-top					
$t\bar{t}$ (5FS)	PowhegBox v2	NLO	`NNPDF3.0nlo`	Pythia8 Herwig7	A14
$t\bar{t}b\bar{b}$ (4FS)	PowhegBoxRes	NLO	`NNPDF3.0NLOnf4`	Pythia8.230	A14
tW	PowhegBox v2	NLO	`NNPDF3.0nlo`	Pythia8	A14
$t(q)b$	PowhegBox v2	NLO	`NNPDF3.0nlo`(s) `NNPDF3.0NLOnf4`(t)	Pythia8	A14
tWZ	MadGraph5_aMC@NLO	NLO	`NNPDF3.0nlo`	Pythia8	A14
tZ	MadGraph5_aMC@NLO	LO	`NNPDF3.0NLOnf4`	Pythia8	A14
$t\bar{t}t\bar{t}$ and $t\bar{t}t$					
$t\bar{t}t\bar{t}$	MadGraph5_aMC@NLO	NLO	`NNPDF3.0nlo`	Pythia8	A14
	MadGraph5_aMC@NLO	NLO	MMHT2014LO	Herwig7	H7-UE-MMHT
	Sherpa	NLO	NNPDF3.0 NNLO	Herwig7	Sherpa
$t\bar{t}t$	MadGraph5_aMC@NLO	LO	`NNPDF2.3lo`	Pythia8	A14
$t\bar{t}V$					
$t\bar{t}H$	PowhegBox v2	NLO	`NNPDF3.0nlo`(Run 2) PDF4LHC21 (Run 3)	Pythia8	A14
	PowhegBox v2	NLO	`NNPDF3.0nlo`	Herwig7	H7.2-Default
$t\bar{t}Z$	MadGraph5_aMC@NLO	NLO	NNPDF3.0 NNLO	Pythia8	A14
$t\bar{t}W$	Sherpa	NLO	NNPDF3.0 NNLO	Sherpa	Sherpa
	Sherpa	LO	NNPDF3.0 NNLO	Sherpa	Sherpa
$t\bar{t}VV$					
$t\bar{t}WW$	MadGraph5_aMC@NLO(Run 2) MadGraph(Run 3)	LO	`NNPDF3.0nlo`	Pythia8	A14
$t\bar{t}WZ$	MadGraph	LO	`NNPDF3.0nlo`	Pythia8	A14
$t\bar{t}WH$	MadGraph	LO	`NNPDF3.0nlo`	Pythia8	A14
$t\bar{t}ZZ$	MadGraph	LO	`NNPDF3.0nlo`	Pythia8	A14
$V(VV)$+jets and VH					
V+jets	Sherpa	NLO	NNPDF3.0 NNLO	Sherpa	Sherpa
VV+jets	Sherpa	NLO LO ($gg \to VV$)	NNPDF3.0 NNLO	Sherpa	Sherpa
VVV+jets	Sherpa	NLO	NNPDF3.0 NNLO	Sherpa	Sherpa
VH	PowhegBox v2	NLO	NNPDF3.0 AZNLO	Pythia8	A14

Table 5.1: Summary of all MC generators used in the analysis of this dissertation for both Run 2 and Run 3, respectively. The ME order refers to the order in perturbative QCD calculation.

Trigger name	Data periods					
	2015	2016	2017	2018	2022	2023
Single electron triggers						
`e24_lhmedium_L1EM20VH`	✓	-	-	-	-	-
`e60_lhmedium`	✓	-	-	-	-	-
`e120_lhloose`	✓	-	-	-	-	-
`e26_lhtight_nod0_ivarloose`	-	✓	✓	✓	-	-
`e60_lhmedium_nod0`	-	✓	✓	✓	-	-
`e140_lhloose_nod0`	-	✓	✓	✓	-	-
`e26_lhtight_ivarloose_L1EM22VHI`	-	-	-	-	✓	-
`e60_lhmedium_L1EM22VHI`	-	-	-	-	✓	-
`e140_lhloose_L1EM22VHI`	-	-	-	-	✓	-
`e26_lhtight_ivarloose_L1eEM26M`	-	-	-	-	-	✓
`e60_lhmedium_L1eEM26M`	-	-	-	-	-	✓
`e140_lhloose_L1eEM26M`	-	-	-	-	-	✓
Single muon triggers						
`mu20_iloose_L1MU15`	✓	-	-	-	-	-
`mu26_ivarmedium`	-	✓	✓	✓	-	-
`mu50`	✓	✓	✓	✓	-	-
`mu24_ivarmedium_L1MU14FCH`	-	-	-	-	✓	✓
`mu50_L1MU14FCH`	-	-	-	-	✓	✓

Table 5.2: Summary of all single triggers used in this analysis for each data taking period.

	Electrons		Muons		Jets	b-jets
	loose	tight	loose	tight		
p_{T}[GeV]	> 15		> 15		> 20	> 20
$\lvert\eta\rvert$	< 1.37 or $1.52 - 2.47$		< 2.7	< 2.5	< 2.5	< 2.5
ID quality	LooseLH	TightLH	Loose	Medium	JVT	GN2
Isolation	`Loose_VarRad`	`Tight_VarRad`	`PflowLoose_VarRad`	`PflowTight_VarRad`		
Track vertex :						
– $\lvert d_0/\sigma_{d_0}\rvert$	< 5		< 3			
– $\lvert z_0 \sin\theta\rvert$ [mm]	< 0.5		< 0.5			

Table 5.3: Summary of object identification and definitions used in this thesis.

5.4 Object Reconstruction and Event Pre-selection

The object reconstruction and selections are optimised for the different $t\bar{t}HH$ final states, using the PFlow jet algorithm and the GN2 b-tagging algorithm. A detailed description of the object reconstruction procedure applied in this analysis is given in

Chapter 4. Looser selections are used to increase the signal acceptance. The physics objects considered in this search are electrons, muons, jets, b-jets and missing transverse energy. The reconstructed and identification criteria used are summarised in Table 5.3.

Electrons must satisfy the loose LH identification criterion along with a loose variable radius isolation WP in the 1L and OS2L final states. In the SS2L final state, the tight LH identification is used together with a tight isolation WP based on the prompt lepton tagging algorithm from Ref. [192], which identifies electrons and muons produced in decays of heavy-flavour hadrons.

For channels sensitive to electron charge mis-identification, such as SS ee and SS $e\mu$, an additional selection is applied to reduce contamination from electrons with incorrect charge assignments. This electron charge identification selector (ECIDS) is a BDT discriminant built on five variables: p_T, η, $q \times d_0$, E/p, $\Delta\phi_2^{\mathrm{re-scaled}}$ (the angle between the cluster position in the second calorimeter layer and the extrapolated track), and the average charge weighted by the number of SCT hits.

Muons are required to meet the loose quality identification WP, with $p_T > 15\,\mathrm{GeV}$ and $|\eta| < 2.7$. For 1L and OS2L final states, muons must pass the loose variable radius isolation WP, while the tight WP is used in the ML final state.

In the 1L channel, events are required to have exactly one reconstructed lepton (e or μ) that passes the loose WP described in Table 5.3. The lepton must have $p_{\mathrm{T}} >$ 27 GeV and match a corresponding trigger level object within $\Delta R < 0.15$ and same flavour. The lepton p_{T} cut guarantees the full efficiency of the single-lepton triggers.

In the OS2L channel, events are required to have exactly two oppositely charged leptons to ensure orthogonality with the ML channel. The two leptons are required to pass the loose WP. The leading lepton must have $p_{\mathrm{T}} > 27$ GeV while the subleading lepton must have $p_{\mathrm{T}} > 20$ GeV. It is required that the invariant mass of the dilepton system to be greater than 15 GeV and outside the Z-boson mass range (81 - 101 GeV). At least one matched lepton is required.

For the ML channels, at least three leptons with $p_{\mathrm{T}} > 15$ GeV passing the loose WP are required, with at least two having the same sign. Furthermore, the leading lepton needs to satisfy $p_{\mathrm{T}} > 27$ GeV with tight WP (Table 5.3). These events are further separated into a same-sign di-lepton (SS2L) and a tri-lepton (3L) channel. In the SS2L channel, exactly two tight leptons with the same charge are required, while events with at least three tight leptons go to 3L. Only the three leading loose leptons are considered for the event classification, so events having any additional leptons might be classed in the SS2L or 3L channels. This means that the fully leptonic decay mode (4L) is automatically included in the 3L selection. For both SS2L and 3L events, the dilepton invariant mass $m_{\ell\ell}$ must not coincide with the Z-boson mass range. In the SS2L channel, the invariant mass of the two tight leptons is checked, while all oppositely charged, same-flavour two-lepton combinations from the three tight leptons are checked in the 3L channel.

The $t\bar{t}HH$ production process is characterised by a high multiplicity of jets and b-jets, along with a large scalar sum of the transverse momenta of the jets in the event (H_{T}). In both the OS2L and 1L channels, the events are required to have at least three b-tagged jets at the 85% WP of GN2. For these channels, all regions are specified with at least six jets, up to a maximum of eleven jets, and $H_{\mathrm{T}} > 400\,\mathrm{GeV}$. In all of the ML channels, at least one b-tagged jet at the 85% WP is required. This lower value is necessary for the definition of the control regions for constraining the backgrounds arising from $t\bar{t}W$ and fake/non-prompt leptons, as described in Section 5.7. Figure 5.3 shows a shape comparison of the distribution of jet and b-jet multiplicity for $t\bar{t}HH(HH \to b\bar{b}b\bar{b})$ events against background.

5.5 Higgs Candidate Reconstruction in 1L and OS2L

Reconstructing the di-Higgs system in $t\bar{t}HH$ events is particularly challenging due to the large number of b-jets in the final states. A pairing strategy is used to identify the most accurate combination of jets that define each Higgs candidate. In $t\bar{t}HH(HH \to b\bar{b}b\bar{b})$ events, at least six jets are expected from Higgs and top decays, leading to numerous pairing possibilities. The pairing is performed in the 1L and OS2L channels, with the purpose of creating high-level variables that can discriminate well between signal and background events and that are used in the BDT method described in Section 5.8. The di-Higgs system is reconstructed from two Higgs candidates, which are themselves reconstructed from two b-jets each (four b-jets in total). We adopt a χ^2 method, which minimises

$$\chi^2_{ijkl} = (m_{ij} - m_H)^2 + (m_{kl} - m_H)^2 \tag{5.4}$$

where $m_{ij,kl}$ are the invariant masses of the two-jet systems and $m_H = 125$ GeV is the mass of the Higgs boson. This is then computed for all combinations of jet pairs, and the two pairs that give the smallest χ^2 value are selected as coming from two Higgs bosons. The jets are then ordered according to reconstructed Higgs p_T and jet p_T, giving the ordering (H_1 leading jet, H_1 sub-leading jet, H_2 leading jet, H_2 sub-leading jet, unpaired jets) for all jet-related variables. The discriminant power of some of the high-level kinematic variables that can be constructed from the pairing of the di-Higgs system is shown in Figure 5.4.

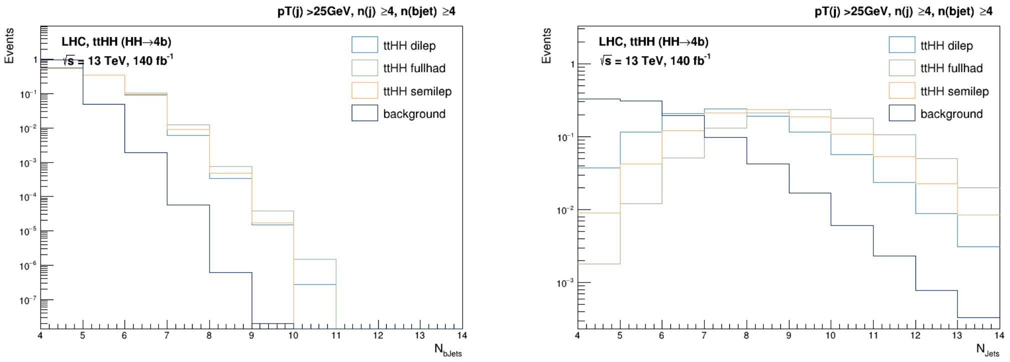

(a) b-jet multiplicity **(b)** Jet multiplicity

Figure 5.3: Jet and b-jet multiplicity in $t\bar{t}HH(HH \to b\bar{b}b\bar{b})$ signal samples compared to $t\bar{t}$ + jets background. The distributions are normalised to the same area.

The HH pairing efficiency of the χ^2 method was compared against the ΔR method, where the jet pairs are selected based on the smallest angular separation ΔR. This method assumes that the Higgs decay products are relatively collimated due to their momentum. The pairing efficiencies are shown in Figure 5.5 for each Higgs candidate. The χ^2 method achieves higher efficiency, particularly for low-p_T Higgs candidates where the ΔR assumption breaks down.

5.6 Background Modelling in 1L and OS2L Final States

Several SM processes can decay into signatures similar to the ones from $t\bar{t}HH$ final states, giving rise to various background processes that contaminate the analysis regions. These backgrounds can be classified into two types: irreducible and reducible backgrounds. Irreducible backgrounds stem from processes that directly produce the same final states as the signal processes, while reducible backgrounds mainly originate from processes that do not naturally produce the same final states but, instead, they are reconstructed as signal due to misidentification and misreconstruction of objects. This section describes the background modelling approaches applied to the 1L and OS2L final states.

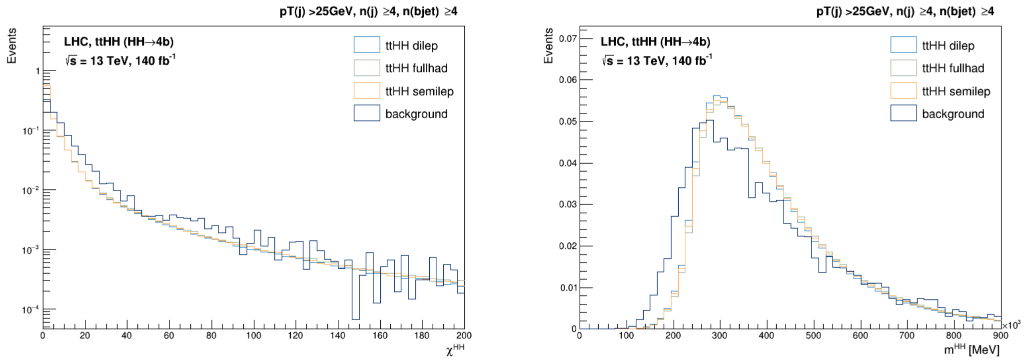

(a) HH χ^2 **(b)** $\mathrm{m_{HH}}$

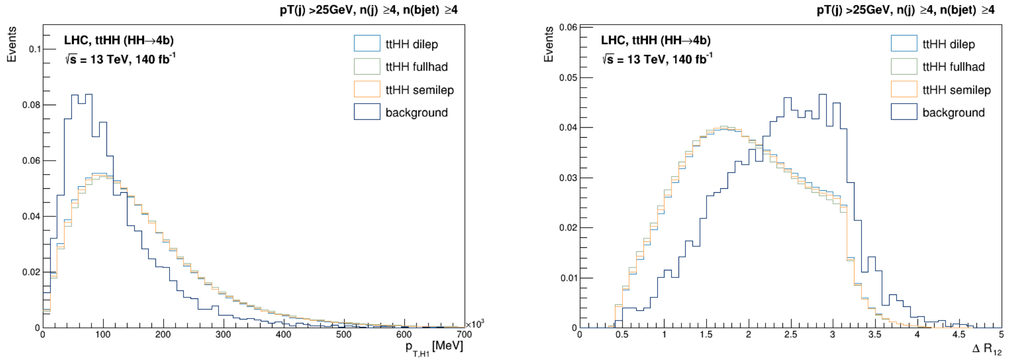

(c) ${p_\mathrm{T}}^{\mathrm{H_1}}$ **(d)** $\Delta R(j_1^{\mathrm{H_1}}, j_2^{\mathrm{H_1}})$

Figure 5.4: Shape comparison of the χ^2 of the di-Higgs pairing (a), di-Higgs invariant mass (b), transverse momentum of the leading Higgs candidate (c) and angular distance between the two pared jets to the leading Higgs candidate (d).

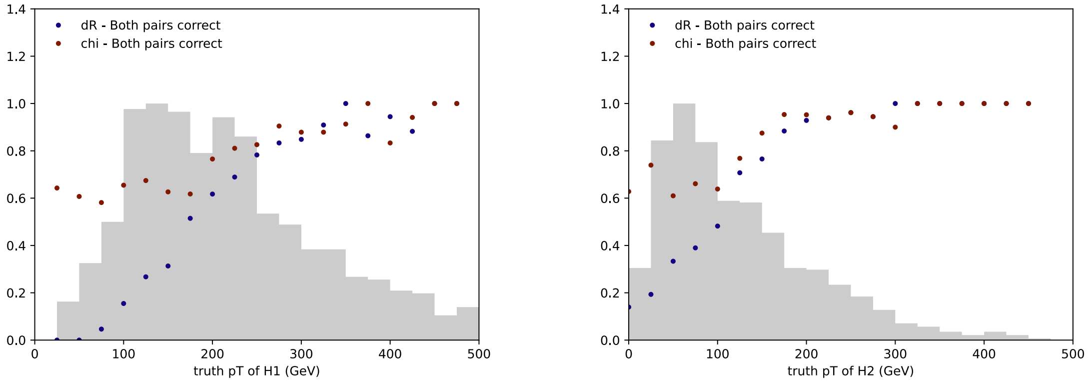

(a) Leading Higgs candidate **(b)** Subleading Higgs candidate

Figure 5.5: Relative pairing efficiency comparing the two different pairing approaches as a function of the truth p_T of the leading (a) and sub-leading (b) Higgs using $t\bar{t}HH(HH \rightarrow b\bar{b}b\bar{b})$ events.

The primary background source for these final states is top-quark pair production in association with multiple jets ($t\bar{t}$ + jets), which predominantly originates from gluon emissions in higher-order processes. The MC prediction of these events is not accurate and two data-driven corrections are applied to correct the observed mismodelling with data.

As demonstrated in previous ATLAS and CMS analyses [193–195], the production rate of $t\bar{t}$ events in the heavy-flavour region ($t\bar{t}$ + HF) is systematically underestimated. To correct for this, the normalisation of each $t\bar{t}$ + jets component is adjusted based on the flavour of the additional jets in the event. These normalisation factors are derived simultaneously with the signal strength in the profile likelihood fit using control regions and signal regions with varying b-tagging requirements.

Furthermore, the MC simulations exhibit inaccuracies in modelling the kinematics and jet multiplicity from additional emissions of QCD radiation. To address this, a reweighting procedure is applied to the scalar sum of the momenta of final-state particles (H_{T}), based on comparisons with data in dedicated reweighting regions (Section 5.6.3).

5.6.1 Truth Classification of $t\bar{t}$ + jets

The $t\bar{t}$ + jets background is categorised based on its truth information using a hadron-jet matching algorithm. The categorisation is determined by the flavour of the additional jets in the event that do not originate from the $t\bar{t}$ decay. The jets are reconstructed from stable truth particles (lifetime longer than 3×10^{11} s) using the anti-k_t algorithm with a radius parameter of $\Delta R = 0.4$, and requiring the jets to have $p_{\mathrm{T}} > 15$ GeV and $|\eta| < 2.5$.

The flavour of a jet is determined by counting the number of $b-$ or $c-$hadrons within a certain ΔR distance to the jet axis. Events are classified as $t\bar{t} + \geq 1b$ if at least one extra jet is matched within $\Delta R < 0.4$ to a b-hadron with $p_{\mathrm{T}} > 5$ GeV that does not originate from the $t\bar{t}$ decay. For the events not classified as $t\bar{t} + \geq 1b$, if at least one particle jet is matched to a c-hadron (which is not a decay product of a b-hadron or a W boson) with $p_{\mathrm{T}} > 5$ GeV, the event is labelled as $t\bar{t} + \geq 1c$. These categories also include events where the additional jets are coming from multiparton interaction (MPI) or final-state radiation (FSR). The remaining events, including those with no additional jets matched to a b-hadron or c-hadron, are labelled as $t\bar{t}$ + light. Events labelled as $t\bar{t} + \geq 1b$ are referred to as $t\bar{t}$ +HF (heavy flavour). The $t\bar{t}$ + jets components receive separate treatments in several aspects of the analysis as will be described below.

At the LHC, the production of $t\bar{t} + \geq 1b$ is primarily dominated by QCD-mediated $t\bar{t}b\bar{b}$ processes. At LO, the cross-section for $t\bar{t}b\bar{b}$ production is dependent on the fourth power of the strong coupling constant α_S, which makes it highly sensitive to variations of the renormalisation scale [196]. The uncertainty due to standard factor-two[2] scale variations can be as high as 70-80%. Including NLO QCD corrections reduces this uncertainty to 20-30%, which is still significantly large. The $t\bar{t}b\bar{b}$ process is characterised by two different energy scales: from $t\bar{t}$ system, which is typically around 500 GeV, and the $b\bar{b}$ system, at much lower energies, typically a few tens of GeV. This difference must be accounted for when selecting the renormalization scale to minimise large corrections beyond NLO.

One approach to account for $t\bar{t} + \geq 1b$ components involves using NLO $t\bar{t}$ ME in 5FS. The additional b-jets originate mostly from gluon splittings ($g \to b\bar{b}$) produced in the PS, and also from the ME process $gb \to t\bar{t}b$, where the b-quark is an initial-state parton within the 5-flavour PDFs. Both scenarios are represented by a $t\bar{t} + j$ ME, but this prediction is only available to LO accuracy. Additionally, the behaviour of b-jet observables is heavily influenced by the PS's treatment of gluon splittings, which can, however, be tuned to experimental data.

In order to minimise the dependence on PS modelling and to maximise the use of higher-order ME, the second approach is to use NLO $t\bar{t}b\bar{b}$ ME in 4FS. In this scheme, b-quarks are treated as massive partons, and gluon splittings into $g \to b\bar{b}$ are directly incorporated into the ME. This eliminates collinear divergences, which reduces the dependence on the PS. This approach covers the full $t\bar{t} + \geq 1b$ phase-space, offering a fully inclusive representation of this process, providing NLO accuracy, not only for observables involving two b-jets but also for more inclusive observables with a single resolved b-jet [196]. Additionally, a practical benefit of this method is that most generated events belong to the $t\bar{t} + \geq 1b$ category, while the other approach requires generating the entire $t\bar{t}+$jets phase-space, with only a small portion corresponding to $t\bar{t} + \geq 1b$.

In this analysis, as described in Section 5.2, the $t\bar{t}b\bar{b}$ 4FS samples are used as variations to the nominal NLO 5FS prediction for $t\bar{t} + \geq 1b$ component in the 1L and OS2L final states. For the $t\bar{t} + \geq 1c$ and $t\bar{t}$ + light component, the NLO $t\bar{t}$ 5FS samples are used without any flavour scheme systematic. In the ML final states, the $t\bar{t}$ + jets modelling is not a major component and only the NLO $t\bar{t}$ 5FS samples are used.

---

[2] Varying the renormalisation scale up and down by a factor two is the standard way of estimating the uncertainty due to missing higher-order contributions.

The $t\bar{t}+\geq 1b$ events can be further classified based on various criteria. Jets matched to exactly one b-hadron, with $p_T > 5$ GeV, are labelled single-b-jets, while those matched to two or more b-hadrons that are collimated are labelled B-jets, with no p_T requirement on the second hadron. Events with exactly one b-jet or exactly one B-jet are labelled as $t\bar{t}$ $+1b$. Events with two b- or B-jets are labelled as $t\bar{t}$ $+2b$, while those with 3 or more are labelled $t\bar{t}+\geq 3b$. Together, these three categories are collectively referred to as $t\bar{t}+\geq 1b$.

The pre-fit normalisation of the different $t\bar{t}$ + jets components is taken directly from the generator prediction of the cross-section. However, they are treated as separate processes, each is associated with distinct modelling uncertainties. The post-fit normalisation of each component is obtained from a free-floating normalisation factor included in the fit, acquiring the value that best adjusts to data, without any initial constraint. Given the negligible contribution of $t\bar{t}$ + light events in the signal regions, a common normalisation factor is used for both $t\bar{t}$ + light and $t\bar{t}+\geq 1c$ components, referred to as the $t\bar{t}+\geq c/l$ normalisation term. In total, the normalisation factors included in the fit are: $t\bar{t}+\geq c/l$, $t\bar{t}$ $+1b$, $t\bar{t}$ $+2b$, and $t\bar{t}+\geq 3b$. Additionally, a separate degree of freedom accounts for the uncertainty in the relative fraction of c- to light-jets. Modelling uncertainties are treated as uncorrelated across the components: $t\bar{t}$ + light, $t\bar{t}+\geq 1c$, $t\bar{t}$ $+1b$, $t\bar{t}$ $+2b$, $t\bar{t}$ $+3b$, and $t\bar{t}+\geq 4b$.

5.6.2 Control and Signal Regions

To benefit from the high multiplicity of jets and b-jets of the $t\bar{t}HH$ signal, the events from different channels are categorised into orthogonal regions, determined by the total number of b-tagged jets at different b-tagging WPs. Only regions with at least three b-jets are considered.

The regions are divided into control and signal regions based on the expected number of signal events in each region. Some regions are labelled *Lo* and *Hi*, corresponding to low and high expected signal-to-background ratios, respectively. A total of two signal regions (SR) for the 1L, one SR for OS2L channel and two control regions (CR) for each channel are defined and used in the fits. Additionally two modelling validation regions (VR) are defined for each channel. In the signal regions the MVA scores are fitted, while in the CRs the sum of pseudo-continuous b-tagging score in the event is used for constraining shape and normalisation of the $t\bar{t}$ + jets background in the fits. In addition, two more regions are defined for the derivation of the re-weighting factors described in Section 5.6.3. Table 5.4 shows the definitions of each analysis region in the 1L and OS2L final states.

$\mathrm{1L4b_{Lo}}$ and $\mathrm{2L4b_{Lo}}$ are close to the phase-space of the SR and show similar kinematics and larger HF contribution to be used for H_T reweighting; these regions are not included in the final fit. 1L3b and 2L3b help with the constraint of the $t\bar{t}+\geq c/l$ background, while $\mathrm{1L4b_{Hi}}$ and $\mathrm{2L4b_{Hi}}$ are useful for the constraint of the HF components of $t\bar{t}$ + jets. The SRs are split into different b-jet multiplicity to improve the sensitivity of these regions. Figure 5.6 shows the pie charts with the background composition of each analysis region fitted in the 1L channel for Run 2 and Run 3. The total pre-fit yields per region in 1L channels for Run 2 and Run 3 are shown in Figure 6.3.

Channel	Region	Type	N_b @85% WP	N_b @77% WP	Fitted variable
1L	1L3b	CR	3	–	$\sum_{i=0}^{6} \text{w}_{\text{GN2}}$
	1L4b$_{\text{Lo}}$	Reweight	4	$\leq$3	–
	1L4b$_{\text{Hi}}$	CR	4	4	$\sum_{i=0}^{6} \text{w}_{\text{GN2}}$
	1L5b$_{\text{Lo}}$	VR	5	$\leq$4	-
	1L5b$_{\text{Hi}}$	SR	5	5	MVA score
	1L6b	SR	$\geq$6	–	MVA score
OS2L	2L3b	CR	3	–	$\sum_{i=0}^{6} \text{w}_{\text{GN2}}$
	2L4b$_{\text{Lo}}$	Reweight	4	$\leq$3	–
	2L4b$_{\text{Hi}}$	CR	4	4	$\sum_{i=0}^{6} \text{w}_{\text{GN2}}$
	2L5b$_{\text{Lo}}$	VR	5	$\leq$4	-
	2L5b$_{\text{Hi}}$	SR	$\geq$5	$\geq$5	MVA score

Table 5.4: Definition of regions for 1L and OS2L, and naming based on leptons and b-jet multiplicity for different b-tagging WPs. $\sum_{i=0}^{6} \text{w}_{\text{GN2}}$ refers to the sum of the GN2 pseudo-continuous b-tagging scores for all the six jets in the event from the pairing algorithm described in Section 5.5.

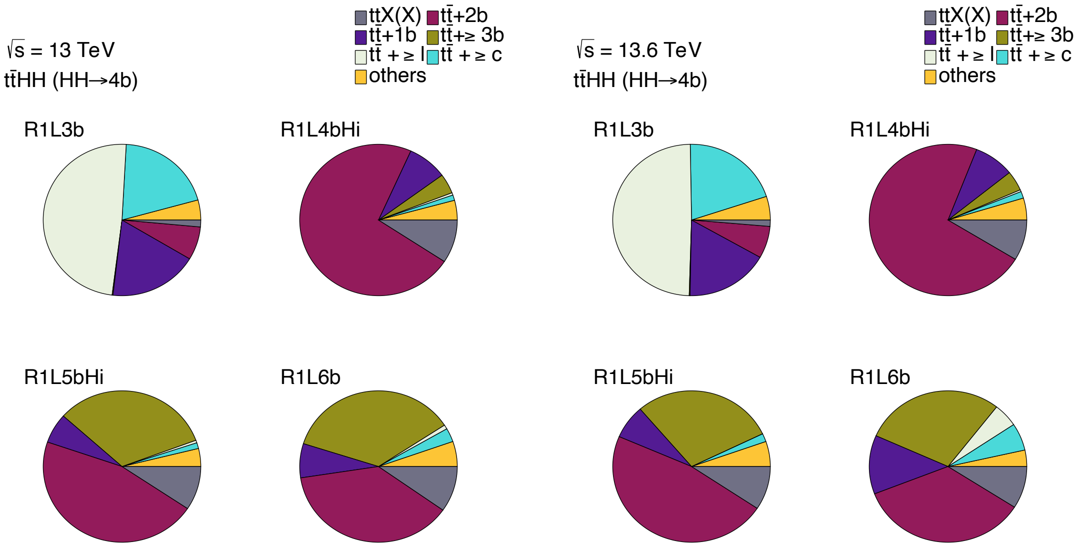

(a) Run 2 **(b)** Run 3

Figure 5.6: Pre-fit background composition of the regions in 1L channel, for Run 2 (a) and partial Run 3 (b).

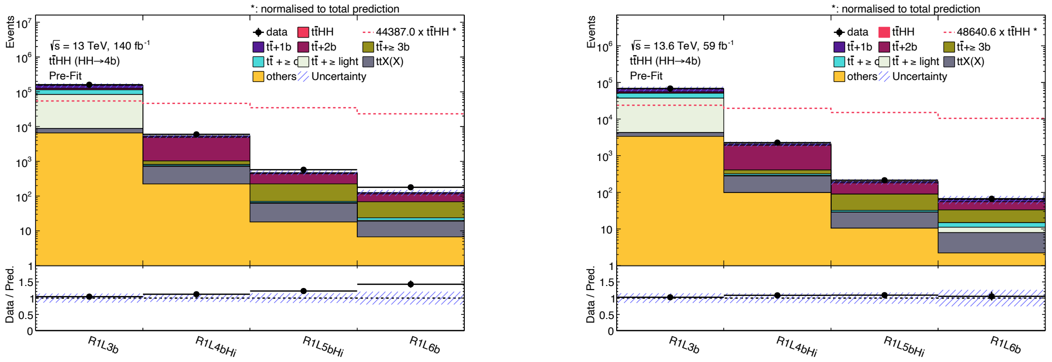

(a) Pre-fit **(b)** Pre-fit

Figure 5.7: Pre-fit total yields in all 1L regions included in the fit, for Run 2 (a) and partial Run 3 (b) datasets.

5.6.3 Data-driven Kinematic Reweighting

The additional radiation modelled in the $t\bar{t}$ MC samples exhibits inaccuracies in the jet kinematics. To address this, a reweighting procedure is applied based on the scalar sum of the momenta of the final-state particles (H_{T}). The reweighting is calculated by comparing the MC with data from $t\bar{t}$-dominated regions, R1L4b$_{\mathrm{Lo}}$ and R2L4b$_{\mathrm{Lo}}$, which are orthogonal to the analysis regions. These regions are chosen for their proximity to the SR phase-space and their similar kinematic properties. The signal contamination in these regions is below 0.01% and is therefore considered negligible.

Before deriving the reweighting, a flavour re-scaling is applied to achieve a more accurate flavour composition of $t\bar{t}$ + jets samples and address the underestimation of the $t\bar{t}$ + HF production rate in the MC samples. This adjustment is done by re-scaling separately the normalisation of $t\bar{t}$ + jets components. A likelihood fit on the sum of the GN2 pseudo-continuous b-tagging scores ($\sum_{i=0}^{6} \mathrm{w}_{\mathrm{GN2}}$) as flavour discriminant is performed to determine the normalisation factors (NFs) of each component. Different regions with varying b-tagging criteria are included in the fit to derive a more accurate prediction of the NFs across the phase-space of the analysis. In this process, events in different regions from both the 1L and OS2L channels are fitted together, as the HF composition is expected to be similar across these channels. The total pre- and post-fit yields per region in both channels for Run 2 are shown in Figure 5.8.

The H_{T} reweighting process is divided in jet multiplicity categories due to the strong correlation between H_{T} and the number of jets. Specifically, jet multiplicity categories of 6, 7, 8, and greater than 9 jets are used. Bins are defined within each $t\bar{t}$ + jets subsample to ensure a minimum of 2000 events per bin and a bin width of at least 50 GeV. Within each subsample, $t\bar{t}$ + jets components are reweighted using post-fit normalization factors derived from the flavour scaling. Before reweighting, non-reweighted MC contributions are subtracted from data based on their MC predictions. This results in histograms containing only $t\bar{t}$ + jets contributions, which are normalized to match the data and MC event counts.

The reweighting factors k_i for each bin i are calculated as the ratio of data to MC events:

$$k_i = \frac{N_i^{\text{data}}}{N_i^{\text{MC}}}. \tag{5.5}$$

To ensure a smooth transition between bins, a continuous smoothing function $f(H_{\text{T}})$ replaces the discrete k_i factors. This function is modelled as a piecewise spline using second-order polynomials:

$$f(H_{\text{T}}) = a_i H_{\text{T}}^2 + b_i H_{\text{T}} + c_i \tag{5.6}$$

The coefficients a_i, b_i, and c_i for each bin i are determined by ensuring continuity, a continuous first derivative, and event conservation compared to the constant k_i. These conditions are expressed as:

$$k_i \sum_j w_j = \sum_j \left(a_i H_{\text{T}}^2 + b_i H_{\text{T}} + c_i \right) w_j \tag{5.7}$$

where the sum runs over all events j in bin i. Solving these linear equations yields the coefficients a_i, b_i, and c_i, which define the reweighting splines for each jet multiplicity. These splines are then used to assign weights to $t\bar{t}$ + jets MC events for the analysis.

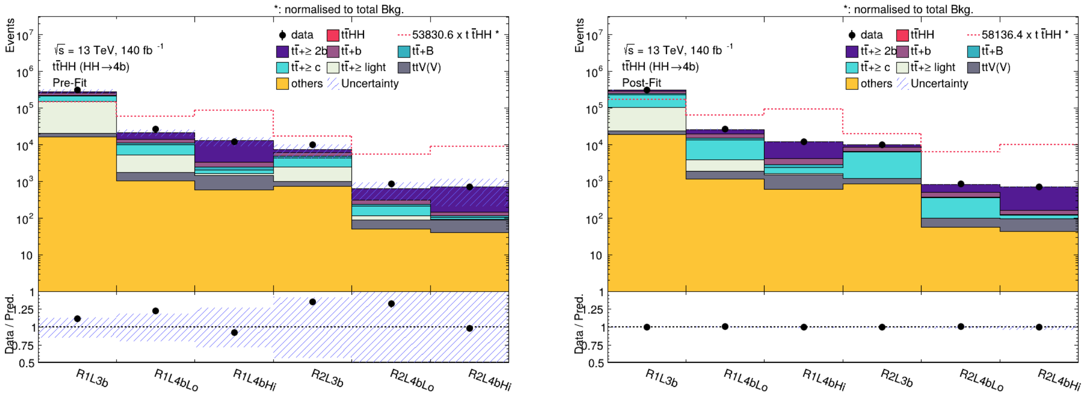

(a) Run 2

(b) Run 3

Figure 5.8: Pre- and post-fit total yields in all 1L and OS2L regions used for the flavour correction fit for Run 2.

To evaluate uncertainties in the H_{T} reweighting, the procedure is repeated for variations of the nominal sample, including FSR, ISR, and μ_F and μ_R scale variations. Additionally, reweighting variations are derived both with and without post-fit normalization factors, taking into account their uncertainties.

The reweighting strategy is validated by assessing its impact on the CRs and VRs for both 1L and OS2L channels. The H_{T} distributions before and after reweighting are shown for the 1L4b$_{Lo}$ and 1L4b$_{Hi}$ regions in Figure 5.9. These regions show improved H_{T} shapes post-reweighting; the normalization factors are applied in the plots and the removal of slope effects is evident in the corrected distributions.

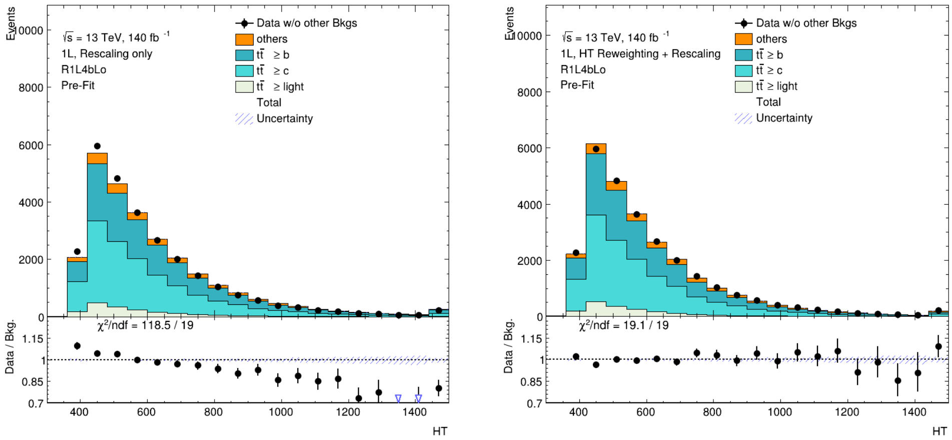

(a) 1L4b$_{Lo}$ rescaling only **(b)** 1L4b$_{Lo}$ rescaling + reweighting

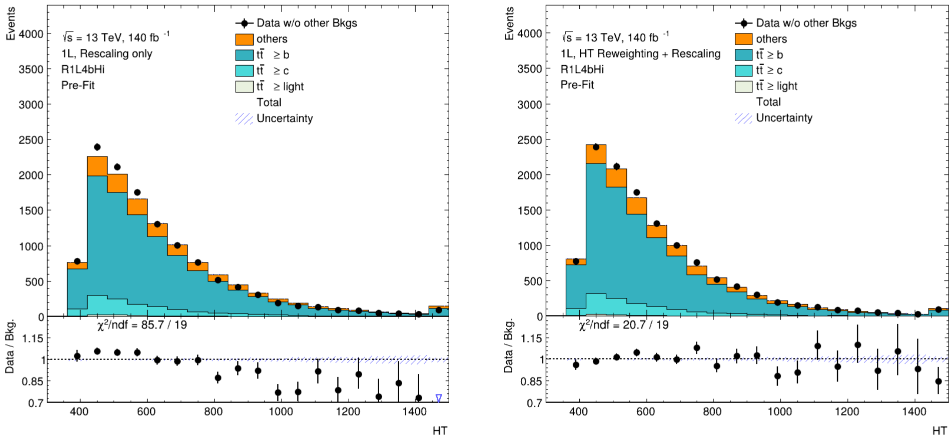

(c) 1L4b$_{Hi}$ rescaling only **(d)** 1L4b$_{Hi}$ rescaling + reweighting

Figure 5.9: Data/MC comparison for H_T distributions of the R1L4bLo (first row) and R1L4bHi (second row) regions before (first column) and after (second column) applying the reweighting factors. The systematic uncertainties are not included in the plots and the $t\bar{t}$ + jets NFs are applied.

5.7 Background Modelling in ML Final State

The irreducible background processes that contaminate the ML final states come from events where all selected leptons are prompt. These prompt leptons predominantly come from the decays of H, W and Z bosons and τ leptons. Processes such as $tttt$, $ttW+$jets, $ttZ+$jets, and $ttH+$jets, which encompass both light-flavour and b-jets are significant contributions to irreducible backgrounds of ML channel. Other minor contributions arise from processes like VV, VVV, VH, as well as rare events including $ttVV$, tWZ, tZq, and ttt. The estimates for irreducible backgrounds are derived from the MC samples from Section 5.2 and are normalised to their theoretical cross-sections. The exception is the $t\bar{t}W$estimation, which is further corrected using a parameterised jet function, as detailed in Section 5.7.5.

The reducible background primarily originates from $t\bar{t}$ + jets, $V+$jets, and $tW+$ jets processes. While these do not inherently produce ML final states, they can be misidentified as signal due to the presence of misreconstructed or non-prompt leptons. These backgrounds are categorised into three main sources: charge misidentification (QmisID), fake leptons, and non-prompt leptons. QmisID refers to reconstructed leptons where an electrical charge flip occurs. This source is evaluated using a data-driven approach for charge flip rates, as detailed in Section 5.7.3. The contribution from fake/non-prompt leptons originates from various sources: non-prompt electrons or muons from semi-leptonic decays of heavy-flavour hadrons, referred to as HF e and HF μ; non-prompt electrons from photon conversions in the detector material, referred to as material conversions (Mat. Conv.); electrons from virtual photon (γ^*) interactions, leading to e^+e^- pairs, referred to as internal conversions (Low m_{γ^*}). These contributions are estimated through the template method described in Section 5.7.4.

5.7.1 Truth Classification of Leptons

In the ML channel all the leptons from MC events are classified accordingly to their truth information as follow:

- **Prompt**: Leptons originating from the decay of W, Z, H bosons, or from a mother particle associated with a final-state radiation (FSR) photon.
- **Charge flip**: Only electron charge flips are considered. An electron is classified as a charge-flip if the charge of its first mother particle differs from its reconstruction-level charge.
- **Material conversion**: An electron's truth origin corresponds to a photon conversion from a real photon. This occurs when high-energy photons interact with the detector material, producing electron-positron pairs within the detector. The electron's mother particle is either an isolated prompt photon, a non-isolated FSR photon, or photons from heavy boson decays.
- **Internal Gamma conversion**: The electron's origin truth origin corresponds to a photon conversion from a virtual photon. These conversions are refereed to as internal conversions and occur when a electron-positron pair is created in a decay that might otherwise have emitted a photon.
- **Heavy flavour**: The truth origin of an electron or muon corresponds to a bottom

meson/baryon, a charm meson/baryon, a b-hadron, or a c-hadron.

- **Fake**: The truth type of the lepton is a hadron, or its origin is a light meson/baryon or a strange meson/baryon.
- **Other**: Leptons that do not fit into any of the above categories.

If all leptons in the MC event are classified as prompt, the event is categorized according to its process. If only one lepton is non-prompt, the event is classified based on the type of that non-prompt lepton. If more than one lepton is non-prompt, the event is classified as "Other".

5.7.2 Control and Signal Regions

In the ML channels, a single SR is defined, requiring events to have at least six jets, among which at least two are b-tagged. Additionally, $H_{\mathrm{T}} > 400$ GeV is required, where H_{T} is defined as the scalar sum of the transverse momenta of all the leptons and jets in the event. CRs are defined for background estimations of both the $t\bar{t}W$ backgrounds and fake/non-prompt lepton backgrounds. An overview of all regions for the ML channels is provided in Table 5.5. Figure 5.11 shows the post-fit pie charts for the background composition in each analysis region. The following sections will describe in more detail the reasons and the background modelling approaches used for the definition of each of these CRs. The total pre-fit yields per region in ML regions for Run 2 and Run 3 are shown in Figure 6.21.

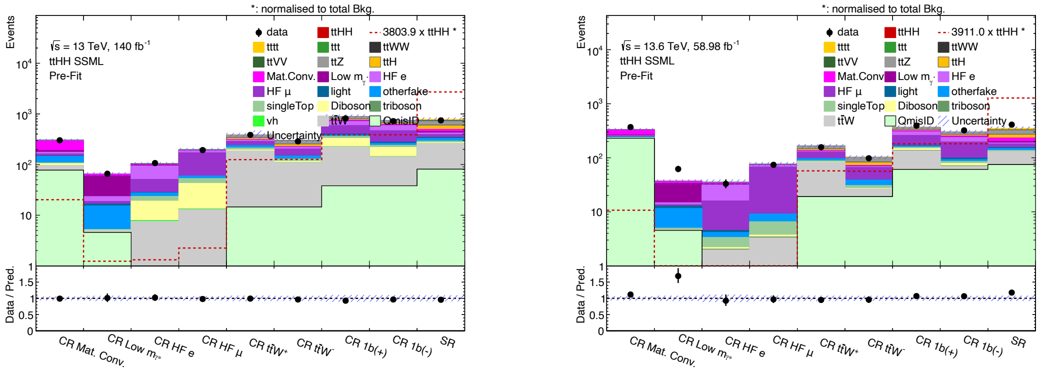

(a) Run2 **(b)** Run 3

Figure 5.10: Pre-fit total yields in all ML regions included in the fit for Run 2 (a) and partial Run 3 (b).

5.7.3 Lepton Charge Misidentification Background

As discussed in Section 4.2.1.2, incorrect electron charge reconstruction can happen for different reasons. Charge misreconstruction becomes an important background contribution when considering decays into final states with two same-sign leptons. The misidentified opposite-sign electrons can contaminate the ML regions as a significant background. For muons, the occurrence of Bremsstrahlung is minimal, and the additional information from the MS allows for precise track curvature reconstruction,

Channel	Region	N_j	N_b @85% WP	Other selections	Fitted variable
SS, ee or eμ	CR Low m_{γ^*}	$4 \leq N_j < 6$	≥ 1	ℓ_1 or ℓ_2 is from virtual photon (γ^*) decay ℓ_1 and ℓ_2 are not from photon conversion	Event yield
SS, ee or eμ	CR Mat. Conv	$4 \leq N_j < 6$	≥ 1	ℓ_1 or ℓ_2 is from photon conversion	Event yield
e$\mu\mu$ or $\mu\mu\mu$	CR HF μ	≥ 1	$= 1$	$100 < H_T < 275$ GeV $E_T^{miss} > 35$ GeV total charge $= \pm 1$	p_T^{l3}
eee or eeμ	CR HF e	≥ 1	$= 1$	$100 < H_T < 275$ GeV $E_T^{miss} > 35$ GeV total charge $= \pm 1$	p_T^{l3}
SS, eμ or $\mu\mu$	CR $t\bar{t}W^+$+jets	≥ 4	≥ 2	$\lvert\eta(e)\rvert < 1.5$ when $N_b = 2$: $H_T < 400$ GeV or $N_j < 6$ when $N_b \geq 3$: $H_T < 400$ GeV total charge > 0	N_j
SS, eμ or $\mu\mu$	CR $t\bar{t}W^-$+jets	≥ 4	≥ 2	$\lvert\eta(e)\rvert < 1.5$ when $N_b = 2$: $H_T < 400$ GeV or $N_j < 6$ when $N_b \geq 3$: $H_T < 400$ GeV total charge < 0	N_j
SS2L+3L	CR 1b(+)	≥ 4	$= 1$	ℓ_1 and ℓ_2 are not from photon conversion $H_T > 400$ GeV total charge > 0	N_j
SS2L+3L	CR 1b(-)	≥ 4	$= 1$	ℓ_1 and ℓ_2 are not from photon conversion $H_T > 400$ GeV total charge < 0	N_j
SS2L+3L+4L	SR	≥ 6 if $N_l = 2$ ≥ 5 if $N_l \geq 3$	≥ 2	$H_T > 400$ GeV	Transformer score
3L	VR $t\bar{t}Z$	≥ 4	≥ 2	$m_{OSSF} \in [81,101]$ GeV	-
SS2L+3L+4L	VR GNN	≥ 6 if $N_l = 2$ ≥ 5 if $N_l \geq 3$	≥ 2	$200 < H_T < 400$ GeV	-

Table 5.5: CRs and SRs for ML channel. All of the selection criteria, the fitted variables and the target channel are shown in the table.

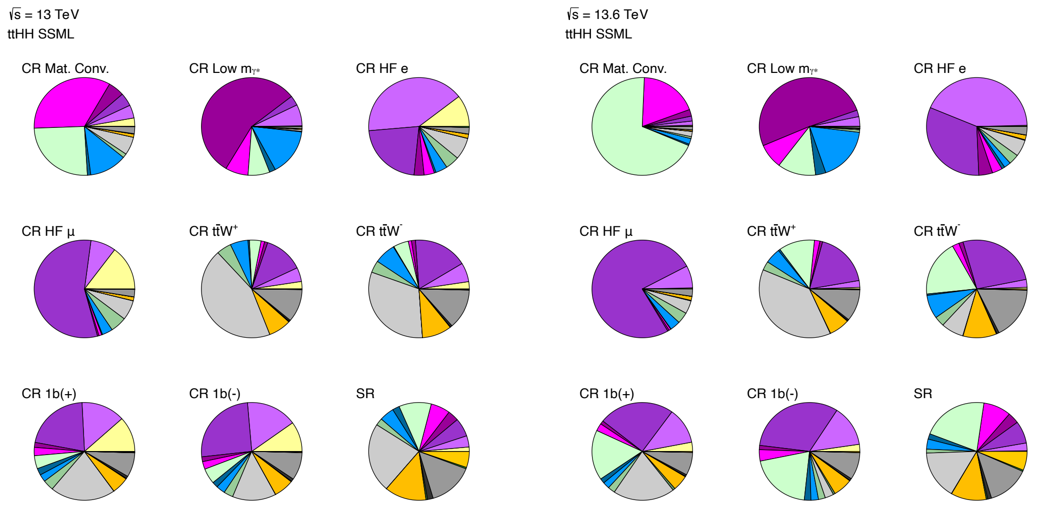

(a) Run 2 **(b)** Run 3

Figure 5.11: Pre-fit background composition of all regions in final state for Run 2 (a) and partial Run 3 (b). The term "Transformer" in the SR refers to the Graph Attention Network described in Section 5.8.

making the misidentification rate for muons negligible.

A data-driven technique is used in the ML final state based on a Poisson likelihood fit on p_{T} and $|\eta|$ to estimate the QmisID background [197]. This approach follows closely the methodology from the ATLAS $t\bar{t}t\bar{t}$ Observation [198]. The charge misidentification rates for electrons are determined from $Z \to e^+e^-$ events. Events are selected with two electrons and at least one additional jet, within a Z-boson invariant mass window cut, without requirement on the charge of the electron tracks.

The misidentification rates vary depending on the four vectors of the electrons. For example, the tracks of high-momentum electrons show a lower curvature, resulting in an increased probability of charge misidentification. Additionally, the angular location of the electron influences the amount of detector material it traverses, which subsequently alters the misidentification rate. For this reason, the rates are measured in 2-dimensional bins of p_{T} and $|\eta|$.

It is assumed that all same-sign (SS) electron pairs arise from incorrect charge identification of one of the two electrons. Based on this assumption, the number of events with SS electron pairs (N_{ij}^{SS}), where the leading electron is in the i^{th} bin and the sub-leading is in the j^{th} bin, can be estimated as:

$$N_{ij}^{SS} = N_{ij}^{tot}(\epsilon_i(1-\epsilon_j) + \epsilon_j(1-\epsilon_i)), \tag{5.8}$$

where i and j are bins in (p_{T}, $|\eta|$), and ϵ_i and ϵ_j are the misidentification rates in the i^{th} bin and the j^{th} bin, respectively. To estimate ϵ, the total number of SS and OS events (N_{ij}^{tot}) in 2-dimensional bins is counted, and the Poisson likelihood for Equation 5.8 is maximized. For this, the number of SS events is expected to follow a Poisson distribution around the expectation value ($\bar{N}_{ij}^{SS}$):

$$f(N_{ij}^{SS}|\bar{N}^{SS}(\epsilon_i,\epsilon_j)) = \frac{(\bar{N}_{ij}^{SS})^{N_{ij}^{SS}} .e^{\bar{N}_{ij}^{SS}}}{N_{ij}^{SS}!}. \tag{5.9}$$

The negative logarithm of this Likelihood function can be written as:

$$\begin{aligned} -\ln(L(\epsilon|N_{SS})) &= -\ln\left(\prod_{i,j} f\left(N_{ij}^{SS}\middle|\bar{N}^{SS}(\epsilon_i,\epsilon_j)\right)\right) \\ &= -\sum_{i,j}\left[N_{ij}^{SS}\ln\left(N_{ij}^{tot}\left(\epsilon_i(1-\epsilon_j)+\epsilon_j(1-\epsilon_i)\right)\right)\right. \\ &\qquad \left. - N_{ij}^{tot}\left(\epsilon_i(1-\epsilon_j)+\epsilon_j(1-\epsilon_i)\right)\right], \end{aligned} \tag{5.10}$$

which is minimized to obtain the misidentification rates ϵ.

Since the electron requirements differ across various analysis regions, the charge flip rates are extracted from likelihood fits that use a distinct selection for each region. The rates obtained are used to correct for the background arising from incorrect charge identification. The following weight is then applied to OS ee and $e\mu$ events to account for the SS events that may pass the region definitions in the analysis:

$$w = \frac{\epsilon_i + \epsilon_j - 2\epsilon_i\epsilon_j}{1 - \epsilon_i - \epsilon_j + 2\epsilon_i\epsilon_j}. \tag{5.11}$$

This method for misidentification rate estimated is found to underestimate the QmisID background as the number of jets increases. Since the signal region of the final state requires $N_{\text{jets}} \geq 6$, the background due to charge misidentified electrons is underestimated and the dependency on the number of jets needs to be accounted for. To determine this dependency, Equation 5.10 is used to calculate $\epsilon_{i,n}$, where i and n are bins in p_{T} and jet multiplicity, respectively. The jet multiplicity bins are then merged into one bin to calculate $\epsilon_{i,\text{inclusive}}$ using the same method. The scale factor for the jet multiplicity correction is defined as:

$$SF_{i,n} = \frac{\epsilon_{i,n}}{\epsilon_{i,inclusive}}, \tag{5.12}$$

where η is assumed to be independent of the number of jets, making the scale factor independent of η. To account for the limited statistics in high jet multiplicity events, a linear fit is used to extrapolate the scale factor in these events. Scale factors for events with fewer than four jets are excluded from this fit. The approach for accounting for QmisID systematic uncertainties will be discussed in Section 5.9.

5.7.4 Template Fit for Fake/non-prompt Background

Non-prompt and fake leptons primarily originate from four categories: non-prompt electron from photon material conversion (Mat. Conv.), e^+e^- pair from a virtual photon decay (Low m_{γ^*}), electron from heavy flavour decay (HF e), and muon from heavy flavour decay (HF μ). A semi-data-driven approach, referred to as template method, is used to estimate the contributions from these backgrounds. The method used in this analysis follows the same approach as the $t\bar{t}H$ multilepton analysis [199]. The normalisation of the various fake/non-prompt backgrounds are determined with fits to data in dedicated CRs for each background. The MC events are classified based on their truth information, and a free-floating NF is assigned to each fake/non-prompt background. To reduce correlations between NFs, the CRs are designed to maximize the purity of the targeted background while minimizing contamination from other sources. All the CRs are included in a likelihood fit together with the SR and the best-fit values for the NFs and the signal strength are determined from a simultaneous fit.

The CRs for the fake estimation are defined as:

- In $\mathrm{CR}_{\text{Mat. Conv.}}$, only events with an SS ee or $e\mu$ pair are selected, with at least one electron from material conversion. To maintain orthogonality with the SR, four or five jets are required with at least one b-jet among them. Only the yield of the region is included in the fit to constrain $\mathrm{NF}_{\text{Mat. Conv.}}$.
- In $\mathrm{CR}_{\text{Low } m_{\gamma^*}}$, only events with a SS ee or $e\mu$ pair are selected, where all electrons are not associated with material conversion, but at least one is an internal conversion candidate. To maintain orthogonality with the SR, four or five jets are required with at least one b-jet among them. The event yield is also used as fitted variable in this region to constrain $\mathrm{NF}_{\text{Low } m_{\gamma^*}}$.
- In $\mathrm{CR}_{\mathrm{HF}e}$, only events with eee or $ee\mu$ triplets and a total lepton charge of ±1 are selected, the leading two leptons must be non-conversion candidates. To maintain orthogonality with the SR, exactly one b-jet is required. To increase the purity of the region for heavy flavour electrons, H_{T} must be between 100 and 275 GeV, and $E_{\mathrm{T}}^{\mathrm{miss}}$ must be greater than 35 GeV. The fitted variable is the transverse momentum of the third lepton ($p_{\mathrm{T}}^{l_3}$).
- In $\mathrm{CR}_{\mathrm{HF}\mu}$, only events with $\mu\mu\mu$ or $\mu\mu e$ and a total lepton charge of ±1 are selected, all leptons must be non-conversion candidates. To maintain orthogonality with the SR, exactly one b-jet is required. To increase the purity of the region for heavy flavour muons, H_{T} must be between 100 and 275 GeV, and $E_{\mathrm{T}}^{\mathrm{miss}}$ must be greater than 35 GeV. The fitted variable is the transverse momentum of the third lepton ($p_{\mathrm{T}}^{l_3}$).

The distribution of the fake/non-prompt CRs and the results of the simultaneous fits are summarized in Chapter 6.

5.7.5 Data-driven Estimation of $t\bar{t}W$ Background

The SR has significant contamination from $t\bar{t}W$ events, whose cross-section has generally been measured to be higher than current theory predictions [200]. To estimate $t\bar{t}W$, dedicated CRs are defined (see Sec.5.6.2), and a validation region (VR) for $t\bar{t}W$ is built based on the charge asymmetry[3] of the $t\bar{t}W$ process to assess the modelling

---

[3] The charge asymmetry is defined as the number of positive-charged events subtracted by the number of negative-charged ones, $N_+ - N_-$.

accuracy. In this $t\bar{t}W$ VR, a discrepancy between the data and the post-fit $t\bar{t}W$ background was observed at high jet multiplicity. To address this, a data-driven method for $t\bar{t}W$ using a parameterises function that describes the $t\bar{t}W$+jets distribution was introduced. This approach provides a more accurate representation of the $t\bar{t}W$ background, particularly in the showering step at high jet multiplicity, and minimizes the induction of large systematic uncertainties due to mismodeling. This approach follows the same strategy as the Run 2 SM $t\bar{t}t\bar{t}$ analysis [198].

A jet multiplicity parameterised function [201] is used to estimate the showering part of the $t\bar{t}W$+jets distributions. The scaling patterns for QCD jets can be described as the ratio of successive exclusive jet cross-sections:

$$R_{(n+1)/n} = e^{-b} + \frac{\bar{n}}{n+1}, \tag{5.13}$$

where the jet multiplicity n refers to the number of jets beyond those produced in the hard process. $R_{(n+1)/n}$ is the ratio between successive jet multiplicity bins $n+1$ and n. Assuming j is the inclusive number of jets in one event with SS leptons, this means that $n \equiv j - 4$, which is the number of jets in the showering part of $t\bar{t}W$ for the dominant SS channel at the tree level. In $t\bar{t}W$ SS dilepton events, the $t\bar{t}W$ ME generates four jets, so the jets beyond the $t\bar{t}W$ hard process begin from the fifth jet.

Two characteristic patterns, known as staircase scaling and Poisson scaling, represent limiting cases for the behavior of most LHC processes. The first term in Equation 5.13 is the staircase scaling (e^{-b}) and is defined as the constant ratio between successive multiplicity cross-sections:

$$R^{\text{Staircase}}_{(n+1)/n} = e^{-b} = a_0 \tag{5.14}$$

where b and a_0 are constants. An exponential function describes the jet multiplicity distribution and the $t\bar{t}W$ SS dilepton yields for a specific number of jets can be described as:

$$\text{Yield}_{\mathrm{t\bar{t}W@n_j}} = \text{Yield}_{\mathrm{t\bar{t}W@4j}} \times e^{-b(\mathrm{n_j}-4)}. \tag{5.15}$$

The second term describes the ratios between the successive multiplicity cross sections for the Poisson scaling with a ratio of Poisson distribution with an expectation value $\bar{n}$:

$$R^{\text{Poisson}}_{(n+1)/n} = \frac{\bar{n}}{n+1} = \frac{a_1}{1+(j-4)}. \tag{5.16}$$

The staircase scaling (a_0) is more sensitive to high jet multiplicities, while the Poisson scaling (a_1) is more sensitive to low jet multiplicities [201]. By combining both the staircase and Poisson scaling terms, the $t\bar{t}W$ jet multiplicity yields can be described as the product of the two ratios of successive multiplicity cross-sections:

$$\text{Yield}_{\mathrm{t\bar{t}W@n_j}} = \text{Yield}_{\mathrm{t\bar{t}W@4j}} \times \Pi_{j=4}^{j=\mathrm{n_j}-1} \left[a_0 + \frac{a_1}{1+(j-4)} \right] \tag{5.17}$$

with the condition that the number of additional jets (n_j) is at least 5. The parameterization starts from the fourth jet, as $t\bar{t}W$ events are predominantly same-sign dilepton events that produce four jets at tree level in the ME.

In the fit, two normalisation factor, $\mathrm{NF}_{\mathrm{t\bar{t}W^{+}@4j}}$ and $\mathrm{NF}_{\mathrm{t\bar{t}W^{-}@4j}}$, are used to control the scaling of $t\bar{t}W^{+}$ and $t\bar{t}W^{-}$ MC at a 4-jet bin. The $t\bar{t}W^{+}$ and $t\bar{t}W^{-}$ yields are accounted separately because of the different magnitude of $t\bar{t}W^{+}$ and $t\bar{t}W^{-}$ production cross-sections ($\sigma(t\bar{t}W^{+}) : \sigma(t\bar{t}W^{-}) \approx 2 : 1$). The $\mathrm{Yield}_{\mathrm{t\bar{t}W^{\pm}@4j}}$ is represented by $\mathrm{NF}_{\mathrm{t\bar{t}W^{\pm}@4j}} \times \mathrm{MC@4j}$ with floating parameter $\mathrm{NF}_{\mathrm{t\bar{t}W^{\pm}@4j}}$. The scaling of the N_{jets} distributions is expected to be the same in $t\bar{t}W^{+}$ and $t\bar{t}W^{-}$ events. Therefore, a_0 and a_1 are assumed to be the same in $t\bar{t}W^{+}$ and $t\bar{t}W^{-}$ events and simultaneously control both the $t\bar{t}W^{+}$ and $t\bar{t}W^{-}$ N_{jets} distributions. The final N_{jets} parameterised function for $t\bar{t}W$ normalisation is:

$$\mathrm{NF}_{\mathrm{t\bar{t}W@nj}} = (\mathrm{NF}_{\mathrm{t\bar{t}W^{+}@4j}} + \mathrm{NF}_{\mathrm{t\bar{t}W^{-}@4j}}) \times \Pi_{j=4}^{j=\mathrm{nj}-1} \left[a_0 + \frac{a_1}{1+(j-4)} \right]. \tag{5.18}$$

The fit is performed with two NFs, $\mathrm{NF}_{\mathrm{t\bar{t}W^{+}@4j}}$ and $\mathrm{NF}_{\mathrm{t\bar{t}W^{-}@4j}}$, which are left free-floating in the fit and two scaling factors, a_0 and a_1, that are fitted together simultaneously with the parameter of interest and other NFs. The jet multiplicity shape in $t\bar{t}W$ events is defined by the parameters a_0 and a_1. Four CRs are defined in total for the $t\bar{t}W$ parameterisation: $\mathrm{CR}_{1b(+)}$ and $\mathrm{CR}_{1b(-)}$ are defined to constrain the yields of $t\bar{t}W^{+}$ and $t\bar{t}W^{-}$ in the 4-jet bin, respectively; $\mathrm{CR}_{t\bar{t}W^{+}}$ and $\mathrm{CR}_{t\bar{t}W^{-}}$ are to constrain the a_0 and a_1 parameters.

- In $\mathrm{CR}_{1b(\pm)}$, only events with a SS dilepton or trilepton are selected, with the total lepton charge being either positive or negative for $\mathrm{CR}_{1b(+)}$ and $\mathrm{CR}_{1b(-)}$, respectively. At least four jets, exactly one b-jet and $H_{\mathrm{T}} > 400$ GeV is required to maintain orthogonality with the SR. The N_{jets} distributions for these regions are included in the fit to constrain the parameterised N_{jets} function, assuming that the N_{jets} shape is similar between events with exactly one b-jet and events with at least two b-jets
- In $\mathrm{CR}_{t\bar{t}W^{\pm}}$, only events with a SS $e\mu$ or $\mu\mu$ pair are selected, with total lepton charge being either positive or negative for $\mathrm{CR}_{t\bar{t}W^{+}}$ and $\mathrm{CR}_{t\bar{t}W^{-}}$, respectively. Both leptons are required to be non-conversion candidates to ensure orthogonality with fake/non-prompt lepton CRs. To achieve a high $t\bar{t}W$ purity while having similar kinematics to the SR, at least four jets and two b-jets are required. To maintain orthogonality with the SR, $H_{\mathrm{T}} < 400$ GeV or $N_{\mathrm{jets}} < 6$ are required in the $N_{\text{b-jets}} = 2$ region, and $H_{\mathrm{T}} < 400$ GeV in the $N_{\text{b-jets}} \geq 3$ region. The N_{jets} distributions for these regions are included in the fit.

Although $t\bar{t}W$ trilepton events exhibit fewer jets, potentially influencing the jet multiplicity shape of inclusive $t\bar{t}W$ events, only 10% of $t\bar{t}W$ events arise from the trilepton channel. Furthermore, the kinematics of $t\bar{t}W$ events are similar between the same-sign dilepton and combined channels. As a result, the jet multiplicity parameterization for $t\bar{t}W$ is expected to describe inclusive $t\bar{t}W$ events with negligible bias. The description of the $t\bar{t}W$ jets multiplicity distribution with the chosen parameterised function was validated for both Run 2 and Run 3 using statistical-only fits to $t\bar{t}W$ MC prediction in the $\mathrm{CR}_{1b(\pm)}$ regions. The improved agreement of $t\bar{t}W$ VRs with $t\bar{t}W$ data-driven fit is shown in Figure 5.12 and compared with a fit performed using MC template with a single NF for $t\bar{t}W$.

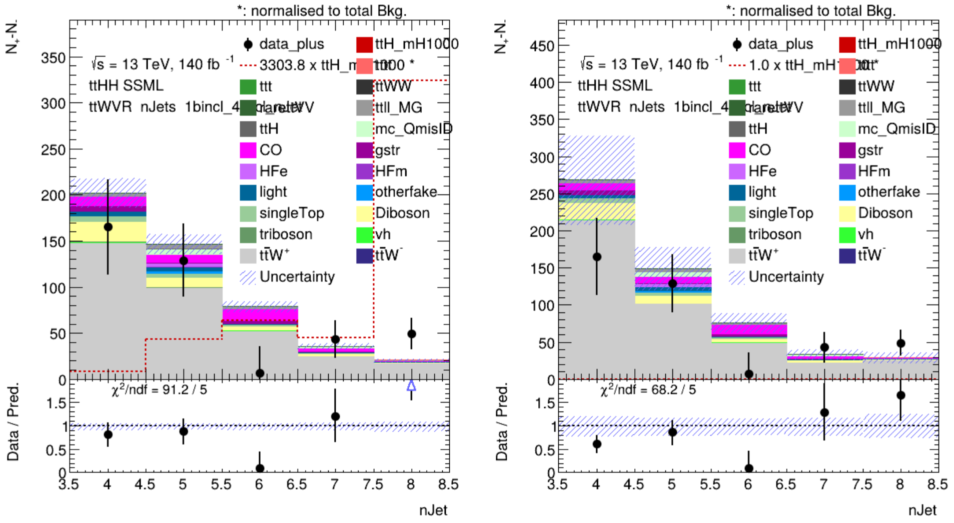

(a) 4j1b template **(b)** 4j1b function form

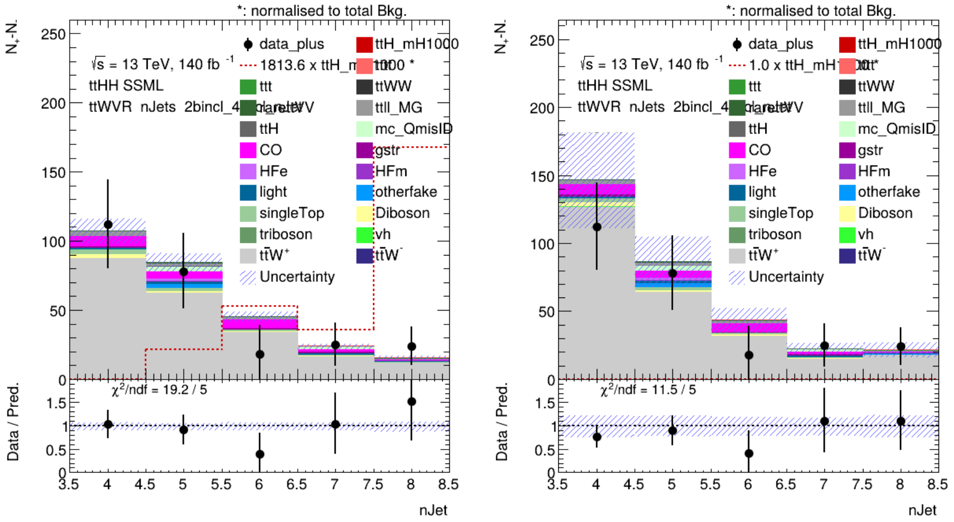

(c) 4j2b template **(d)** 4j2b function form

Figure 5.12: Distribution of $N_+ - N_-$ in 4j1b (upper row) and 4j2b (lower row) VRs, comparing the MC template fit using a single NF (left column) and the data-driven function form approach (right column). Uncertainties on NF $t\bar{t}W^+$, NF $t\bar{t}W^-$, a_0 and a_1 are included in the figures.

5.8 Multivariate Approaches for Signal Classification

Multivariate analysis (MVA) techniques are used to separate the signal from the background in the SRs. Two different models were tested for cross-checking: a Boosted Decision Tree (BDT) trained with high-level variables and a Graph Attention Network (GAT) [137], referred to as transformer, trained with low-level variables. The models are trained on a MC sample subset that is statistically independent of the one used for the evaluation. The models are built by combining several input variables that exploit the different kinematics of signal and background events, as well as b-tagging information. The input variables are selected to maximise the performance of the classification. Different models are optimised and trained separately in the 1L, OS2L and ML channels.

5.8.1 Boosted Decision Trees

The signal typically results in higher transverse activity compared to the background, which is primarily composed of additional jets from radiation. For this reason, variables such as H_{T} and p_{T} of b-jets are included to capture the transverse energy distribution of the signal. The list of BDT input variables is provided in Table 5.6 for 1L, OS2L and ML trainings. A greater focus on leptonic information is given for the ML final state, while variables related to the reconstructed Higgs bosons (Section 5.5) are used for 1L and OS2L, as the two Higgs bosons in signal events provide strong discrimination against the $t\bar{t}$ + jets background.

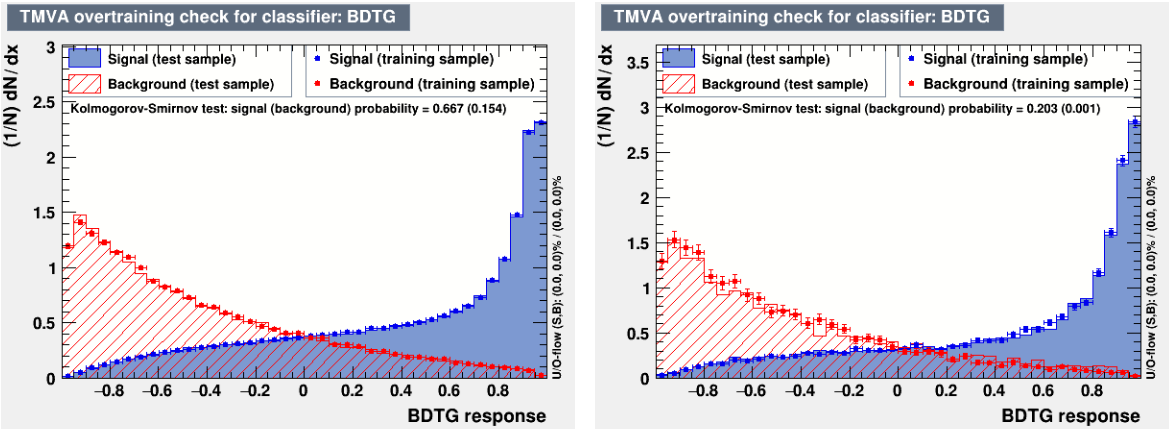

(a) 1L **(b)** OS2L

Figure 5.13: BDT output score distribution for signal (blue) and background (red) samples for both 1L (a) and OS2L (b) channels. The distributions are shown for both the training and testing samples. The invariant mass of the di-Higgs system, the sum of the pseudo-continuous b-tagging scores of the event and the radius distance of between jets are some of the variables that show highest discrimination between signal and background in 1L and OS2L events.

Several metrics are used to test the performance of the BDTs: variable importance, Receiver Operating Characteristic (ROC) curves, and checks for overfitting. Figure

Variable	Description	Final State
$\sum \mathrm{w}_{\mathrm{GN2}}$	Sum of the b-tagging scores of jets, ranked by their GN2 scores.	All
N_{jets}	Jet multiplicity.	All
E_{T}	Missing transverse energy.	All
H_{T}	Scalar sum of the transverse momenta of reconstructed jets and leptons in the event. In ML the leading jet is excluded.	All
$p_{\mathrm{T}}^{l_1}$	Transverse momentum of the leading lepton.	All
m_{H_1} and m_{H_2}	Invariant masses of the b-jet pair assigned to each Higgs candidate by the χ^2 HH pairing algorithm.	1L & OS2L
$m_{H_1 H_2}$	Invariant mass of the combination of the four b-jets assigned to each Higgs candidate by the χ^2 HH pairing algorithm.	1L & OS2L
χ^2	Minimum χ^2 value from HH pairing used to determine the Higgs candidates' reconstruction.	1L & OS2L
$\Delta R^{b_i b_j}_{\text{Max, Min, Mean}}$	Smallest, largest and mean distances in the η-ϕ plane between pairs of b-tagged jets assigned to each Higgs candidate by the χ^2 HH pairing algorithm.	1L & OS2L
$p_{\mathrm{T}}^{b_i}$	Transverse momentum of six b-jets selected and ordered the χ^2 HH pairing.	1L & OS2L
$m_{l_1 l_2}$	Invariant mass of the di-lepton system.	OS2L
$p_{\mathrm{T}}^{j_1}$	Transverse momentum of leading jet.	ML
$p_{\mathrm{T}}^{b_1}$	Transverse momentum of leading b-tagged jet.	ML
$p_{\mathrm{T}}^{j_2}$	Transverse momentum of the sub-leading jet.	ML
$p_{\mathrm{T}}^{j_6}$	Transverse momentum of the 6th leading jet.	ML
$\sum \Delta R^{l_i, l_j}$	Sum of the distance between all leptons in event.	ML
$\Delta R^{l_i l_j}_{\mathrm{Min}}$	The minimum distance between any lepton pair.	ML
$\Delta R^{l_i b_j}_{\mathrm{Max}}$	The maximum distance between leptons and b-tagged jets.	ML
$\Delta R^{j_i b_j}_{\mathrm{Min}}$	The minimum distance between b-tagged jets and jets.	ML

Table 5.6: Input variables used in the training of the BDTs for all final states.

5.13 presents overfitting checks through the distribution of the BDT output scores for both the training and testing datasets. The close alignment between these distributions indicates that the model does not suffer from significant overfitting. The area under the ROC curve (AUC) for the testing samples are 0.876, 0.877, and 0.764 for the 1L, OS2L, and ML channels, respectively.

5.8.2 Graph Attention Networks

At the time of writing of this document, a two-class GAT classification ($t\bar{t}HH$ vs. $t\bar{t}$ + jets) is implemented for the 1L and OS2L channels, with ongoing studies exploring multi-class classification. In ML channel, a four-class model is being trained to classify $t\bar{t}HH$, multi-top ($t\bar{t}t\bar{t}$ and $t\bar{t}t$), $t\bar{t}V$, and the remaining backgrounds. For the multi-class classification, the output probability of the signal class is not directly used as the fit discriminator. Instead, a discriminator is built as the logarithm of the ratio between the probability of the signal class and a weighted sum of the probabilities of the other classes:

$$D = \ln\left[\frac{p_{t\bar{t}HH}}{w_1 \cdot p_{\mathrm{multi-top}} + w_2 \cdot p_{t\bar{t}V} + w_3 \cdot p_{\mathrm{others}}}\right], \tag{5.19}$$

where each class contribution can be optimised with weights w_i.

The GAT is constructed by integrating several low-level kinematic variables, lepton definitions and b-tagging information. Each event is represented as a fully connected graph, where the nodes correspond to the reconstructed jets, leptons, and missing transverse energy. Each node is characterized by features that include the object's four-momentum, the jet's GN2 pseudo-continuos (PCBT) score, the lepton's charge, and an integer that identifies the type of object represented by the node. The edges between nodes capture the angular separations between the objects, incorporating variables such as $\Delta\eta$, $\Delta\phi$, and ΔR. Furthermore, the jet multiplicity of the event is included as a global feature. The specific list of input variables for each object in the 1L, OS2L and ML channels is provided in Table 5.7.

To avoid biasing the transformer classifier towards one output class (e.g., signal or background) due to class imbalances, the event weights are normalized per class. Since all training data is weighted, the event weight of an event i from class c is re-weighted using the formula:

$$\text{normalised weight}_i = \text{event weight}_i \frac{N_{\text{events, total}}}{\sum_{j,c} \text{event weight}_j}, \tag{5.20}$$

where $N_{\text{events, total}}$ represents the total number of unweighted events, and the sum in the denominator runs over all events j and classes c. This approach ensures that the different distribution shapes between classes are preserved and the total sum of event weights across all classes equals the total number of events in the dataset.

The model architecture employed in this analysis is built with multiple layers, each consisting of multi-head self-attention mechanisms and feed-forward neural networks. Figure 5.14 provides a visual representation of the model architecture used. This model follows a structure similar to the GN2 tagger and has been implemented within the SALT framework [202]. Table 5.8 offers an overview of the network parameters used.

Variable	Description
Event-level	
N_{jets}	Number of jets
$N_{\text{b-jets}}$	Number of *b*-tagged jets
N_{leptons}	Number of leptons
H_{T}	The scalar sum of the transverse momenta of the leptons and jets in an event.
Object-level	
$(p_{\text{T}}, \eta, \phi, E)$	Kinematic variables of the object, i.e. transverse momentum, pseudorapidity, azimuthal angle, and energy.
w_{GN2}	GN201 *b*-tagging pseudo-continuous score for identifying jets. Non-jet objects are assigned a value of zero.
$\text{ID}_{\text{Lep.}}^{\text{Tight}}$	Boolean flag indicating if the object passes the tight lepton identification working point. Non-lepton objects are assigned a fixed negative constant.
$q_{\text{Lep.}}$	Charge of the object. Non-lepton objects are assigned a value of zero.
(isJet, isLep, isMET)	Boolean flags indicating the object type: jet, lepton, or MET. In the ML channel the isLep variable is divided into isElectron and isMuon.
DFCAA	Variable to determine if a lepton is from conversion or not. This variable is used only in the ML channel.

Table 5.7: Input variables used for each object in the training of the transformer model for 1L, OS2L and ML channels.

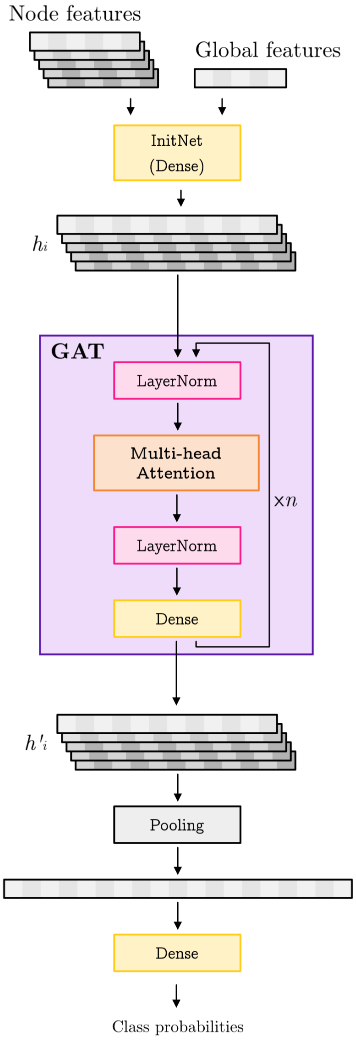

Figure 5.14: The GAT architecture used for event classification in this analysis. Schematic created by R. Wierda.

A k-fold cross-validation technique is employed to mitigate bias while improving training statistics, with $k = 4$. In k-fold validation, the data is divided into k subsets (folds). Each fold is used as the test sample once, while the remaining k-1 folds are used for training and validation. This rotation process repeats until all folds have been tested, ensuring no bias and full use of the MC statistics. Once the optimal hyper-parameters are established, the entire dataset (the sum of all k folds) is used for final training.

The performance was evaluated for each channel separately. The results were compared to the previous BDT and show improvement in sensitivity. The testing AUC is 0.884 for 1L and 0.878 for OS2L. For ML channel the AUC for all folds are within 0.7672 and 0.8494 with an average of 0.8252.

In addition to the improved AUC score, the sensitivity of each channel was evaluated comparing the fit using the BDT against the GAT classifier. The statistical-only limits on the signal strength of the 1L, OS2L, and ML final states have shown significant improvements of 15.8%, 14.5%, and 30.9%, respectively, when using the GAT classifier. Figure 5.15 shows examples of the GAT train and test output distributions for two different folds in ML final state for each class for Run 2. Figure 5.16 shows examples of the GAT output score distributions in various analysis regions used for validation of data/MC agreement.

Network parameters	1L & OS2L	ML
InitNet	Dense(n_{input}, 128, 64, 64)	Dense(n_{input}, 32, 64, 64)
n_{layers}	6	4
n_{heads}	8	8
Activation function	ReLU	ReLU

Table 5.8: GAT network hyper-parameters used for each final state. The InitNet step is a multi-layer dense neural network that integrates event-level information with object-level feature vectors, creating a unified representation for further processing as shown in Figure 5.14.

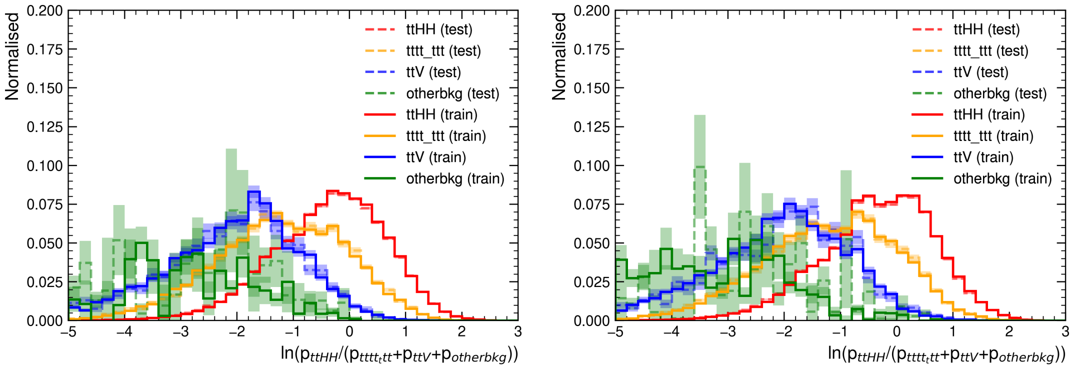

(a) **(b)**

Figure 5.15: Distribution of GAT discriminator of two different folds for Run2 in ML final state.

5.9 Systematic Uncertainties

This analysis considers various sources of systematic uncertainties. All of these, except for the uncertainty related to luminosity, impact both the overall normalisation of the samples and their shape. Cross-section and normalisation uncertainties influence only the normalisation of the specific sample. However, normalisation uncertainties can alter the relative fractions of different samples, leading to a shape uncertainty in the distribution of the final discriminant across the various analysis categories. Each systematic uncertainty is introduced as a nuisance parameter (NP) in the statistical analysis discussed in Section 6.1. Section 5.9.1 provides details on all experimental uncertainties, which include those associated with luminosity, pile-up effects, and the reconstruction and identification of jets and leptons. These uncertainties are uniformly applied across all MC samples. Uncertainties related to signal and background modelling are covered in Section 5.9.2 and may vary depending on the process.

5.9.1 Experimental Uncertainties

Luminosity and Pileup Uncertainty

The uncertainty in the integrated luminosity for the complete Run 2 dataset is 0.83% [203], as determined using the LUCID-2 [204] detector for the primary luminosity measurements, complemented by measurements from the inner detector and calorimeters. The uncertainty in the integrated luminosity for the combination of 2022 and 2023 data for partial Run 3 dataset is 2.0% [54]. A systematic variation is introduced in the pile-up reweighting of simulated events to account for the uncertainty in the ratio between the predicted and measured pile-up [205]. In practice, this involves modifying the nominal SFs applied to the data pileup distribution during reweighting. The SF is adjusted from its nominal value to determine the upward and downward systematic uncertainties.

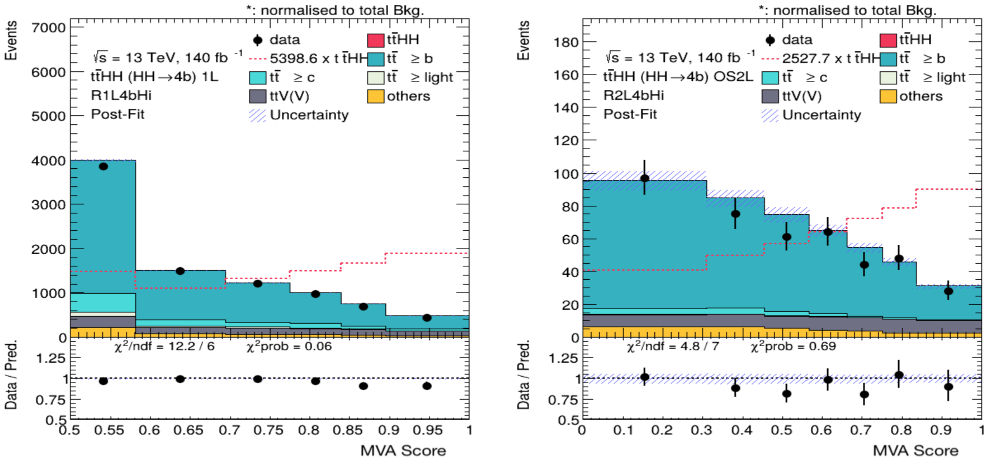

(a) R1L4b$_{\mathrm{Hi}}$ **(b)** R2L4b$_{\mathrm{Hi}}$

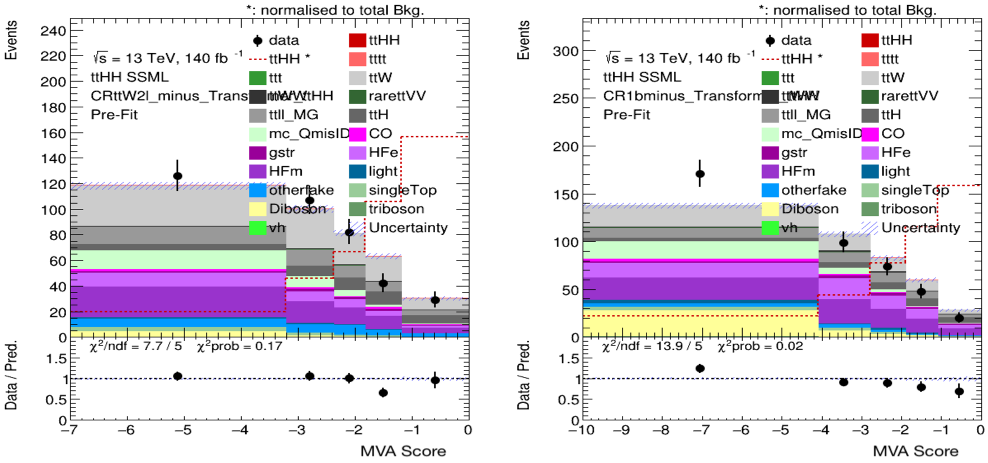

(c) ML CR $t\bar{t}W^{-}$+jets **(d)** ML CR 1b(-)

Figure 5.16: Example of data/MC plots used for validation of MVA agreement in various analysis control regions. The observed data points are represented by black markers, while the MC expectations are displayed as stacked filled histograms. The lower panel shows the ratio of the observed data to the sum of the MC.

Leptons Uncertainty

Lepton systematic uncertainties arise from several factors, including trigger, reconstruction, identification and isolation efficiencies, as well as the energy or momentum scale and resolution of the leptons.

Trigger, reconstruction, identification, and isolation: The SFs used for compensating the different efficiencies for the reconstruction, identification, and isolation of electrons and muons with respect to data are derived with uncertainties, which must be propagated. These SFs are determined using tag-and-probe methods on $Z \rightarrow \ell\ell$ events in both data and simulated samples, as described in Chapter 4. The impact of these SFs, along with their associated uncertainties, is propagated as a correction to the MC event weight.

Energy or momentum scale and resolution: Additional uncertainties originate from corrections to the momentum scale and resolution of leptons in the simulation with those measured in data. These adjustments are determined using mass distributions of reconstructed $Z \rightarrow \ell\ell$ and $J/\psi \rightarrow \ell\ell$ events, as well as the ratio of energy to momentum (E/p) observed in $W \rightarrow e\nu$ events, where E is the electron energy measured by the calorimeter, and p is the momentum measured by the tracking system [117, 119]. To evaluate the impact of momentum scale uncertainties, the lepton energy or momentum is varied by $\pm 1\sigma$ and the event selection is recalculated. For uncertainties in momentum resolution, a smearing is applied to the lepton energy or momentum, followed by a re-evaluation of the event selection.

Jet-related Uncertainties

Similarly to leptons, jet-related uncertainties originate from several factors, including the efficiency of pileup rejection using the Jet Vertex Tagger (JVT), the Jet Energy Scale (JES) and Resolution (JER), and the flavour tagging algorithms, specifically GN2v01 in this analysis.

Jet Vertex Tagging: SFs are applied to account for differences between data and MC simulations for JVT efficiencies. These SFs are determined using $Z \rightarrow \mu\mu$ events with tag-and-probe techniques [206]. The impact of these SFs, along with their uncertainties, is propagated as corrections to the MC event weight.

Jet energy scale and resolution: The jet energy scale and its associated uncertainties are derived by combining data from test beams, LHC collision data, and simulation [125]. The jet energy resolution is measured in data and simulations as a function of jet p_{T} and rapidity using di-jet events, following a method similar to that described in Ref. [207]. The combined uncertainty is propagated by applying smearing to the jet p_{T} in the MC simulations.

GN2 flavour tagging: The b-tagging efficiency and mis-tag rates for c- and light-flavour jets in the simulation are calibrated to align with observed data. This calibration uses scale factors derived separately for b-, c-, and light-flavour jets as functions of jet p_{T}. To reduce the number of associated uncertainties, principal component analysis is applied, resulting in uncorrelated eigen-variations for b-, c- and light-flavour jets. The number of the these eigen-variations correspond to the product of the p_{T} bins and the pseudo-continuous GN2v01 discriminant bins.

Missing Transverse Energy

All systematic uncertainties described above related to the resolutions or energy scales of the reconstructed objects (referred to as the hard components) are propagated to the missing transverse momentum. In addition, uncertainties in the scale and resolution of the soft term are included to account for discrepancies between data and MC simulations regarding the p_{T} balance between the hard and soft components. These uncertainties are represented by three additional independent sources: an offset along the axis of the hard component p_{T}, along with resolution smearing both along and perpendicular to this axis [208, 209].

5.9.2 Modelling Uncertainties

Besides instrumental uncertainties, modelling uncertainties are also considered. This section covers both the general modelling uncertainties applied to both signal and background processes, and the additional modelling uncertainties that are specific to either the signal or a certain background. All of these uncertainties are implemented in accordance with the guidelines provided by the ATLAS collaboration.

General Modelling Uncertainties

The general modelling uncertainties are theoretical systematic uncertainties associated, for example, to missing higher-order terms in the perturbative expansion of the partonic cross-section and uncertainties in the proton-parton distribution functions (PDFs). These uncertainties are applied only to the $t\bar{t}HH$ signal and the primary backgrounds. For all other background processes, these uncertainties are considered negligible.

Renormalisation and factorisation scale (μ_{r} and μ_{f}). To estimate the uncertainty arising from missing higher-order corrections in MC generation, variations in the renormalisation (μ_{r}) and factorisation (μ_{f}) scales are applied. These scales influence the calculated cross-sections and distributions, and varying them allows an assessment of the impact of theoretical uncertainties on the results. The samples are generated with up and down variations for each scale across seven different combinations: $\{\mu_{\mathrm{r}}, \mu_{\mathrm{f}}\} = \{0.5, 0.5\}$, $\{0.5, 1\}$, $\{1, 0.5\}$, $\{1, 1\}$, $\{2, 1\}$, $\{1, 2\}$, and $\{2, 2\}$. The overall uncertainty is determined by taking the envelope of these variations, which is the range (maximum and minimum) of the predicted values across all combinations. For the $t\bar{t}$ + jets backgrounds, the cross-section normalisation component of the scale uncertainty is excluded, as their normalisation's are determined directly in the fit; therefore, only the shape component of the uncertainty is considered for these cases.

ISR and FSR modelling. The uncertainty associated with Initial-State Radiation (ISR) is estimated by varying both (μ_{r}) and (μ_{f}) scales in the ME along with the ISR renormalisation scale ($\mu_{\mathrm{R}}^{\mathrm{ISR}}$) in the PS. The radiation level is increased and decreased by applying scale variations, which modify the strong coupling constant $\alpha_{\mathrm{s}}^{\mathrm{ISR}}$ associated with ISR. These adjustments follow established variations from the simulation A14 tune [154]. For Final-State Radiation (FSR), the uncertainty is evaluated by varying the FSR renormalisation scale ($\mu_{\mathrm{R}}^{\mathrm{FSR}}$) in the PS. Similarly, this involves scaling the QCD emission rates to simulate both increased and decreased radiation levels, modifying the strong coupling constant $\alpha_{\mathrm{s}}^{\mathrm{FSR}}$ for FSR. For both ISR and FST uncertainty estimation, up variations involve scaling μ_{r} and μ_{f} by a factor of about 0.5, while down variations use factors of about 2. Reducing the scale factors increases the strong coupling constant, α_S, in that component of the event generation, leading to a greater amount of radiation.

PDF uncertainties. The uncertainties related to parton distribution functions (PDFs) follow the PDF4LHC guidelines [189] and are incorporated as weights within the samples. The uncertainty associated with the strong coupling constant α_{s} is calculated using the same PDF set but evaluated at two different α_{s} values. The uncertainties from both the PDFs and α_{s} are combined by adding them in quadrature.

Background Modelling Uncertainties

This section outlines additional modelling uncertainties considered exclusively for the main background processes, all of which involve top-quark production. These uncertainties are evaluated by comparing the nominal samples with alternative ones, based on the ATLAS Physics Modelling Group's guidelines. The uncertainties on $t\bar{t}$ + jets background are treated differently for the $4b$ and ML channels, since this background is treated differently between the channel. Additionally, in the $4b$ channel, uncertainties on the H_{T} reweighting are also considered (Section 5.9.3), while in the ML channel, uncertainties on charge mis-identification and non-prompt leptons are considered (Section 5.9.4). The different treatment of systematic uncertainties will be detailed throughout the text.

Cross-section uncertainties are also considered. For the major backgrounds, details can be found in the description for each process below. The cross-section uncertainties on the minor backgrounds are briefly mentioned here. The uncertainty on tZ cross-section is evaluated based on the total uncertainty of the measured cross-section presented in [210]. For tWH, the uncertainty is estimated given the various different NLO predictions in [211]. The uncertainties on the VV production cross-section is evaluated according to Ref. [212]. They are taken as the discrepancies between the measured differential cross-section and the prediction from Sherpa, and are evaluated as a function of jet multiplicities. For the VVV, $t\bar{t}XX$, and VH production, a conservative uncertainty of 50% is applied.

In addition, for processes produced in association with additional heavy-flavour jets, an additional group of uncertainties are applied. These events are the main components that enter the most signal-like region (high tail of the MVA in the signal region), and are difficult to model in the simulation. For the major backgrounds, the evaluation of this uncertainty is described below for each process. For minor backgrounds $t\bar{t}XX$ and $VV(V)$ with at least one truth b-jets not from top-quark decay, an uncertainty of 50% is applied.

$t\bar{t}$ + jets: Systematic uncertainties affecting both acceptance and shape are evaluated by comparing the nominal simulation to alternative MC configurations. These variations can lead to changes in the composition of the different $t\bar{t}$ + jets components within the analysis phase-space. However, the overall normalization of these processes is constrained by data through the profile likelihood fit. To isolate the impact of modelling on the shape and acceptance between regions, all alternative samples are "re-normalised" at pre-fit level to match the nominal sample's fractions of $t\bar{t}$+1b, $t\bar{t}$+2b, $t\bar{t}$+≥3b and $t\bar{t}$ + ≥ c/l in the analysis phase-space. Uncertainties in the ME are evaluated by comparing nominal sample with an alternative sample using `pThard=1`. Additional radiation variation is considering by comparing the nominal samples with varied h_{damp} parameter. For PS and hadronization uncertainties, the nominal Powheg+Pythia 8 sample is compared with an alternative Powheg+Herwig 7 sample. Finally, 4FS samples are used to account for uncertainties on the flavour scheme of $t\bar{t}$ + ≥ 1b component. All modelling uncertainties are uncorrected for each component: $t\bar{t}$ + light, $t\bar{t}$ + ≥ 1c, $t\bar{t}$ +1b, $t\bar{t}$ +2b, $t\bar{t}$ +3b, and $t\bar{t}$ + ≥ 4b.

***tW*:** For the tW sample, ME uncertainties are estimated by comparing the nominal sample with an alternative MadGraph5_aMC@NLO+Pythia 8 sample. PS uncertainties are treated similarly to those for the $t\bar{t}$ + jets background using an alternative Powheg+Herwig 7 sample. Additionally, an extra sample is used to account for uncertainties due to interference between $t\bar{t}$ + jets and tW, where the nominal sample generated with the diagram removal (DR) method is compared to a sample generated with the diagram subtraction (DS) method.

$t\bar{t}X$: For the $t\bar{t}H$ process, MadGraph5_aMC@NLO+Pythia 8 samples are compared to the nominal ones for uncertainties on the ME. For PS, the nominal samples are compared with Powheg+Herwig 7 samples. For $t\bar{t}Z$, the uncertainty related to the generator choice is evaluated by comparing the nominal MadGraph5_aMC@NLO sample with the Sherpa sample. The cross-section uncertainties for $t\bar{t}H$ and $t\bar{t}Z$ are taken from the CERN Yellow Reports [213]. For $t\bar{t}W$, the uncertainty related to the generator choice is evaluated by comparing the nominal Sherpa samples (QCD and EW corrections) with the MadGraph5_aMC@NLO FxFx QCD and MadGraph5_aMC@NLO EW. In the ML final state, no uncertainty on the inclusive cross-section of $t\bar{t}W$ is considered given the data-driven estimation. For each of the three processes, an uncertainty of 50% is assigned to events with an additional truth b-jet not from the top-quark decay, and a separate 50% to events with two or more additional truth b-jets not from the top-quark decay.

$t\bar{t}t\bar{t}$: The uncertainty related to the generator choice, including ME, PS and hadronisation, is considered by comparing the nominal MadGraph5_aMC@NLO sample with the Sherpa sample. An uncertainty related to the PS generator choice is considered by comparing the nominal sample, which is interfaced Pythia8, with the one interfaced with Herwig7. Since this process was measured with a significant excess from the SM [214], an uncertainty on the cross-section that covers the SM and the measured value was included.

$t\bar{t}t$: The uncertainty on the $t\bar{t}t$ production cross section is set to 30%. The acceptance uncertainty is evaluated by comparing the samples generated with 5FS and 4FS schemes. An uncertainty of 50% is applied for events with at least four truth b-jets, i.e. with extra b-jets.

5.9.3 H_{T} Reweighting uncertainties

In the 1L and OS2L final states, additional uncertainties are assigned to $t\bar{t}$ + jets events due to the H_T reweighting applied to the different contributions. These uncertainties are treated independently for the 1L and OS2L final states. The first source of uncertainty is related to the normalization factors of $t\bar{t}$ + jets used in deriving the reweighting. This introduces nuisance parameters that account for the effects of varying the normalisation of each component in each channel's reweighting derivation. Additionally, on/off systematic uncertainties are introduced for both channels, split by jet multiplicity, allowing the reweighting to be reverted via corresponding nuisance parameters.

5.9.4 Charge Misidentification and Non-prompt Lepton Uncertainties

The following uncertainties are only included in the ML final state. The procedure is taken from previous analyses in a similar final states, such as Ref. [214].

Charge Misidentification Uncertainties

These uncertainties originate from uncertainties on the data-driven measurement of the electron charge flip rates described in Section 5.7.3. The uncertainty is determined independently in the material conversion and $t\bar{t}W$ control regions and treated as correlated among all regions. Three sources of uncertainty are considered and added in quadrature, given the small contribution of the QmisID background:

- The statistical uncertainty from the Poisson likelihood fit to data used to determine the rates. The uncertainty is calculated from the square root of the diagonal elements of the error matrix, which is defined as the inverse of the matrix of second derivatives of the likelihood function.
- A non-closure uncertainty in the QmisID estimation method. The relative difference ($\frac{|N_{OS}-N_{SS}|}{N_{SS}}$) is taken as the non-closure systematics.
- The statistical uncertainty from the jet multiplicity correction of misidentification rate. This is determined by the error of fitting parameter from the linear fitting of the scale factor.

Material Conversion and γ^* Uncertainties

The normalisations of these backgrounds are free parameters of the fit, and the uncertainty comes only from the shape of the distributions used in the template fit method. It is obtained by comparing the data with simulation of $Z(\rightarrow \mu\mu) + \gamma$ and $Z(\rightarrow \mu\mu)$+jets production in a validation region enriched in $Z(\rightarrow \mu\mu) + \gamma$ events, with the photon converting into a pair of OS electrons with one of them being very soft.

Heavy Flavour Decay Uncertainties

The normalisations of $t\bar{t} + \geq c/l$, $t\bar{t} + b$, $t\bar{t} + 2b$ and $t\bar{t}+ \geq 3b$ backgrounds are free parameters of the fit, and the uncertainty comes only from the shape of the distributions. It is estimated by bin-by-bin comparison of the data and the background prediction in every analysis region. For the comparison, events with at least one of the leptons used to define the channel is required to be a loose lepton not passing the tight criteria (to guarantee orthogonality to the analysis regions). The shape uncertainty is derived for each region included in the fit and treated as correlated between all regions. The systematic is derived separately for muons and electrons.

Fake Leptons from Light Jets Uncertainties

A normalisation uncertainty on light-flavour non-prompt leptons of 100% is assigned, which covers the discrepancy between data and simulation in loose lepton regions [199]. The uncertainty in the shape is negligibly small and is not considered.

Other Fakes

An ad-hoc uncertainty of 30% is applied on the normalisation for all other minor sources of fake/non-prompt background. The uncertainty in the shape is not considered since it is negligibly small.

6

Limits on $t\bar{t}HH$ production with the full Run 2 and partial Run 3 dataset

Contents

This chapter presents the results obtained in the $t\bar{t}HH$ search described in the previous chapters using the full Run 2 and partial Run 3 dataset considering the graph attention network score as final discriminant. Sections 6.1 and 6.2 describe the statistical treatment and methodology used in the analysis, focusing on the binned likelihood fit employed to extract results of this search.

Section 6.3 presents the results for the 1L final state, obtained extracting the signal strength as parameter of interest of the fit, including the derivation of expected and observed upper limits on the SM expectation, post-fit modelling of analysis regions and the impact of systematic uncertainties on the fit. This is followed by Section 6.4, which shows the expected results for the ML final state. Section 6.5 presents the combined upper limits on the SM $t\bar{t}HH$ signal strength. Finally, Section 6.6 describes the obtained constraints on $c_{t\bar{t}HH}$ coupling modifier.

6.1 Statistical Treatment

To assess the presence of a potential $t\bar{t}HH$ signal, a binned maximum-likelihood fit is performed on data across all signal and control regions for each analysis final state individually (1L and ML). The definitions of these regions and the variables included in the fits are detailed in Sections 5.6.2 and 5.7.2. The event yields in each region are modelled as Poisson-distributed counts, where the expected number of events depends on contributions from both the signal and background MC processes. These expectations are parameterised in terms of the signal strength parameter, μ, which scales the predicted signal cross-section, and a set of nuisance parameters (NPs), $\vec{\theta} = (\theta_1, ..., \theta_i, ..., \theta_N)$, which account for systematic uncertainties and statistical uncertainties in the simulated samples. The best-fit values of μ and $\vec{\theta}$ are those that globally maximize the likelihood function.

6.1.1 Likelihood Function and Profile Likelihood Fit

The statistical inference in this analysis is based on the likelihood function, which quantifies the probability of observing the data given a particular signal strength hypothesis. The binned likelihood function is defined as:

$$\mathcal{L}(\alpha) = \prod_{i=1}^{N_{\text{bins}}} P(n_i|\nu_i(\alpha)) \times \prod_{j=1}^{N_{\text{nuis}}} \pi(\theta_j), \tag{6.1}$$

where $P(n_i|\nu_i(\alpha))$ represents the probability of observing n_i events in bin i given an expectation $\nu_i(\alpha)$. The parameter $\vec{\alpha}$ includes the parameter of interest (POI), nuisance parameters θ, and background normalization factors (described below). The POI represents the primary quantity of interest in the measurement, which in this dissertation corresponds to the signal strength μ. Finally, $\pi(\theta_j)$ are prior constraints on the nuisance parameters, usually modelled as Gaussian or log-normal distributions.

The signal strength is defined as the ratio of the observed number of $t\bar{t}HH$ signal events to the predicted number of events based on the SM expectation:

$$\mu = \frac{N^{\text{fitted}}_{t\bar{t}HH}}{N^{\text{predicted}}_{t\bar{t}HH}}. \tag{6.2}$$

A value of $\mu = 1$ indicates that the observed $t\bar{t}HH$ production rate matches the theoretical expectation, while $\mu = 0$ corresponds to the background-only hypothesis, implying no contribution from the $t\bar{t}HH$ signal in the data. Values of μ greater than or less than unity indicate an excess or deficit of the observed signal events relative to the SM expectation.

Each bin follows a Poisson probability distribution:

$$P(n_i|\nu_i) = \frac{\nu_i^{n_i} e^{-\nu_i}}{n_i!}, \tag{6.3}$$

where ν_i is given by:

$$\nu_i(\alpha) = \mu S_i + B_i(\theta, k), \tag{6.4}$$

where S_i is the expected signal yield in bin i and $B_i(\theta, k)$ represents the expected background yield, which depends on nuisance parameters θ and normalisation factors $k = (k_1, k_2, ...)$.

Besides NPs associated with systematic uncertainties, additional free parameters can be incorporated into the likelihood function, known as normalization factors (NFs), which act as unconstrained multiplicative scaling factors applied to specific background components. Unlike systematic NPs, normalization factors are not constrained by prior distributions and are treated as free parameters in the fit:

$$B_i(\theta, k) = \sum_j k_j \cdot B_{ij}(\theta), \tag{6.5}$$

where, $B_{ij}(\theta)$ represents the expected background yield as a function of the nuisance parameters θ in bin i for different background processes (index j). k_j is the normalization factor that scales each background contribution. These normalization factors provide additional flexibility in the fit, allowing for the adjustment of major background components that lack precisely known theoretical cross-sections based on data constraints without imposing external priors.

The total likelihood is then:

$$\mathcal{L}(\alpha) = \prod_{i=1}^{N_{\text{bins}}} \frac{(\mu S_i + B_i(\theta, k))^{n_i} \, e^{-(\mu S_i + B_i(\theta, k))}}{n_i!} \times \prod_{j=1}^{N_{\text{nuis}}} \pi(\theta_j). \tag{6.6}$$

6.1.2 Test Statistic, Likelihood Ratio and p-Value

To test an hypothesised value of μ, the maximum likelihood estimate (denominator) and the conditional maximum likelihood estimate (numerator) are compared in a profile likelihood ratio defined as:

$$\lambda(\mu) = -2 \ln \frac{\mathcal{L}(\mu, \hat{\hat{\theta}}(\mu))}{\mathcal{L}(\hat{\mu}, \hat{\theta})}. \tag{6.7}$$

The maximum likelihood estimate is obtained by profiling both μ and the NPs to find the values that maximise the overall likelihood function. These best-fit parameters are denoted as $\hat{\mu}$ and $\hat{\theta}$, respectively. Alternatively, in the conditional maximum likelihood estimate, μ is fixed at a specific value while profiling over θ to determine the values that maximize the likelihood function under this constraint. The resulting set of nuisance parameter values is denoted as $\hat{\hat{\theta}}(\mu)$.

From the definition of the likelihood ratio, it follows that $0 \leq \lambda(\mu) \leq 1$, where values of $\lambda(\mu)$ close to 1 indicate strong agreement between the data and the hypothesized value of μ. A more convenient way to express the likelihood ratio for statistical testing is through the test statistic:

$$t_\mu = -2 \ln \lambda(\mu). \tag{6.8}$$

Larger values of t_μ correspond to increasing incompatibility between the data and the assumed hypothesis. Therefore, t_μ serves as a direct measure of the discrepancy between the observed data and the tested value of μ.

The level of disagreement is quantified using the p-value, which provides the probability of obtaining a test statistic at least as extreme as the observed t_μ, assuming the hypothesis is true:

$$p_\mu = \int_{t_{\mu,\text{obs}}}^{\infty} f(t_\mu|\mu)\, dt_\mu, \tag{6.9}$$

where $t_{\mu,\text{obs}}$ is the observed value of the test statistic and $f(t_\mu|\mu)$ is the probability density function of t_μ under the given signal strength assumption.

In high-energy-physics searches, the null hypothesis (H_0) is typically defined as the background-only hypothesis, which assumes that no signal contribution is present in the observed data, i.e., $\mu = 0$. This hypothesis is tested against the alternative hypothesis (H_1), which assumes that the observed data contains both signal and background contributions. The decision to accept or reject the tested hypothesis is made at a predefined confidence level (CL), based on the obtained p-value assuming the null hypothesis is true. Different formulations of the p-value are used depending on the specific objectives of the statistical analysis, such as discovery significance, exclusion limits, or confidence interval estimation.

6.1.3 Discovery of a Positive Signal

In a model where $\mu \geq 0$, if the best-fit value of the signal strength, $\hat{\mu}$, is found to be negative, the highest level of agreement between the data and any physically meaningful value of μ is achieved by setting $\mu = 0$. Therefore the test statistics is defined as:

$$\tilde{t}_\mu = \begin{cases} -2\ln \frac{\mathcal{L}\left(\mu,\hat{\hat{\theta}}(\mu)\right)}{\mathcal{L}\left(\hat{\mu},\hat{\theta}\right)} & \hat{\mu} \geq 0, \\ -2\ln \frac{\mathcal{L}\left(\mu,\hat{\hat{\theta}}(\mu)\right)}{\mathcal{L}\left(0,\hat{\hat{\theta}}(0)\right)} & \hat{\mu} < 0 \end{cases}$$

To test for the presence of a positive signal ($\mu > 0$) against the background-only hypothesis ($\mu = 0$), the test statistic for discovery is used and defined as:

$$\tilde{t}_0 = \begin{cases} -2\ln \frac{\mathcal{L}(0,\hat{\hat{\theta}}(0))}{\mathcal{L}(\hat{\mu},\hat{\theta})}, & \text{if } \hat{\mu} \geq 0, \\ 0, & \text{if } \hat{\mu} < 0. \end{cases} \tag{6.10}$$

If the hypothesis $\mu = 0$ is rejected, this provides evidence for the presence of a new signal. A large value of $\tilde{t}_0$ suggests that the background-only hypothesis ($\mu = 0$) is strongly disfavoured in favour of a positive signal. The p-value for discovery is defined as:

$$p_0 = \int_{t_{0,\text{obs}}}^{\infty} f(t_0|0)\, dt_0, \tag{6.11}$$

and quantifies the level of disagreement between data and the background-only hypothesis.

The asymptotic distribution of these test statistics under the null hypothesis follows a chi-squared distribution in the large-sample limit, which enables the computation of confidence intervals and significance levels. The statistical significance of the excess is expressed in terms of standard deviations (σ), using the one-sided Gaussian quantile:

$$Z = \Phi^{-1}(1 - p_0), \tag{6.12}$$

where Φ^{-1} is the inverse of the cumulative standard normal distribution. A five-standard-deviation excess ($p_0 \approx 2.87 \times 10^{-7}$) is conventionally required for claiming discovery in high-energy physics.

6.1.4 Confidence Intervals and Limit Setting with the CL$_s$ Method

The test statistic used to establish upper limits on the signal strength is defined as:

$$q_\mu = \begin{cases} -2\ln\lambda(\mu), & \text{if } \hat{\mu} \leq \mu, \\ 0, & \text{if } \hat{\mu} > \mu. \end{cases} \tag{6.13}$$

The test statistic q_μ is set to zero for cases where $\hat{\mu} > \mu$ because, when establishing an upper limit, data yielding $\hat{\mu} > \mu$ should not be considered less compatible with the tested value of μ than the observed data. The upper limit is determined by testing the hypothesis for μ against alternative hypotheses with smaller values of μ.

The p-values are then used to set upper limits on $t\bar{t}HH$ production by employing the CL$_\mathrm{s}$ method [215]. This approach determines the maximum signal strength that can be excluded within a given CL. Instead of simply rejecting hypotheses based on individual p-values, the CL$_\mathrm{s}$ method compares the p-values of the signal+background hypothesis (p_{s+b}) to those of the background-only hypothesis (p_b). The CL for excluding a given μ is then defined as:

$$\mathrm{CL}_s = \frac{p_{s+b}}{p_b} < 0.05, \tag{6.14}$$

where the signal-plus-background hypothesis corresponds to the scenario where the $t\bar{t}HH$ production occurs with a signal strength $\mu = 1$.

If CL$_s$ < 0.05, the corresponding μ value is excluded at the 95% CL. This method ensures a conservative approach by reducing the probability of excluding signal hypotheses that are consistent with background fluctuations.

6.2 Likelihood Fit Setup

6.2.1 Asimov Dataset

To estimate the expected sensitivity of the analysis and evaluate the background constraining power while designing and optimising the analysis, an Asimov dataset is used. This dataset is constructed using the exact expected event yields for both signal and background, as predicted by the nominal MC simulations. By providing a statistically representative sample without fluctuations, the Asimov dataset allows for the validation of the fit model and assessment of the analysis performance before applying the fit to real data. Ideally, when fitting an Asimov dataset, the best-fit values for the POI should, by definition, converge to their nominal values, ensuring a self-consistent validation of the statistical model.

6.2.2 Re-binning the MVA Score Distributions

The binning of the MVA distributions is optimized individually for each region where it is applied in the fit. The final-discriminant histograms are initially created with 100 bins, and the binning optimization is performed before the fit by re-binning each histogram. The optimization method iteratively determines the binning using the formula:

$$Z = Z_b \frac{n_b}{N_b} + Z_s \frac{n_s}{N_s}, \tag{6.15}$$

where s and b denote signal and background, respectively. Here, n_s and n_b represent the yield of signal or background in a single bin, while N_s and N_b corresponds to the total signal or background yields of the distribution. The input parameters Z_b and Z_s typically sum to the total number of bins in the re-binning process. The algorithm starts at the lowest boundary of the variable and extends a bin's upper edge once $Z \geq 1$. For example, setting $Z_b = n_{\text{bins}}$ and $Z_s = 0$ results in binning where $n_b = N_b/n_{\text{bins}}$ in each bin, leading to a background distribution that appears flat.

6.2.3 Smoothing of Systematic Uncertainties

Systematic uncertainties are derived from MC samples using various methods. When comparing different MC samples or applying generator weights, the available MC statistics may become diluted, leading to increased fluctuations. These fluctuations can potentially affect the fit convergence. To mitigate these effects, smoothing algorithms are applied to the histograms before the fit. The smoothing algorithm performs a re-binning to reduce statistical fluctuations per bin and is applied to all the systematic variations across all regions. In the first step, bins are merged until the varied distribution relative to the nominal distribution exhibits a single maximum. In the second step, further grouping of bins is performed until the statistical uncertainty in each bin is reduced to below 5%.

6.2.4 Pruning of Systematic Uncertainties

Only some NPs have a sizeable impact on the fit. To reduce the number of NPs in order to improve computational efficiency and fit stability, a pruning procedure is applied. The procedure removes systematic uncertainties that have a negligible impact on the final result. Pruning is carried out by evaluating the bin-by-bin variations of each systematic uncertainty relative to the corresponding sample in each region. Normalisation and shape uncertainties are separately dropped if their variation with respect to the nominal value is below 0.5%.

Process-dependent modelling uncertainties, b-tagging uncertainties, as well as jet energy and resolution uncertainties are fully or partially retained across all samples and regions for all final states of this analysis. Lepton-related uncertainties are predominantly removed in the 1L final state due to their minimal impact in the fit.

6.3 Results in the 1L Final State

This section presents the results for the 1L final state. The binned maximum-likelihood fits are performed to the various signal and control region distributions under the signal-plus-background hypothesis assuming a Higgs boson mass of $m_H = 125$ GeV. Nuisance parameters account for $t\bar{t}$ + jets background normalisation, systematic uncertainties, and one parameter per bin to model statistical uncertainties and are fitted together with free-floating POI and NFs. The uncertainties are categorized into two parts: statistical and systematic. The statistical uncertainty is derived by evaluating the signal strength in a fit where all nuisance parameters are held constant at their best-fit values, isolating statistical contributions. The systematic uncertainty is then calculated by subtracting the statistical uncertainty from the total uncertainty in quadrature. The uncertainties and confidence levels are estimated using the asymptotic approximation, which is validated to agree with results obtained from pseudo-data experiments. Upper limits on the signal strength are set using the CLs method described previously.

As discussed in Chapter 5, due to the limited contribution of $t\bar{t}$ + light events in the signal regions, a shared normalisation factor is assigned to both the $t\bar{t}$ + light and $t\bar{t} + \geq 1c$ components, denoted as the $t\bar{t} + \geq c/l$ normalisation term. The fit therefore includes four normalisation factors: $t\bar{t} + \geq c/l$, $t\bar{t}+1b$, $t\bar{t}+2b$, and $t\bar{t} + \geq 3b$. An additional degree of freedom is introduced to account for the uncertainty in the relative rate of charm- versus light-flavour jet production. All modelling uncertainties are treated independently for each component: $t\bar{t}$ + light, $t\bar{t} + \geq 1c$, $t\bar{t} + 1b$, $t\bar{t} + 2b$, $t\bar{t} + 3b$, and $t\bar{t} + \geq 4b$.

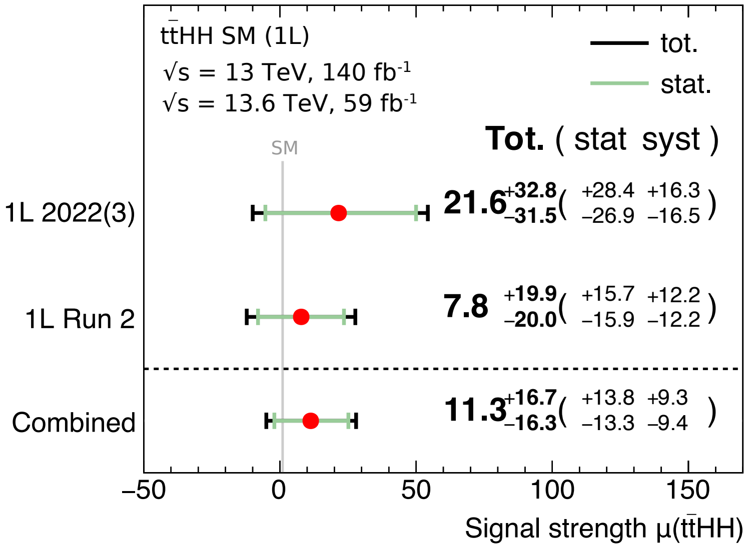

Figure 6.1: Best-fit value of the signal strength $\mu_{t\bar{t}HH}$ in the 1L final state for Run 2, partial Run 3 and statistical combination. The black error bands correspond to the total uncertainty on $\mu_{t\bar{t}HH}$ and the green bands correspond to the statistical component. The SM expectation is shown with a grey vertical line at one.

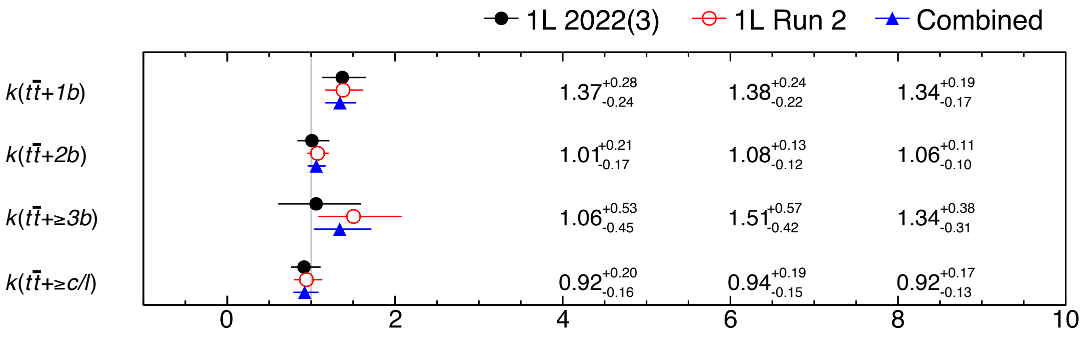

Figure 6.2: Best-fit values of all $t\bar{t}$ + jets free-floating normalization factors in the 1L final state for Run 2 (red), partial Run 3 (black) and statistical combination (blue). The 1L components are divided into $t\bar{t} + \geq c/l$, $t\bar{t} + b$, $t\bar{t} + 2b$ and $t\bar{t} + \geq 3b$.

The fits are performed to data collected during Run 2 and partial Run 3 (2022 and 2023), corresponding to an integrated luminosity of 140 and 59 fb^{-1}. Run 2 and 3 datasets are kept separately and a statistical combination is performed at the fit level. Combining Run 2 and Run 3 presents challenges in correlating certain uncertainties, particularly instrumental systematics, as they can represent different meanings between the runs. Modelling uncertainties could be correlated if the same sample prescriptions are used and if the variations behave consistently between Run 2 and Run 3. In this thesis all instrumental systematic uncertainties were decorrelated between runs, while the theoretical and modelling uncertainties were correlated. The effect of decorrelating the systematics was also studied, and it did not show a significant impact at the current level of precision.

Figure 6.1 presents the best-fit values and uncertainties for the signal strengths, both from the combined fit and from the individual contributions of each run. The observed best-fit value obtained from the combined fit to the data is $\mu_{t\bar{t}HH} = 11.3^{+16.7}_{-16.3}$, which is compatible with the SM expectations within statistical uncertainties. This combination yields an observed upper limit on the $t\bar{t}HH$ signal strength of 42.63 times the SM at 95% CL, with an expected upper limit of 32.64 assuming no $t\bar{t}HH$ production. Figure 6.26 shows the observed and expected limits on the signal strength, where the individual contributions of each run to the overall analysis sensitivity is assessed. The measured values of $t\bar{t}$ + jets NFs are presented in Figure 6.2 separately for each run and the statistical combination. Consistent values are obtained between the two runs.

Figures 6.4 - 6.7 present the pre- and post-fit modelling in the CRs and SRs for Run 2 and Run 3 data compared to MC predictions. Figure 6.3 shows a summary of the total pre- and post-fit yields per region. In the post-fit plots, the signal strengths, background normalizations, and all nuisance parameters are set to their best-fit values, with both statistical and systematic uncertainties included. The results show good agreement between the data and the MC predictions across all regions. The binning definition of SRs follow the description of Section 6.2.2.

The impact of each NP is quantified as the difference between the nominal uncertainty on $\mu_{t\bar{t}HH}$ and the uncertainty obtained in a fit where that NP is individually removed. The dominant contributions come from modelling uncertainties related to the $t\bar{t}$ + jets backgrounds, which are the primary processes in the SR. MC statistics from high MVA bins also rank highly. Pointing to the need for MC samples that cover better the phase-space of the analysis. Additionally, the $t\bar{t}HH$ and $t\bar{t}H$ cross-sections are among the top 40 highest-ranked uncertainties. The fitted nuisance parameters are shown in Figures 6.8 and 6.9, separately for modelling uncertainties, b-tagging uncertainties and other instrumental uncertainties.

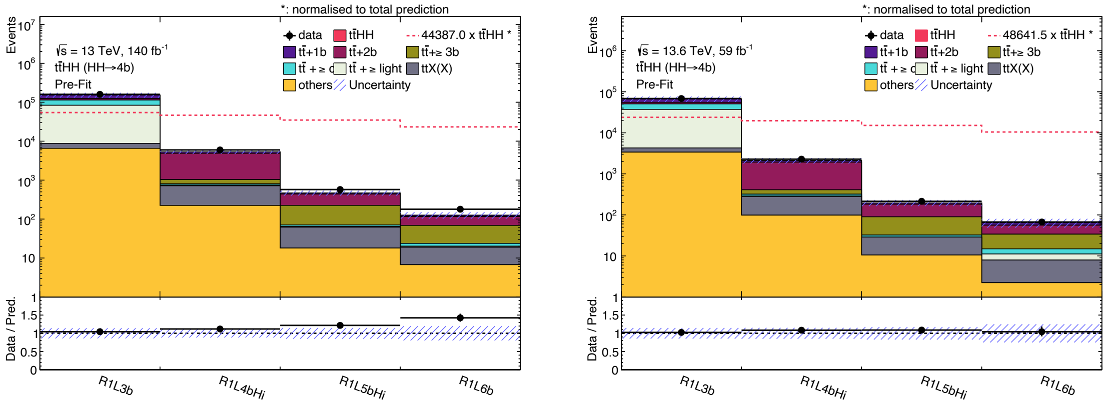

(a) Pre-fit Run 2 **(b)** Pre-fit Run 3

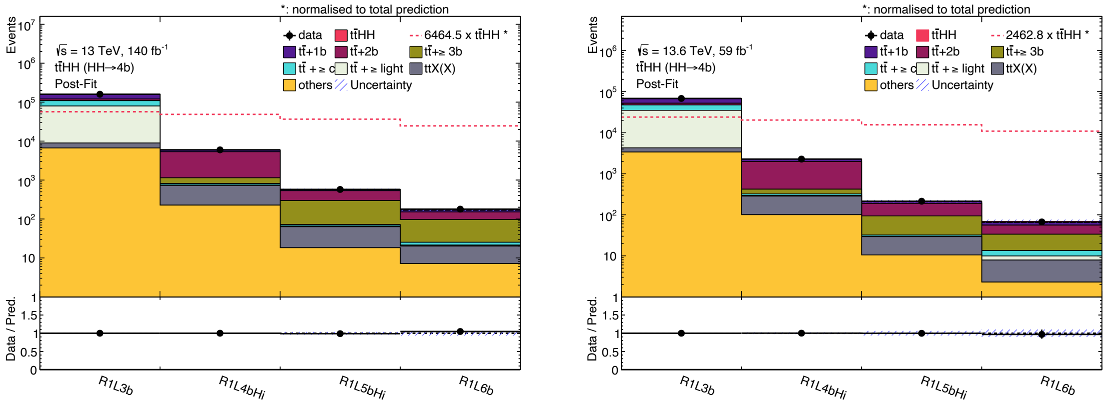

(c) Post-fit Run 2 **(d)** Post-fit Run 3

Figure 6.3: Pre- and post-fit total yields in all 1L regions included in the fit, for Run 2 (a) and partial Run 3 (b) datasets. The observed data points are represented by black markers, while the MC expectations are displayed as stacked filled histograms. The $t\bar{t}HH$ signal is shown both overlaid on top of the fitted background and as an unfilled histogram, scaled by the integral of the MC background. The hatched band includes both statistical and systematic uncertainties. The lower panel shows the ratio of the observed data to the sum of the MC.

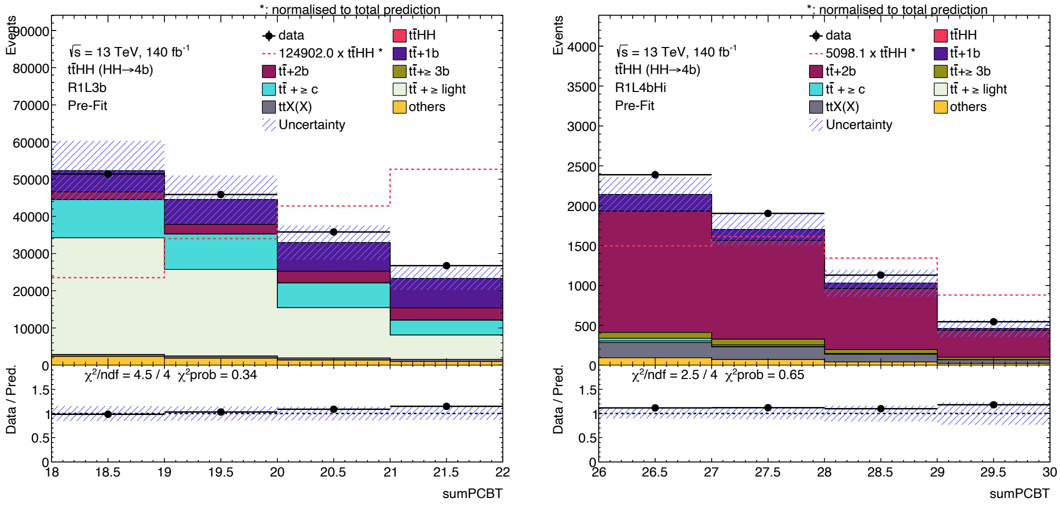

(a) R1L3b

(b) R1L4b$_{\text{Hi}}$

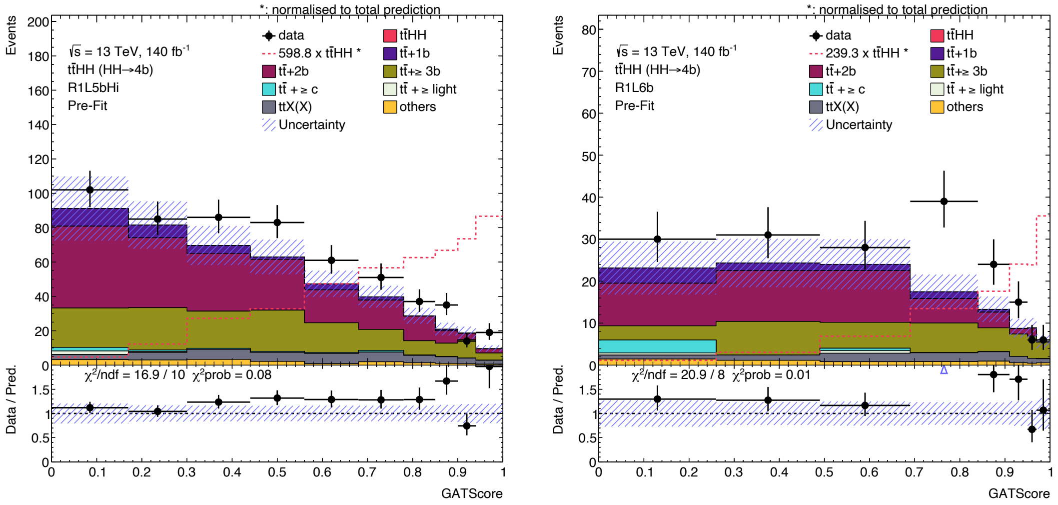

(c) R1L5b$_{\text{Hi}}$

(d) R1L6b

Figure 6.4: Run 2 pre-fit CRs and SRs in the 1L final state. The observed data points are represented by black markers, while the MC expectations are displayed as stacked filled histograms. The $t\bar{t}HH$ signal is shown both overlaid on top of the fitted background and as an unfilled histogram, scaled by the integral of the MC background. The hatched band includes both statistical and systematic uncertainties. The lower panel shows the ratio of the observed data to the sum of the MC.

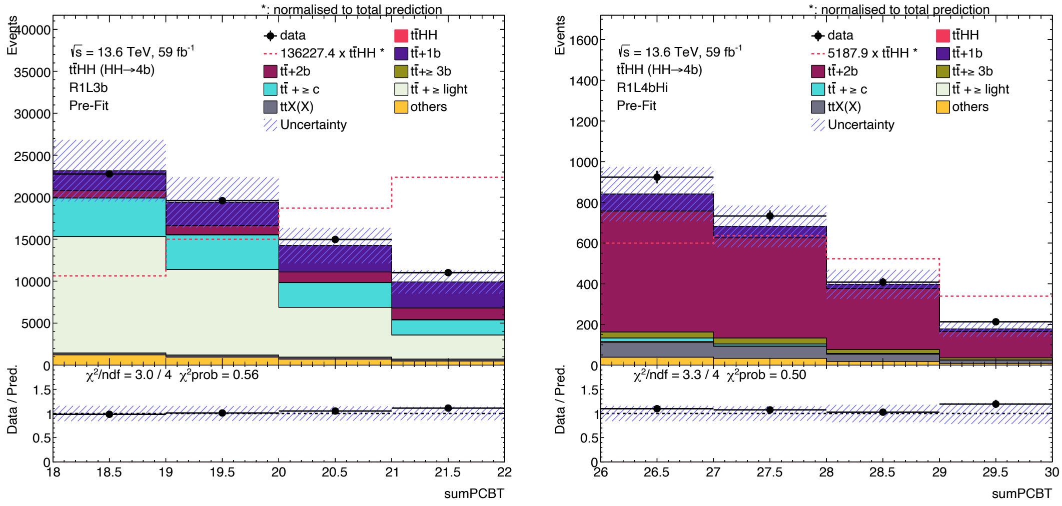

(a) R1L3b **(b)** R1L4b$_{\mathrm{Hi}}$

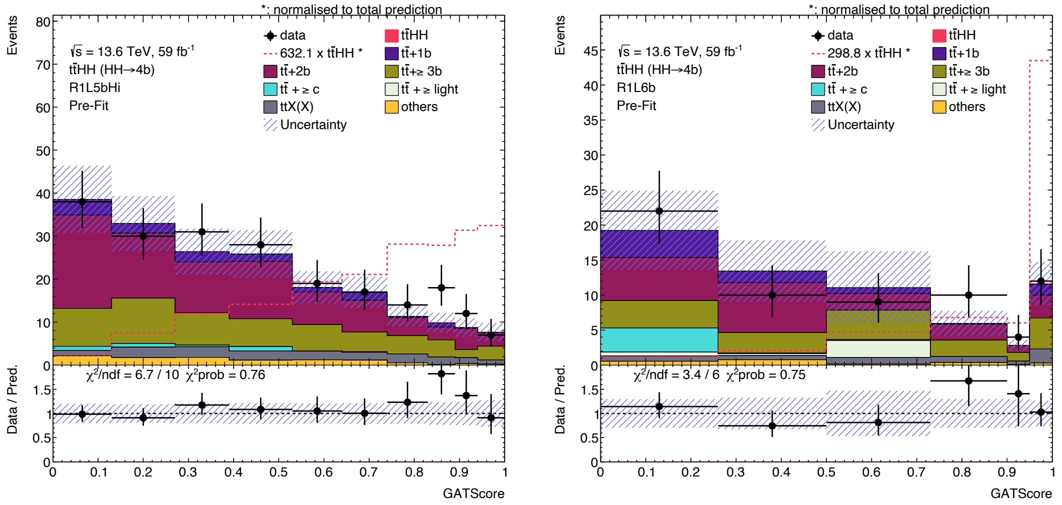

(c) R1L5b$_{\mathrm{Hi}}$ **(d)** R1L6b

Figure 6.5: Run 3 pre-fit CRs and SRs in the 1L final state. The observed data points are represented by black markers, while the MC expectations are displayed as stacked filled histograms. The $t\bar{t}HH$ signal is shown both overlaid on top of the fitted background and as an unfilled histogram, scaled by the integral of the MC background. The hatched band includes both statistical and systematic uncertainties. The lower panel shows the ratio of the observed data to the sum of the MC.

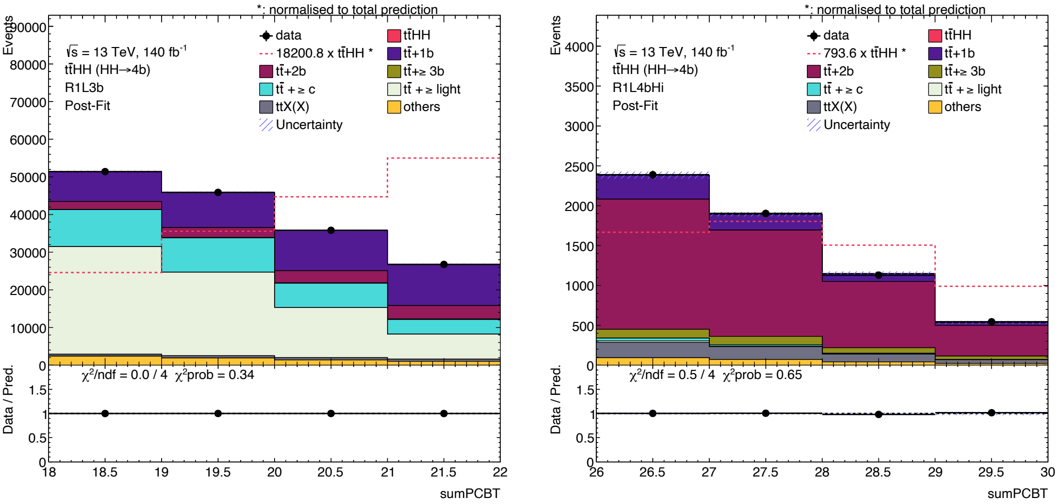

(a) R1L3b **(b)** R1L4b$_{\text{Hi}}$

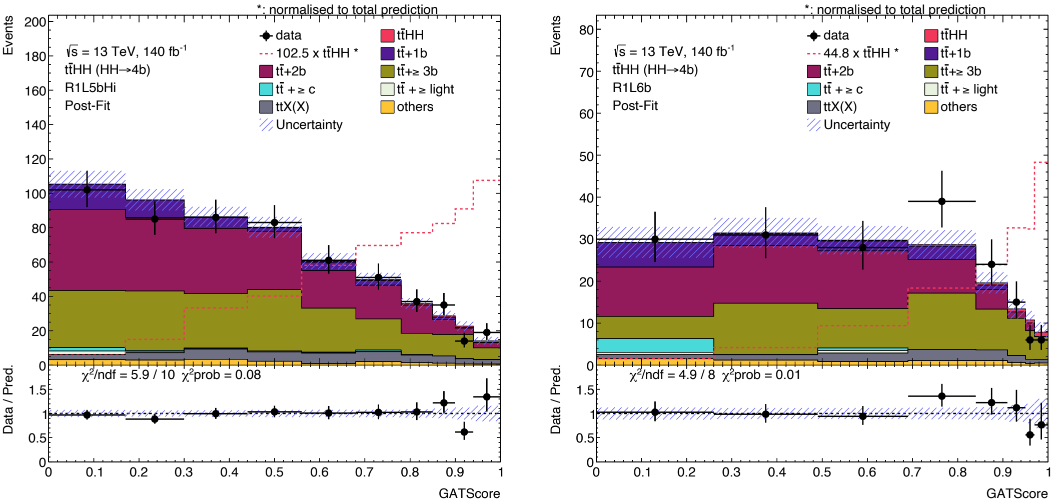

(c) R1L5b$_{\text{Hi}}$ **(d)** R1L6b

Figure 6.6: Run 2 post-fit CRs and SRs in the 1L final state. The observed data points are represented by black markers, while the MC expectations are displayed as stacked filled histograms. The $t\bar{t}HH$ signal is shown both overlaid on top of the fitted background and as an unfilled histogram, scaled by the integral of the MC background. The hatched band includes both statistical and systematic uncertainties. The lower panel shows the ratio of the observed data to the sum of the MC.

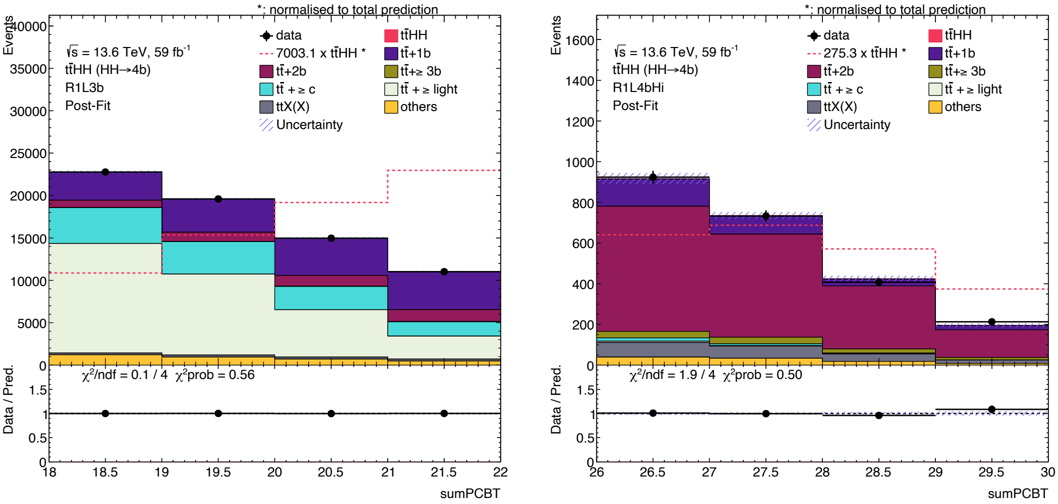

(a) R1L3b

(b) R1L4b$_{\text{Hi}}$

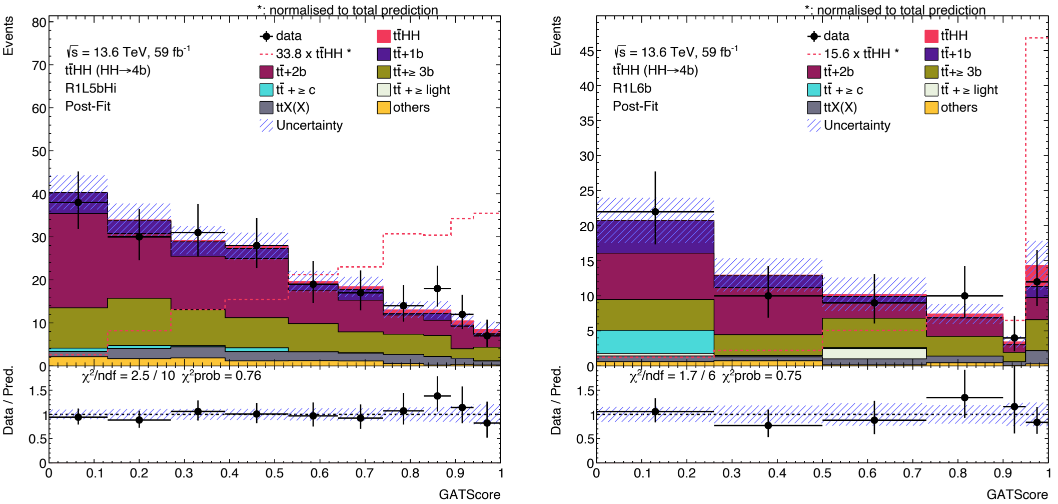

(c) R1L5b$_{\text{Hi}}$

(d) R1L6b

Figure 6.7: Run 3 post-fit CRs and SRs in the 1L final state. The observed data points are represented by black markers, while the MC expectations are displayed as stacked filled histograms. The $t\bar{t}HH$ signal is shown both overlaid on top of the fitted background and as an unfilled histogram, scaled by the integral of the MC background. The hatched band includes both statistical and systematic uncertainties. The lower panel shows the ratio of the observed data to the sum of the MC.

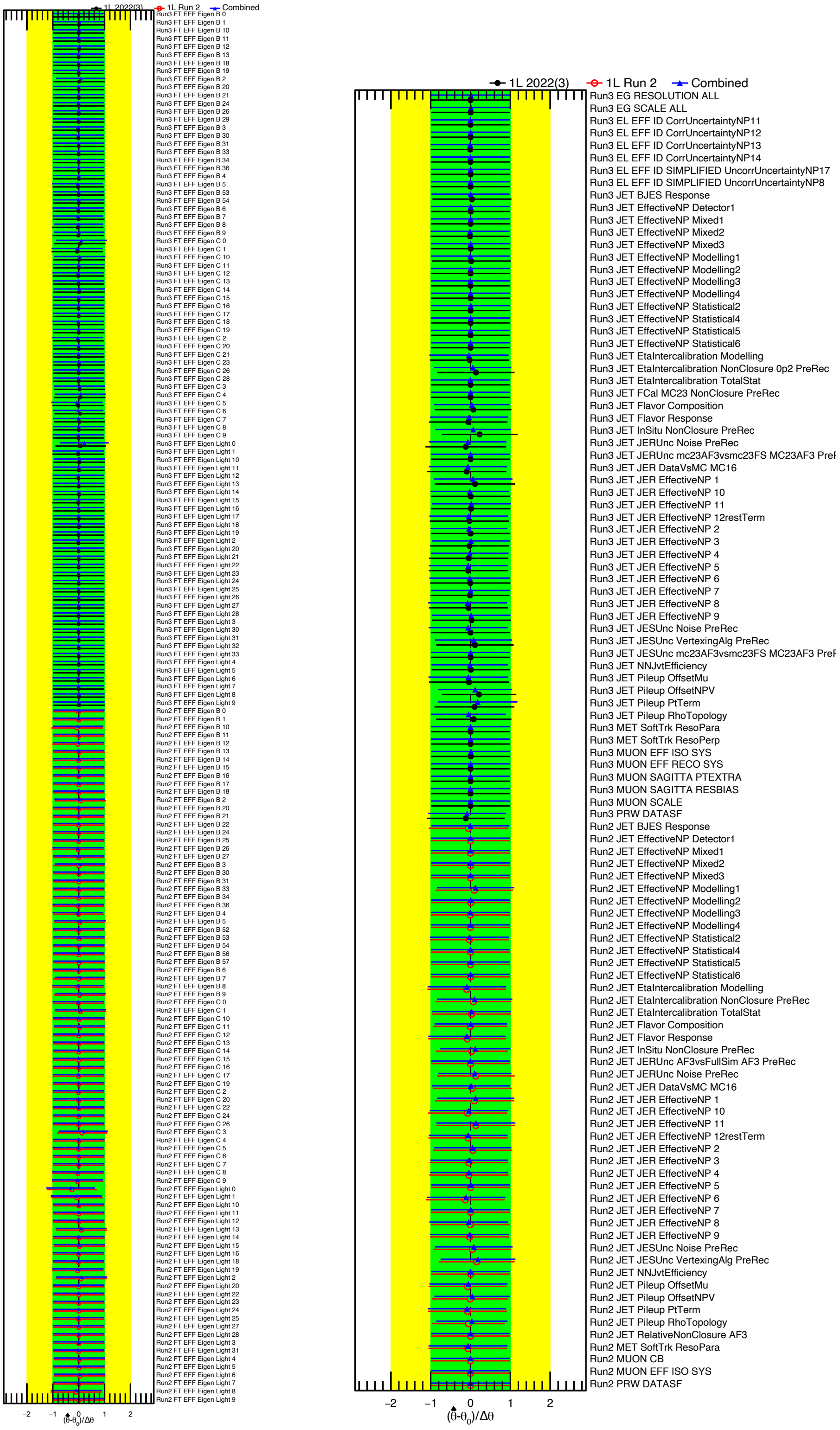

(a) b-tagging uncertainties **(b)** Other instrumental uncertainties

Figure 6.8: Pulls and constrains from each instrumental nuisance parameter in the 1L final state the fits on Run 2 and partial Run 3 dataset separately, as well as for the combined fit. Theory uncertainties are correlated between the runs, while instrumental ones are kept uncorrelated.

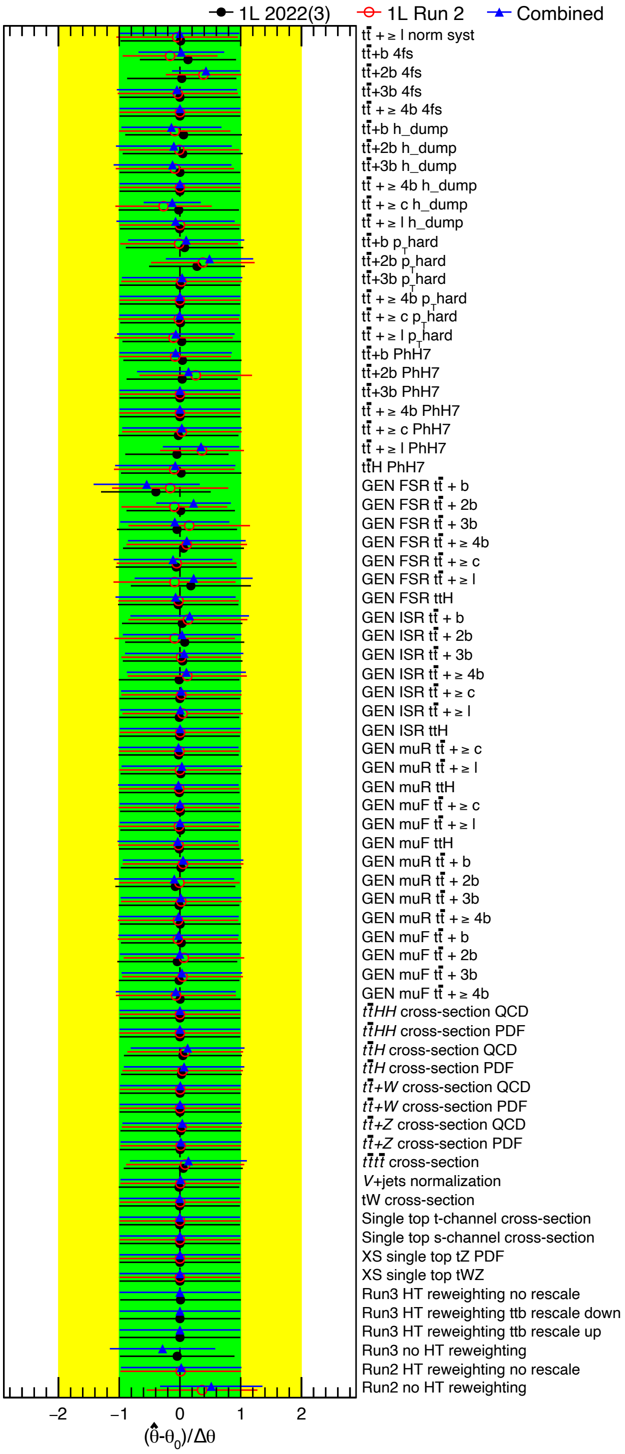

(a) Modelling uncertainties

Figure 6.9: Pulls and constrains from each MC modelling and theoretical nuisance parameter in the 1L final state for the fits on Run 2 and partial Run 3 dataset separately, as well as for the combined fit. Theory uncertainties are correlated between the runs, while instrumental ones are kept uncorrelated.

6.4 Results in the ML Final State

This section presents the results for the ML final state. The background from misreconstructed or non-prompt leptons and $t\bar{t}W$ contribution are estimated through the data-driven approach described in Chapter 5 and are derived simultaneously in the fit. The binned maximum-likelihood fits are performed to the various signal and control region distributions under the signal-plus-background hypothesis assuming a Higgs boson mass of $m_H = 125$ GeV. The fits simultaneously extracts the signal strength, background normalization factors, and systematic uncertainties. The fits are performed to data collected during the Run 2 and partial Run 3 (2022 and 2023), corresponding to an integrated luminosity of 140 and 59 fb^{-1}. Run 2 and 3 datasets are kept separately and a later statistical combination is performed at the fit level. All instrumental systematic uncertainties are treated as uncorrelated between runs, while theoretical and modelling uncertainties are kept correlated.

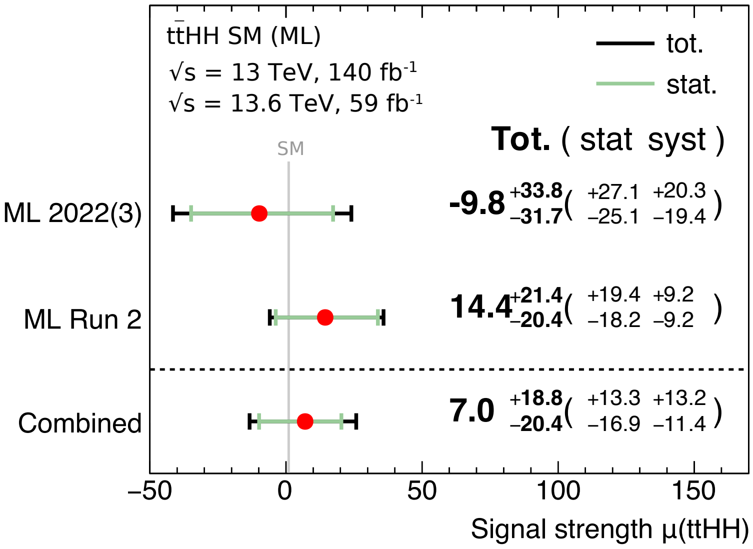

Figure 6.10: Best-fit value of the signal strength $\mu_{t\bar{t}HH}$ in the ML final state for Run 2, partial Run 3 and statistical combination. The black error bands correspond to the total uncertainty on $\mu_{t\bar{t}HH}$ and the green bands correspond to the statistical component. The SM expectation is shown with a grey vertical line at one.

At the time of writing this thesis, the charge misidentification background estimation (ECIDS) has not yet been implemented for Run 3. As a result, the Mat. Conv. and Low m_{γ^*} control regions in Run 3 suffer from significant charge misidentification contamination, which prevents a reliable determination of the corresponding normalization factors. To address this issue, these control regions are excluded from the Run 3 fits. Instead, we apply the two normalization factors derived from Run 2 to the Run 3 dataset, carrying over the associated normalization uncertainties from the Run 2 fit. Additionally, we compare the pre-fit yields in the control and signal regions between Run 2 and Run 3 (normalized to the Run 3 luminosity), and include the observed differences in quadrature with the original normalization uncertainties.

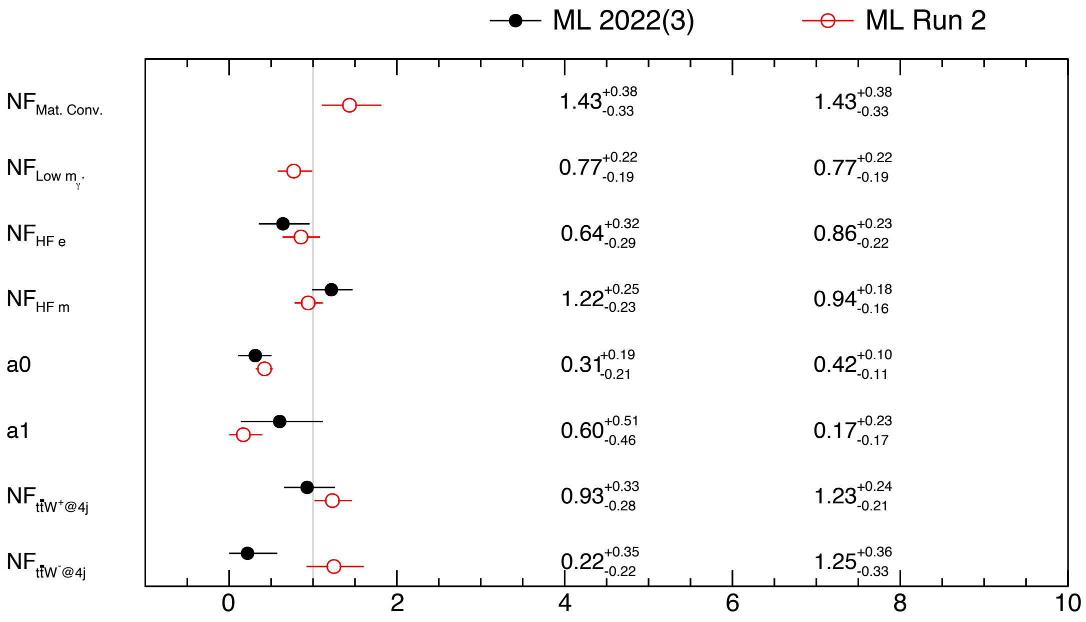

Figure 6.11: Best-fit values of all normalization factors in the ML final state for Run 2 (red) and partial Run 3 (black). The Mat. Conv. and Low m_{γ^*} normalization factors derived from Run 2 are applied to Run 3 dataset, carrying over the associated normalization uncertainties, as described in the text.

Figure 6.10 displays the best-fit signal strength values and their associated uncertainties, derived both from the combined fit and from the fits performed separately for each data-taking period. The observed best-fit signal strength from the combined fit is $\mu^{ML}_{t\bar{t}HH} = 7.0^{+18.8}_{-20.4}$ which is consistent with the SM expectation within statistical uncertainties. This combined result leads to an observed upper limit on the $t\bar{t}HH$ signal strength of 42.38 times the SM prediction at 95% confidence level, with an expected limit of 38.61 under the background-only hypothesis. The expected and observed limits are shown in Figure 6.26, where contribution of each run to the overall sensitivity is evaluated. Figure 6.11 presents the measured normalization factors for the data-driven backgrounds, shown separately for each run and for the combined result.

The pre-fit modelling in the CRs are shown for Run 2 and Run 3 data and MC from Figure 6.12 to 6.15. The post-fit modelling in the CRs and SRs are shown for Run 2 and Run 3 data and MC from Figure 6.16 to 6.20, where the signal strengths, background normalisations and all NPs are set to their best-fit values. Figure 6.21 shows a summary of the total post-fit yields in all regions. Both statistical and systematic uncertainties are included in the plots. A good agreement between data and MC predictions is achieved for all regions.

The fitted nuisance parameters are shown in Figures 6.22 and 6.23, separately for modelling uncertainties, b-tagging uncertainties and other instrumental uncertainties. Figure 6.24 presents the impact of the highest ranked uncertainties on the extracted signal strength. The most significant contributions arise from modelling uncertainties associated with the $t\bar{t}t\bar{t}$ and $t\bar{t}X$ backgrounds, as these processes dominate the SR. In particular, the cross-section and scale uncertainties of $t\bar{t}t\bar{t}$ and $t\bar{t}H$, as well as the generator choice uncertainty and shape modelling of $t\bar{t}Z$ and $t\bar{t}H$. Finally, the modelling uncertainty of $t\bar{t}H$ and $t\bar{t}Z$ events with additional b-jets are also highly ranked.

The uncertainty on the $t\bar{t}t\bar{t}$ cross-section has one of the largest impacts due to the small separation between this background and $t\bar{t}HH$ signal. The signal strength correlates with the $t\bar{t}t\bar{t}$ cross-section and scale uncertainties at around 20%. At the time of writing, the measured $t\bar{t}t\bar{t}$ cross-section is found to be significantly higher than the SM prediction. To account for this discrepancy, an additional uncertainty that encompasses both the theoretical SM prediction and the measured cross-section was incorporated into the fit as described in Section 5.9.

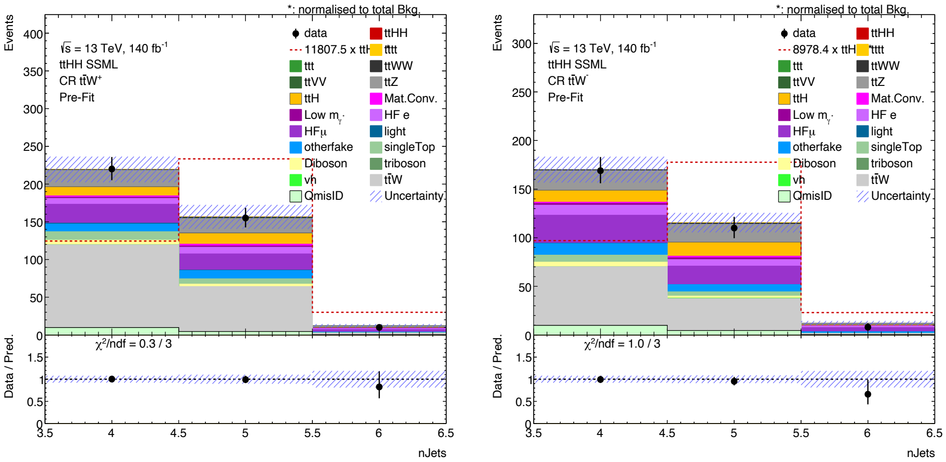

(a) CR $t\bar{t}W^{+}$+jets

(b) CR $t\bar{t}W^{-}$+jets

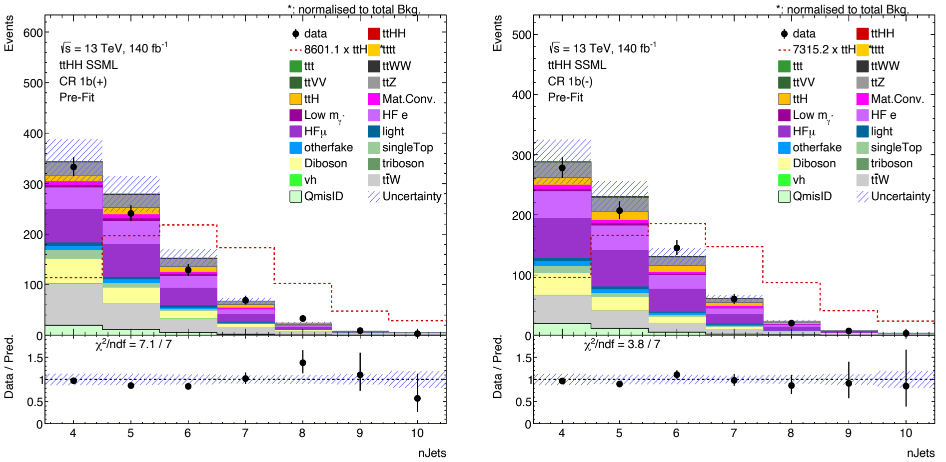

(c) CR 1b(+)

(d) CR 1b(-)

Figure 6.12: Pre-fit CRs for $t\bar{t}W$ background modelling for Run 2 in the ML final state. The observed data points are represented by black markers, while the MC expectations are displayed as stacked filled histograms. The $t\bar{t}HH$ signal is shown both overlaid on top of the fitted background and as an unfilled histogram, scaled by the integral of the MC background. The hatched band includes both statistical and systematic uncertainties. The lower panel shows the ratio of the observed data to the sum of the MC.

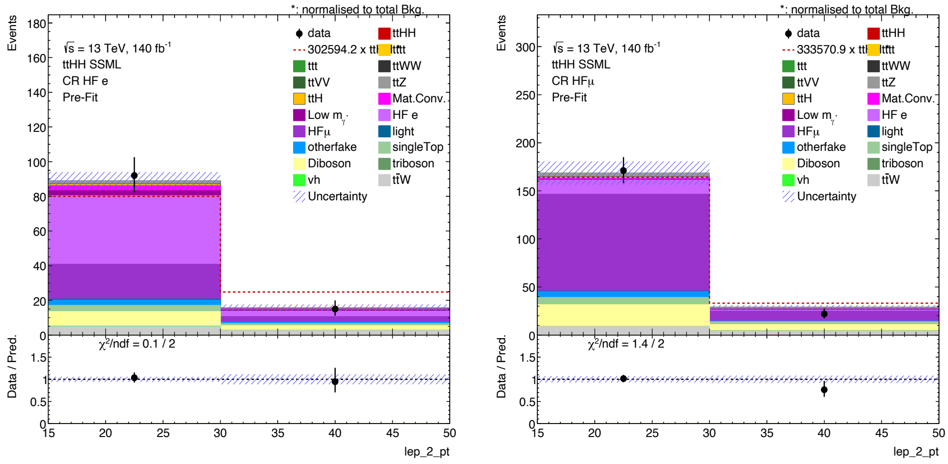

(a) CR HF e

(b) CR HF m

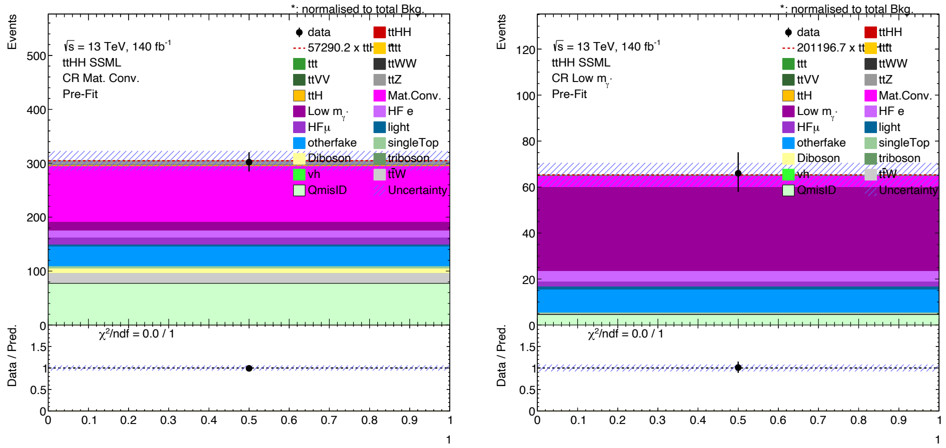

(c) CR Mat. Conv

(d) CR Low m_{γ^*}

Figure 6.13: Pre-fit CRs for backgrounds arising from fakes and non-prompt leptons for Run 2 in the ML final state. The observed data points are represented by black markers, while the MC expectations are displayed as stacked filled histograms. The $t\bar{t}HH$ signal is shown both overlaid on top of the fitted background and as an unfilled histogram, scaled by the integral of the MC background. The hatched band includes both statistical and systematic uncertainties. The lower panel shows the ratio of the observed data to the sum of the MC.

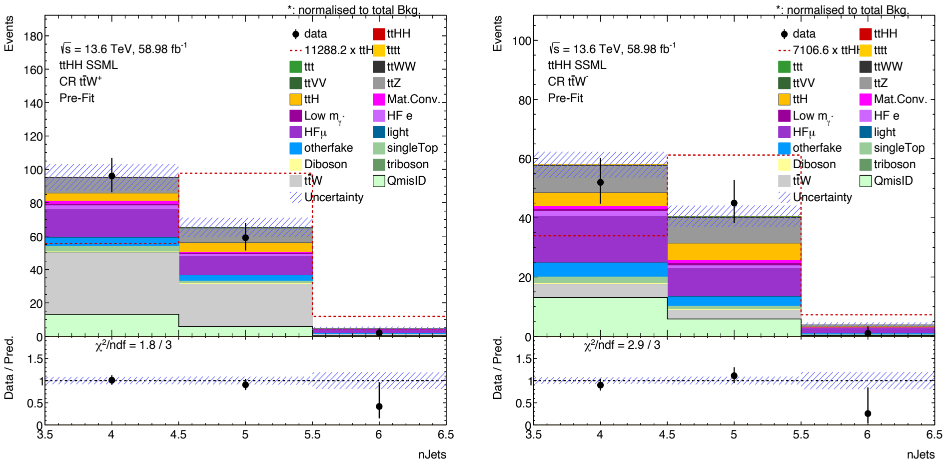

(a) CR $t\bar{t}W^{+}$+jets **(b)** CR $t\bar{t}W^{-}$+jets

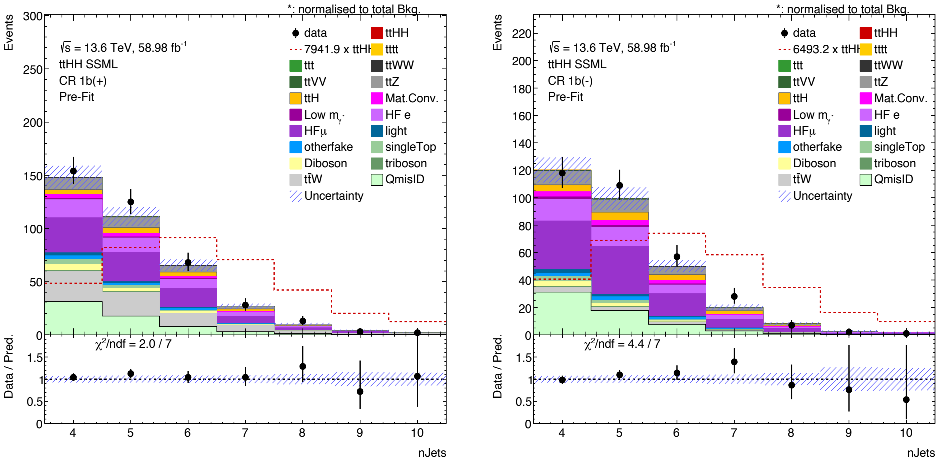

(c) CR 1b(+) **(d)** CR 1b(-)

Figure 6.14: Pre-fit CRs for $t\bar{t}W$ background modelling for Run 3 in the ML final state. The observed data points are represented by black markers, while the MC expectations are displayed as stacked filled histograms. The $t\bar{t}HH$ signal is shown both overlaid on top of the fitted background and as an unfilled histogram, scaled by the integral of the MC background. The hatched band includes both statistical and systematic uncertainties. The lower panel shows the ratio of the observed data to the sum of the MC.

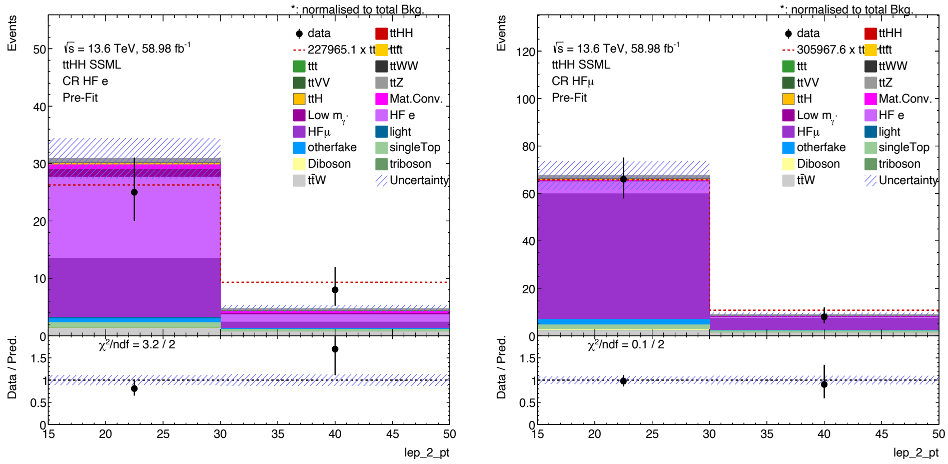

(a) CR HF e **(b)** CR HF m

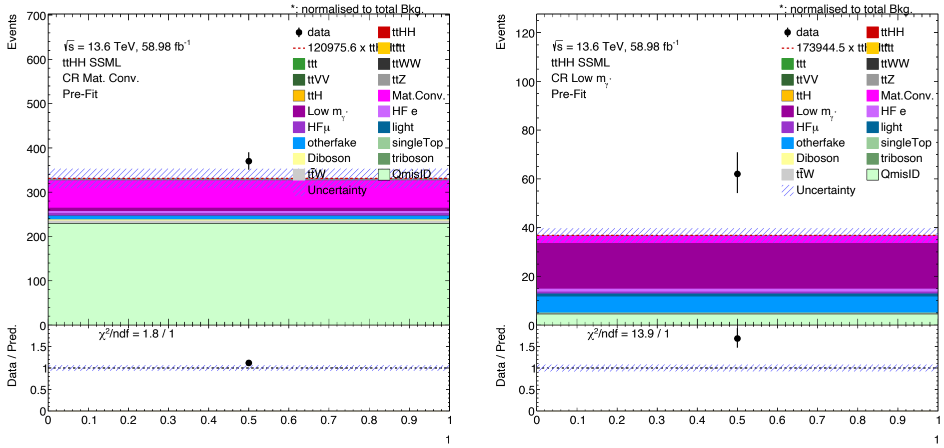

(c) CR Mat. Conv **(d)** CR Low $m_{\gamma *}$

Figure 6.15: Pre-fit CRs for backgrounds arising from fakes and non-prompt leptons for Run 3 in the ML final state. The observed data points are represented by black markers, while the MC expectations are displayed as stacked filled histograms. The $t\bar{t}HH$ signal is shown both overlaid on top of the fitted background and as an unfilled histogram, scaled by the integral of the MC background. The hatched band includes both statistical and systematic uncertainties. The lower panel shows the ratio of the observed data to the sum of the MC.

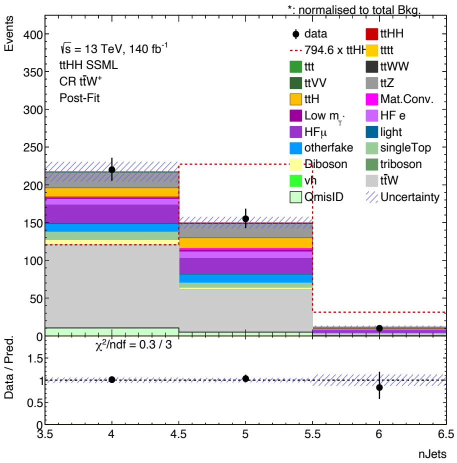

(a) CR $t\bar{t}W^{+}$+jets

(b) CR $t\bar{t}W^{-}$+jets

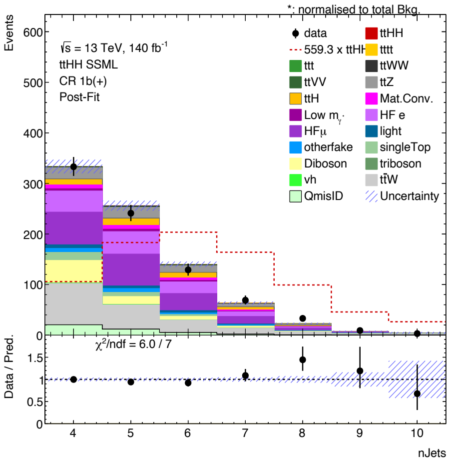

(c) CR 1b(+)

(d) CR 1b(-)

Figure 6.16: Post-fit CRs for $t\bar{t}W$ background modelling for Run 2 in the ML final state. The observed data points are represented by black markers, while the MC expectations are displayed as stacked filled histograms. The $t\bar{t}HH$ signal is shown both overlaid on top of the fitted background and as an unfilled histogram, scaled by the integral of the MC background. The hatched band includes both statistical and systematic uncertainties. The lower panel shows the ratio of the observed data to the sum of the MC.

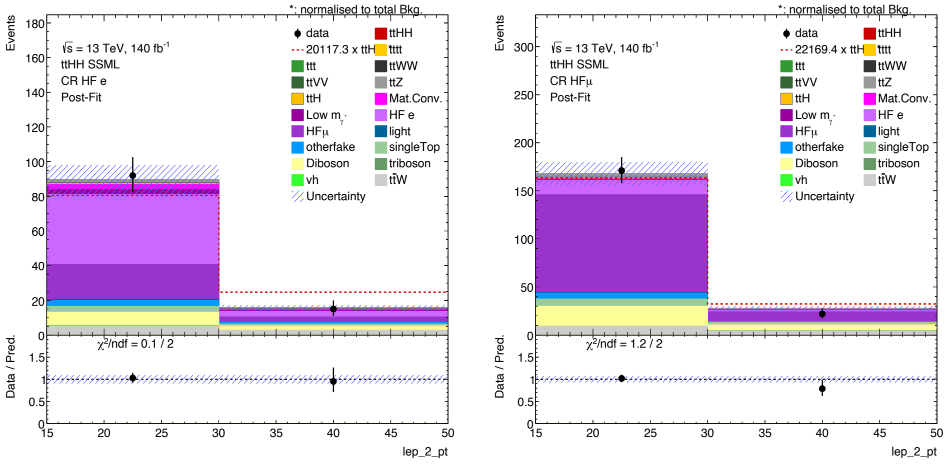

(a) CR HF e **(b)** CR HF m

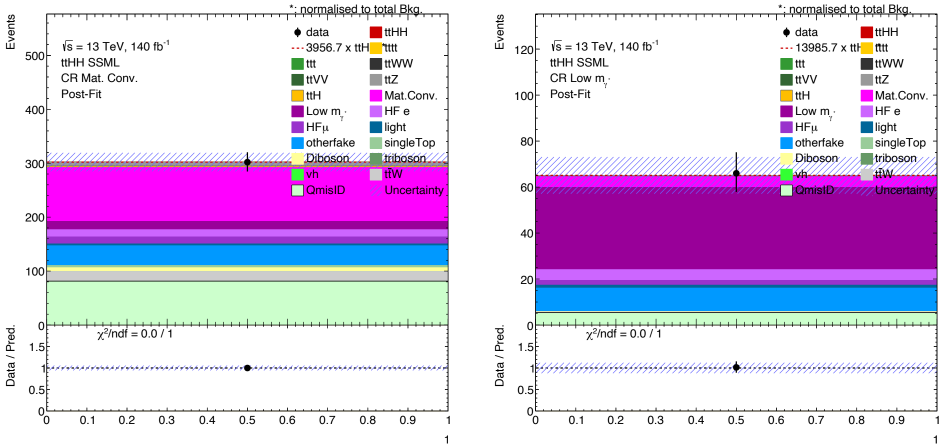

(c) CR Mat. Conv **(d)** CR Low m_{γ^*}

Figure 6.17: Post-fit CRs for backgrounds arising from fakes and non-prompt leptons for Run 2 in the ML final state. The observed data points are represented by black markers, while the MC expectations are displayed as stacked filled histograms. The $t\bar{t}HH$ signal is shown both overlaid on top of the fitted background and as an unfilled histogram, scaled by the integral of the MC background. The hatched band includes both statistical and systematic uncertainties. The lower panel shows the ratio of the observed data to the sum of the MC.

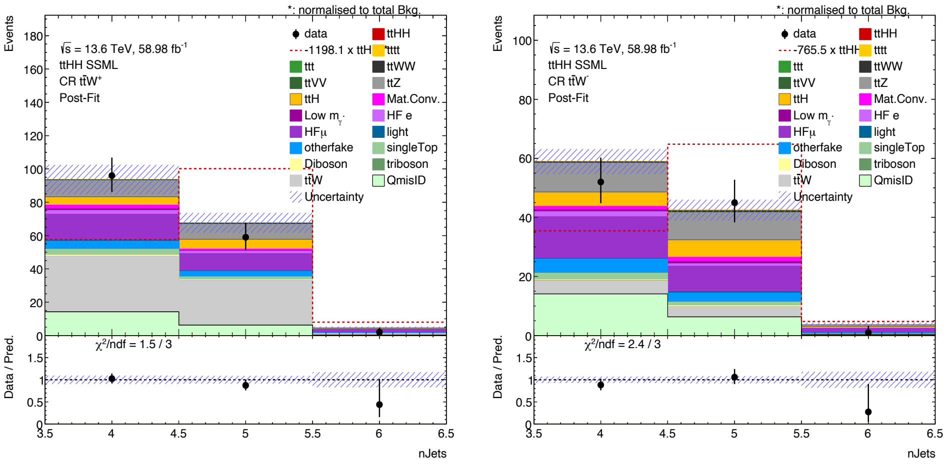

(a) CR $t\bar{t}W^{+}$+jets

(b) CR $t\bar{t}W^{-}$+jets

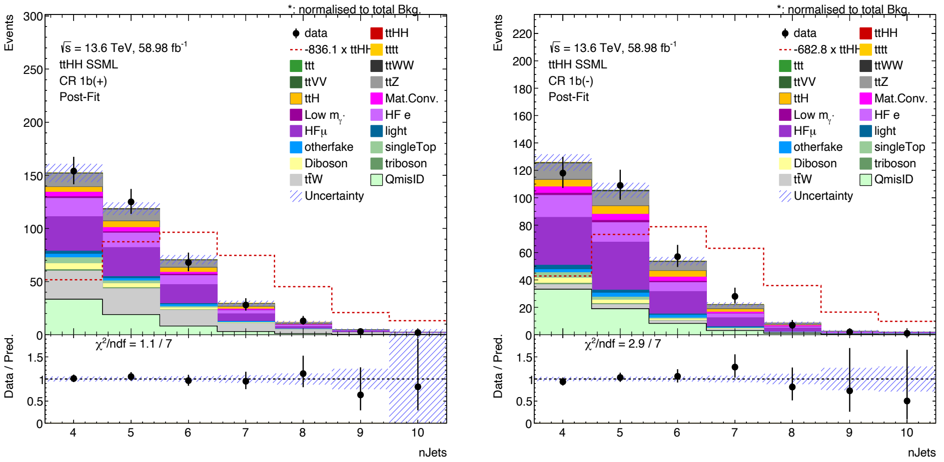

(c) CR 1b(+)

(d) CR 1b(-)

Figure 6.18: Post-fit CRs for $t\bar{t}W$ background modelling for Run 3 in the ML final state. The observed data points are represented by black markers, while the MC expectations are displayed as stacked filled histograms. The $t\bar{t}HH$ signal is shown both overlaid on top of the fitted background and as an unfilled histogram, scaled by the integral of the MC background. The hatched band includes both statistical and systematic uncertainties. The lower panel shows the ratio of the observed data to the sum of the MC.

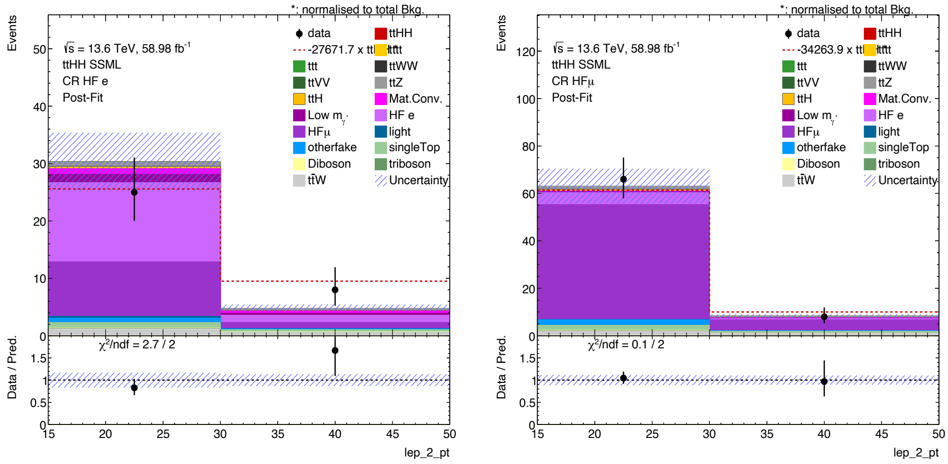

(a) CR HF e **(b)** CR HF m

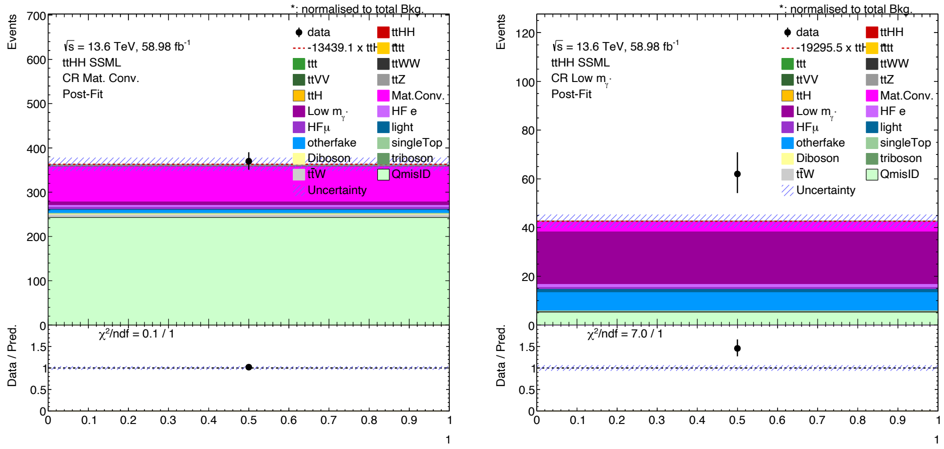

(c) CR Mat. Conv **(d)** CR Low m_{γ^*}

Figure 6.19: Post-fit CRs for backgrounds arising from fakes and non-prompt leptons for Run 2 in the ML final state. The observed data points are represented by black markers, while the MC expectations are displayed as stacked filled histograms. The $t\bar{t}HH$ signal is shown both overlaid on top of the fitted background and as an unfilled histogram, scaled by the integral of the MC background. The hatched band includes both statistical and systematic uncertainties. The lower panel shows the ratio of the observed data to the sum of the MC.

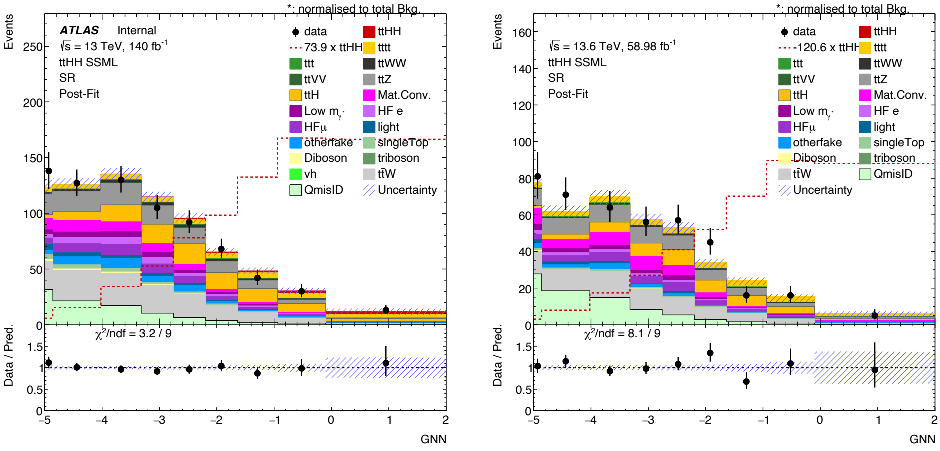

(a) Run 2 **(b)** Run 3

Figure 6.20: Post-fit SR for Run 2 (a) and Run 3 (b) in the ML final state. The MC expectations are displayed as stacked filled histograms. The $t\bar{t}HH$ signal, assuming $m_H = 125$ GeV, is overlaid on top of the fitted background, scaled by the signal strength. The signal is also shown separately as an unfilled histogram, scaled by the integral of the total MC background. The hatched band includes both statistical and systematic uncertainties.

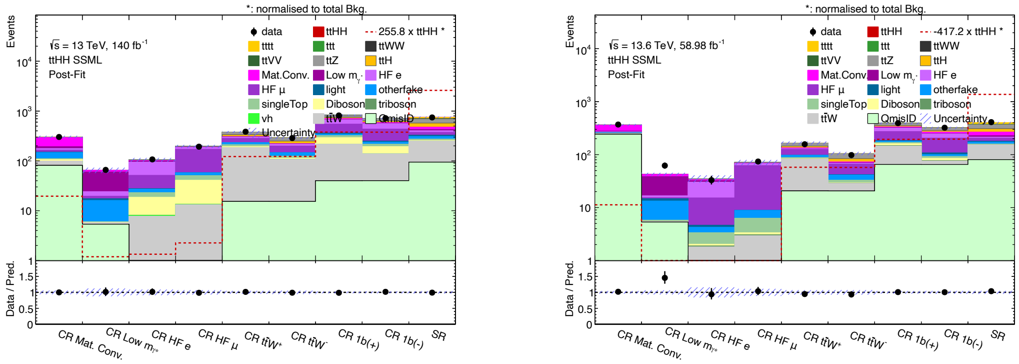

(a) Run2 **(b)** Run 3

Figure 6.21: Post-fit total yields in all ML regions included in the fit for Run 2 (a) and partial Run 3 (b). The $t\bar{t}HH$ signal is shown both overlaid on top of the fitted background and as an unfilled histogram, scaled by the integral of the MC background. The hatched band includes both statistical and systematic uncertainties. The lower panel shows the ratio of the observed data to the sum of the MC.

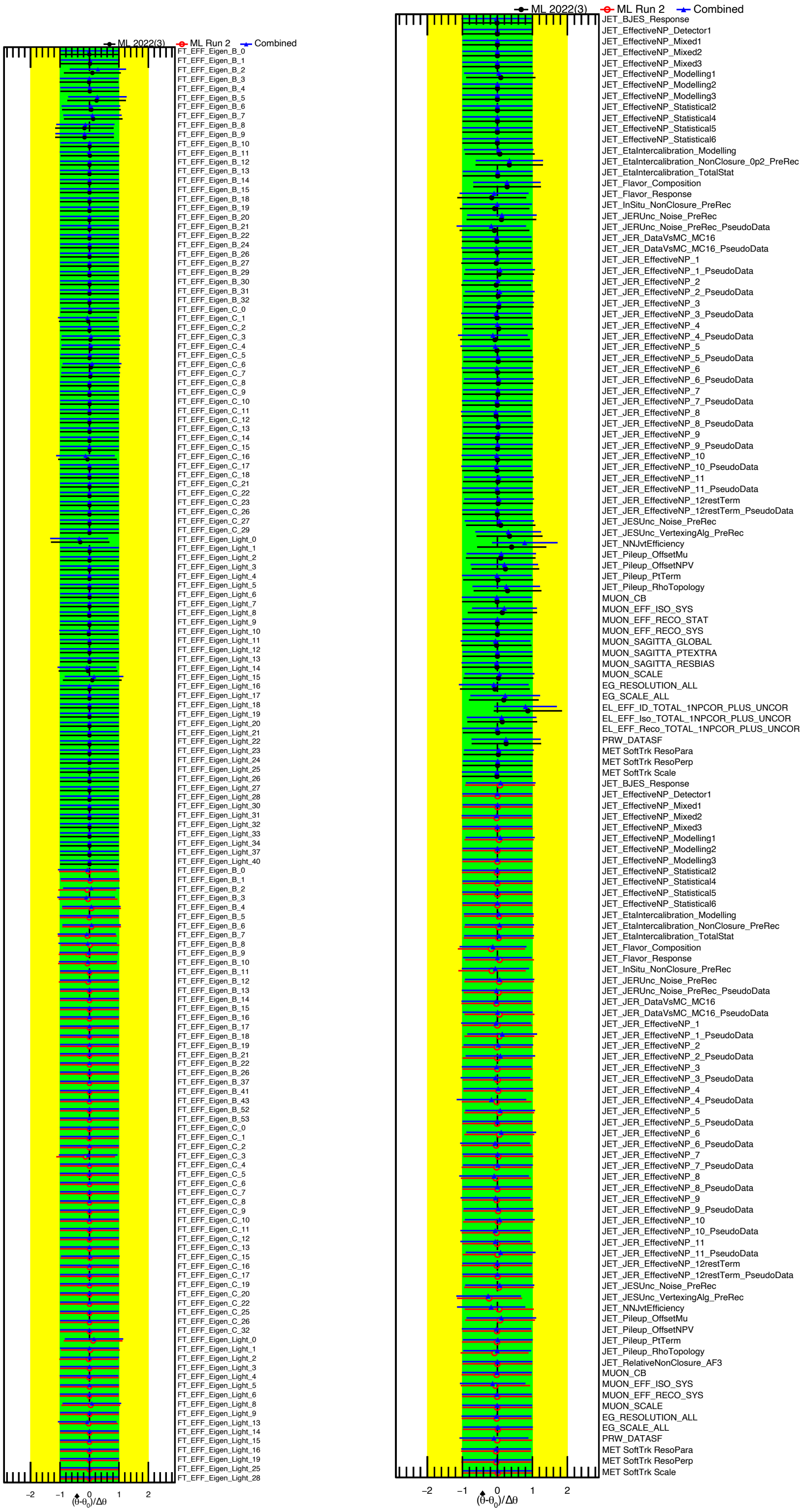

(a) *b*-tagging uncertainties

(b) Other instrumental uncertainties

Figure 6.22: Pulls and constrains from each instrumental nuisance parameter in the ML final state the fits on Run 2 and partial Run 3 dataset separately, as well as for the combined fit. Theory uncertainties are correlated between the runs, while instrumental ones are kept uncorrelated.

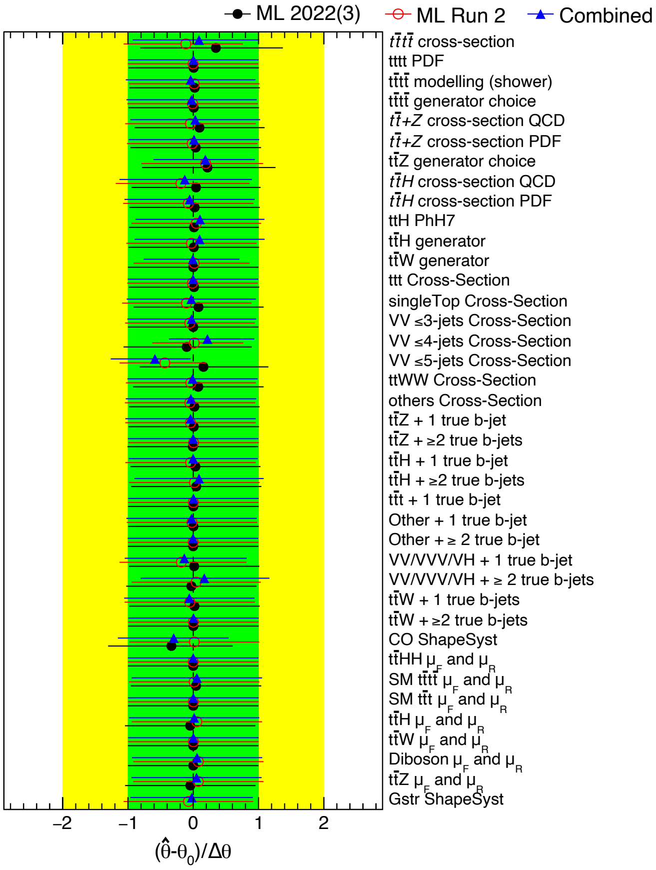

(a) Modelling uncertainties

Figure 6.23: Pulls and constrains from each MC and theoretical modelling nuisance parameter in the ML final state for the fits on Run 2 and partial Run 3 dataset separately, as well as for the combined fit. Theory uncertainties are correlated between the runs, while instrumental ones are kept uncorrelated.

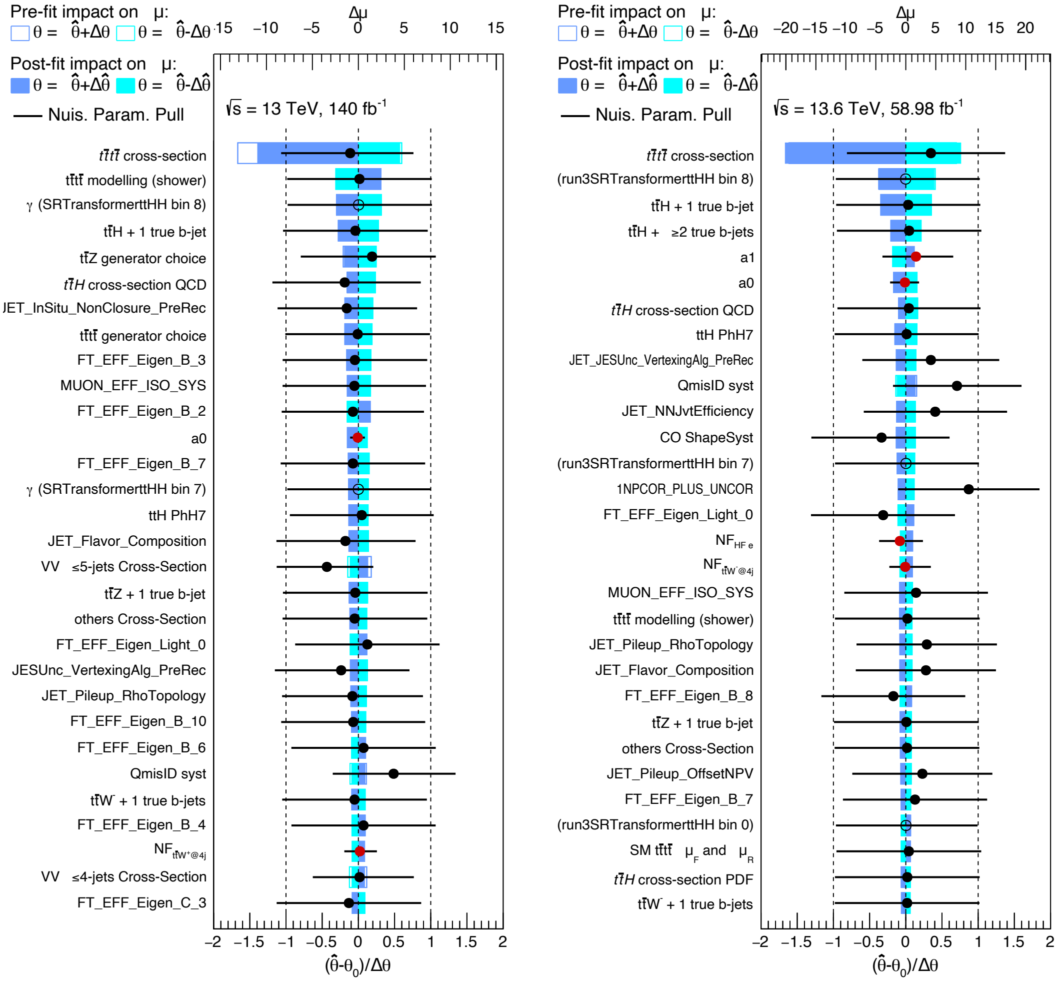

(a) Run 2 **(b)** Run 3

Figure 6.24: Ranking of the impact on the signal strength from each nuisance parameter for the plain Asimov fit for Run 2 (a) and Run 3 (b) in the ML final state. The blue rectangles represent the up (dark blue) and down (light blue) impact on μ. These impacts are computed by subtracting in quadrature the uncertainty on μ between the nominal fit and a fit where each nuisance parameter is individually changed to its pre- or post-fit values plus its uncertainties, as indicated at the upper scale. The black points and lines correspond to the pulls and post-fit uncertainties of the nuisance parameters relative to their nominal values, as indicated at the bottom scale. Only the nuisance parameters with the highest impact are displayed. The normalization factors are represented by red markers.

6.5 Combined Limits on SM $t\bar{t}HH$ Production

The $t\bar{t}HH$ search in the 1L and ML final states are combined in order to place constraints on the production cross-section. All final states are designed to be statistically orthogonal. This allows for a straightforward combination of the individual likelihoods when creating the joint likelihood and achieve stronger constraints on $t\bar{t}HH$ production. All instrumental and theoretical uncertainties are correlated between channels when possible. The theoretical uncertainties are correlated between runs, while instrumental uncertainties are decorrelated.

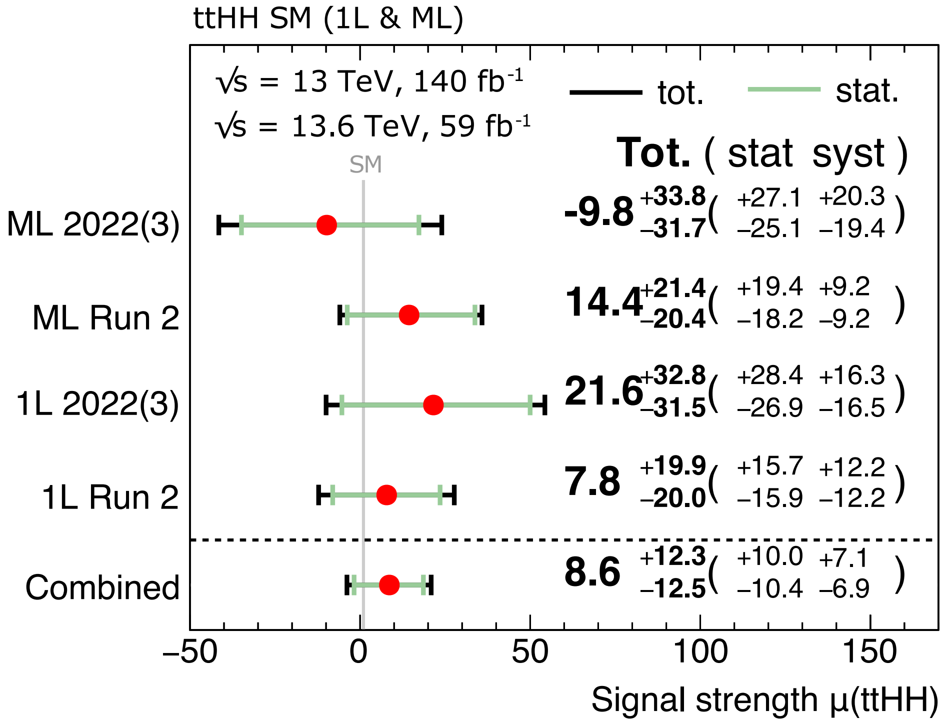

Figure 6.25: Best-fit value of the signal strength $\mu_{t\bar{t}HH}$ in each final state and each run, and statistical combination. The black error bands correspond to the total uncertainty on $\mu_{t\bar{t}HH}$ and the green bands correspond to the statistical component. The SM expectation is shown with a grey vertical line at one.

The combined value of the signal strength is determined to be:

$$\mu_{t\bar{t}HH} = 8.6^{+10.0}_{-10.4}(\mathrm{stat})^{+7.1}_{-6.9}(\mathrm{syst}). \tag{6.16}$$

The measured signal strength is compatible with the SM prediction ($\mu = 1$) within statistical uncertainties, with a p-value of 0.24. The observed statistical significance for $t\bar{t}HH$ production is 0.69σ. Figure 6.25 shows the best-fit values of the signal strength and their uncertainties for the combined fit and for each individual channel compared to SM predictions. The systematic uncertainty is dominated mostly by the uncertainties on the theoretical modelling of MC backgrounds, such as $t\bar{t}$ and $t\bar{t}t\bar{t}$. The

MC statistical uncertainty also has an important impact on the 1L channel, pointing to the need for future MC samples produced closer to the phase-space of the analysis. The combination yields an expected 95% CL upper limit on $\mu_{t\bar{t}HH}$ of 24.6 times the SM in the absence of $t\bar{t}HH$ production. The observed limit corresponds to 30.8 times the SM. The limits on the signal strength obtained from the individual final states for Run 2 and partial Run 3 and their combination are shown in Figure 6.26.

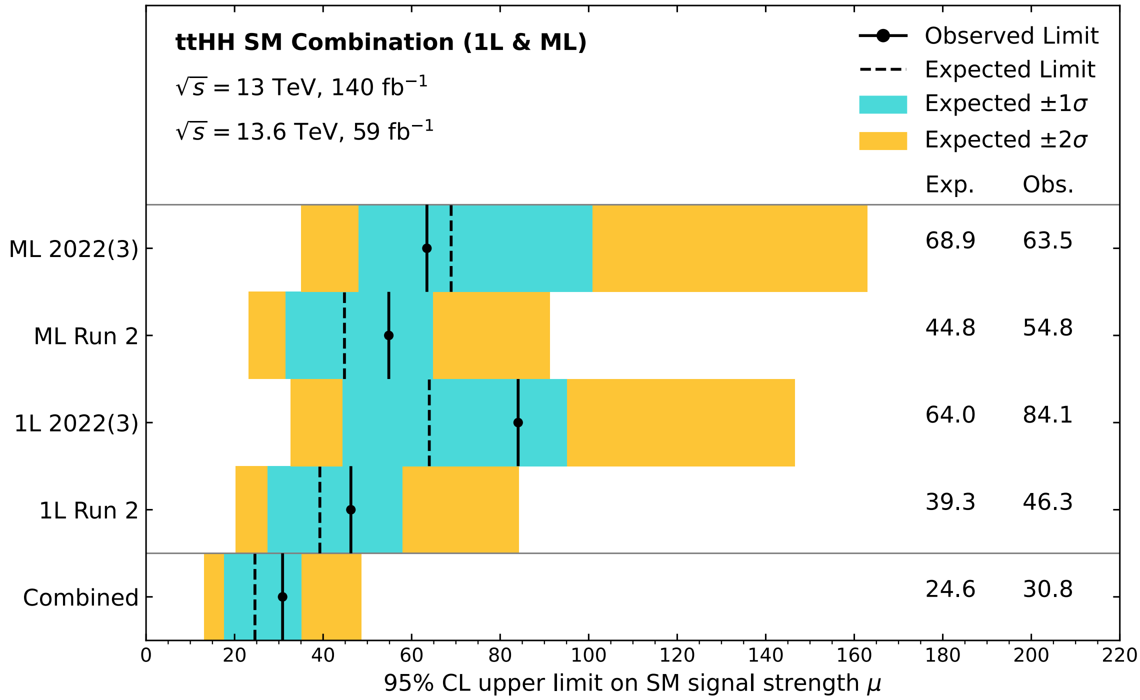

Figure 6.26: Expected and observed 95% CL upper limits on the signal strength for $t\bar{t}HH$ production from 1L and ML final states and their statistical combination. The results are shown and combined for both Run 2 and partial Run 3 datasets, corresponding to an integrated luminosity of 140 fb^{-1} and 59 fb^{-1}, respectively.

6.6 Effective Field Theory Interpretations

In the context of Effective Field Theory described in Section 3.3, the production of a Higgs boson pair can be sensitive to BSM modifications of the top-Higgs quartic interaction. As discussed in Section 3.6, the $t\bar{t}HH$ process gives direct access to this anomalous interaction. In particular, the presence of a non-zero top-Higgs quartic coupling, which is parameterised by the effective coupling modifier $c_{t\bar{t}HH}$, can alter both the rate and kinematic distributions of Higgs pair production. Figure 6.27 shows the dependence of the $t\bar{t}HH$ production cross-section on the $c_{t\bar{t}HH}$ coefficient, overlaid with a quadratic fit, while Figure 6.28 shows the impact of varying $c_{t\bar{t}HH}$ coupling on selected kinematic distributions.

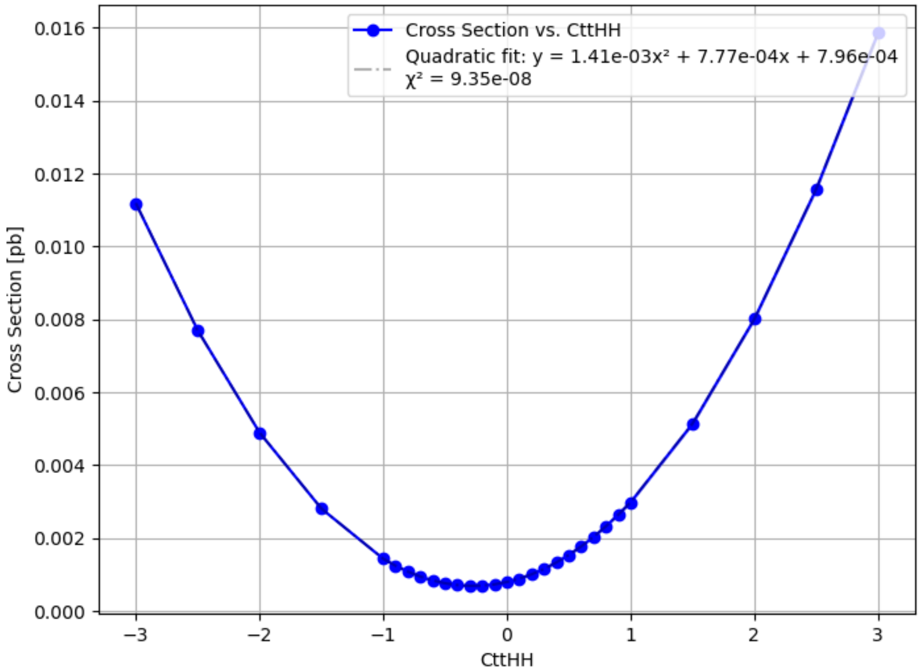

Figure 6.27: Variation of the $t\bar{t}HH$ production cross-section as a function of the top-Higgs quartic interaction $c_{t\bar{t}HH}$.

In this section, the 1L channel is used to set limits on $c_{t\bar{t}HH}$ within the EFT framework. Only the 1L final state was used for this study. Figure 6.29 shows the profile-likelihood scans for fits to the coupling modifier $c_{t\bar{t}HH}$, with all other Higgs coupling modifiers fixed to their SM values. The result is compatible with the SM prediction of $c_{t\bar{t}HH} = 0$. The observed (expected) 95% CL interval derived from the profile likelihood is $-4.77 < c_{t\bar{t}HH} < 4.32$ ($-4.04 < c_{t\bar{t}HH} < 3.58$), assuming the SM scenario.

These limits provide a first direct constraint on the $t\bar{t}HH$ interaction and contribute to a broader effort of probing the structure of the Higgs sector and possible deviations from the SM in multi-Higgs processes.

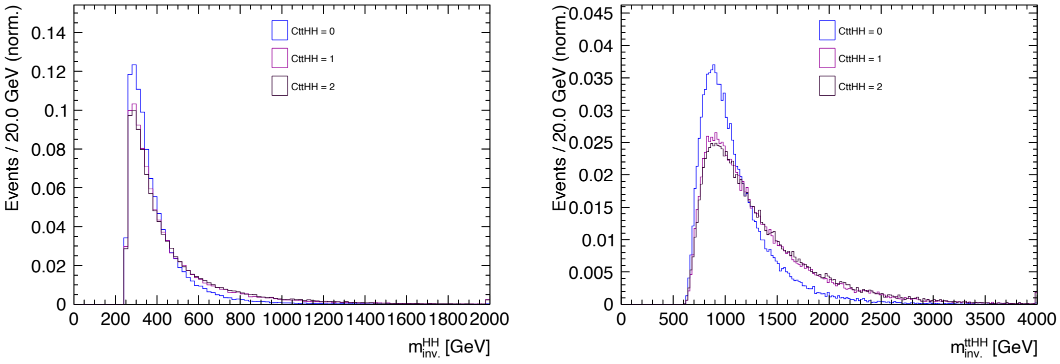

(a) Run 2 **(b)** Run 3

Figure 6.28: Comparison of the distributions of the invariant masses of the HH system (a) and the $t\bar{t}HH$ system (b) between the SM scenario ($c_{t\bar{t}HH} = 0$), and two non-zero $c_{t\bar{t}HH}$ scenarios. All distributions are normalized to 1.

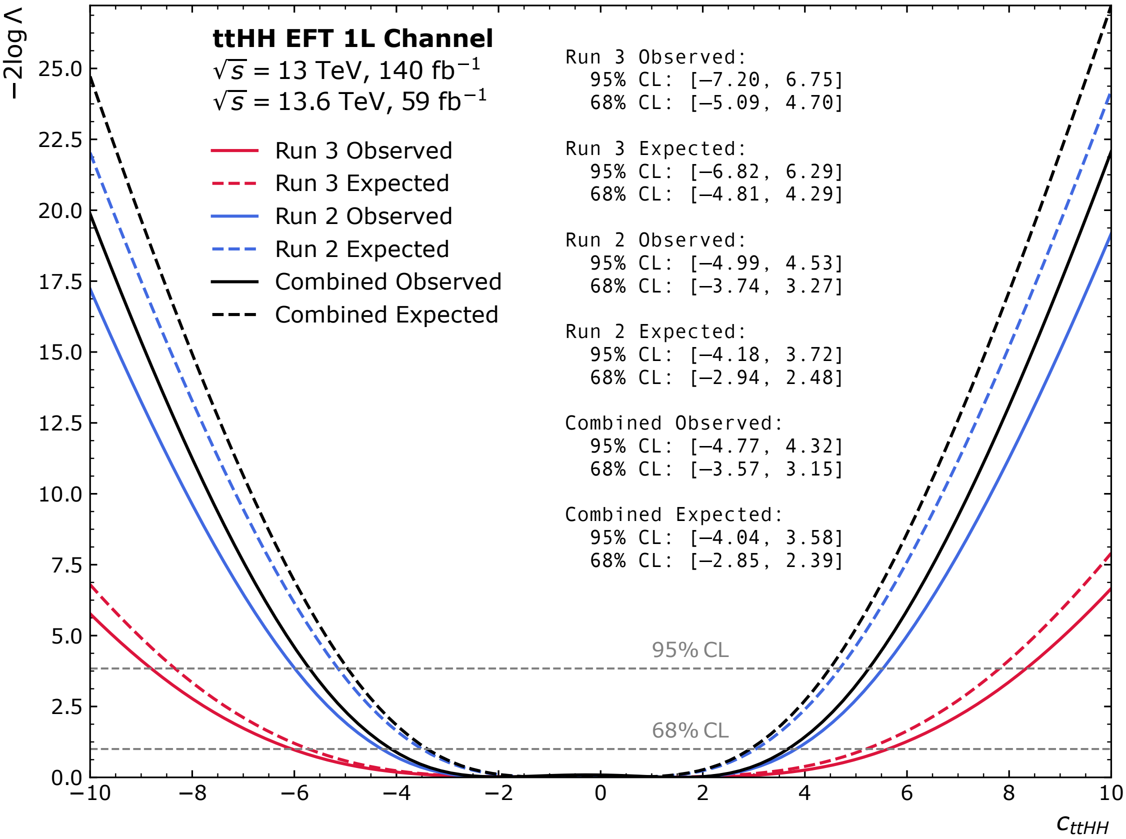

Figure 6.29: Observed and expected profile likelihood scans of $c_{t\bar{t}HH}$. The scans are performed under the framework of Higgs Effective Field Theories by varying only the top-Higgs quartic coupling modifier, while all other relevant coupling modifiers are fixed to unity.

6.7 Discussion

This chapter concludes Part II of this thesis by presenting the latest results of the search for $t\bar{t}HH$ production using the full Run 2 and partial Run 3 dataset. The work presented here is ongoing, with an expected ATLAS publication aiming to combine the multiple final states described earlier.

This analysis follows a well-defined strategy for distinct final states, each contributing with different levels of sensitivity. It targets a previously unexplored production mode in a phase-space that remains largely uncovered by ATLAS and CMS. Additionally, it is the first $t\bar{t}HH$ analysis incorporating Run 3 data. However, the search is inherently challenging due to the extremely low production rate of $t\bar{t}HH$, the high b-jet multiplicity in the targeted phase-space and the presence of large and mismodelled backgrounds in this heavy-flavour region. This makes the event reconstruction, identification and the analysis particularly complex. Nevertheless, this analysis offers a unique opportunity to probe new physics and constrain EFTs.

The results for the 1L and ML final state show no significant excess above the SM background expectation. An upper limit is set on the combined signal strength, with the observed (expected) upper limit on $\mu_{t\bar{t}HH}$ being 30.8 (24.6) times the SM prediction at 95% CL. The 1L channel is used to constrain the top-Higgs quartic coupling modifier $c_{t\bar{t}HH}$, providing sensitivity to new physics effects. The top-Higgs quartic modifier is constrained to be in the range $-4.77 < c_{t\bar{t}HH} < 4.32$ ($-4.04 < c_{t\bar{t}HH} < 3.58$ expected) at 95% CL, assuming the SM scenario.

The expected HH discovery potential for the Run 3 of LHC still remains very constrained even in the main production modes (ggF and VBF), with only the possibility of hints of evidence. The next part of this thesis will focus on the expected improvements and optimizations in track reconstruction, which will play a crucial role in enhancing the sensitivity of HH analyses at the HL-LHC in the ongoing search for new physics.

Part III

Phase-II Tracking for ITk

“Bobeira é não viver a realidade”
Cássia Eller

Motivation for Phase-II Tracking

The first part of this document has described the search for $t\bar{t}HH$ production using Run 2 and partial Run 3 datasets, stabilising expected 95% CL upper limits of about 20 times the SM expectations. In Chapter 3, the state of the art of di-Higgs production was presented, with combined upper limits of 2.4 times the SM using Run 2 dataset. Despite the significant progress in understanding the SM and the Higgs boson, several important questions remain unanswered: the self-coupling of the Higgs boson has not yet been measured, and there is still no direct evidence of new physics. Furthermore, the potential for groundbreaking discoveries when extrapolating to the expected luminosity by the end of Run 3 remains limited, where only hints of evidence for HH production might be seen.

To extend the reach of discovery, the high-energy physics community has two main options: a longer term upgrade of the accelerator to probe higher-energy regions and a shorter term option for the following decade to increase the luminosity of the accelerator to collect a significantly larger dataset. The HL-LHC is designed to achieve the latter goal, enabling the collection of up to 3000 fb^{-1} of data, thereby enhancing both the statistical sensitivity to rare phenomena and the precision of SM measurements. Projections for combined di-Higgs searches suggest a significance of 3.4σ for HH production in the baseline scenario at the HL-LHC (Section 3.4.3).

The HL-LHC will also present unprecedented challenges for the LHC experiments. The ATLAS experiment will face up to 200 simultaneous collisions per bunch crossing and extremely high radiation levels that exceed the design specifications of the current detector. To meet these demands and achieve the ambitious physics goals of the HL-LHC, the ATLAS and CMS detectors must undergo significant upgrades to maintain or improve their performance. As outlined in Section 2.3, the Phase-II upgrade includes a complete redesign of the current Inner Detector (ID) with a new all-silicon tracker, the Inner Tracker (ITk), which will be described in Section 7.1. Scheduled for installation during Long Shutdown 3, the ITk is designed to provide comparable or improved tracking performance, even in these demanding conditions, while also coping with the increased integrated radiation dose.

The ITk will bring critical performance improvements (Section 7.2): it will ensure high reconstruction efficiency for a variety of physics objects, enable precise vertex reconstruction, and enhance pile-up mitigation by extending track-to-vertex matching into the forward pseudo-rapidity region. Furthermore, it will improve tracking in dense environments and deliver good b-tagging performance, which is crucial for many physics analyses.

As for the tracking software, the expected increase in event complexity will have a major impact on particle track reconstruction: the additional hits and high track density will create a particularly challenging environment for pattern recognition and track-finding algorithms. The increased combinatorics in this high-multiplicity environment will also lead to a significant rise in CPU consumption, justifying the need for the development of more efficient and scalable tracking software. To address these challenges, ATLAS will extensively use the ACTS (A Common Tracking Software) framework (Section 7.3), which integrates new approaches and algorithms to optimize tracking performance in high-occupancy environments.

The next part of this document is dedicated to presenting the current state of the art and the ongoing efforts for Phase-II upgrade of the ATLAS track reconstruction. The improvements in tracking software and performance are expected to not only maintain the detector's capability to deliver high-precision measurements but also to open up new opportunities for discovery. With the enhanced tracking resolution, extended coverage, and improved efficiency, the HL-LHC provides a unique opportunity to push the boundaries of particle physics in the search for new physics.

7

Phase-II Tracking for ATLAS ITk Upgrade

Contents

As discussed in Section 2.3, one important goal of the ATLAS Phase-II Upgrade Program is to replace the ID with an entirely new tracking system that matches or exceeds its performance. This upgrade must ensure high reconstruction efficiency for all physics objects, improve vertex definition, enhance pile-up mitigation by extending track-to-vertex matching into the currently uncovered forward pseudorapidity region, improve tracking in dense environments and *b*-tagging performance. Additionally, the increased computational demands of reconstructing charged particle tracks at the high pile-up levels expected at the HL-LHC calls for the development of more efficient and optimised tracking algorithms to handle the higher complexity.

This chapter outlines the tracking aspects of the Phase-II Upgrade Program. It begins with a detailed overview of the new Inner Tracker (ITk) detector in Section 7.1. Section 7.2 provides a motivation for the ITk upgrade, describing the performance requirements necessary to meet the physics goals of the HL-LHC. The same section also highlights the connection between ITk improvements and their benefits for di-Higgs production searches, as well as the analysis discussed earlier in this thesis. Finally, Section 7.3 focuses on the computing challenges of the upgrade and the need for advances in algorithm development.

7.1 The Inner Tracker Detector at the HL-LHC

The ITk [217–219] was designed for an operation of 10 years at instantaneous luminosity of 7.5×10^{34} cm^{-2}s^{-1}, 25 ns between bunch crossings and an integrated luminosity of 4000 fb^{-1}. It will provide an improved granularity and an extended track-reconstruction coverage up to $|\eta| = 4$ while maintaining excellent tracking efficiency and performance. It will consists of two subsystems: a Pixel sub-detector surrounded by a Strip sub-detector. The Strip detector will have four layers in the barrel region and six disks in the end-cap region. Each of these layers is composed of double modules of strips, each with a small stereo angle between them to achieve a 3-dimensional space-point reconstruction. The Strip detector covers up to $|\eta| < 2.7$, which is complemented by the Pixel detector extending the coverage up to $|\eta| < 4$ composed of five pixel layers. The Pixel and Strip detector volumes are divided by a Pixel Support Tube (PST). Due to the intense radiation environment anticipated at the HL-LHC, the two innermost layers of the Pixel detector are designed to be easily replaceable. These two layers are separated from the outer three layers by an Inner Support Tube (IST), which allows for the easy replacement of the inner layers. The number of layers in the barrel region of the Pixel detector will be increased to five instead of four. In the forward region we have a series of coupled rings with services routed between the inner and outer pixel systems (to minimise material between measurements close to the interaction point).

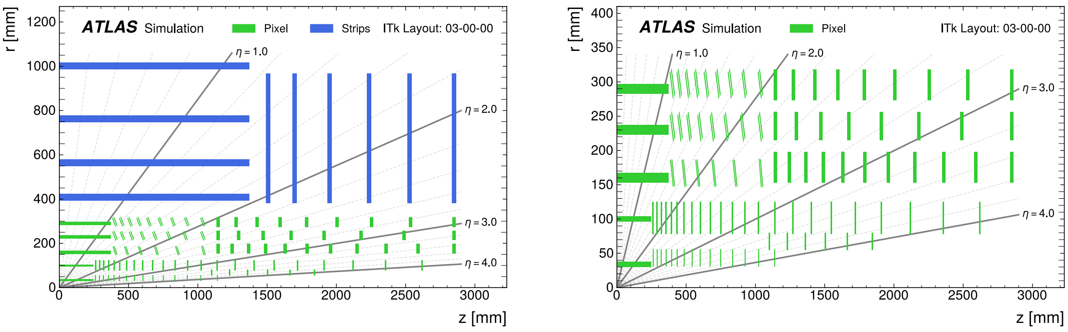

(a) **(b)**

Figure 7.1: (a) Layout of the ITk detector for the HL-LHC upgrade showing the active elements of the Pixel (blue) and Strip (green) detectors in the $r - z$ plane. (b) A zoomed-in view of the active elements of the Pixel detector. In both images, only one quadrant is shown. The horizontal axis is along the beam pipe with zero at the IP. The vertical axis is the radial distance from the IP.

The position of each layer of the ITk detector is represented in Figure 7.1 showing the Pixel and Strip sub-detectors in the $r - z$ plane. A schematic display of the full ITk layout presented in Figure 7.2 and 7.3. Figure 7.4 shows the overall anticipated count of combined pixel and strip hits along a track depending as a function of its pseudorapidity. The values are derived from simulated single-μ events with $p_T = 1$ GeV. Throughout the entire detector acceptance, at least 9 measurements are expected. Exceptions to this are rare and occur only when tracks pass through gaps between the pixel or strip barrel modules.

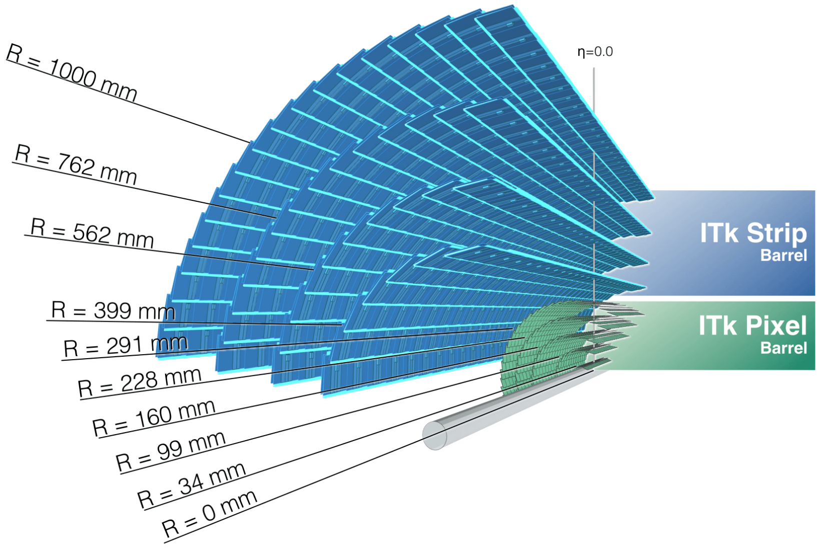

Figure 7.2: Transverse view of the ITk layout. The Pixel and Strip sub-detectors are represented in the image, together with the radial distance from the beam pipe.

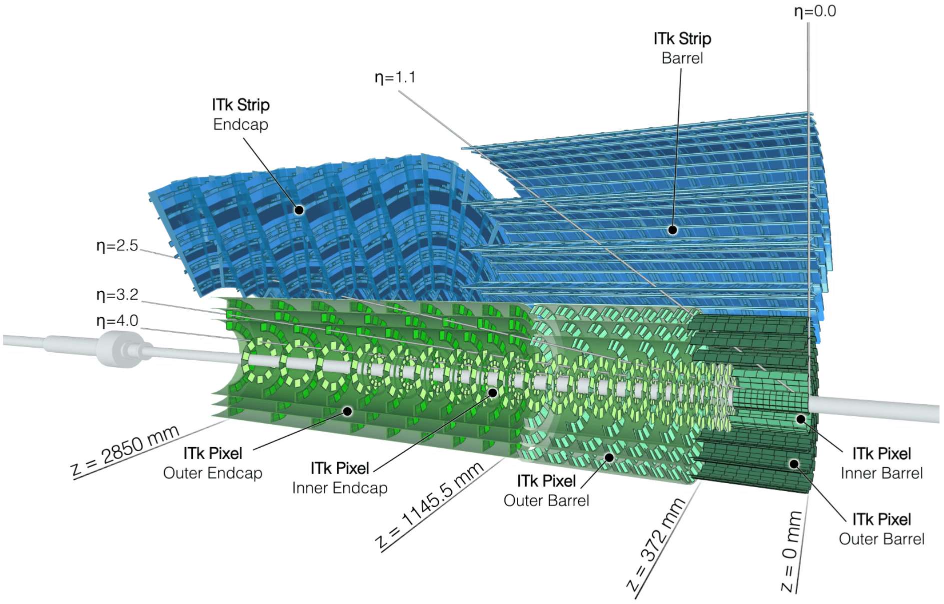

Figure 7.3: Longitudinal view of the ITk layout. The Pixel and Strip sub-detectors are represented in the image, together with their pseudorapidity coverage and the z-position from the interaction point.

7.2 Performance Requirements and Motivation for ITk

The ITk performance requirements [217, 218, 220] that motivate the replacement of the ID are justified by the physics program of Phase-II and aim at an equal or better tracking when compared to the Run-2 data taking at the LHC. This section describes

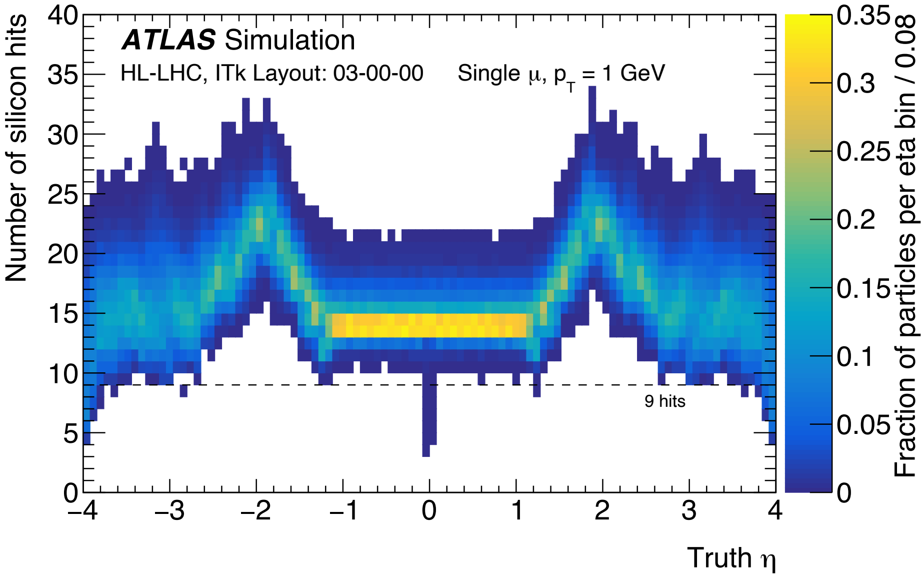

Figure 7.4: Number of combined silicon hits left by single-μ events with $p_T = 1$ GeV as a function of η for the ITk detector. Muons are generated with a uniform distribution in transverse distance from the beam line, ranging from 0 to 2 mm at fixed z positions of -15 cm, 0 cm, and 15 cm.

the performance requirements of the detector emphasizing the ITk optimisations that can benefit the HL-LHC physics motivation, such as the search for di-Higgs production.

7.2.1 Extended Pseudorapidity Coverage

The new pixel detector will extend tracking coverage up to $|\eta| = 4.0$, significantly enhancing the tracking acceptance of the ATLAS experiment compared to the current ID, which is limited to $|\eta| = 2.7$. This wider acceptance will benefit numerous analyses that rely on accurate track reconstruction in the forward regions. For instance, the VBF channel (Section 1.2.1) produces forward jets with large pseudorapidity and high di-jet invariant masses. Distinguishing these forward jets from background is essential for the VBF process, and studies have demonstrated that the significance for single Higgs production in the VBF mode can be improved with the extended tracking coverage [221].

The performance of track-to-vertex association, forward jet reconstruction, missing transverse energy resolution, and pile-up jet rejection, will all benefit substantially from the increased tracking acceptance [80, 217, 222]. These improvements will also be important for signatures involving high jet multiplicities in the final state, such as $t\bar{t}HH$ production, where jet reconstruction is critical for identifying the signal from the background.

7.2.2 *b*-Tagging Performance

The *b*-tagging performance is specifically important to many physics analyses, particularly in final states with multiple *b*-jets. Most of the HH analysis include bottom quarks in the final state ($HH \rightarrow b\bar{b}b\bar{b}$, $HH \rightarrow b\bar{b}\gamma\gamma$, $HH \rightarrow b\bar{b}\tau^+\tau^-$) and, as described in Section 3.2.2, $H \rightarrow b\bar{b}$ is the Higgs decay mode with the largest branching ratio. Improvements in *b*-tagging performance plays a crucial role in enhancing the sensitivity of these searches. This is especially relevant for the leading final state discussed in this thesis, $t\bar{t}HH(HH \rightarrow b\bar{b}b\bar{b})$ (Section 3.6), which features a signature with six *b*-jets. The overall $t\bar{t}HH$ acceptance is heavily dependent on the probability of correctly tagging each *b*-jet. Therefore, improvements in *b*-tagging efficiency will significantly impact the acceptance, scaling roughly to the sixth power in a six-b-jet region.

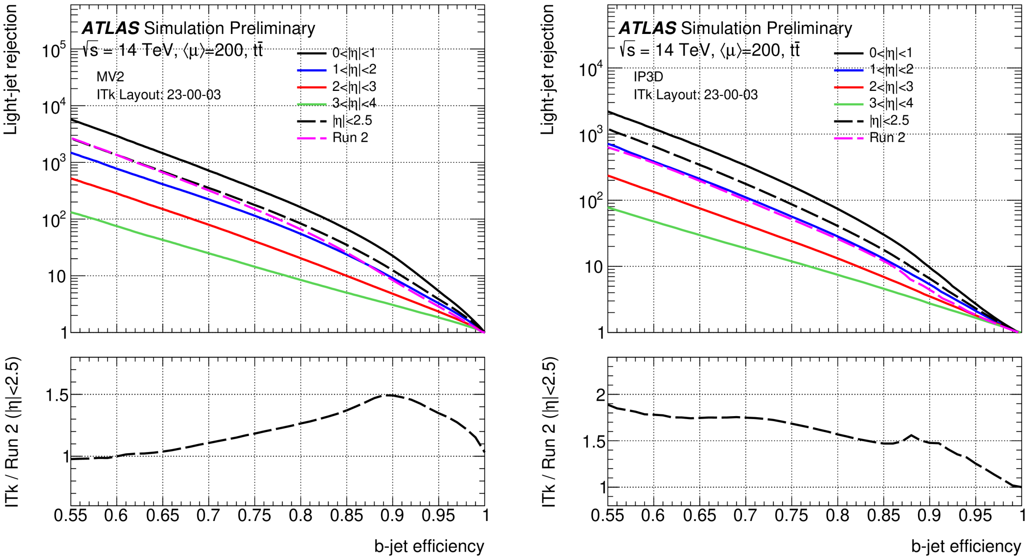

(a) **(b)**

Figure 7.5: Light-jet rejections vs *b*-tagging efficiency for the MV2 (a) and IP3D (b) tagging algorithms, evaluated in $t\bar{t}$ events with 200 pile-up events. The results are compared in different $|\eta|$ regions. For comparison, the performance obtained with the current Run-2 ID with an average pile-up of 30 is also shown [223].

The algorithms used for the identification of the *b*-jets strongly rely on track reconstruction information to identify the primary and secondary vertex of the *b*-jets and the displacement between them. The *b*-tagging performance is therefore heavily dependent on the ITk detector design and is expected to be improved over the previous Run-2 performance, resulting in an increase in acceptance that is multiplied for each *b*-quark in the final state.

Algorithms such as IP3D+SV1 [224, 225] and MV2 [226] were heavily utilised throughout Run-2. A study was performed with these algorithms to account for the new ITk shape and the HL-LHC data-taking circumstances [223]. Figure 7.5 shows the performance obtained with the new implementations of the MV2 and IP3D algorithm compared to the Run-2 performance. For example, the *b*-jet efficiency with the MV2 tagger can be raised by about 2% compared to Run-2 at a given light-jet rejection rate, leading to an increase in acceptance of up to 8% for final states with four b-quarks, such as $HH \rightarrow b\bar{b}b\bar{b}$, and up to 4% for final states with two b-quarks, such as $HH \rightarrow b\bar{b}\gamma\gamma$ and $HH \rightarrow b\bar{b}\tau^{+}\tau^{-}$.

Overall, despite of the more challenging conditions, the searches of di-Higgs production and analyses involving final states with b-quarks will strongly benefit from improvement in b-tagging performance.

7.2.3 Photon Reconstruction

When interacting with the Electromagnetic Calorimeter (ECAL) detector, both photons and electrons produce electromagnetic showers that give rise to clusters of signals in neighbouring cells. Track information is used to discriminate between them: electrons are defined to have a reconstructed track pointing towards the cluster in the calorimeter. Photons can be categorized to converted and unconverted photons. Cluster of unconverted photons are not matched to any track or a vertex, while converted photons have interacted with the tracking system and produced an electron–positron pair and have at least one matched track originating from a conversion vertex. Correctly identifying photon conversions is primarily of importance for maximizing the acceptance for events with photons in the final state, such as $HH \rightarrow b\bar{b}\gamma\gamma$, particularly where final data selections will be statistics limited.

A dedicated ITk photon conversion reconstruction and calibration may improve the photon energy resolution and increase the signal-to-background ratio for processes involving photons as it will allow for a better rejection of prompt and heavy-flavour electrons. This improvement can benefit multi-lepton (ML) final states, such as the one presented in this thesis in Chapter 5, by enhancing fake lepton rejection.

The choice of layout influences the efficiency of reconstructing converted photons, the amount of material increases the likelihood of a photon converting into an electron-positron pair. Figure 7.6 (left) illustrates the lower percentage of converted photons in the ITk when compared with the Run-2 layout. An example of the conversion reconstruction efficiency for converted photons as a function of the conversion radius is shown in Figure 7.6 (right). Up to the first ITk strip layer at $R = 400$ mm, an efficiency above 80% was achieved, and approaching 1 at smaller radius.

7.2.4 Tau Identification

τ-leptons decay mostly hadronically into charged and neutral pions, creating a signature that can contain up to three narrow jets. The identification and reconstruction of the visible part of its decay products employs information from reconstructed charged-particle tracks and clusters of energy in the calorimeter associated to τ candidates as well as high-level discriminating variables into a multivariate identification procedure, such as a BDT. So the τ identification can benefit from improvements in charged particle track reconstruction and thus benefit the $HH \rightarrow b\bar{b}\tau^{+}\tau^{-}$searches.

The τ identification efficiency expected at the HL-LLHC is represented in Figure 7.7 for one-prong τ-leptons candidates (signature containing a single charged particle track). The efficiency is reasonably constant as a function of p_T. While as a function

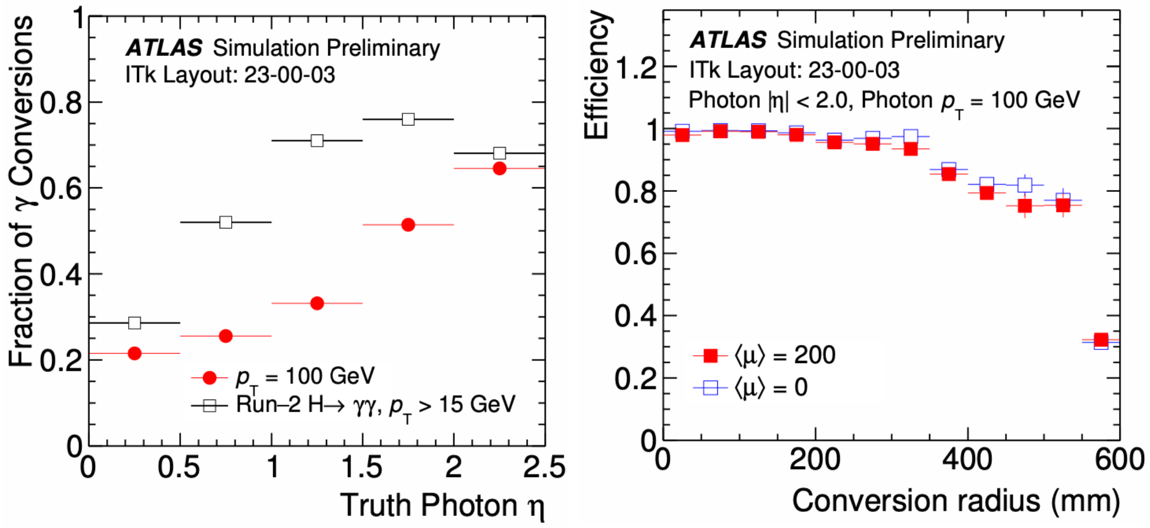

(a) **(b)**

Figure 7.6: (a) Comparison between the fraction of converted photons obtained with the ITk and Run-2 layout as a function of $|\eta|$ for photons from $H \to \gamma\gamma$ decays. (b) Reconstruction efficiency for converted photons as a function of the conversion radius [220].

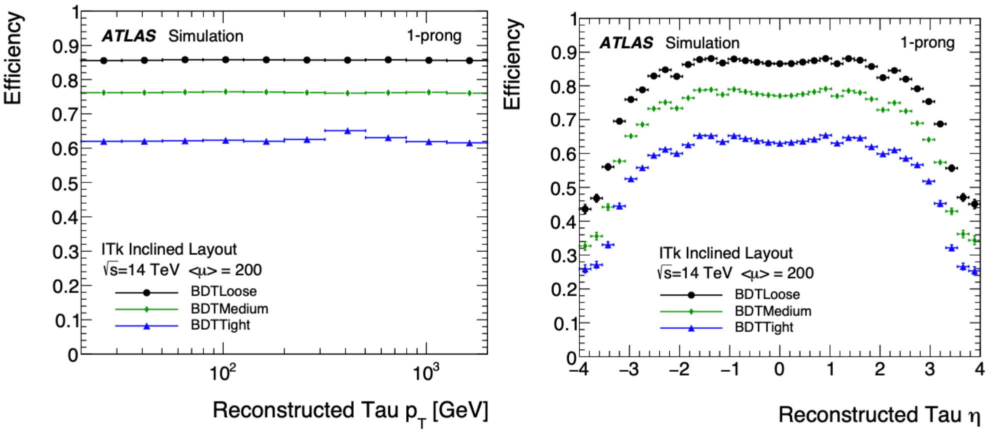

Figure 7.7: Identification efficiency of hadronic τ for 1-prong decays using the ITk layout as a function of p_T and η [217].

of η it is stable for $|\eta| < 3$ and starts to decrease after that. For three-prong candidates the efficiency starts to decrease at $|\eta| \approx 1.5$ [217]. The rejection factor for fake τ is represented in Figure 7.8 for the ITk and Run-2 layouts as a function of the τ identification efficiency. Despite the large pile-up, the identification of hadronic τ in the ITk will maintain very similar efficiencies to those obtained in Run-2, with the ITk covering a wider pseudorapidity range.

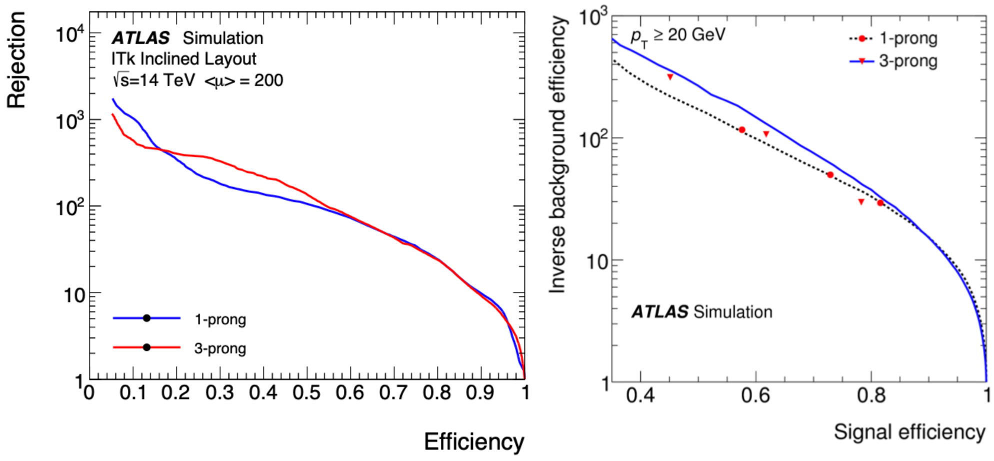

Figure 7.8: Rate of hadronic fake τ rejection (defined as the inverse of the fake rate) as a function of the τ identification efficiency for the ITk layout (left) [217] and at the beginning of Run 2 (right) [227]. The rate for 1-track and 3-track candidates are shown by two different lines. The Loose, Medium and Tight WPs are superimposed as red markers on these lines. The WPs do not exactly overlap the line because variable cuts were used to achieve a reduced p_{T}-dependency of the efficiency.

7.2.5 Vertex Reconstruction

A high efficiency in correctly associating the reconstructed objects coming from the same vertex is required, especially with the HL-LHC pile-up conditions, where the mean separation between primary vertices is expected to be approximately less than 1 mm. The vertex reconstruction with ITk will rely on the Adaptive Multi-Vertex Finder (AMVF) algorithm [228], which achieved a very robust performance for the pile-up density expected in HL-LHC and is currently used in Run 3, replacing the Iterative Vertex Finder (IVF) algorithm used in Run 2 [229].

7.3 Tracking Software and Computing for Phase-II and the ACTS project

With the unprecedentedly complex events that will be delivered by the HL-LHC at a prodigious rate, the ATLAS detector is expected to record data at 10 kHz [230], which is approximately ten times more than during previous runs. In addition, with an expected integrated luminosity of about 7 times the previous runs combined the HL-LHC will bring challenges involved in collecting, storing, reconstructing and analysing, as well as simulating Monte Carlo events in a similar volume of data. Figure 7.9a presents the projected CPU requirements for ATLAS during the HL-LHC era. Figure 7.9b shows the breakdown of processing steps for both data and MC simulation production. A significant portion of the MC samples is expected to be produced using fast simulation techniques. Without improvements to the offline event reconstruction, it could be the primary CPU consumer for the experiment.

Additionally, the effects of increased combinatorics on processes like seed generation

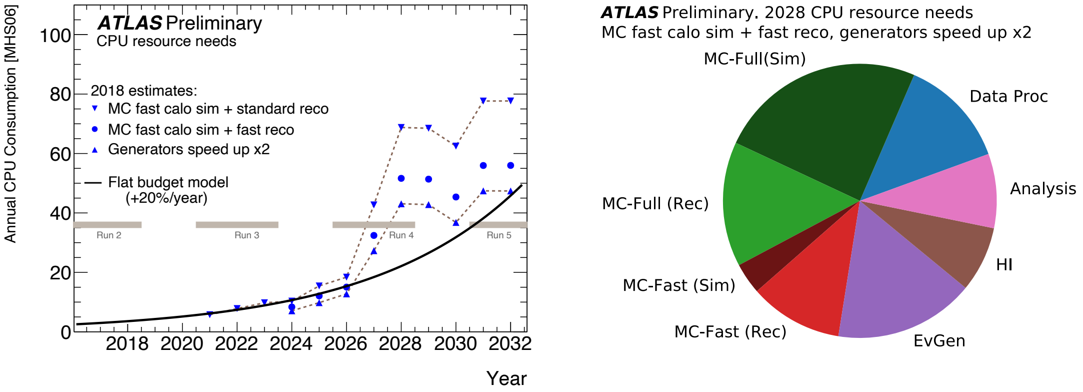

(a) **(b)**

Figure 7.9: (a): The projected ATLAS annual CPU consumption requirements for the HL-LHC, based on the current offline software. Different scenarios are shown, including the production of 75% of MC events using fast simulation, and potential improvements from fast reconstruction and faster event generators. (b): The CPU budget breakdown for 2028, the contributions are shown for a model where 75% of MC events are produced using fast simulation with standard event reconstruction [231, 232].

and track finding will significantly affect track reconstruction. Algorithmic advances will be required in order to balance CPU usage with the resources available, as well as compute and storage improvements to keep the computing costs within feasible levels. The current strategies being taken by ATLAS to meet the challenges of the HL-LHC are outlined in [230]. This section focus mainly on software updates related to the tracking of charged particles.

7.3.1 Phase-II Tracking Software and Computing Strategy

The Phase-II ITk tracker upgrade introduces a design [220] that is optimised to minimise CPU usage for track reconstruction while delivering exceptional performance under an average pile-up of 200. With enhanced granularity, consistent hit coverage, a reduced material budget within the active tracking volume, and strategically optimised sensor placement, the design aims to reduce the CPU demand for pattern recognition and track finding. The five-layer ring-shaped Pixel Detector is particularly beneficial for rapid seeding and track-finding techniques, especially at $\eta > 1$ and in the very forward region. Figure 7.10 illustrates the CPU time requirements for track reconstruction as a function of average pile-up, comparing the current ID and the upgraded ITk using an adapted version of the Run-2 tracking software. Notably, the CPU usage for the ID tracking software scales significantly after $\langle\mu\rangle = 20$. At an average pile-up of $\langle\mu\rangle = 200$, the ITk enables a substantial reduction in CPU time, which is also expected to lead to improvements in physics performance.

The silicon track finding and ambiguity resolution tracking algorithms are two most CPU-intensive components of track reconstruction. In contrast to the situation in Run-2, where seeding consumed approximately 20% of the CPU time and 80% was dedicated to road building and the combinatorial track finder, the ITk sees a significant increase

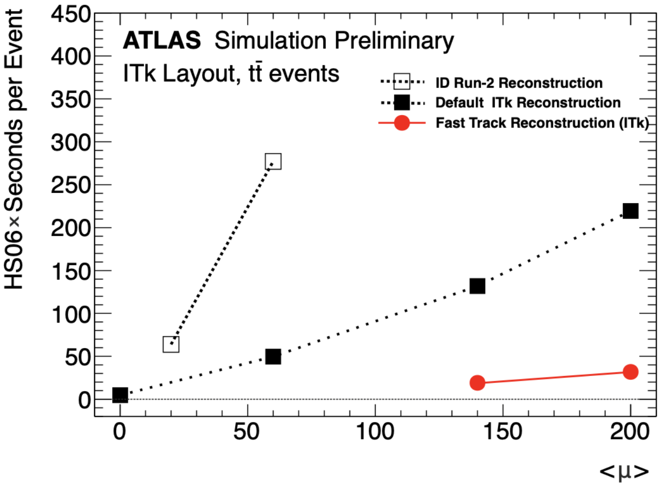

Figure 7.10: CPU time as a function of pile-up required to reconstruct $t\bar{t}$ events in the ID and ITk detectors. For the current ID, an adapted version of Run-2 reconstruction was used, while for the ITk results are shown using the Run 2 software (black line) and the fast track reconstruction (red) [232].

in the fraction of CPU time spent on seeding. For a sample with high pile-up $\langle\mu\rangle = 200$, seeding now constitutes approximately 50% of the total track-finding execution time, while the other 50% is spent on CKF. Improvements in CPU performance are expected by optimising these classical algorithmic approaches to take full advantage of the ITk detector architecture, enabling faster track reconstruction while maintaining physics performance.

Beyond achieving optimal physics and CPU performance, the software update also seeks to modernise the software infrastructure, fully leveraging current and future processing technologies. Anticipated technical performance enhancements include advancements in the Event Data Model (EDM) [233], data structures, data locality, and the optimisation of mathematical libraries and reconstruction algorithms.

Another key component of the ATLAS Phase-II reconstruction strategy is an extensive R&D program focused on enhancing all aspects of event reconstruction to further reduce CPU demands while maximising physics performance. This program encompasses a wide range of initiatives, including the application of machine learning and novel algorithmic approaches, as well as the exploration of accelerators such as GPUs for offline event reconstruction.

To achieve both CPU efficiency and exceptional physics performance in Phase-II reconstruction, ATLAS is adopting a new cross-experiment tracking software called A Common Tracking Software (ACTS) [16, 17]. The implementation, integration and validation of ACTS are detailed in Chapter 9 and 10. As a modern software framework, ACTS incorporates modern software development practices, is thoroughly documented, offers extensive opportunities for R&D and GPU capabilities. ACTS is ideally suited to meet the demands of Phase-II reconstruction. ACTS integration for Phase-II tracking is one of the main areas of work of this thesis, and will be detailed in the following Sections.

7.3.2 Fast Tracking Configuration for ITk Reconstruction

Developing fast track reconstruction strategies is essential to ensure the sustainability of computing resources as the experiment enters the HL-LHC era. ATLAS has explored potential modifications to the current track reconstruction chain, focusing on optimising execution time under Phase-II pile-up conditions, with only a minimal trade-off in physics performance [232]. This optimised strategy for fast tracking algorithms is referred to as Fast Tracking throughout this thesis. The version presented here is a prototype that serves as the foundation for the ACTS-based track reconstruction software, as the ACTS framework aims to overcome the approximations mentioned below.

To reduce duplicate tracks and false positives, tighter track selection and cluster calibration are applied during the track finding phase, reducing the number of tracks. This allows the elimination of the ambiguity resolution step, where also a final track fit is performed. Additionally, the usage of cluster calibration allows for better track parameter estimation, and the track fit is not necessary. In the default chain, about 60% of the input track candidates at $\mu = 200$ are passed to the ambiguity resolution step, and the final track fit consumes a significant portion of the total tracking time, as will be shown in Chapter 10.

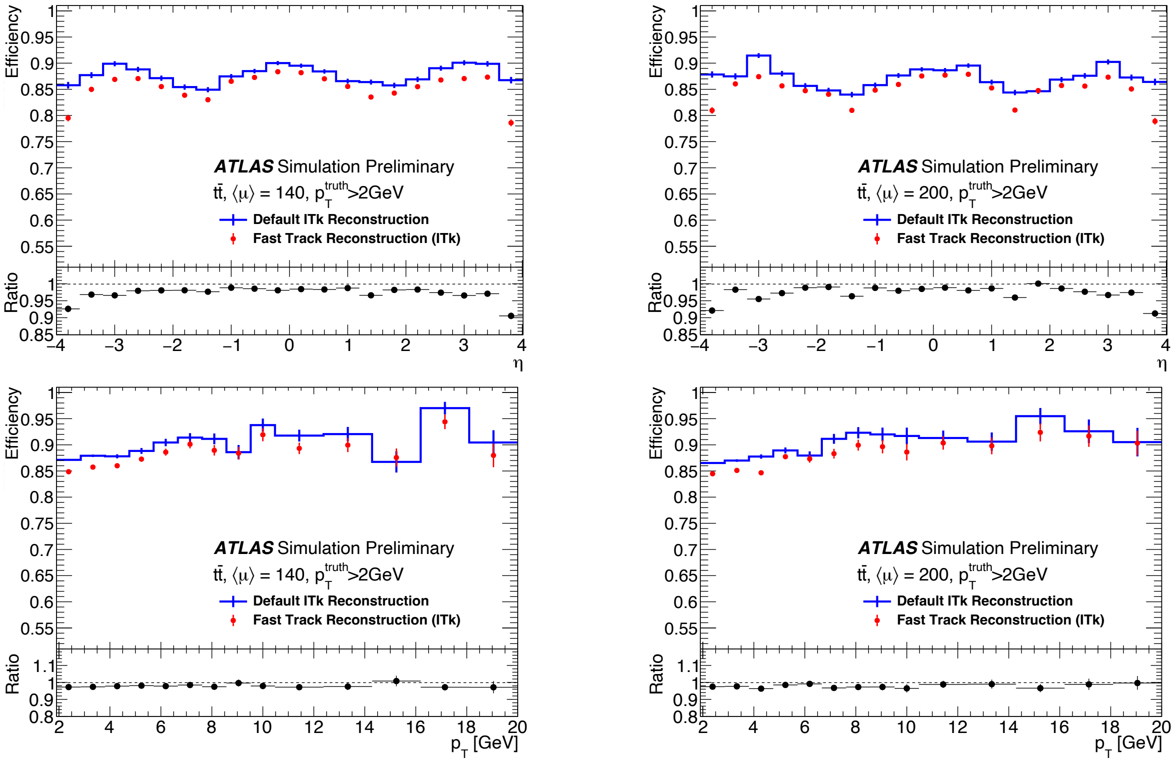

Figure 7.11: Tracking efficiency for Fast Tracking and default ITk reconstruction as a function of η (top) and p_T (bottom) using samples of $t\bar{t}$ events with $\langle\mu\rangle = 140$ (left column) and 200 (right column). A p_T threshold of 2 GeV is applied to the generated particles to avoid turn-on effects. The ratio, representing the efficiency of the Fast Tracking relative to the default reconstruction, is shown at the bottom of each plot [232].

Improvements in seed finding, achieved by tuning selection cuts to enhance the purity of the output seed collection, lead to significant CPU time reduction, as they also reduce the subsequent time needed for road building and the combinatorial track finder. The five-layer pixel detector, covering the full range of $|\eta| < 4$, allows the removal of the strip seeding step, relying solely on pixel hit combinations for seed finding. Since space points are only used for finding track seeds, and strip seeding is disabled for the Fast Tracking reconstruction, space point finding on strip clusters is no longer required, further reducing CPU usage. While this procedure is valid for reconstructing prompt tracks, additional track-finding passes using strip seeds are required to reconstruct non-prompt particles.

Additionally, cuts on the final number of hits and non-shared hits, previously applied during the Ambiguity Resolution, are now integrated into the Track Finding stage to further eliminate fake and duplicate track candidates. The p_T threshold in the central region has been increased from 900 MeV to 1 GeV, and the impact parameter cut has been set to $|z| < 150$ mm (instead of $|z| < 200$ mm), aligning with the beam interaction region length for the ITk.

For track parameter estimation, the fast Kalman Filter track fit is utilised directly, as employed by the combinatorial filter in the Track Finding algorithm, which reconstructs track candidates from pixel and strip clusters. The fast Kalman Filter now incorporates precise cluster calibrations but uses an approximate material model and cluster correction approximations, resulting in a slight loss in resolution compared to the full offline track fit.

The overall Fast Tracking reconstruction chain is approximately eight times faster than the combined default Silicon Track Finding and Ambiguity Resolution for high pile-up conditions, as shown in Figure 7.10. Figure 7.11 shows the efficiency for $t\bar{t}$ events with $\langle\mu\rangle = 140$ and 200 as a function of η and p_T for both the Fast Tracking and default ITk reconstruction. The fast reconstruction exhibits a slightly lower efficiency across all η, with no strong dependence on p_T. The efficiency is found to be independent of pile-up. Overall, while the efficiency and resolution losses with the Fast Tracking reconstruction chain are not negligible compared to the default ITk reconstruction, this approach demonstrates the potential for further improvements in the fast ITk track reconstruction chain, offering a viable replacement for the current default reconstruction in the HL-LHC era, and that classical CPU based algorithmic approaches can exploit the ITk detector design for a faster reconstruction.

8

Expected ITk Tracking Performance

Contents

The expected tracking performance of the ATLAS ITk during the HL-LHC operation phase is presented in this chapter. The evaluation is necessary for understanding how the design of the ITk detector and recent developments will perform under the demanding conditions expected in the HL-LHC. The results presented in this chapter were also published in Ref. [2].

This chapter starts with a detailed description of the ITk track reconstruction chain in Section 8.1. The tracking performance evaluation considers the current latest available layout and developments, starting with a description of the the simulated samples, detector model, digitisation simulation and selection requirements applied during the track reconstruction for the performance evaluation in Sections 8.2, 8.3, 8.4 and 8.5. A description of the metrics used for performance evaluation for seed and track reconstruction are given in Section 8.6. Finally the expected ITk seeding, tracking and vertexing performance are shown in Sections 8.7-8.10.

8.1 Track and Vertex Reconstruction for ITk Detector

After the signals produced by the interactions of the particles with the detector components are recorded. Each event undergoes an offline reconstruction. Tracking can be divided into the procedure of finding the collection of hits in the detector left by one single particle, which is called pattern recognition, and the estimation of the parameters that describe their associated trajectories, which is the track fit. This section provides a description of the sequence of algorithms composing the ITk track reconstruction [220].

8.1.1 Parameterization of Tracks

To fully describe a charged particle's trajectory in a magnetic field, a choice of parameterization has to be made, considering a certain reference frame, that can be a global frame, characterised by the detector symmetry and the solenoid magnetic field orientation, or a local frame, represented with respect to detector elements or surfaces [234].

In the global frame, the parameterization, $\vec{G} = (\vec{r}, \vec{p}, q)$, is fully described by the global position, $\vec{r} = (x,y,z)$, global momentum, $\vec{p} = (p, \phi, \theta)$, and the charge, q, of the track. While in the local frame the parameterization is given by

$$\vec{L} = (l_0, l_1, \phi, \theta, {}^{q}\!/\!{}_{p}) \,, \tag{8.1}$$

where l_0 and l_1 are the local coordinates of the 2-dimensional surface with respect to which the track quantities are represented, ϕ and θ represent the global transverse and longitudinal angle of the particle's momentum in the current position of the particle's trajectory. Figure 8.1 shows a schematic representation of the particle track parameters with respect to a local 2-dimensional surface.

A commonly used track parameterization choice is the perigee parameterization. It expresses the track's parameters at the point of closest approach in the transverse plane relative to a reference line aligned with the beam axis. The point of closest approach in the transverse plane is usually refereed to as perigee. The transverse distance from the perigee to this reference line is referred to as d_0, and the corresponding z-coordinate is z_0. These parameters, d_0 and z_0, represent the transverse and longitudinal impact parameters, respectively. By using the point of closest approach as the local position, the longitudinal and transverse impact parameters completely describe the track's location.

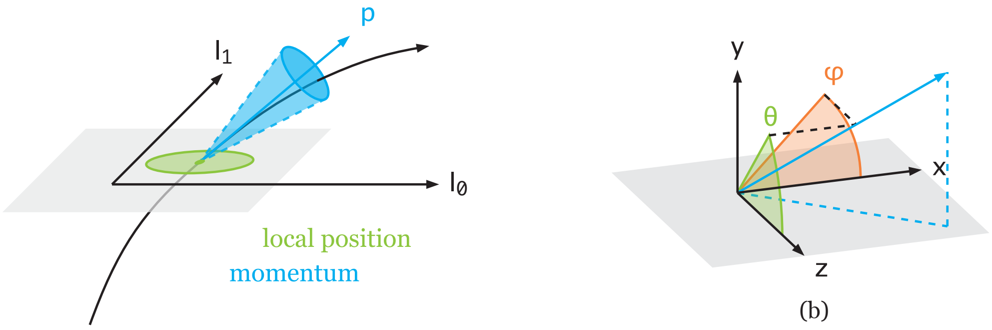

(a)

(b)

Figure 8.1: Parameterization of a particle track in relation to a two-dimensional surface. The image shows the local position and global momentum of the particle (a), along with their associated uncertainties, and the angles defining the particle's trajectory (b), with ϕ representing the angle in the transverse plane and θ representing the angle in the longitudinal plane [1, 235].

8.1.2 Data Preparation and Pattern Recognition

The first step in the implementation of the ATLAS ITk track reconstruction is data preparation and pattern recognition[1]. This involves forming clusters from the individual channels of the pixel and strips in the ITk Pixel and Strip sub-detectors when the charge deposited is above a certain threshold. These clusters are then transformed into three-dimensional representations called space-points (SP), which are used in the seeding process to combine meaningful sets of three SPs that will provide enough directional information for initiating the track finding.

8.1.2.1 Cluster Formation

In the clustering step, the raw readout data from the detector sensors are transformed into objects that represent the estimated positions where particles traversed the sensors. The raw readouts are clustered to extract an estimate of where particles intersect the sensor. This is achieved through clustering algorithms that employ the Connected Component Analysis (CCA)[236] method: neighbouring readout channels in the Pixel and Strip sub-systems with deposited charges above a certain threshold are iteratively grouped together into clusters. For the Pixel detector, clustering occurs in two dimensions, corresponding to the segmentation of its sensors, while the Strip detector is segmented in only one dimension, so the clustering algorithm operates only within this dimension.

The effective position of a cluster in silicon detectors can be estimated using different methods depending on the readout data available. When the readout is performed in a binary manner, i.e., where only the information whether the segments[2] were fired or

---

[1] Pattern recognition methods can be divided into global and local methods. In a global method all detector hits are treated equally, and all track candidates are found simultaneously. In contrast, a local method begins with a specific subset of hits used to identify initial seed candidates, which are then extended to complete the full track candidates.

[2] The word segment is used to refer to the active region of the sensor, in the form of pixels or strips.

not is recorded, the position of the cluster can be estimated by calculating the average geometric position of the segments as

$$\vec{x} = \frac{1}{N}\sum_{i=1}^{N}\vec{l}_i, \tag{8.2}$$

where N is the number of segments in the cluster, and $\vec{l}_i$ is the local position of the i-th segment.

Some readout technologies allow to have a measurement of the charge deposited in each segment. When the amount of charge collected in each segment is recorded, the position of the cluster can be estimated by calculating the analogue charge-weighted average position of the segments. This accounts for the charge collected in each segment as

$$\vec{x} = \frac{1}{\sum_{i=1}^{N} q_i}\sum_{i=1}^{N} q_i\vec{l}_i, \tag{8.3}$$

where q_i is the amount of charge measured in the i-th segment.

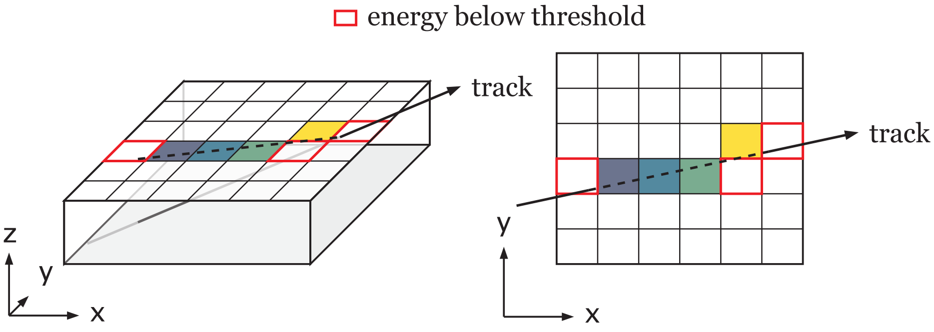

Figure 8.2: Schematic illustration of the clustering of multiple pixels into a single cluster. A particle traverses several segments and exits the sensor at the top right. The colour of each pixel cell indicates its relative position along the particle's trajectory [1, 235].

The ATLAS ITk pixel readout is able to record the time-over-threshold (ToT) [111], which, for each pixel, represents the duration for which the signal exceeds a predefined threshold. This duration is proportional to the amount of charge deposited in the segment. The ToT is used as representative charge measurement for individual channels and allows for a more precise estimate of the cluster position. The calibration process also uses an estimate of the local incident angle of the track as a function of pseudorapidity to enhance the accuracy of cluster error measurements. The ToT becomes even more important for track reconstruction in high-density environments. When the local track density increases to the point where clusters from nearby particles merge or overlap, such as in the core of boosted jets or from the decay of a boosted object, the charge distribution within these shared clusters can be used to split them apart [237].

8.1.2.2 Space-point Formation

Cluster are subsequently converted to global three-dimensional measurements called space points (SPs) by incorporating geometry information, such as the sensors' positions and orientations.

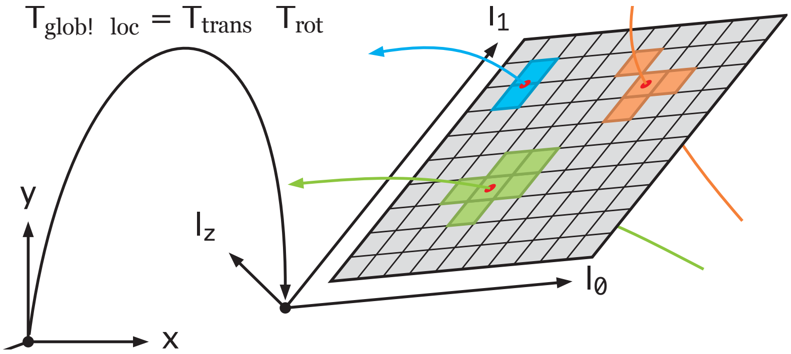

Figure 8.3: A pixel sensor and its local coordinate system with respect to the global laboratory frame. A transformation between these two systems allows for coordinate conversion. The image illustrates three tracks intersecting the sensor, along with the corresponding clusters they generate [1, 235].

For the Pixel detector, the process involves converting local two-dimensional position of clusters into global coordinates using a transformation matrix that accounts for the sensor's information, as shown in Figure 8.3. For the strip detector, measurements are initially constrained to one dimension due to the segmentation of the strips and clusters from both sides of the double-sided modules are combined to form SPs. The two-dimensional positions are derived by using paired strip modules with a stereo angle between them and the assumption that tracks point toward the interaction region. The combination of these positions are then transformed into global coordinates.

To transform the strip clusters from both sides of the module into a two-dimensional representation on one surface, some assumption about the track trajectory is needed. In the standard reconstruction setup for collisions, SPs in the strip detector are generated based on the assumption that particles originate from the point using a straight-line track model. However, this can lead to inaccuracies for particles originating from a displaced vertex or cosmic rays. The ITk SP formation algorithm builds on the original ATLAS SCT cluster-to-space-point conversion, which was designed for a smaller strip detector with a narrower gap between sensors. Modifications were made to account for the larger gap present in the ITk strip layout, ensuring accurate SP formation.

8.1.2.3 Seed Formation

Once the global SPs are produced a seed formation algorithm is applied to identifying combinations of SPs that are likely to belong to the same particle track and create seeds that will be used in the track finding. The seeding algorithm seeks to identify triplets of SPs from increasing radii, which are likely part of the same track based on geometrical and physics assumptions. Seeds are built from SPs that are entirely formed by pixel SPs (PPP) or strip SPs (SSS), starting from SSS seeds. Because of the

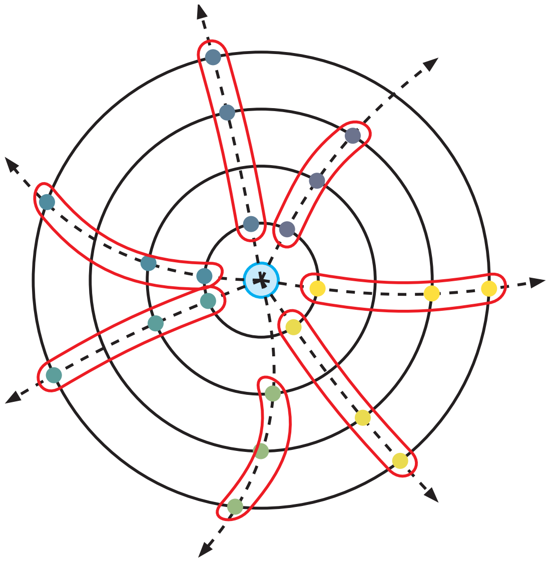

Figure 8.4: Representation of seed formation in the transverse plane for several tracks spanning four detector layers. These seeds are formed by combining hits from any three of these layers. The seed curvature must be consistent with a track originating from the centre of the detector [1, 235].

different spatial resolution of the SPs and hit density in different layers of the detector, the purity and efficiency of the PPP and SSS seeding configurations are different.

Figure 8.4 shows an illustration of seeds in the transverse plane of the detector. As shown in the figure, a triplet of measurements (i.e. the seeds) perfectly define the helical path of a charged particle in a homogeneous magnetic field. A seed defines, within close bounds, where tracking must search for additional measurements to form a track that spans the entire detector. The challenge lies in selecting the correct measurements, as any three measurements in a collision event—with potentially hundreds of thousands of measurements—can fit a helix.

Finding multiple seeds for the same particle or seeds that do not correspond to any particle increases the seeding time and, consequently, the overall tracking time. A high rate of seed duplication puts pressure on downstream ambiguity resolution methods, potentially leading to track duplicates. Several cut requirements and confirmation conditions are applied to reduce the number of seed candidates. For example, filtering the triplet combinations based on estimated momentum and impact parameters to enhance the accuracy of track identification. These cuts may specify the origin of particles, the momentum range of particles to be found, or otherwise limit the combinations of measurements used for seed creation. With the addition of this *seed filter*, a reduction in the number of fake seeds is observed in ATLAS, resulting in fewer fake tracks. The process of track reconstruction becomes more computationally efficient, enabling precise identification and analysis of particle tracks within complex detector environments. The seeds that pass this set of constraints undergo further selection, where an additional confirmation SPs are required in the projected direction of the track seed. Only a certain number of selected high quality seeds proceed to the combinatorial track finding stage.

The ACTS implementation of the seeding algorithm employed by ATLAS for the ITk detector is one of the main topics of this thesis and will be described in deep details in Section 9.2.

8.1.3 Track Finding

The ATLAS ITk Track Finding uses seeds to define a search road and applies a Combinatorial Kalman Filter to find track candidates compatible with the initial seed direction. Each track candidate is handled separately, beginning with a seed and searching for additional measurements for that candidate. In practical applications, a particle's trajectory is influenced by random perturbations due to material interactions, which must be considered in the track finding process.

Two iterations of the Track Finding are performed sequentially, initiated by SSS seeds and PPP seeds, respectively, in order to improve the overall track reconstruction efficiency. Seeds are skipped if they are constructed from clusters already associated with a track candidate. The compatibility of clusters on the detector modules within the search road is tested for a given track hypothesis. First, the Track Finding is run assuming a pion hypothesis to account for the energy loss from particle's interactions with the detector layers. If a seed cannot be propagated to a complete track but is compatible with an electromagnetic cluster reconstructed in the calorimeter, an electron hypothesis is used, where up to 30% energy loss through bremsstrahlung is accounted at each crossing of a detector material layer.

During Track Finding, multiple scattering and deterministic energy loss are approximately taken into account with a simplified material modelling and the magnetic field to improve computing performance. It does not include calibrations for the measurements, which is later on used in the full track fitting using a Global χ^2 during the Ambiguity Solver step, with a more refined material model and magnetic field. The Ambiguity Solver will be described in the next section.

The result of this process is a collection of track candidates. Those lacking sufficient clusters are discarded. Maximising track candidate efficiency is crucial since candidates missed at the Track Finding cannot be recovered later.

8.1.4 Ambiguity Resolution

Due to the large number of measurements and the large combinatorial nature of the track finding procedure discussed above, there are often many possible ways to combine these measurements, resulting in a large number of fake track candidates, i.e. candidates that do not correspond to a real trajectory of a particle. Measurements can also be shared between track candidates. The Ambiguity Solver [112, 239] is used to addresses overlaps between track candidates and eliminates incorrect combinations of clusters mis-assigned to track candidates. Throughout this process, the hit content and the track fit quality are used to evaluate and rank the candidates. Only the top-ranking candidates are retained to improve the overall quality of the final track collections. The ambiguity resolution process becomes an even more important step for tracking in dense environments.

At this stage, tracks are fitted with a global χ^2-minimisation technique incorporating precise information about the tracker material model and magnetic field. Missing measurements where a track is expected to intersect an active sensor (i.e. holes), are assessed based on the track trajectory, along with details about the detector geometry and its status. Tracks are then ranked according to their hit content and various quality criteria to evaluate track candidates and determine the track score. A larger number of hits increases the score since longer series of compatible hits have a lower probability to be produced from random combinations. Conversely, holes in expected sensor locations reduce the score. Hits from different detector subsystems are assigned different weights based on their intrinsic resolution and expected multiplicity. The track candidate's overall χ^2 value also influences the score, with higher χ^2 values leading to penalties. The logarithm of the momentum of the track candidate is also considered to prioritise tracks with high momentum and suppress low p_T tracks, which typically come from incorrectly assigned clusters. Finally, duplication is discouraged by penalising candidates sharing hits with other candidates.

Ambiguities between multiple track candidates are resolved by comparing their scores, with the highest-scoring track being selected. The ambiguity resolution process suppress fake tracks, while produces a set of track candidates with an enhanced fraction of true particle tracks. These refined candidates are then used to extract parameter estimates and for subsequent reconstruction tasks.

In a high track density environment, such as the core of high-p_{T} jets, the separation between different charged particles is close to the detector granularity. In such cases, charge depositions from different particles can overlap and be reconstructed as single merged clusters. Tracks that share clusters are penalised in the Ambiguity Solver stage and they may consequently fail the quality criteria and be rejected. The identification of merged clusters is thus crucial for ensuring high track reconstruction performance in dense environments, as it has a strong impact on the reconstruction efficiency and the precision of the reconstructed track parameters. To optimise the tracking performance in this regime in Run 1–3, ATLAS uses machine-learning-based algorithms dedicated to distinguishing clusters compatible with deposits from a single or multiple charged particles [112, 237]. This identification is performed only when a cluster is used by multiple tracks.

8.1.5 Vertex Reconstruction

To fully understand the kinematics of the physics processes, reconstructed tracks are utilised to reconstruct interaction vertices in the event. Each event involves interactions of protons during the bunch crossing that results in two types of interaction vertices: primary vertices and secondary vertices. The primary vertex arises from the primary interactions of the colliding particles along the beam line. A single event produces multiple primary vertices. Secondary vertices, on the other hand, are produced from processes such as photon conversions or decays of long-lived particles, such as B-hadrons, and are significantly displaced from the primary vertex. Reconstructing secondary vertices is crucial for identifying objects such as b-jets originating from b-quarks, as detailed in Section 4.3.3. A primary vertex can be categorised as a hard-scatter vertex, representing the vertex of a physically significant process accepted by the trigger. The primary vertex associated with the hard-scatter event is typically identified as the one with the highest sum of squared transverse momenta of the tracks originating from it. If not classified as hard-scatter, the primary vertex is considered a pile-up vertex, which results from additional primary minimum-bias collisions that occur alongside the physics process of interest and make the reconstruction more complex. These amount of pile-up vertices increase with high instantaneous luminosities. Figure 8.5 the hard-scatter, pile-up and secondary vertices in one *pp* collision.

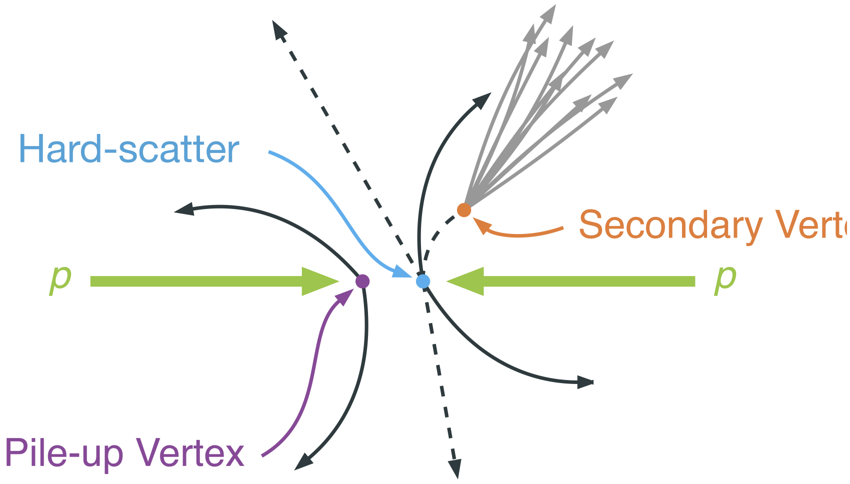

Figure 8.5: Representation possible vertices that are present in a *pp* collision. The hard-scatter, pile-up and secondary vertices are represented [1, 235].

In high pile-up environments with a high density of primary vertices, vertex reconstruction becomes particularly challenging. Vertex finding algorithms involve vertex seeding and vertex fitting. The vertex seeding provides an initial estimate of the vertex position, called vertex seed. In ATLAS, primary vertices are assumed to align with the beam spot, and an algorithm that clusters tracks along the z-axis using a histogram approach is used to identify primary vertex seeds. With this approach, only tracks that are assumed to come from the IP are taken into account and the secondary vertices are removed. For the high pile-up conditions, the ITk vertex reconstruction uses the Adaptive Multi-Vertex Finder (AMVF) algorithm [228], as mentioned in Section 7.2.5

The AMVF employs a vertex seed finder to detect possible vertex candidates along the beam-line in the z axis. In an iterative procedure, a new vertex candidate is identified and added to a collection of potential vertices. Tracks that are within a certain z-window of this candidate are associated with it. Each vertex undergoes a refitting process using the adaptive Kalman filter multi-vertex fitting technique, which allows each track to potentially contribute to more than one vertex. During this process, tracks that receive a low adaptive weight in the fit are excluded from the vertex fit they contribute to. A vertex candidate is preserved if it fulfils specific criteria: it is associated with more than two tracks, its cumulative adaptive weights are sufficiently high, and it is separated by more than three σ from any other vertex candidate. This procedure continues until no further vertex candidates are identified or a predefined number of iterations is completed. Among all reconstructed vertices, the hard-scatter vertex, is chosen as the primary vertex with the highest $\sum p_T^2$ of its associated tracks.

8.2 Simulated Samples

To evaluate the performance of the generic track reconstruction, single particle (muon, electron and pion) samples were simulated with $|\eta| < 4.0$ and a fixed transverse momentum of 2, 10, or 100 GeV. To replicate the expected HL-LHC beam spot dimensions and positions, the particle origin positions were generated based on a Gaussian distribution with a width of 50 mm centred at $z = 0$ in the longitudinal direction, while a width of 12 μm was used for the transverse direction.

In addition, a $t\bar{t}$ sample at $\sqrt{s} = 14$ TeV was simulated to assess the performance of the track and vertex reconstruction, with different pile-up ranges around 60, 140 and 200. For comparisons with the Run 3 detector performance, a $t\bar{t}$ sample at $\sqrt{s} = 13.6$ TeV and a flat pile-up profile between 0 and 80 is used. The production of $t\bar{t}$ events was modelled using the POWHEG BOX v2 [145–148] generator at NLO with the NNPDF3.0NLO [150] PDF set and the h_{damp} parameter set to $1.5\, m_{\text{top}}$ [160]. The events were interfaced to PYTHIA 8.230 [151] to model the parton shower, hadronisation, and underlying event, with parameters set according to the A14 tune [154] and using the NNPDF2.3LO set of PDFs [175]. The decays of bottom and charm hadrons were performed by EVTGEN 1.6.0 [179]. Only $t\bar{t}$ events with a single leptonic W-boson decay have been considered.

Finally, a Z' sample with a mass of $m_{Z'} = 4$ TeV decaying with roughly equal probabilities into b-, c-, and light-quark jets is used to study tracking performance in the core of high-p_{T} jets. The sample is constructed so that the resulting jet p_{T} spectrum is roughly flat up to 5 TeV. Z' events were produced using the PYTHIA 8.307 [240] Monte Carlo generator, using the A14 set of tuned parameters and the NNPDF2.3LO PDF set. The decay of heavy flavour hadrons was handled by the EVTGEN 2.1.1 [179] package. No additional p–p interaction are included in this sample.

8.3 Detector Model and Material

To model the detector material used in the performance evaluation, the ITk full simulation [241] based on the GEANT4 toolkit [158] is used. The results presented in this document are obtained using the most updated version of the ITk layout detector implementation 03-00-00 described in Ref. [220] that incorporates new software improvements.

The most recent simulation of the ITk Pixel detector makes use of the GeoModel tool suite [242] and relies on atomic XML configuration files which are assembled to create the full detector. It benefits from significantly improved clarity and long-term maintainability, the latter guaranteed by the commitment of the ATLAS Collaboration to use the GeoModel library as basis for its detector simulation for Run 4 and beyond [243]. The placement of the active detector elements as well as the passive material distribution have been carefully validated with the new simulation and an excellent agreement with the previous ITk Pixel detector simulation used in [220] was obtained. It also includes a more accurate description of the material implementation of the services in the transition region between the barrel region and the endcap disks of the strip sub-system.

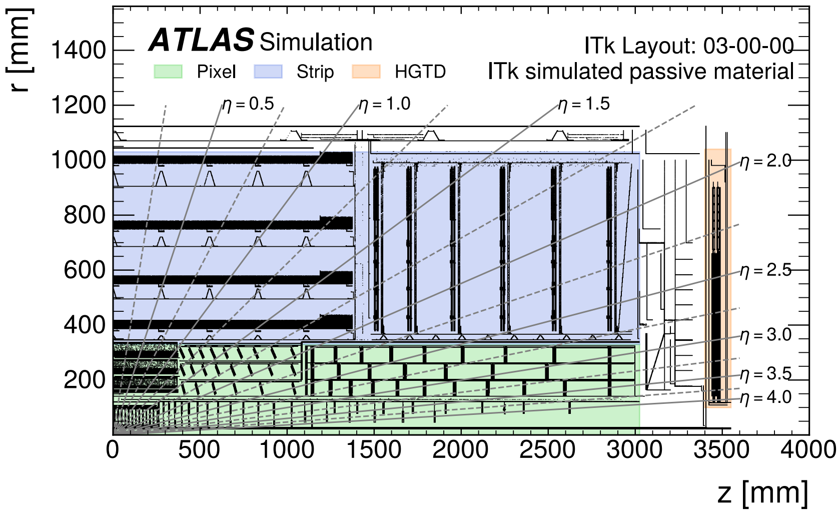

Figure 8.6: Material location for one $r - z$ quadrant of the ITk model. The pixel and strip detectors are illustrated in red and blue, respectively. The HGTD is shown in orange.

A precise description of the material within the detector volume is important to account its effect on tracking performance and the measurement of particles. All components need to be considered within the detector volume at their specific location and characterised by their actual material properties, including chemical composition and density. The material distribution simulated for the evaluation of tracking performance is illustrated in the $r - z$ frame in Figure 8.6.

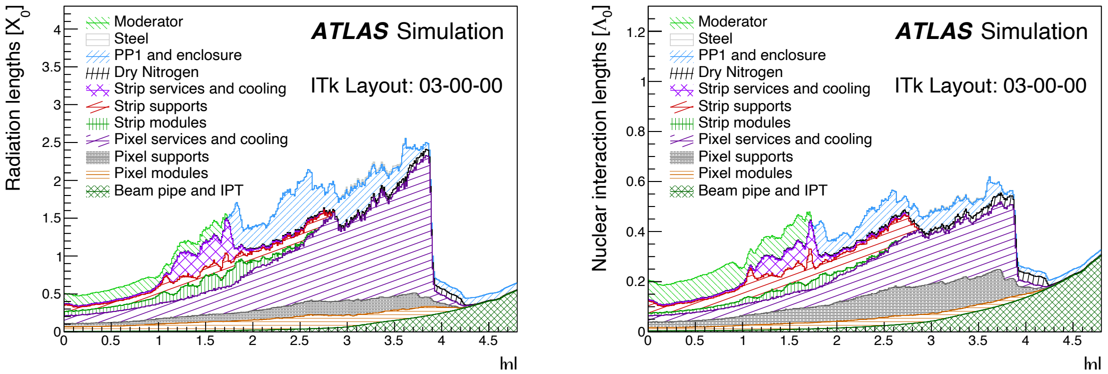

(a) **(b)**

Figure 8.7: (a) Integrated radiation length (X_0) and (b) integrated nuclear interaction length (Λ_0) traversed by a straight track as a function of $|\eta|$ at the exit of the ITk volume, broken down by sub-system and material category. The Inner Positioning Tube (IPT) is a support carbon-fibre cylinder just outside the beam pipe. The moderator is located beyond the active detector area.

Figure 8.7 presents the breakdown of the material components for the ITk model described in terms of integrated radiation length (X_0) and nuclear interaction length (Λ_0)

traversed by a straight track as a function of the absolute pseudorapidity. As expected, a smaller amount of material is transversed in the very central region, $0.0 \leq |\eta| \leq 1.0$, since the Pixel detector provides a light design that minimises non-active material and reduce energy losses. Conversely, as the pseudorapidity increases, the material traversed by the track also increases, particularly in the forward regions where additional components are required for the detector's functionality, such as services and cables from the inner region that are routed outwards. Figure 8.8 shows the mean values of X_0 and Λ_0 that particles traverse before reaching the minimum number of hits required for reconstruction comparing the ITk and ID layouts.

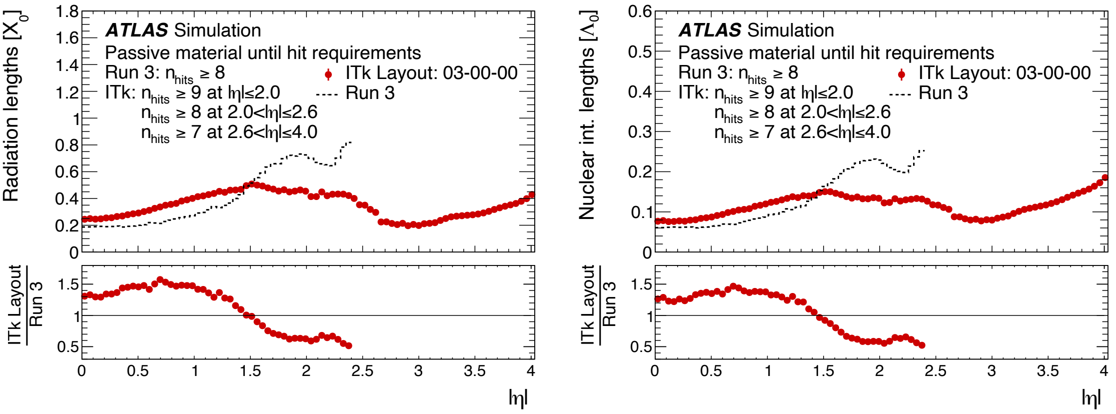

(a) **(b)**

Figure 8.8: Thickness of material that is transversed by particles until reaching the minimum number of hits required for ITk tracking represented in (a) radiation lengths (X_0) and (b) nuclear interaction lengths (Λ_0). The ITk and Run 3 ID layouts are compared. At least 8 silicon hits on a track are required for Run 3 reconstruction, whereas the ITk reconstruction requires at least 9 hits for $|\eta| < 2.0$, 8 for $|\eta| < 2.6$ and 7 otherwise.

8.4 Digitised Readout Signals Simulation

The simulated hits created by Geant4 are processed in a subsequent digitisation step to mimic the behaviour of detector electronics and produce the readout signals. During the digitisation step, the energy deposited for each Geant4 step within the active ITk volume is used to calculate the free charge and the drift time to the readout surface. These calculations consider several factors, including sensor thickness, depletion and bias voltages, carrier mobility, as well as magnetic field effects, such as the directional drift of electrons, commonly referred to as the Lorentz shift. The simulation of the response of the front-end electronics to charges with different drift times accounts for contributions from noise and capacitive coupling to nearby pixels or strips channels. Then the algorithm estimates the total amount of signals collected in each channel and checks if it surpasses a given threshold If a pixel or strip channel is above the threshold, the corresponding channel is labelled as fired and is collected as output of the digitisation algorithms. In the innermost layer of the barrel, the modules are equipped with pixels with a size of 25×100 μm^2 and use a discriminator threshold of 900 electrons, while all other modules use a threshold of 600 electrons. When the charge collected by a pixel exceeds the threshold, a 4-bit ToT measurement is emulated using a calibration function. In the innermost barrel layer, the simulation approximates the three-dimensional pixel sensors as planar sensors, and the Lorentz drift effect is disabled to mimic three-dimensional sensor designs.

8.5 Track and Vertex Selections

To assess the tracking performance, a set of requirements are applied to the final reconstructed tracks based on the track's pseudorapidity range. These criteria ensure that only high-quality tracks are considered and are outlined in Table 8.1.

A minimum number of hits from both Pixel and Strip detectors is required to ensure sufficient measurement points for accurate track reconstruction. This requirement takes into account the varying detector coverage and hit density across different η regions. In low $|\eta|$ region, a greater number of combined pixel and strip hits are needed. In addition, at least one hit in the pixel detector is required for all tracks across all η regions to contribute to a precise determination of the track's impact parameters, d_0 and z_0.

A maximum number of holes is also required. Holes are defined as intersections of the predicted particle's trajectory with an active sensor element from which no measurement is assigned to the track. The hole counting is restricted to layers between the first and last hits on a track, and tracks are allowed a maximum of 2 holes in all pseudorapidity regions.

Requirements	Pseudorapidity interval		
	$|\eta| < 2.0$	$2.0 < |\eta| < 2.6$	$2.6 < |\eta| < 4.0$
pixel + strip hits	≥ 9	≥ 8	≥ 7
pixel hits	≥ 1	≥ 1	≥ 1
holes	≤ 2	≤ 2	≤ 2
p_T [MeV]	> 900	> 400	> 400
$|d_0|$ [mm]	≤ 2.0	≤ 2.0	≤ 10.0
$|z_0|$ [cm]	≤ 20.0	≤ 20.0	≤ 20.0

Table 8.1: Track selection applied during the track reconstruction in different pseudorapidity intervals. The longitudinal and transverse impact parameters, z_0 and d_0, are defined with respect to the mean position of the beam spot.

For tracks with $|\eta| < 2.0$, a higher p_T threshold of 900 MeV is set, while in high $|\eta|$ regions, where the track density is lower, a threshold of 400 MeV is required due to the worse momentum resolution and magnetic field variations. Finally the transverse impact parameter, $|d_0|$, is limited to 2.0 mm for tracks with $|\eta| < 2.6$ and 10.0 mm for $2.6 < |\eta| < 4.0$. The longitudinal impact parameter, $|z_0|$, is constrained to within 20.0 cm for all pseudorapidity regions.

The vertex reconstruction for both the Run 3 ID and ITk uses the AMVF algorithm [228] described in Section 8.1.5. The process of identifying the primary vertex involves only a subset of the entire set of the reconstructed tracks. In addition to the previous general track selection criteria applied during reconstruction, additional requirements listed in Table 8.2 are imposed to ensure reliable estimation of the impact parameter.

	Requirements
pixel hits	≥ 3
pixel holes	≤ 1
p_T [MeV]	> 900
$\lvert d_0 \rvert$ [mm]	≤ 1.0
$\sigma(d_0)$ [mm]	≤ 0.35
$\sigma(z_0 \sin\theta)$ [mm]	≤ 2.5

Table 8.2: Track selection applied during the AMVF vertex reconstruction. $\sigma(d_0)$ and $\sigma(z_0 \sin\theta)$ are the uncertainties associated to d_0 and $z_0 \sin\theta$, respectively.

A minimum of three hits in the pixel detector is required. Tracks are allowed a maximum of one hole in the pixel detector. All tracks must have a transverse momentum greater than 900 MeV. The absolute value of the transverse impact parameter must be within 1.0 mm and the uncertainty in the transverse impact parameter, $\sigma(d_0)$, and in the longitudinal impact parameter times $\sin\theta$, $\sigma(z_0 \sin\theta)$, must be less than or equal to 0.35 mm and 2.5 mm, respectively. This selection criterion helps ensure that only tracks with precise impact parameter measurements are considered.

8.6 Evaluation of Tracking Performance

The performance of the seeding and tracking algorithms were evaluated using different metrics: the efficiency, the duplicate rate and the fake rate. The seeding performance evaluation relies on associating seeds with stable charged particles produced by MC simulation. If more than half of the seed measurements (i.e. at least two SPs) originate from a certain particle the seed is considered matched with that particle. The fraction of particles matched to at least one seed defines the seeding efficiency. The seed duplicate rate corresponds to the fraction of particles matched to more than one seed, and the number of seeds per particles is also used as a measure for robustness against pile-up.

For tracking performance evaluation, to separate the effects of pattern recognition from those related to the detector's material and geometry, two distinct definitions of track reconstruction efficiency are used in the evaluation: *physics track reconstruction efficiency* and the *technical track reconstruction efficiency*.

- **Physics Track Reconstruction Efficiency:** This is defined as the fraction of charged particles that are associated with a reconstructed track passing the track quality criteria outlined in Section 8.5. This efficiency is sensitive to the amount of detector material a particle encounters before reaching the required number of measurements, as well as the overall coverage of the detector layout. It depends on factors such as the particle type, momentum, direction, and the position of its production vertex.

- **Technical Track Reconstruction Efficiency**: This efficiency focuses only on "reconstructable" tracks. It is defined as the fraction charged particles that are associated with a reconstructed track and that provide enough measurements in the detector to meet the reconstruction criteria. Unlike the physics efficiency, the technical efficiency is independent of the detector's material and layout, allowing it to isolate the performance of the algorithm itself.

To determine the tracking efficiency, a matching procedure between simulated truth particles and reconstructed tracks is employed. Detailed information about individual truth particles contributions to silicon hits in the detector is used. The matching probability is calculated using a weighted fraction of common measurements between a reconstructed track and the truth particle, given by:

$$P_{match} = \frac{2 \times N^{pixel}_{common} + N^{strip}_{common}}{2 \times N^{pixel}_{reco} + N^{strip}_{reco}}, \tag{8.4}$$

where $N^{\text{pixel/strip}}_{\text{common}}$ represents the number of pixel or strip clusters shared between the reconstructed track and the truth particle, and $N^{\text{pixel/strip}}_{\text{reco}}$ is the total number of pixel or strip measurements used in reconstructing the track. Different weights are applied to the pixel and strip measurements to reflect the fact that pixel clusters provide two-dimensional measurements, whereas strip clusters are based on a single measurement. If all clusters of a selected reconstructed track are associated with the same truth particle, the matching probability P_{match} reaches 1.0. The presence of clusters from other truth particles lowers this value. A track is deemed successfully matched if its matching probability exceeds 0.5.

The tracking efficiency is defined as:

$$\epsilon = \frac{N^{matched}_{reco}}{N_{truth}}, \tag{8.5}$$

where $N^{\text{matched}}_{\text{reco}}$ is the number of selected reconstructed tracks that are successfully matched to truth particles, and N_{truth} is the total number of truth particles that meet the selection criteria: the truth particles considered must satisfy $p_{\text{T}} > 1$ GeV and $|\eta| < 4.0$, and be produced by the primary interactions.

Tracks with a matching probability below 0.5 are classified as fake tracks. The fake rate refers to the proportion of reconstructed tracks that are incorrectly reconstructed from random combinations of hits, rather than corresponding to actual particle trajectories. It is defined as:

$$r = \frac{N^{not\ matched}_{reco}}{N_{reco}}, \tag{8.6}$$

where $N^{\text{not matched}}_{\text{reco}}$ is the number of reconstructed tracks that do not match any truth particle, and N_{reco} is the total number of reconstructed tracks that pass the selection criteria. The fake rate can be controlled by requiring a sufficient number of hits for track reconstruction and applying stringent criteria on the number of holes in the tracks [80, 222].

8.6.1 Resolutions of Track Parameter

Track parameter resolutions quantify the difference between the measured track parameters and the true parameters obtained from the truth particles. To determine the resolution of the track parameters, the Root Mean Square (RMS) of the core of the distribution is calculated for the difference between the reconstructed and true parameter values. The RMS is preferred as it is sensitive to non-Gaussian shapes in the distribution, providing a more robust measure. Only tracks that are successfully matched to a truth particle, with a matching probability $P_{\text{match}} > 0.5$, are considered in this calculation.

The trajectory of a charged particle is parameterised using the perigee parameterisation, as described in Section 8.1.1. While the angular parameters (θ, ϕ) often show very precise measurements, emphasis is given to the impact parameters and the momentum resolution. In addition, the accuracy in reconstructing both primary and secondary vertices is highly dependent on the resolution of the impact parameters. Accurate impact parameter resolution is essential for correctly associating tracks to their originating vertex, and it plays a crucial role in the identification of b-hadrons and τ leptons through the reconstruction of secondary vertices. The impact parameter resolution is mainly affected by the intrinsic detector resolution, the amount and placement of material, and the radial configuration of the detector elements near the interaction point. On the other hand, the momentum resolution is more sensitive to the trajectory of the track as it traverses the entire tracking volume.

8.7 Expected Seeding Performance

The seeding efficiency, evaluated in simulated $t\bar{t}$ events with an average pile-up of $\langle\mu\rangle = 200$, is shown in Figure 8.9 as a function of the truth η and transverse momentum. Only particles originating from the hard-scatter event with p_{T} greater than 1 GeV are considered. From the seeding efficiency and the ITk detector layout shown in Figure 7.1, it can be seen that the availability of hits in the different η regions of the detector directly impact the efficiency.

Overall, the seeding efficiency exceeds 85% across the entire phase-space, with values reaching 95% or higher for particles with p_{T} above 10 GeV. Lower efficiencies at smaller p_{T} values are mainly due to the increased impact of interactions with the detector material, as low-p_{T} particles are more susceptible to such interactions. These interactions make it more challenging to reconstruct the tracks of low-p_{T} particles accurately. This is particularly relevant for strip seeds, which are reconstructed after particles have traversed more material layers.

While the efficiency for pixel seeds is almost identical to the overall seeding efficiency, the inclusion of strip seeds offers useful redundancy, especially in cases where pixel detector defects may arise. Figures 8.10 and 8.11 show the duplicate rate and the number of seeds per particle as a function of η and p_{T}. On average, more than six seeds are created per particle, ensuring robustness of the seeding algorithm against potential detector defects or misalignment.

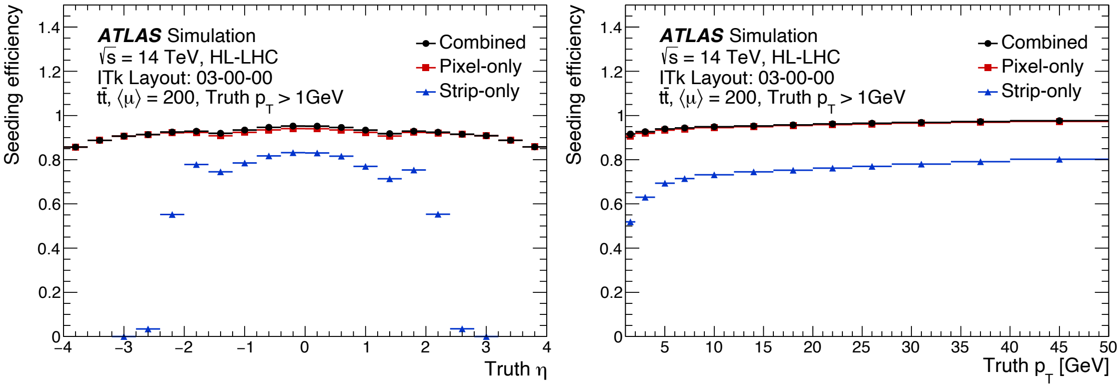

(a) (b)

Figure 8.9: Expected PPP, SSS and inclusive seeding efficiency for $t\bar{t}$ events at $\langle\mu\rangle = 200$ for hard-scatter particles with p_T>1 GeV as a function of truth η and p_T.

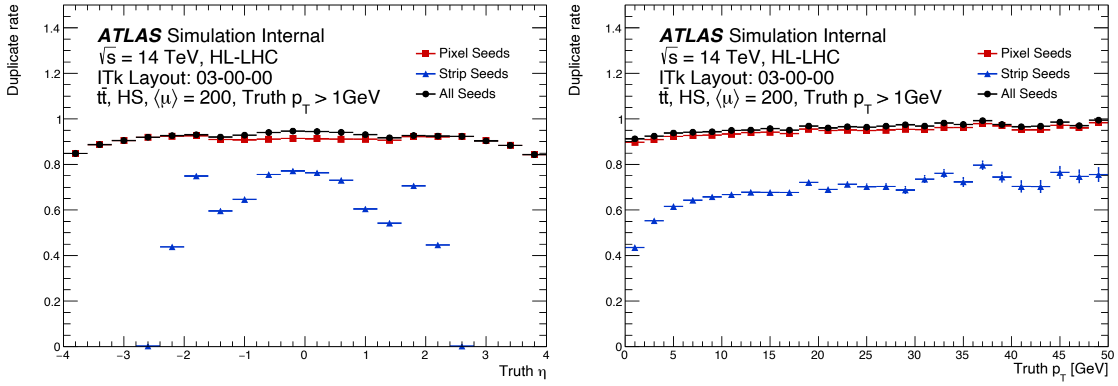

(a) (b)

Figure 8.10: Expected PPP, SSS and inclusive seeding duplicate rate for $t\bar{t}$ events at $\langle\mu\rangle = 200$ for hard-scatter particles with p_T>1 GeV as a function of truth η and p_T.

8.8 Expected Tracking Performance

Figures 8.12a, 8.12b and 8.13a show the ITk and current Run 3 expected track reconstruction efficiencies for single muon events without pile-up and for p_T=2, 10 and 100 GeV, respectively. The efficiencies are consistent between ITk and ATLAS Run 3 detector, exceeding 99.5% for 2 GeV muons and approaching 100% for higher p_T up to $|\eta| = 3.6$. In the very forward region of the ITk detector, there is a slight efficiency reduction to about 99%, which is attributed to the reduced number of hits available in that region. Figure 8.13b illustrates the track reconstruction efficiency for 10 GeV muons, electrons, and pions. While electrons and pions show slightly lower efficiency due to higher rate of interaction with the material of the detector, the tracking efficiency remains above 85% for all types of prompt, stable charged particles.

Figure 8.14 highlights the expected track reconstruction performance at an average pile-up of $\langle\mu\rangle = 200$ for $t\bar{t}$ events, only for particles with p_T greater than 1 GeV that are

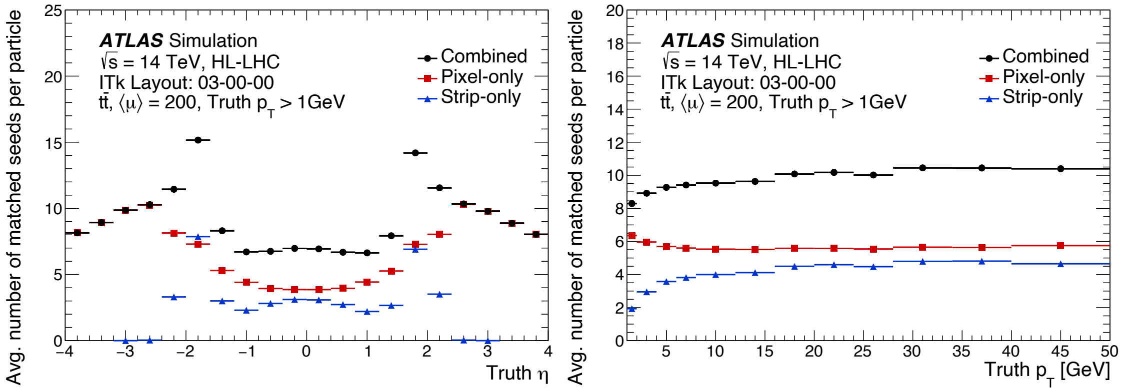

(a) **(b)**

Figure 8.11: Expected number of PPP, SSS and inclusive seeds per particle for $t\bar{t}$ events at $\langle\mu\rangle = 200$ for hard-scatter particles with p_{T}>1 GeV as a function of truth η and p_{T}.

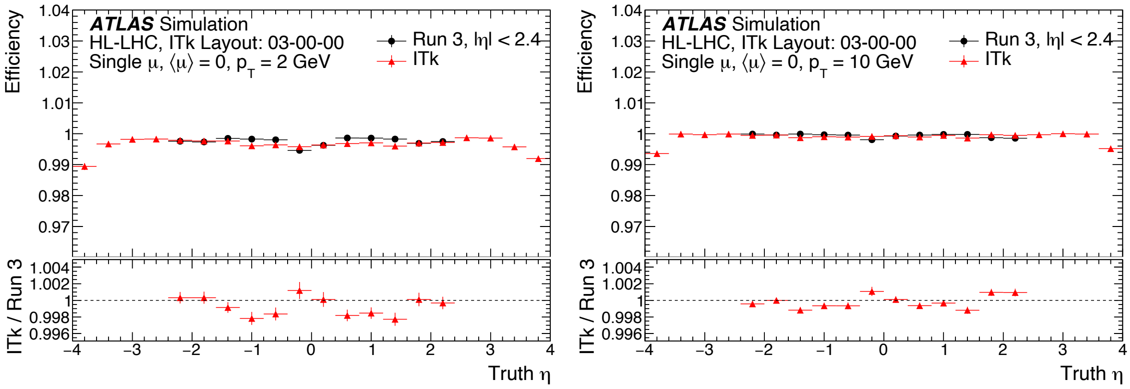

(a) **(b)**

Figure 8.12: Expected track reconstruction efficiency for single muons events with p_{T}=2 GeV (a) and p_{T}=10 GeV (b) without pile-up, comparing ITk and the Run 3 detector as a function of truth η and p_{T}.

within the detector's acceptance range and originate from the hard-scatter interaction. The efficiency is compared to that of the Run 3 detector, under pile-up conditions with a flat $\langle\mu\rangle$ distribution between 0 and 80. The track reconstruction efficiency in the central region of the ITk detector remains within 5% of the efficiency observed with the Run 3 detector. Additionally, the performance in the forward region of the ITk detector is found to be comparable to the central region, indicating robust tracking across the detector.

The technical and physics track reconstruction efficiencies for tracks originating from the hard-scatter interaction in $t\bar{t}$ events are shown in Figure 8.15 at an average pile-up of $\langle\mu\rangle = 0$ and 200. As describe in Section 8.6 the technical efficiency provides a way of isolating and evaluating only the algorithmic aspect of tracking. Any source of the inefficiency in the technical efficiency must come from the track finding or fitting stage. As seen in the figure, the technical efficiency is higher than the physics efficiency

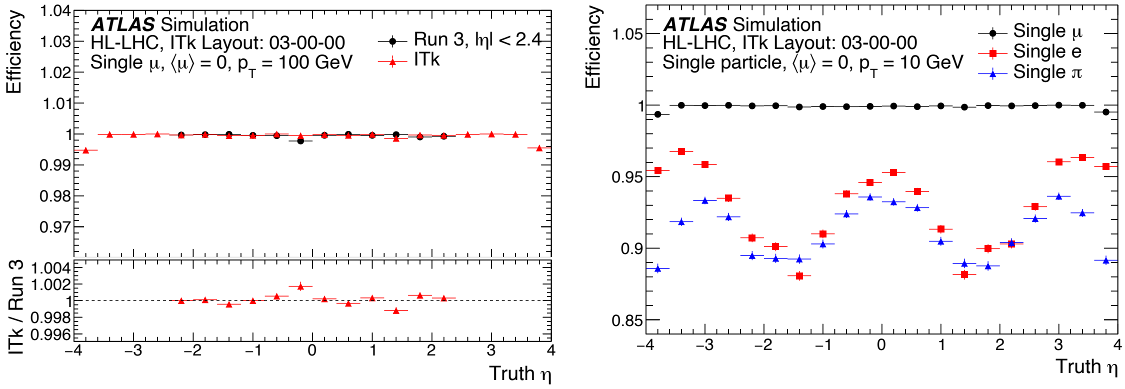

(a) **(b)**

Figure 8.13: (a) Expected track reconstruction efficiency for single muons events with p_{T}=100 GeV without pile-up, comparing ITk and the Run 3 detector. (b) Expected track reconstruction efficiency for single muons, pions and electrons with p_{T}=10 GeV without pile-up. The deficiencies are shown as a function of truth η

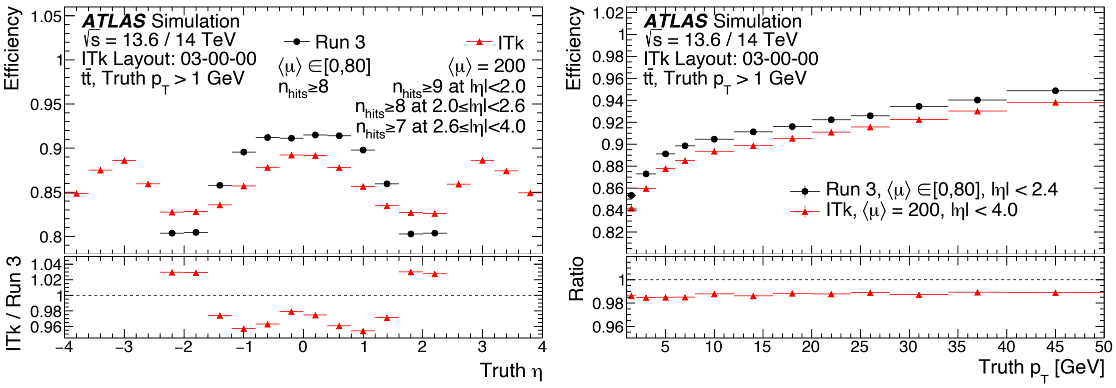

(a) **(b)**

Figure 8.14: Expected track reconstruction efficiency for ITk as a function of truth η and p_{T} and Run 3 detector in $t\bar{t}$ events at different pile-up conditions.

and approaches 100%.

Figures 8.16 and 8.17 present the stability of the track reconstruction efficiency across different pile-up conditions and $|\eta|$ ranges. The efficiency at $\langle\mu\rangle = 200$ remains within 0.5% of that achieved at $\langle\mu\rangle = 0$ and remains practically unchanged for small variations of pile-up near $\langle\mu\rangle = 200$.

The count of reconstructed tracks with $p_{\mathrm{T}} > 1$ GeV at $\langle\mu\rangle = 200$ is shown in Figure 8.18. The plot demonstrates a highly linear trend with the ITk detector, showcasing both the resilience of tracking efficiency across a wide pile-up range and the minimal tracking fake rate, even in the $\langle\mu\rangle = 200$ setting.

The number of reconstructed tracks with $p_{\mathrm{T}} > 1$ GeV at $\langle\mu\rangle = 200$ is presented in Figure 8.18. The image shows a nearly linear relationship between the number of tracks and pile-up, indicating the robust performance of the ITk detector. Overall the

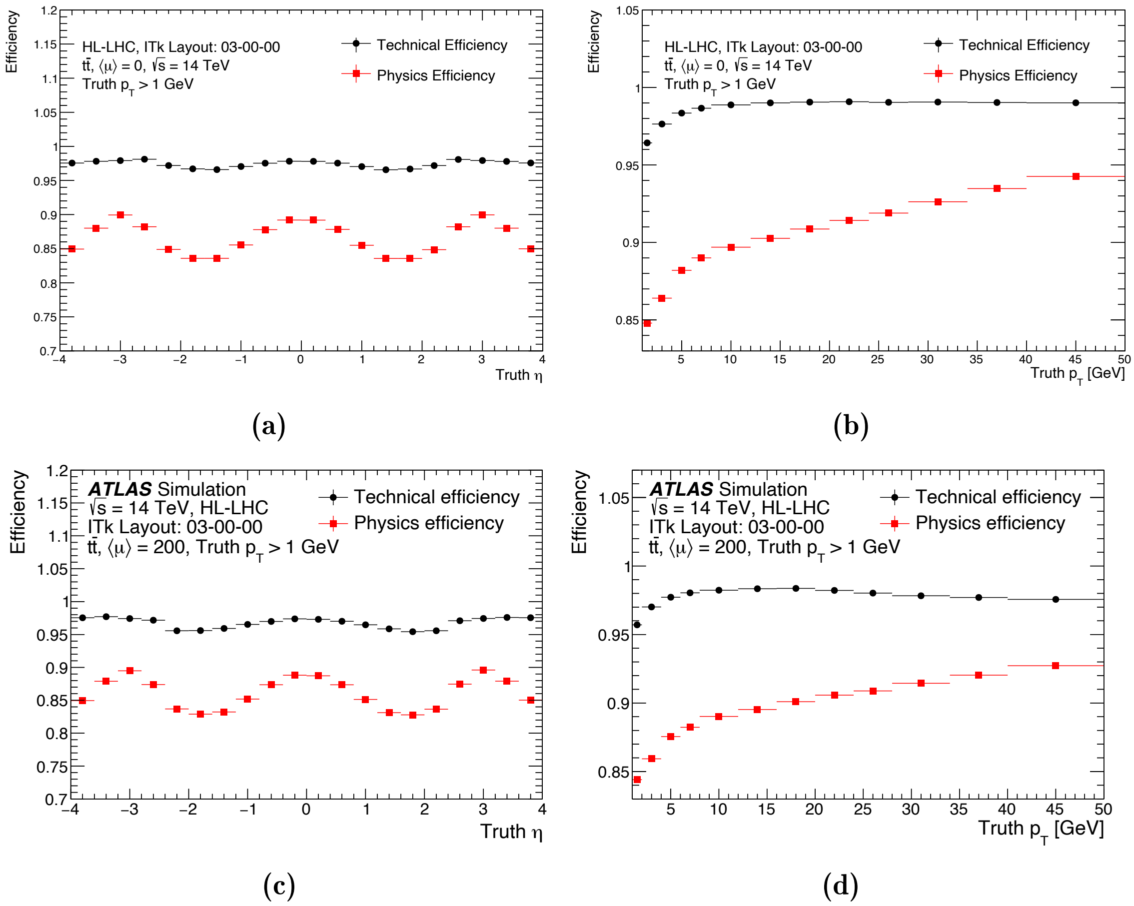

(a) **(b)**

(c) **(d)**

Figure 8.15: Expected technical and physics track reconstruction efficiency as a function of η and p_{T} for ITk detector in $t\bar{t}$ events at low and high pile-up ($\langle\mu\rangle = 0$ and 200) for hard-scatter particles with p_{T}>1 GeV.

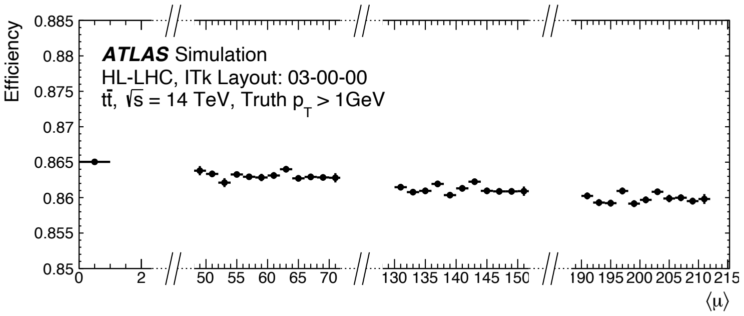

Figure 8.16: Expected track reconstruction efficiency for various pile-up conditions with the ITk detector in $t\bar{t}$ events for hard-scatter particles with p_{T}>1 GeV.

ITk reconstruction is able to maintain high track reconstruction efficiency, while also keeping the fake track rate low, even at the highest density tracking environments.

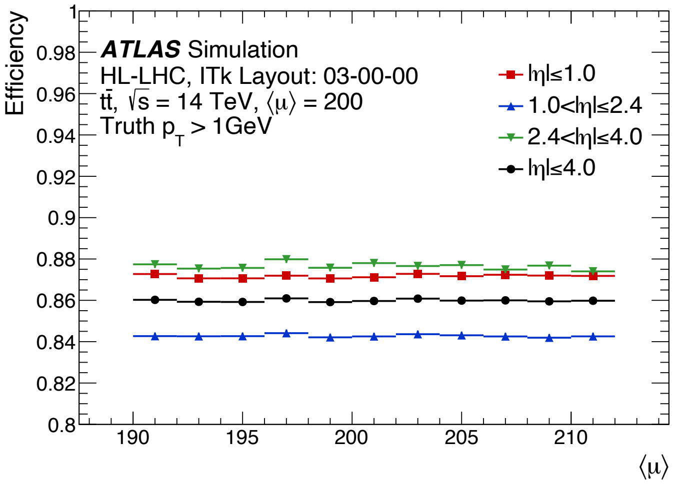

Figure 8.17: Expected track reconstruction efficiency as a function of pile-up in different $|\eta|$ ranges with the ITk detector in $t\bar{t}$ events for hard-scatter particles with p_{T}>1 GeV.

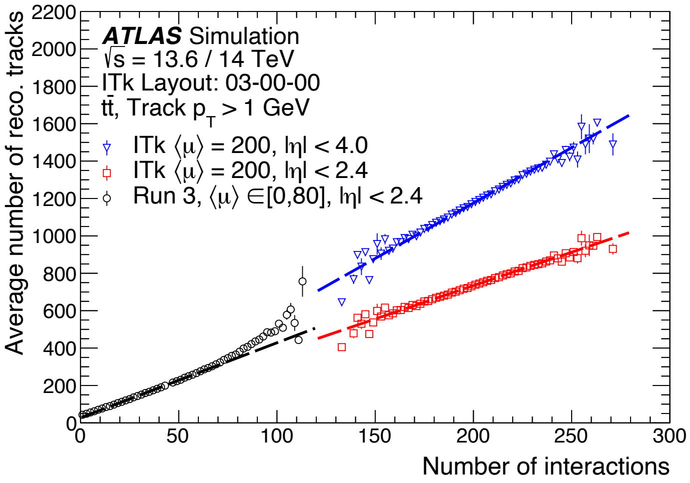

Figure 8.18: Count of reconstructed tracks per $t\bar{t}$ event with p_{T}> 1 GeV as a function of the number of interactions with the ITk detector at $\langle\mu\rangle = 200$ against the Run 3 detector, in conditions with a flat $\langle\mu\rangle$ distribution between 0 and 80. A linear fit was performed over the range of 160-200 interactions for the ITk detector, and 0-40 interactions for the Run 3 detector, to illustrate the dependence of this quantity on pileup. The resulting fit is represented by dashed lines.

8.8.1 Effect of Merged-cluster Identification

As described in Section 8.1.4, the identification of merged clusters can strongly benefit tracking performance in high track-density environments. Studies using a perfect truth-based cluster identification approach suggest that algorithms for identifying merged clusters, similar to the current neural-network-based algorithm used in the ID ATLAS pixel clustering [112, 237], can significantly reduce tracking losses [244].

The expected track reconstruction efficiency for charged particles within high-p_{T}

jets is shown in Figure 8.19a when no dedicated merged-cluster identification is used. A MC sample of hadronically decaying Z' events is used for the efficiency calculation since the rate of cluster merging in these events is much higher than in $t\bar{t}$ events due to the larger fraction of high-p_{T} jets. The image shows that the efficiency decreases with increasing jet p_{T}, particularly in the jet core ($|\Delta R| < 0.02$), where particle density is highest. Figure 8.19b highlights the potential improvement from a dedicated merged-cluster identification algorithms, comparing the performance with no merged pixel cluster identification to that with perfect truth-based identification. Therefore, the final approach is expected to achieve performance that lies between the red and black lines shown in the figure. The machine-learning-based merged pixel cluster identification algorithm used by ATLAS ID reconstruction has not yet been adapted for use in Run 4, and the development of dedicated algorithms for the ITk pixel detector is ongoing.

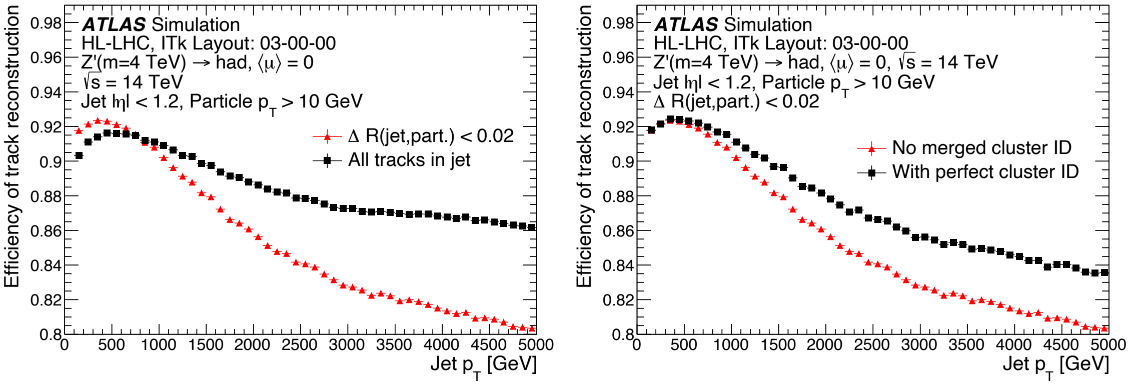

(a) (b)

Figure 8.19: Expected track reconstruction efficiency for tracks in jets as a function of the jet p_T, comparing the inclusive efficiency for all tracks associated with the jet ($|\Delta R| < 0.4$) or within the core of the jet ($|\Delta R| < 0.02$) in (a), and comparing two reconstruction scenarios with perfect or no merged-cluster classification in the core of the jet in (b). Both images use simulated $Z' \rightarrow had$ events.

8.9 Expected Track Parameter Resolution

The expected transverse and longitudinal impact parameter resolutions, comparing the ITk with the Run 3 ATLAS detector, are shown in Figures 8.20-8.22, along with transverse momentum, for simulated muons with $p_{\mathrm{T}} = 2$ and 100 GeV. With ITk, the d_0 resolution improves by up to 20%, and the z_0 resolution by up to a factor of 2, due to both the similar radius of the innermost pixel layers and the finer pixel pitch for pixel sensors in the innermost layers (25×100 or $50 \times 50 \mu\mathrm{m}^2$ for ITk compared to the Run 3 detector's $50 \times 250 \mu\mathrm{m}^2$ in the IBL [65]). This improvement becomes even more substantial for 100 GeV muons, which are less influenced by material effects but more influenced by detector resolution, leading to enhancements of up to factors of 2 and 4 in d_0 and z_0 resolutions, respectively.

In Figure 8.21, a slight degradation in z_0 resolution near $\eta = 0$ is observed. This effect arises because the pixel detector's position measurements are calibrated based on the charge distribution within clusters and the angle of incidence of tracks. Particles with $\eta \sim 0$ typically produce single-pixel-wide clusters with perpendicular angles, providing minimal information to be used for improving the position resolution.

As seen in Figure 8.22, the transverse momentum resolution with ITk is expected to surpass that of Run 3, owing to the improved bending-plane resolution from the silicon strip sensors in ITk compared to the straw tubes in the Run 3 detector. The resolution in the forward region for 100 GeV muons is not ideal, but the rate of such high-energy muons (equivalent to 3 TeV forward muons) in this region is anticipated to be very low and the impact on overall performance is minimal.

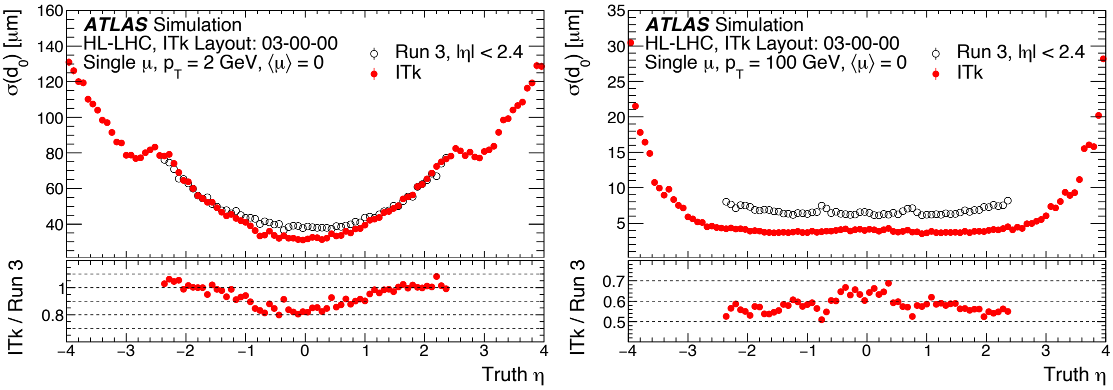

(a) **(b)**

Figure 8.20: Resolution of the transverse impact parameter (d_0) as a function of η for single muon events with $p_T = 2$ GeV (a) and 100 GeV (b) without pileup, comparing the ITk to the Run 3 detector.

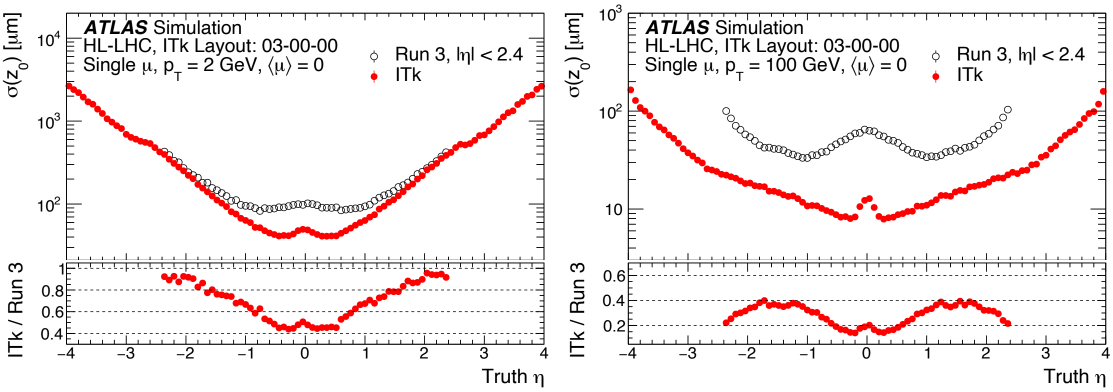

(a) **(b)**

Figure 8.21: Resolution of the longitudinal impact parameter (z_0) as a function of η for single muon events with $p_T = 2$ GeV (a) and 100 GeV (b) without pileup, comparing the ITk with the Run 3 detector.

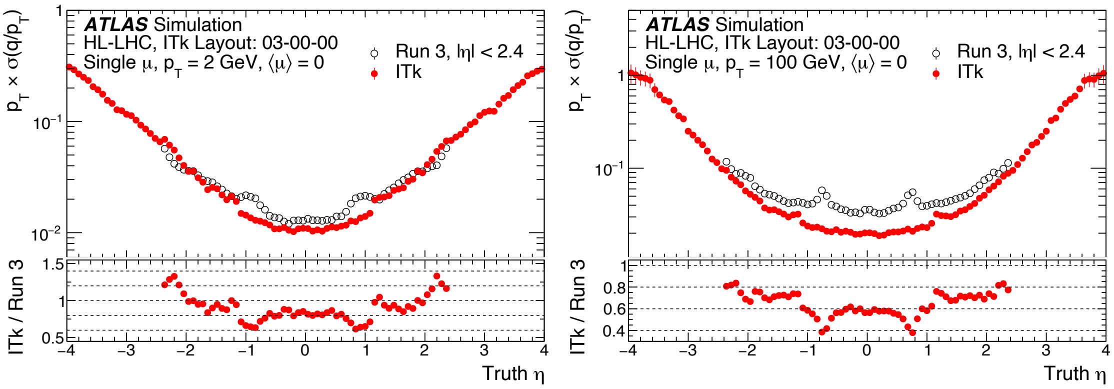

(a) (b)

Figure 8.22: Relative transverse momentum resolution as a function of η for single muon events with $p_T = 2$ GeV (a) and 100 GeV (b) without pileup, comparing the ITk with the Run 3 detector.

8.10 Expected Vertex Reconstruction Performance

Figure 8.23 shows the projected number of interactions and local pile-up density under Run 4 conditions, assuming an average $\langle \mu \rangle$ of 200, compared to those used in Run 3. The local pile-up density is defined as the number of p-p interactions within a 4 mm range of the true hard-scatter vertex, normalized to this distance.

In Figure 8.24, the efficiency of hard-scatter vertex reconstruction is shown, representing the fraction of events where a vertex is reconstructed within 0.1 mm of the true hard-scatter position along the longitudinal axis. The vertexing shows great expected efficiency, even under the highest anticipated pile-up density at HL-LHC.

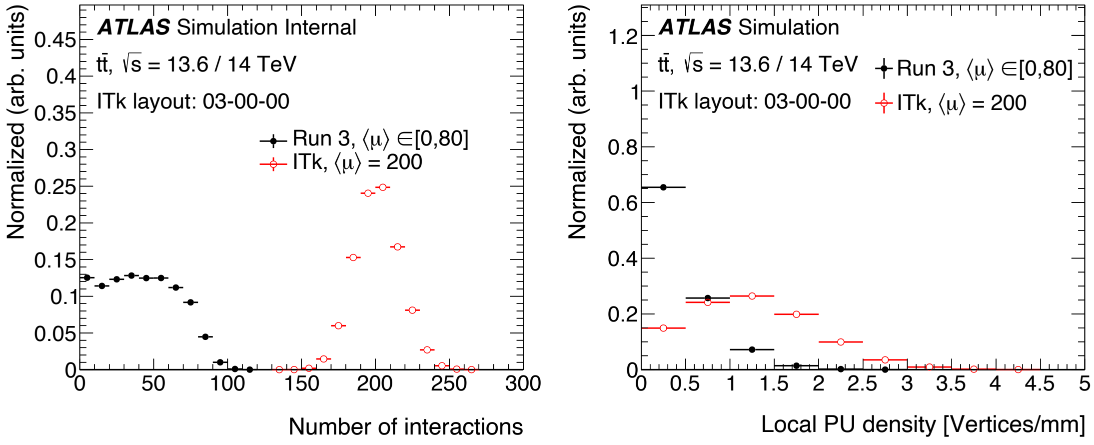

(a) (b)

Figure 8.23: Number of interactions (a) and local pileup density around the hard-scatter vertex (b) distributions for $t\bar{t}$ events at $\langle \mu \rangle = 200$ pile-up in the ITk sample and for $t\bar{t}$ with a flat pileup profile from 0 to 80 in the Run 3 sample.

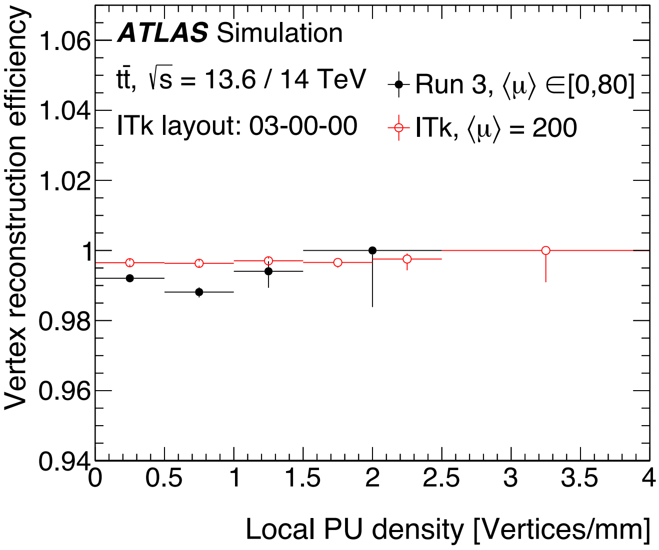

Figure 8.24: Expected efficiency for primary vertex reconstruction, shown as a function of the local pileup density around the hard-scatter vertex. The efficiency is evaluated for $t\bar{t}$ events at $\langle \mu \rangle = 200$ pile-up in the ITk sample and for $t\bar{t}$ with a flat pileup profile from 0 to 80 in the Run 3 sample.

Figure 8.25a shows the combined reconstruction and selection efficiency of the signal hard-scatter vertex, which is defined as the reconstructed primary vertex containing the highest number of tracks matched to true particles from the simulated hard-scatter interaction. This efficiency is sensitive to several factors. For instance, splitting of the hard-scatter vertex into multiple reconstructed vertices in the presence of nearby pile-up vertices reduces the probability of selecting the vertex with the highest $\Sigma \mathrm{p_T}^2$ as the primary vertex. This effect is mainly correlated with the local pile-up density, where efficiency remains highly robust, as illustrated in the figure.

Even with perfect vertex reconstruction, a small chance exists for a pile-up interaction to yield a higher $\Sigma \mathrm{p_T}^2$ than the simulated hard-scatter process. Moreover, true pile-up vertices may merge tougher, producing a into a single reconstructed vertex with increased $\Sigma \mathrm{p_T}^2$. These effects are expected to increase primarily with the number of interactions, as shown in Figure 8.25b, where the combined reconstruction and selection efficiency declines to an average of 92% at a pile-up level of 200.

Finally, Figure 8.26 shows the longitudinal position resolution achieved with the ITk detector, which exhibits high resilience to pile-up, reaching approximately 10 μm even at high pile-up densities, which is more than twice the performance of the Run 3 detector. This enhanced resolution, along with improved track parameter accuracy, is expected to significantly enhance pile-up rejection in jets, hadronic τ reconstruction, lepton isolation, and flavour-tagging algorithms.

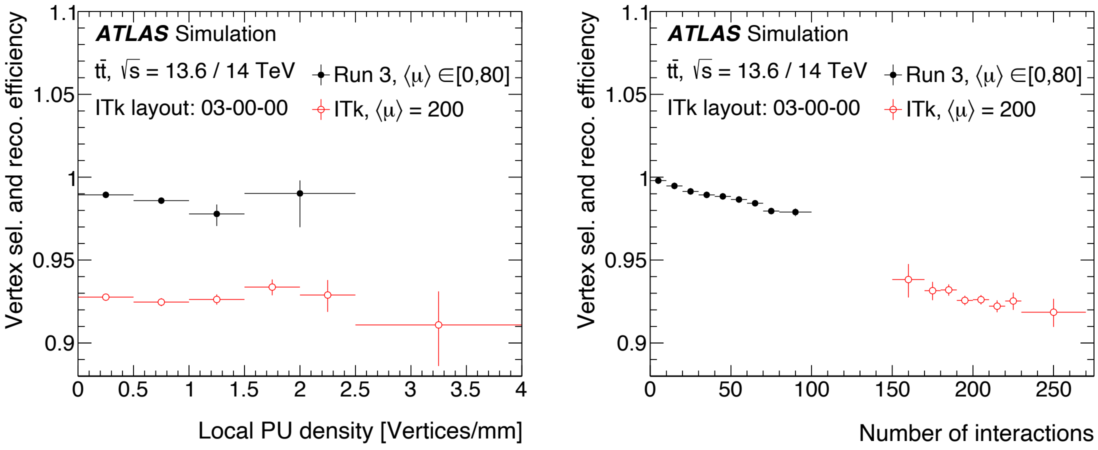

(a) **(b)**

Figure 8.25: Primary vertex combined reconstruction and selection efficiency as a function of (a) the local pileup density around the hard-scatter vertex and (b) the number of interactions. The efficiency is evaluated for $t\bar{t}$ events at $\langle\mu\rangle = 200$ pile-up in the ITk sample and for $t\bar{t}$ with a flat pileup profile from 0 to 80 in the Run 3 sample.

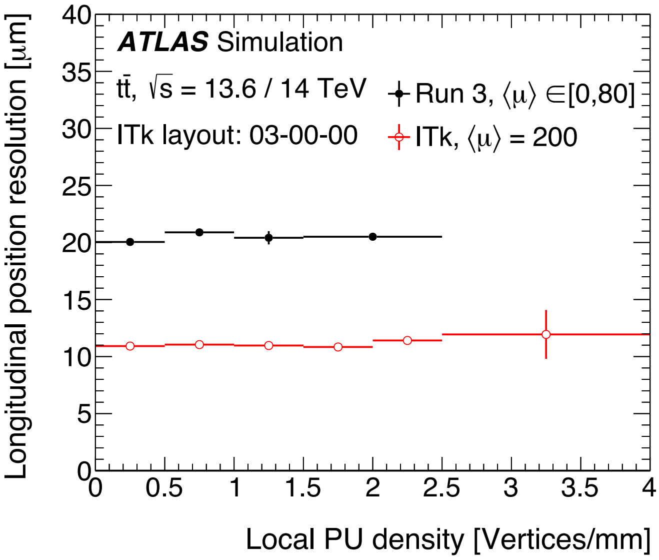

Figure 8.26: Resolution of the longitudinal position of the reconstructed primary vertex in $t\bar{t}$ events with 200 pileup events. The resolution is evaluated for $t\bar{t}$ events at $\langle\mu\rangle = 200$ pile-up in the ITk sample and for $t\bar{t}$ with a flat pileup profile from 0 to 80 in the Run 3

8.11 Discussion

This chapter presented the expected tracking performance of the ITk detector for the high-luminosity LHC operation phase, showing that the ITk design and ATLAS tracking software maintain high efficiency despite the challenges posed by increased pileup. The results presented in this chapter led to the ATLAS publication from Ref. [2].

The redundancy in the high-precision silicon measurements is exploited in track seeding to maintain a high efficiency and duplicate rate, enhancing robustness against detector misalignment and sensor defects. The overall tracking efficiency is expected to match Run 3 levels, while the multiple silicon measurements on each track allow for a quasi-linear scaling of track multiplicity. This indicates that, despite the higher pileup, the rate of fake tracks is projected to be significantly lower compared to Run 3. Another major improvement is seen in impact parameter resolution, which is an important factor for flavour tagging and pileup rejection. This enhancement is primarily driven by the smaller pixel pitch in the ITk. Furthermore, the forward tracking performance in the newly covered region of $2.4 < |\eta| < 4.0$ is found to meet the high standards required for object reconstruction and identification algorithms. In addition, the vertex reconstruction performance is expected to improve over Run 3, both in terms of position resolution and efficiency, exhibiting strong resistance to pileup effects. However, in the core of high-p_{T}jets, tracking performance is observed to degrade due to merged charge clusters. Mitigation strategies, inspired by techniques used in Run 3, will be necessary to ensure reliable ITk track reconstruction in these dense environments.

Overall, the current expected performance defines a solid baseline for future improvements and optimizations in ATLAS tracking performance, serving as a reference for upcoming software developments and ensuring that the ITk achieves the highest possible efficiency and precision in the HL-LHC era.

9

ACTS Seeding Integration for Phase-II ATLAS Track Reconstruction

Contents

A Common Tracking Software (ACTS) [16, 17] is an experiment-independent toolkit for track reconstruction, which is designed from the ground up for thread-safety and high performance. ACTS is built to accommodate different experiment deployment scenarios, and also serves as community platform for research and development of new algorithms and approaches in tracking. Using ACTS for ATLAS Phase-II reconstruction software allows us to directly profit from its thread-safety, high performance and code maintainability.

A significant portion of the author's work has been dedicated to optimizing the seeding algorithm in ACTS to meet ATLAS requirements and integrating this component into the ATLAS tracking software. This work is presented in this chapter. Section 9.1 introduces and motivates the use of ACTS as the ATLAS Phase-II tracking software. Section 9.2 details the implementation of the ITk seeding algorithm in ACTS, providing an in-depth discussion of its theoretical foundations. Section 9.3 discusses the validation of ACTS ITk seeding against its non-ACTS counterpart, while Section 9.4 focuses on CPU optimizations implemented in ACTS to enhance performance. Finally, Section 7.3.2 describes the implementation of the Fast Tracking configuration.

9.1 The ATLAS Phase-II Software at HL-LHC

The HL-LHC tracking environment will present several challenges to the existing ATLAS tracking software (Athena) [245], which was initially designed without much consideration of thread-safety. To profit of the high-performing software, the ATLAS collaboration is dedicating effort in the optimisation of ACTS for the ITk detector and integration into the Athena framework. All object reconstruction and identification at Phase-II must meet or, where possible, outperform the existing Run-2 physics performance. The restrictions of the CPU resources must be taken into account while fully optimising each method in the reconstruction chain for the large pile-up environment.

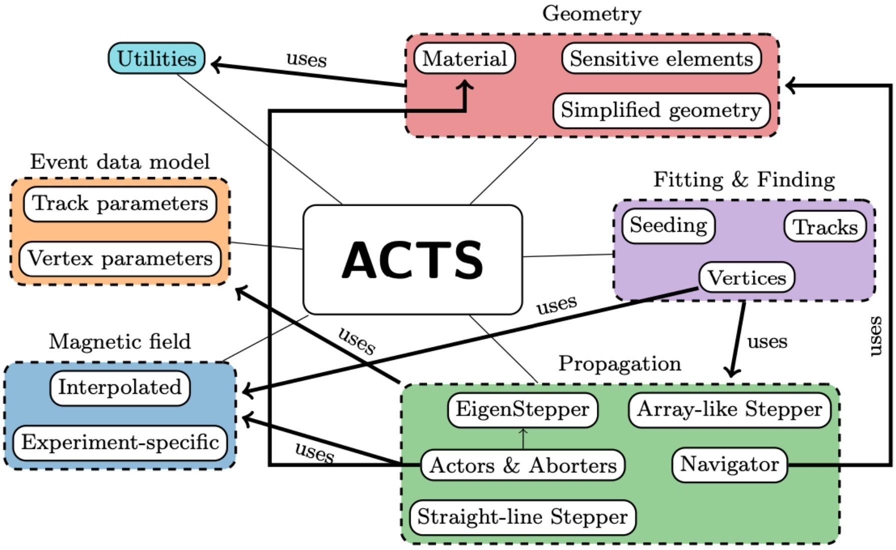

Figure 9.1: Schematic representation of selected components in the ACTS repository and their interactions. The components are categorized into modules, such as geometry, propagation or event data. The arrows indicate the communication between components in different modules [16].

ACTS is an experiment-independent toolkit for charged particle track reconstruction implemented in modern C++, designed for modern computing architectures and multi-threaded event processing. ACTS was initially developed based on tracking algorithms designed for the ATLAS detector, but it is composed of a set of algorithms that are entirely agnostic to the details of the detection technologies and magnetic field configuration, which makes it suitable for several distinct experiments. The core library of ACTS is divided into modules containing tools and algorithms with similar functionality as shown in Figure 9.1. The code is inherently thread-safe to support parallel code execution, and the data structures are optimised for vectorization to speed up linear algebra operations. ACTS is highly customizable and extendable. The best physics performance can be achieved by tuning the algorithms for specific detectors.

ACTS features a cutting-edge layout and a compact event data model. This is anticipated to result in additional savings and efficiencies. The ACTS tracking software package was created with multi-threaded event processing and data locality in mind from the beginning. It greatly reduces the technical overheads compared to the current

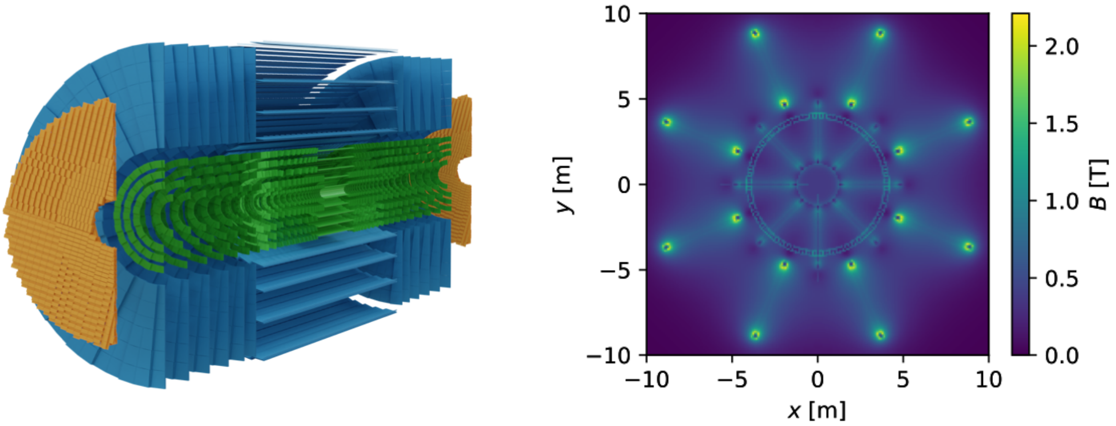

Figure 9.2: Left: ITk detector geometry defined in ACTS. Right: Projection of the ATLAS magnetic field in the $x - y$ plane defined in ACTS [16].

ATLAS tracking program and aims to make greater use of the vector computing power of contemporary CPUs. The ACTS suite's functional components and tracking tools are being integrated into ATLAS event reconstruction and a significant CPU gains will be realised throughout the integration program, from the tracking of the Inner Detector and Muon Spectrometer to the entire charged particle reconstruction. Figure 9.2 shows an example of the ITk geometry and the magnetic field of the ATLAS detector defined in ACTS.

The enhanced technical performance of ACTS tools will be beneficial to all aspects of charged particle track reconstruction [230]. The ACTS Combinatorial Kalman Filter (CKF) will be employed in the silicon track finding exploiting the detailed knowledge of the detector material, magnetic field propagation, and measurement calibration. This allows to develop a fast track finding based on the Fast Tracking prototype described in Section 7.3.2 with the benefit of removing its limitations. Good quality tracks are then passed to the ambiguity resolution step, where the ambiguity between clusters and tracks are resolved and a machine-learning-based cluster splitting algorithm will be used to establish if clusters are shared in the jets's core. Only the small fraction of tracks changing their hit content will be refitted instead of the full track container, providing significant savings in execution time.

In addition, the current software for combined electron reconstruction will be replaced by the new ACTS Gaussian Sum Filter implementation. The particle flow algorithm will use the ACTS extrapolation code combining calorimeter and tracking measurements for missing energy reconstruction and jet finding. The ACTS vertexing package will serve as the foundation for primary and secondary vertex reconstruction, conversion detection and b-tagging. Finally, ACTS will be used to associate timing hits with forward tracks during the reconstruction of the Phase-II High Granularity Timing Detector.

The integration of ACTS into the ATLAS software began with a modern and optimized implementation of the ITk tracking chain within the ACTS framework in a stand-alone manner. The primary focus was on maintaining the same physics performance where applicable, such as when the same logic was implemented, while also emphasizing CPU performance improvements and code modernization. Once ready, the ACTS algorithms for the ITk tracking chain were fully deployed into the ATLAS software.

9.2 Implementation of the ITk Seeding in ACTS

The seeding algorithm (described in Section 8.1.2.3) is an important phase of event reconstruction and is necessary to reduce the time required for track reconstruction. This section presents the work conducted to implement and integrate in ACTS the ITk seed maker algorithm developed in current ATLAS track reconstruction software (Athena) [245]. All the ITk code optimizations were ported from Athena to ACTS and the ACTS ITk seeding implementation was validated against the ATLAS software.

The ACTS ITk seeding implementation and its validation against the ATLAS algorithm are detailed in Sections 9.2.2 and 9.3. The algorithm was optimized to enhance execution time, with both algorithmic and implementation improvements discussed in Section 9.4, which also includes a comparison of the time performance within ACTS.

The seeding implementation in ACTS core was designed to be as detector-agnostic as possible and focus on parallelism and maintainability. It operates under the assumption of a (near) homogeneous magnetic field with particles originating from the centre of the detector. The algorithm is structured in sequential steps: Seed Finding and Filtering, followed by Seed Confirmation. The seeding uses measurements referred as space points (SP) (as described in Section 8.1.3), which determine (x,y,z) coordinates of the hits, with the z axis parallel to the the magnetic field.

The primary CPU-based seeding strategy in ACTS is referred as mid-point seeding. It provides an implementation that is heavily based on the ATLAS approach and has been integrated into Athena and optimised for Phase-II reconstruction. The following sections provide a detailed description of the mid-point ITk seeding algorithm. Appendix **??** presents R&D studies on seeding, focusing on the implementation different seeding approaches and machine learning-based optimizations of the seeding.

9.2.1 The ACTS Mid-point Seeding

The mid-point seeding algorithm generates track seeds by combining SPs to define a helical trajectory in a homogeneous magnetic field. The presence of multiple seeds for the same particle (duplicates) or seeds that do not correspond to any particle (fakes) increases tracking time. To mitigate this, multiple constraints and confirmation conditions are applied to decrease the number of seed candidates while ensuring a minimal number of duplicate seeds. This approach maintains robustness in track reconstruction, even in the presence of detector misalignment and defects.

This seeding algorithm is heavily inspired by collider experiments at the LHC, specifically ATLAS [246]. As a result, the configuration parameters are well-suited for these types of geometries, assuming a reference frame based on a right-handed Cartesian coordinate system with the origin at the interaction point (IP). The positive z-axis aligns with the beam direction, while cylindrical coordinates r and ϕ are used in the transverse plane. The transverse momentum, p_T, represents momentum in the transverse plane, and pseudorapidity is defined as $\eta = -\ln(\tan(\theta/2))$, where θ is the polar angle measured from the beam direction.

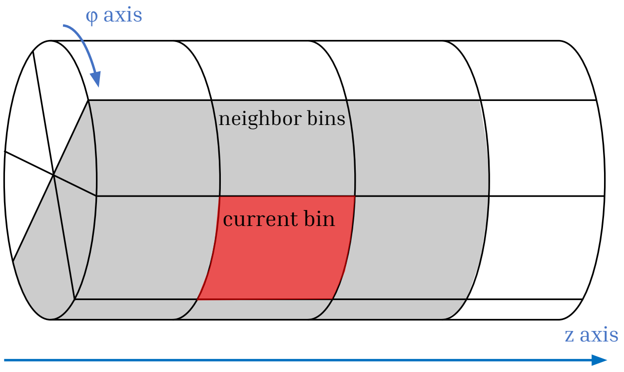

Figure 9.3: Schematic representation of the 3-dimensional space segmentation of the detector into $\phi - z$ bins.

The ACTS mid-point seeding algorithm is utilized by numerous high-energy physics experiments. As detailed in the following sections, it has been optimized for the ATLAS ITk detector [217, 218, 220] and integrated into the ATLAS framework as part of the Phase-II software upgrade program [230, 232], maintaining similar CPU performance. The algorithm has been successfully integrated into the reconstruction of other experiments such as sPHENIX [247, 248], CEPC [249, 250], and STCF [251], and is currently under optimization for NA60+ [252].

9.2.2 The Space Point Grid

The seed formation algorithm starts by producing seeds consisting of triplets of SPs in either the Pixel detector (referred to as PPP seeds) or the Strip detector (SSS seeds). The SPs are first organized into $(\phi,\ z)$ bins within a fully customizable grid that covers the entire detector acceptance to ensure fast retrieval of measurements. The optimal ϕ axis of the grid is calculated based on the maximum azimuthal deflection considering the position of the sensitive layers in the detector and the lowest allowed seed p_T value. For each bin, the SP search process begins by selecting the central SP from the (ϕ, z) region. Subsequent SPs are then sought in adjacent bins on the inner and outer transverse layers of the detector. The specific $(\phi,\ z)$ neighbouring bins used in the search can be configured based on geometrical assumptions relative to the IP to reduce combinatorial complexity and enhance execution speed. Figures 9.3 and 9.4 provide a depiction of the SP grid and the SP search in neighbouring grid bins.

9.2.3 The Seed Finder and Filter

The search process begins by considering doublets of SPs (inner-middle and middle-outer) within the specified bins. Potential middle, outer, and inner SP candidates are selected based on geometric criteria determined by the detector layout. This includes verifying that the positions of the SPs lie within the $(\phi,\ r,\ z)$ region of interest. For

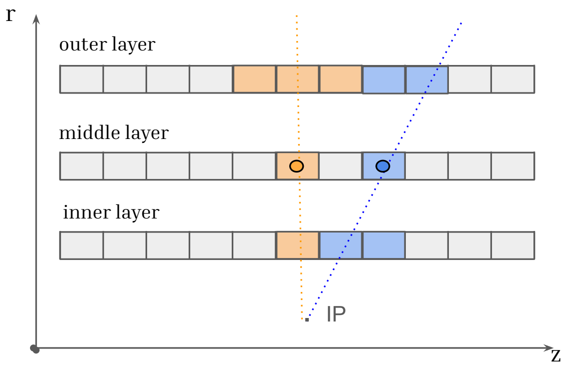

Figure 9.4: Schematic representation of selected bins in $r - z$ plane used in the triplet formation in various search layers for different middle SP position. Two middle SP are represented in different colors, together with the neighboring z bins used in the search. A map of each bin used in the search is defined based on geometrical assumptions according to the IP position and the middle SP z-position.

instance, middle SPs in the outermost and innermost layers of the detector are not considered. The distance between the components of the doublet in the r and z directions must also fall within a specified range. Additionally, the propagation of the doublet to the z-axis must lie within the collision region, and the forward angle (the angle in the r-z plane between doublet components) must fall within reasonable limits.

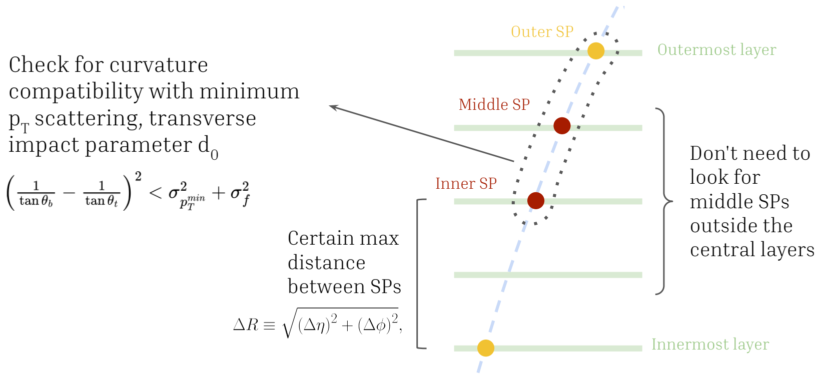

Figure 9.5: Schematic representation of the seed candidate formation and some of the compatibility and geometrical cuts applied to the SP combinations.

The code then iterates through the doublets that pass the previous selections and constructs triplets by combining inner-middle and middle-outer pairs that share the same middle SP (inner-middle-outer), which are referred as triplets. It checks the compatibility of these combinations by comparing the r-z slopes of the inner-middle and middle-outer doublets. These slopes must be within the bounds defined by the maximum multiple scattering effect (produced by the minimum allowed p_T particle) and a specific uncertainty. A further refinement of this slope constraint is applied using a scattering term scaled by the actual estimated seed p_T. For the remaining combinations, the estimated helix radius of the triplets must be greater than the minimum allowed radius, and the transverse impact parameter (d_0)[1] must be smaller than the maximum allowed. Table 9.1 lists some of the parameters used to configure the constraints applied during the doublet and triplet finding steps.

The first cuts between triplet combinations checks the compatibility between the (r, z) slope of the bottom and top seed segments. Assuming Gaussian error propagation, which allows adding the two errors if they are uncorrelated (fair assumption for scattering and measurement uncertainties), the seed is removed if the top and bottom segments have a too large angle between them that is incompatible with the limit of minimum p_T scattering, i.e. the seed is accepted if

$$\left(\frac{1}{\tan\theta_b} - \frac{1}{\tan\theta_t}\right)^2 < \sigma^2_{p_T^{min}} + \sigma^2_f, \tag{9.1}$$

where σ^2_f is the squared uncertainty in the difference between slopes and $\sigma^2_{p_T^{min}}$ is the scattering term calculated assuming the minimum particle p_T expected to be reconstructed.

The minimum scattering term ($\sigma^2_{p_T^{min}}$) is an approximate worst-case multiple scattering term assuming the lowest p_T allowed and the estimated theta angle:

$$\sigma^2_{p_T^{min}} = \left[\left(\frac{1}{\tan\theta_b}\right)^2 + 1\right]\left(\sigma_{scattering}\cdot\Theta_0^{min}\right)^2, \tag{9.2}$$

where $\sigma^2_{scattering}$ is the number of sigmas of scattering angle that should be considered and Θ_0^{min} is the Lynch & Dahl correction [253, 254] to the Highland equation which, assuming the lowest p_T allowed, results in:

$$\Theta_0^{min} = \frac{13.6\text{MeV}}{p_T^{min}}\cdot\sqrt{\frac{z_q^2 L}{\beta^2 L_0}}\left(1 + 0.038\ln\left(\frac{z_q^2 L}{\beta^2 L_0}\right)\right), \tag{9.3}$$

where β, and z_q are the velocity, and charge number of the incident particle, and $L/L0$ is the thickness of the scattering medium in radiation lengths. In ACTS, the parameters for Equation 9.3 are fully configurable.

Factorising p_T^{min} from the Highland equation, one can write $\sigma^2_{p_T^{min}}$ in term of a constant k:

$$\sigma^2_{p_T^{min}} = \left[\left(\frac{1}{\tan\theta_b}\right)^2 + 1\right]\frac{k}{(p_T^{min})^2}. \tag{9.4}$$

The second cut during triplet check exploits the (inverse) conformal transformation:

$$u = \frac{x}{x^2+y^2}, \qquad v = \frac{y}{x^2+y^2}, \tag{9.5}$$

that transforms the circle containing the three SPs into straight lines in the u/v plane,

---

[1] The transverse impact parameter, d_0, is defined as the distance of closest approach in the transverse plane between the track and the z axis of the global coordinate system. While the longitudinal impact parameter, z_0, is the z-coordinate of the point of closest approach.

Table 9.1: List of selected configurations parameters used in ACTS seed finder algorithms.

`rMax` `rMin` `zMin` `zMax` `phiMin` `phiMax`	Definition of region of interest in (r,z,ϕ) for all SPs
`rMinMiddle` `rMaxMiddle`	Minimum and maximum r boundaries for middle SPs
`deltaRMinTopSP` `deltaRMaxTopSP`	Minimum and maximum radial distance between middle-outer doublet components
`deltaRMinBottomSP` `deltaRMaxBottomSP`	Minimum and maximum radial distance between inner-middle doublet components
`deltaZMax`	Maximum value of z-distance between SPs in doublet
`cotThetaMax`	Maximum allowed $\cot(\theta)$ between two SPs in doublet
`collisionRegionMin` `collisionRegionMax`	Limiting location of collision region in z-axis used to check if doublet origin is within reasonable bounds
`minPt`	Minimum allowed value for the transverse momentum of particles
`sigmaScattering`	Number of sigmas of scattering angle to be considered in the minimum p_T scattering term
`radLengthPerSeed`	Term that accounts for the thickness of scattering medium in radiation lengths in the Lynch & Dahl correction to the Highland equation [253, 254]
`maxPtScattering`	Maximum transverse momentum for scattering calculation
`impactMax`	Maximum value of impact parameter estimation of the seed candidate

with line equation given by

$$v = Au + B, \quad \text{with} \quad A = -\frac{x_0}{y_0} \quad \text{and} \quad B = \frac{1}{2y_0}. \tag{9.6}$$

A and B can be evaluated transforming the coordinates of two space-points, for example SP_b and SP_t, from x/y to u/v using Equation 9.5. (u_b,v_b) and (u_t,v_t) can be derived and the angular coefficient A can be evaluated by the slope of the linear function using the δu and δv between the top and bottom SPs:

$$A = \frac{v_t - v_b}{u_t - u_b}. \tag{9.7}$$

B can be obtained by inserting A into the linear equation for the bottom SP:

$$v_b = Au_b + B \rightarrow B = v_b - Au_B. \tag{9.8}$$

Assuming that the circle goes through the origin and inserting A and B in the circle equation $x_0^2 + y_0^2 = R^2$, one can obtain the radius of the circle:

$$(2R)^2 = \frac{A^2 + 1}{B^2}. \tag{9.9}$$

A cut on the minimum helix diameter can be applied directly on the estimate of $(2R)^2$ without the extra overhead of conversions or computationally complex calculations. The seed is accepted if

$$\frac{A^2 + 1}{B^2} > (2R^{min})^2 = \left(\frac{2 \cdot p_T^{min}}{300 \cdot B_z}\right)^2, \tag{9.10}$$

where B_z is the magnetic field component in the z axis.

A refinement of the cut from Equation 9.1 is also applied to the triplets using a scattering term calculated with the actual measured p_T, instead of the minimum allowed p_T:

$$\left(\frac{1}{\tan\theta_b} - \frac{1}{\tan\theta_t}\right)^2 < \sigma^2_{p_T^{estimated}} + \sigma_f^2, \tag{9.11}$$

where $\sigma^2_{p_T^{estimated}}$ is the approximated multiple scattering term assuming the measured p_T that is obtained from seed curvature using Equation 9.9:

$$\sigma^2_{p_T^{estimated}} = \left[\left(\frac{1}{\tan\theta_b}\right)^2 + 1\right] \frac{B^2}{(1 + A^2)} \left(2 \cdot \sigma_{scattering}\right)^2. \tag{9.12}$$

9.2.4 Strip Coordinate Compatibility Checks

For SSS seed candidates the procedure in the previous section is slightly different. First, a new compatibility cut is also applied to check if the position of all the seed components (hence a seed direction) in $x - y - z$ frame is compatible with the positions of the strip channels used to build the SPs.

First the cross product between the direction of the bottom and top strip clusters used to build the SPs is calculated, referred to as ($\vec{s_{b,t}}$), and the vector defining the SP position ($\vec{r}_{SP}$):

$$\vec{d_b} = \frac{l_b}{2}\vec{s_b} \times \vec{r}_{SP} \quad \text{and} \quad \vec{d_t} = \frac{l_t}{2}\vec{s_t} \times \vec{r}_{SP}, \tag{9.13}$$

where $l_{b,t}$ is the strip length for the bottom or top channel. $\vec{d_{b,t}}$ is a vector perpendicular to the distance between the two strip channels.

Then, the scalar product between bottom strip direction ($\vec{s_b}$) and $\vec{d_t}$ is calculated:

$$b_1 = \frac{l_b}{2}\vec{s_b} \cdot \vec{d_t}. \tag{9.14}$$

The distance between the strips ($\vec{\Delta s}$) is used to evaluate if the SP position is inside the bottom and top detector element:

$$\left|\frac{\vec{\Delta s} \cdot \vec{d_b}}{b_1}\right| < \alpha_{tol} \quad \text{and} \quad \left|\frac{\vec{\Delta s} \cdot \vec{d_t}}{b_1}\right| < \alpha_{tol}, \tag{9.15}$$

where the tolerance parameter α_{tol} is configured to be 1.1 mm.

The candidate seed moves to the next checks if the seed direction is compatible with the channels fired by the seed components, as defined in Equation 9.15. Then, the SP position is corrected with respect to the top strip centre position ($\vec{r^t}_{strip}$), top strip direction and the distance between the strips:

$$\vec{r'}_{SP} = \vec{r^t}_{strip} + \frac{l_t}{2}\vec{s_t} \cdot \frac{\vec{\Delta s} \cdot \vec{d_t}}{b_1} \tag{9.16}$$

For strip SPs, the procedure of Section 9.2.3 is done using the corrected positions in the $x - y - z$ reference frame.

9.2.5 Estimation of Seed Parameters

The curvature of the seed can be defined as the inverse diameter using Equation 9.9:

$$\text{curvature} = \frac{1}{2R} = \sqrt{\frac{B^2}{1 + A^2}}. \tag{9.17}$$

The transverse momentum [255] of the seed can be calculated from the radius (Equation 9.9) as:

$$p_T[MeV] = 300 \times B_z[kT] \times R[mm] \times q[e] = \frac{300 \cdot B_z}{2}\sqrt{\frac{1 + A^2}{B^2}}. \tag{9.18}$$

The pseudorapidity is calculated as:

$$\eta = -\log\left(\tan\left(\frac{\theta}{2}\right)\right) \quad \text{with} \quad \theta = \arctan\left(\frac{1}{< \cot\theta_{b,t} >}\right). \tag{9.19}$$

where $< \cot\theta_{b,t} >$ is the estimated average between $\cot\theta$ for the inner and outer SPs, which gives an approximation to the slope at the location of the middle SP. The geometric average for PPP seeds and arithmetic average for SSS seeds is used.

To estimate the transverse impact parameter d_0 some approximations need to be considered. Assuming that the x/y frame is such that the middle space-point SP$_m$ is in the origin of the frame, as shown in Figure 9.6. The IP corresponds to the centre of the detector and its distance to SP$_m$ is given by r_m. The distance between the centre of the circle and IP is

$$(x_0 + r_m)^2 + y_0^2 = (R + d_0)^2, \tag{9.20}$$

and using $R^2 = x_0^2 + y_0^2$:

$$\frac{d_0^2}{R^2} + 2\frac{d_0}{R} = \frac{2x_0 r_m + r_m^2}{R^2}. \tag{9.21}$$

Considering that $d_0 << R$, the term $\frac{d_0^2}{R^2}$ can be neglected, obtaining

$$d_0 \approx \frac{r_m^2 + 2x_0 r_m}{2R} = \frac{r_m(r_m - A/B)}{2R}, \tag{9.22}$$

and using Equation 9.6 to replace x_0 by $-\frac{A}{2B}$.

Assuming that close to the origin the circle can be approximated as a line parallel to x axis and expand $(2R)^2$ around $A = 0$, considering only the first term of the expansion:

$$(2R)^2 = \frac{1 + A^2}{B^2} \approx \frac{1}{B^2} + O(A). \tag{9.23}$$

Replacing R in Equation 9.22, d_0 will be given by:

$$d_0 = \frac{r_m(r_m - A/B)}{1/B} = r_m(Br_m - A) = -r_m(A - Br_m). \tag{9.24}$$

Now, the impact parameter can be calculated by A and B in the u/v plane with a linear function instead of a quadratic function in x/y plane:

$$d_0 = |(A - B \cdot r_M)\, r_M| \tag{9.25}$$

9.2.6 Seed Filter and Seed Confirmation

After selecting the triplet candidates, a Seed Confirmation step is used to compare seeds with similar curvature and rank them based on a configurable weight score. This process enhances computational performance and the quality of the final track collections by rejecting lower-quality seeds. For prompt particles originating from the IP, the scoring system prioritizes seeds with a large number of outer SPs with compatible curvature (N_t) and smaller values of d_0 and z_0. Seeds that share the same inner-middle SP-doublet but outer SPs located at different detector layers in the same or close-by z-bin are considered compatible with the same particle track if they have a similar helix radius with the same sign (indicating the same charge). To improve the seed

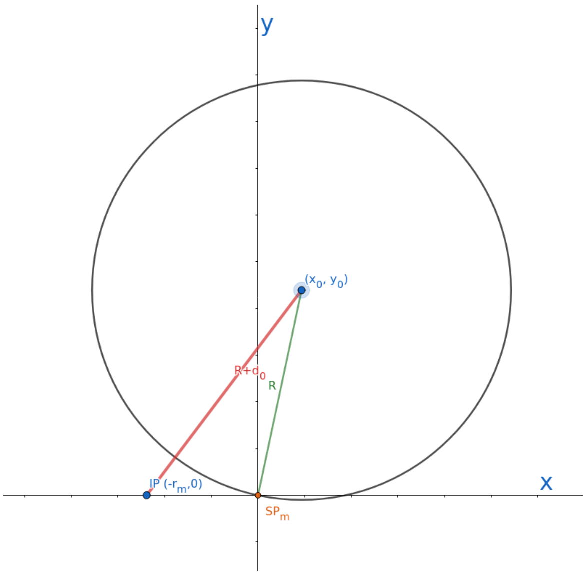

Figure 9.6: Schematic representation of the x/y reference frame with the central space-point in the origin of the frame.

reconstruction execution time while maintaining the high quality of the final track collections, only a limited number of high-quality seeds per middle SP are selected.

The seed weight (or quality score) is defined as:

$$w = c_1 \times N_t - c_2 \times d_0 - c_3 \times z_0 + \text{detector specific cuts} \tag{9.26}$$

where $c_{1,2,3}$ are configurable coefficients for each term. For PPP, $c_1 = 100$, $c_2 = 100$ and $c_3 = 1$. For SSS, $c_1 = 1$, $c_2 = 100$ and $c_3 = 0$. Table 9.2 shows the configuration parameters used for seed confirmation.

Table 9.2: List of selected configurations parameters used in ACTS seed confirmation algorithms.

`deltaInvHelixDiameter`	Allowed difference in curvature between two compatible seeds
`deltaRMin`	Minimum distance between compatible outer SPs to be considered
`compatSeedWeight`	c_1 factor in eq:score for seed score calculation
`impactWeightFactor`	c_2 factor in eq:score for seed score calculation
`zOriginWeightFactor`	c_3 factor in eq:score for seed score calculation
`maxSeedsPerSpM`	Maximum number minus one of accepted seeds per middle SP

Requirements on the number of compatible SPs and impact parameters can also be defined for different (r, z) regions of the detector (i.e. forward or central region) to classify seeds as "high-quality" seeds. Seeds that are not confirmed as "high-quality" are only selected if no other "high-quality" seed has been found for that inner-middle doublet. For optimization reasons, the algorithm only calls the seed confirmation for a certain inner-middle doublet, in case a minimum number of inner-middle-outer triplets have been found.

A limit to the number of seeds produced for each middle SP is also applied that keeps only the higher quality ones. If this limit is exceeded, the algorithm will check if there is a lower quality seed that can be removed in the seed container of that middle SP.

When a seed is accepted, the weight of that seed will be assigned to the weight of each of the SPs that form that seed if the seed weight is greater than the weight of the individual SPs. In summary, each SP will hold the weight of the best seed containing that SP. This information will be used to further select the next seeds: one seed is kept only if its weight is greater than the weight of at least one of its SP components, i.e., a seed is discarded if another seed with greater weight is constructed from at least one of its SPs.

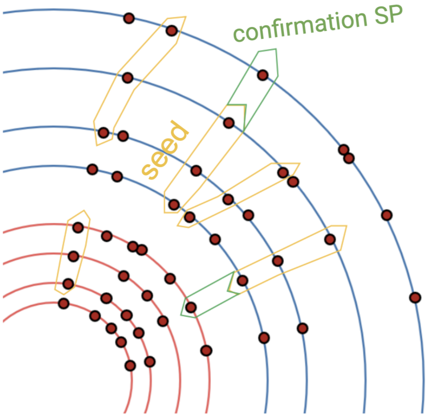

Figure 9.7: Schematic representation of track seeds consisting of triplets of space-points in different sub-detectors. The seed is represented in yellow and example of confirmation space-points compatible with the seed curvature are represented in green. Image taken and adapted from [256].

9.3 Validation of ACTS ITk Seeding

The implementation procedure was divided into two steps: the first step is the implementation of the changes to ACTS and validation of the code using ACTS stand-alone to quickly understand the differences between each step of the two seeding algorithms to guarantee equivalent performance. In order to do so, an SP reader was implemented in ACTS to read SPs produced from Athena via CSV files. After achieving a one-to-one comparison in ACTS stand-alone, the second step consists of the integration of ACTS in Athena and the final validation. For the ACTS integration, it was necessary to define an Event Data Model (EDM) that contains the event information and allows for the communication between the different components of Athena and ACTS. The proper configuration that runs ACTS ITk seeding was implemented in Athena. These features were ported into the master branch of Athena.

In this section, the results of the seeding performance comparison between the two implementations is presented for both SSS and PPP seeds. $50k$ single μ events with different values of transverse momentum ($p_T = 1, 10, 100$ GeV) were used in the validation, together with $10k$ $t\bar{t}$ events with no pile-up and 500 $t\bar{t}$ with pile-up $<\mu>= 200$ with center-of-mass energy $\sqrt{s} = 14$ TeV. Several different seed quantities from seeds produced after the seeding algorithms were used in the comparison, such as the seed impact parameter (d_0), pseudorapidity (η) and transverse momentum (p_T). For each seed produced, PPP or SSS, if a reconstructed track was obtained, then the properties of the track were compared between ACTS and Athena. The result of the comparison between the two implementations was presented for tracks reconstructed from both SSS and PPP seeds. Different track quantities were used in the comparison. Finally, the tracking efficiency was also validated, comparing the tracking efficiency as a function of η, the width of resolution for the transverse and longitudinal impact parameters (d_0 and z_0), azimuthal angle (ϕ) and polar angle (θ) of the transverse momentum resolution ($p_T \cdot \frac{q}{p_T}$).

Figure 9.8 to 9.10 show examples of quantities used in the validation between the two implementations. An excellent agreement was achieved for both PPP and SSS seeds. This shows that the same logic of the seed finding algorithm present in the ATLAS software was implemented in ACTS and that ACTS can be an excellent tool in the reconstruction of charged particles for the HL-LHC. ACTS parameters can still be optimized creating possibilities for achieving an even better performance. Additionally, the code is designed to be flexible, maintainable, and easily configurable. Written in modern C++, it leverages state-of-the-art libraries and is well-documented in Ref. [1].

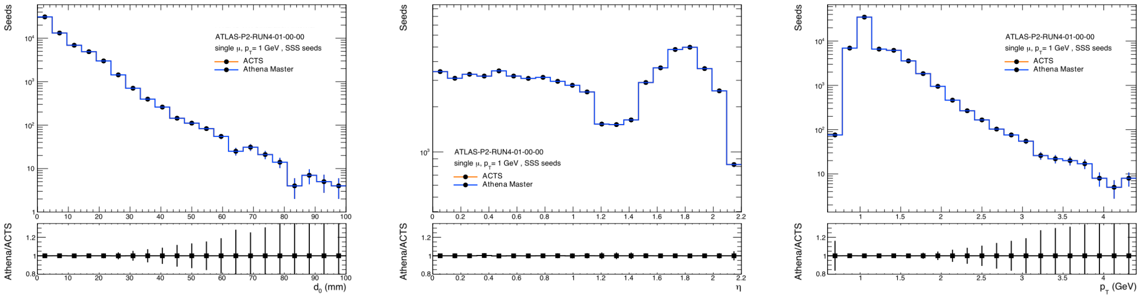

(a) Number of seeds vs d_0 **(b)** Number of seeds vs η **(c)** Number of seeds vs p_T

Figure 9.8: Comparison between Athena and ACTS seeding algorithm for SSS seeds produced from $50k$ single μ events with $p_T = 1$ GeV.

9.4 CPU Optimization of the Seeding

To handle high multiplicity environments effectively, the mid–point seeding algorithm has been significantly enhanced with algorithmic and implementation optimizations. These improvements aim to reduce processing time while maintaining overall physics performance. Key changes include strategies to minimize unnecessary computations and iterations during seed formation. This involves organizing objects such as doublets, and triplets based on specific criteria (e.g., SP radius, doublet slope, triplet

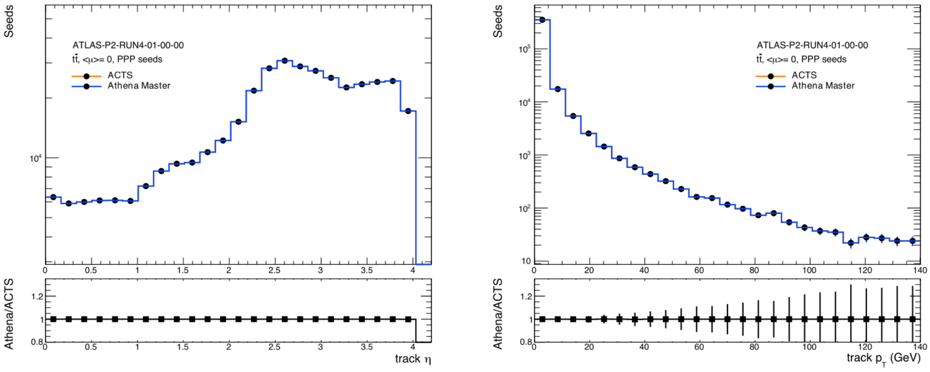

(a) Number of seeds vs track η **(b)** Number of seeds vs track p_T

Figure 9.9: Comparison between Athena and ACTS tracks reconstructed from PPP seeds for $10k$ $t\bar{t}$ events with $<\mu>=0$.

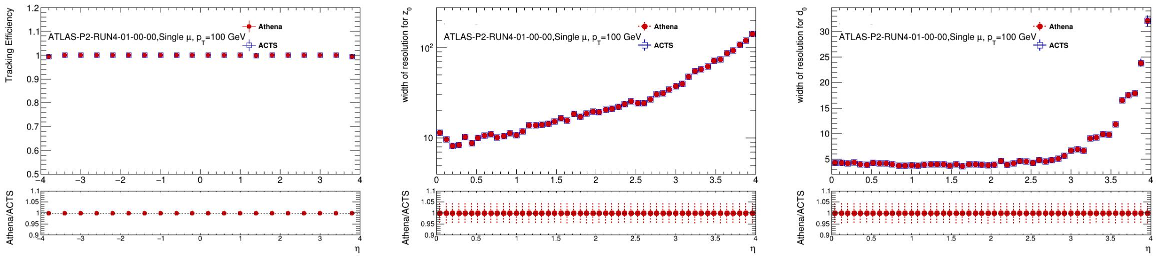

(a) Tracking efficiency vs η **(b)** Resolutions for z_0 vs η **(c)** Resolutions for d_0 vs η

Figure 9.10: Tracking efficiency between Athena and ACTS tracks reconstructed from SSS seeds for $50k$ single μ events with $p_T = 100$ GeV.

helix radius) at different stages of the code (doublet finding, triplet finding, seed confirmation). This allows for the use of binary searches instead of linear searches, the efficiency of finding combinations in large datasets is significantly improved, resulting in a time complexity of $\mathcal{O}(\log n)$ instead of $\mathcal{O}(n)$. Additionally, the sorting process is relatively cost-effective compared to iterating through all elements.

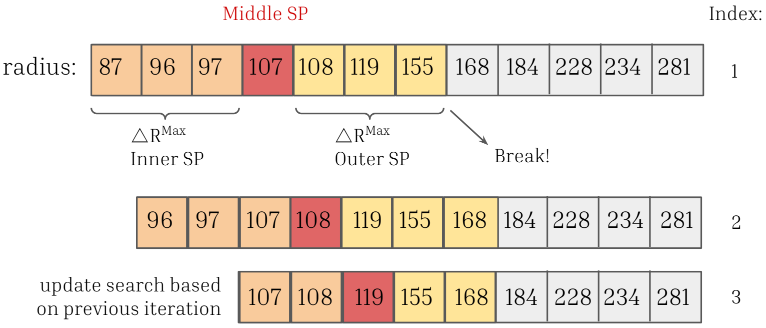

Figure 9.11: Illustration of the triplet formation process using a binary range search implemented in ACTS mid-point seeding.

Figure 9.11 provides a schematic representation of triplet formation. For each middle SP, the algorithm checks for compatible inner and outer doublet candidates, considering factors such as the radial distance between components. Since the SPs are sorted, subsequent iterations can update based on previous results, thereby skipping unnecessary combinations and improving overall efficiency.

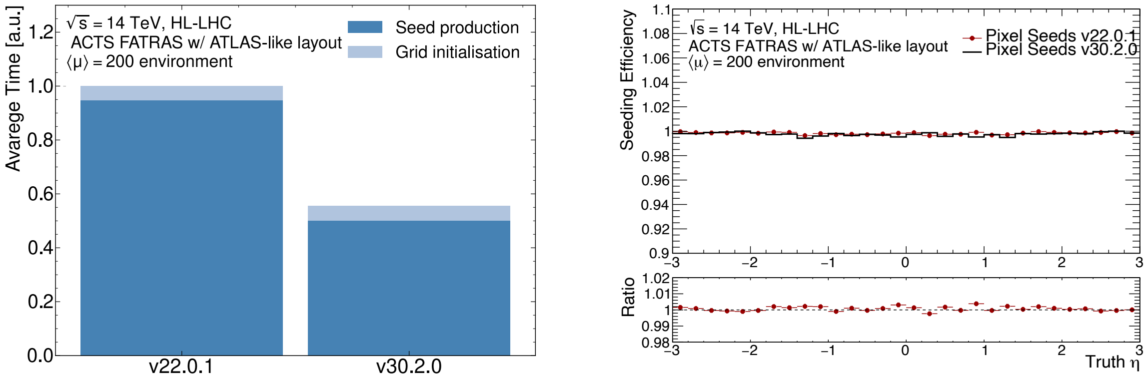

(a) **(b)**

Figure 9.12: Average seeding time in arbitrary units (a) and seeding efficiency (b) comparing ACTS version 22.0.1 and 30.2.0 using an ATLAS-like geometry. The average time for reconstructing triplets from hits in the pixel detector (PPP) is plotted separately for grid initialisation and seed production for pixel sub-detector [3].

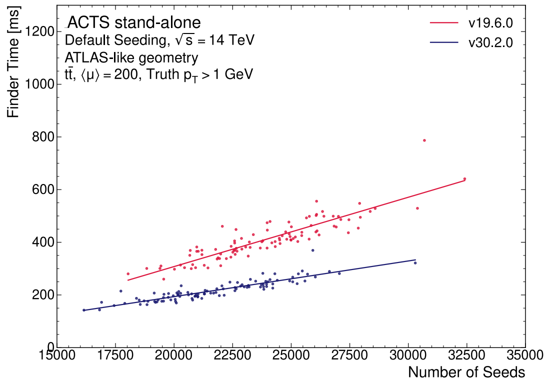

Figure 9.13: Seed finder time as a function of the number of output seeds comparing ACTS version 22.0.1 and 30.2.0 using an ATLAS-like geometry. The average time for reconstructing triplets from hits in the pixel detector (PPP) is plotted separately for grid initialisation and seed production for pixel sub-detector.

Additionally, the neighboring SP search logic was completely refactored to improve its efficiency and add new features. Memory usage was optimized through better memory allocation techniques, and a significant code restructuring was undertaken to enhance readability, maintainability, and performance, all without altering functionality.

To assess performance changes compared to previous versions of ACTS, studies were conducted within the ACTS example framework using a detector geometry similar to that of the Phase-II ATLAS. Pythia8 [257] was used to generate $t\bar{t}$ events with $\langle\mu\rangle = 200$. Detector interactions of the generated particles were simulated using the ACTS FAst TRAcking Simulation (FATRAS) [258], and a smearing algorithm was applied to replicate the input measurements based on the simulated hits in the Pixel detector. It is important to note that FATRAS currently does not simulate hadronic activity [16]. Seed efficiency is determined on a truth particle basis: a seed is matched to a truth particle if all three hits are associated with that particle. The seeding efficiency is determined by the ratio of truth particles matched to at least one seed to the total number of truth particles. Selection criteria, applied to retain only relevant truth particles, can vary depending on the algorithm's performance evaluation. Unless specified otherwise, the criteria are: only charged truth particles originating from interaction points ($R < 20\,\mathrm{mm}$ and $z_0 < 1\,\mathrm{m}$) with momentum greater than 150 MeV.

A reduction of about two times in execution time per pixel seed (PPP) when comparing version 22.0.1 and 30.2.0 was achieved, as shown in Figure 9.12a. Figure 9.12b shows the seeding efficiency as a function of the truth particle pseudorapidity. The results are basically identical, with differences smaller than one permille point. Figure 9.13 shows the performance improvements in the seed finder time as functions of the number of output seeds.

10

Expected ACTS Performance for Phase-II Reconstruction

Contents

As detailed in Section 7.3.1 and Chapter 9, the ATLAS Collaboration has adopted the ACTS framework for the Phase-II reconstruction software. The complete set of algorithms in the ITk track reconstruction chain has been successfully deployed and integrated into the ATLAS ITk tracking workflow. The integration of the seeding algorithm was described in Chapter 9. This chapter focuses on the current physics and CPU performance results for Phase-II track reconstruction with ACTS, beginning with a comparison to the Athena counterpart in Section 10.1, where the performance of various algorithms is evaluated. Section 10.2 describes the ongoing optimization campaign of ACTS within the ATLAS software. Finally Section 10.3 presents the current status and performance of the ACTS-based Fast Tracking configuration.

10.1 Performance of the ATLAS ACTS-based Tracking

A fully ACTS-based tracking chain has been successfully implemented for the ITk, with conceptually equivalent implementations of the algorithms used in the standard ATLAS tracking software. The performance of several algorithms within this chain has been evaluated. The results presented here reflect the current performance; however, ongoing optimization efforts are expected to yield further improvements. These algorithms and tools are integrated into the Athena framework, and each Athena release is coupled with a specific version of ACTS, incorporated as an external dependency. The tracking performance results in this section are based on Athena release 24.0.12 built including ACTS version v29.1.0 and compared to non-ACTS counterpart. All the quantities have been evaluated using the same set of $t\bar{t}$ events at $\langle\mu\rangle = 200$ with a center-of-mass energy of $\sqrt{s} = 14$ TeV.

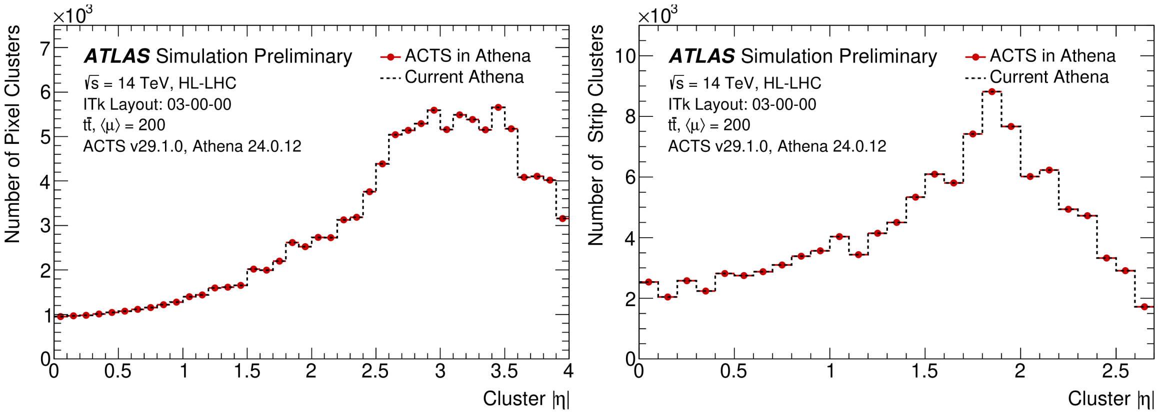

(a)

(b)

Figure 10.1: Average number of reconstructed pixel (a) and strip (b) clusters per event as a function of the cluster $|\eta|$. The distributions are shown both for the Athena framework running the current implementation of the clustering algorithm (comparable to the one used during Run 3 operations) and a modified version including the ACTS toolkit. The quantities have been computed on the same set of $t\bar{t}$ events at $\langle\mu\rangle = 200$ with a centre of mass energy of $\sqrt{s} = 14$ GeV, using the ITk Layout 03-00-00. Exactly identical physics results are achieved with the Athena software's version 24.0.12 and ACTS v29.1.0 [259].

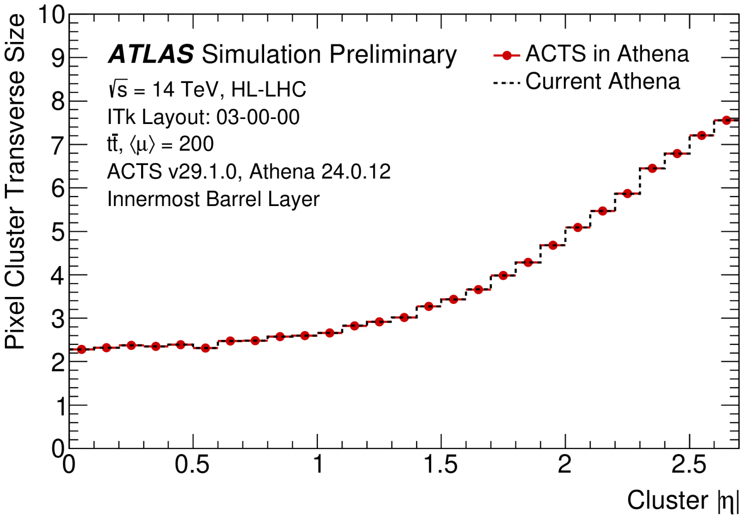

Figure 10.2: Average pixel cluster size for the innermost barrel layer along the transverse direction expressed in number of cells as a function of the cluster $|\eta|$. The distributions are shown both for the Athena framework running the current implementation of the clustering algorithm (comparable to the one used during Run 3 operations) and a modified version including the ACTS toolkit. The quantities have been computed on the same set of $t\bar{t}$ events at $\langle\mu\rangle = 200$ with a centre of mass energy of $\sqrt{s} = 14$ GeV, using the ITk Layout 03-00-00. Exactly identical physics results are achieved with the Athena software's version 24.0.12 and ACTS v29.1.0 [259].

For efficiency and resolution plots, tracks are truth-matched to particles using a truth-matching probability. This probability is defined as the ratio of shared hits between a track and a particle to the total hits on the track. Pixel hits are assigned a double relative weight with respect to strip measurements. All results were obtained using the ITk Layout 03-00-00, described in Section 7.1. The reconstruction chain follows the methodology outlined in Section 8.1.

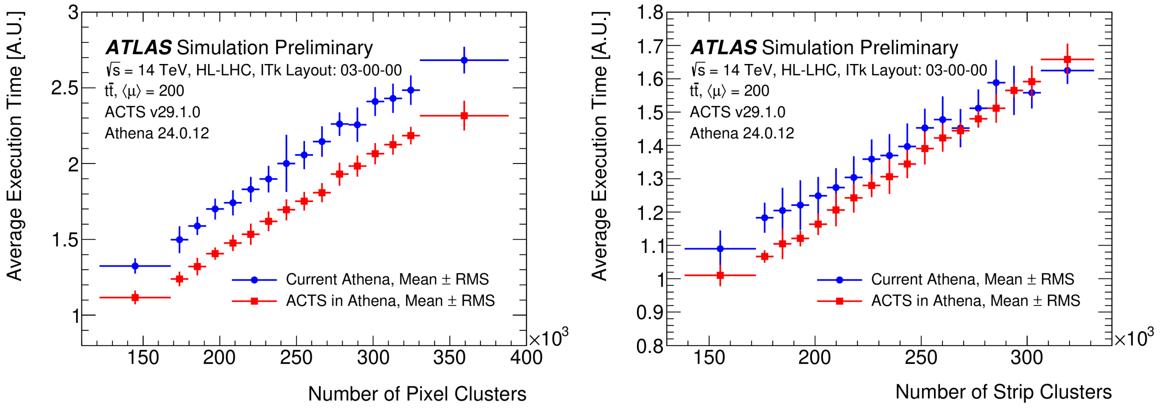

(a) **(b)**

Figure 10.3: Average execution wall-time, in arbitrary units, of the pixel (a) and strip (b) clustering algorithms as a function of the number of reconstructed pixel clusters, comparing the current Athena algorithm (similar to the one used during Run 3 operations) and a modified version including the ACTS toolkit. The time measurements were computed by running on a x86_64 machine on the same set of $t\bar{t}$ events at $\langle\mu\rangle = 200$ with a centre of mass energy of $\sqrt{s} = 14$ GeV, using the ITk Layout 03-00-00 [259].

Figure 10.1 shows the average number of reconstructed pixel and strip clusters per event as a function of the cluster $|\eta|$, while Figure 10.2 presents the average transverse size of pixel clusters for the innermost barrel layer as a function of $|\eta|$, comparing the Athena and ACTS clustering algorithms. Both ACTS and Athena clustering algorithms yield identical physics results, with complete agreement in the number and size of clusters. Figure 10.3 illustrates the average execution time of the pixel and strip clustering algorithms for both ACTS and Athena as a function of the number of reconstructed clusters. The ACTS algorithm demonstrates consistent timing improvements, reducing the average execution time per event by 15% for pixel clustering and 5% for strip clustering, all while maintaining identical physics performance.

The seeding efficiency is defined as the ratio between the number of reconstructed seeds matched to truth particles and all selected truth particles. The particles considered must satisfy $p_{\mathrm{T}} > 1$ GeV and $|\eta| < 4.0$, and be produced by the primary interactions. A seed is matched to a truth particle if at least 50% of the seed measurements belongs to the truth particle, which means that two out of the three SP components are matched. The total seeding efficiency as a function of η of the associated truth particle is shown in Figure 10.4 comparing the Athena and ACTS seeding algorithms. The independent pixel-only and strip-only seeding efficiencies are shown for ACTS algorithm. Identical results are obtained with comparable CPU performance.

More detailed performance evaluation of ACTS seeding was presented in Chapter 9.

Requirements	Pseudorapidity interval		
	$\|\eta\| < 2.0$	$2.0 < \|\eta\| < 2.6$	$2.6 < \|\eta\| < 4.0$
pixel + strip hits	≥ 7	≥ 7	≥ 7
pixel hits	≥ 1	≥ 1	≥ 1
holes	≤ 2	≤ 2	≤ 2
p_T^{reco} [MeV]	> 900	> 400	> 400
$\|d_0\|$ [mm]	≤ 2.0	≤ 2.0	≤ 10.0
$\|z_0\|$ [cm]	≤ 20.0	≤ 20.0	≤ 20.0

Table 10.1: Track selection applied during the track reconstruction in different pseudorapidity intervals. The longitudinal and transverse impact parameters, z_0 and d_0, are defined with respect to the mean position of the beam spot.

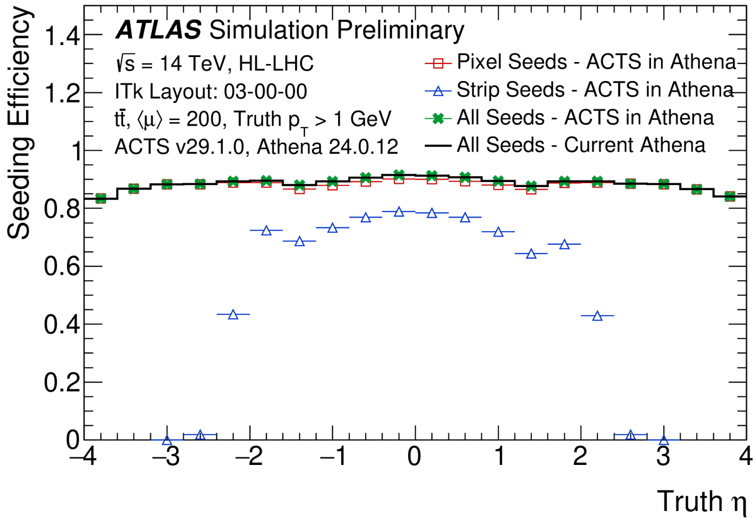

Figure 10.4: Seeding efficiency as a function of the pseudo-rapidity η of the associated truth particle, in $t\bar{t}$ events at $\langle\mu\rangle = 200$ with a centre of mass energy of $\sqrt{s} = 14$ GeV, using the ITk Layout 03-00-00. Results are obtained with the Athena framework running the current implementation of the seeding algorithm, optimised for the ITk detector and Run 4 operations, or a modified version including the ACTS toolkit. Exactly identical seeding efficiency is achieved using the Athena software's version 24.0.12 and ACTS v29.1.0. The independent pixel-only and strip-only seeding efficiencies are also shown for seeds computed using the ACTS toolkit [259].

Tracking efficiency of the ACTS CKF algorithm is shown in figure 10.5 and the resolution of the reconstructed transverse impact parameter in Figure 10.6 both as a function of η of the associated truth particle. The performance of the ACTS CKF is shown for $t\bar{t}$ events at $\langle\mu\rangle = 200$, as well as single-muon events with p_{T} of 1 GeV and 10 GeV without pile-up. This algorithm is a reimplementation and improvement of the current Athena CKF, with ongoing physics and resource optimizations. The efficiency is defined as the ratio between the number of reconstructed tracks matched to truth particle and all selected truth particles. The truth particles considered must satisfy $p_{\mathrm{T}}> 1$ GeV and $|\eta| < 4.0$, and be produced by the primary interactions and are matched to a reconstructed track if the matching probability is larger than 50%. Ambiguities between measurements and tracks are resolved using the ambiguity solver module implemented in Athena and used during Run 3 operations. Final tracks are fulfilling the following list of requirements described in Table 10.1.

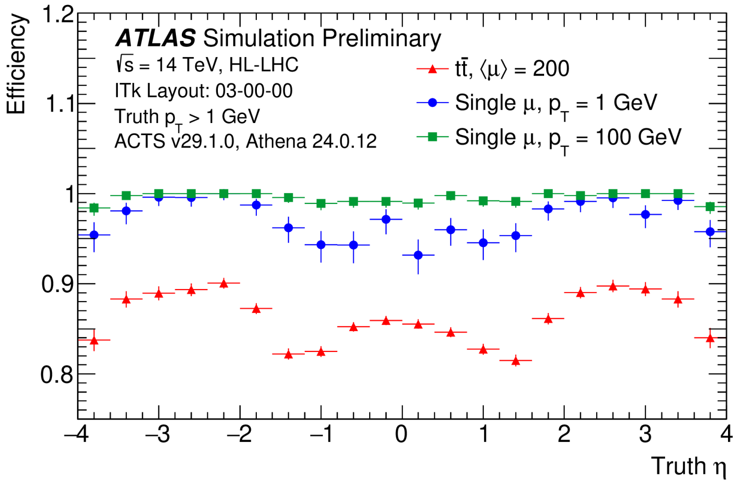

Figure 10.5: Tracking efficiency as a function of the pseudo-rapidity η of the associated truth particle using the ITk Layout 03-00-00 for $t\bar{t}$ events at $\langle\mu\rangle = 200$, as well as single muon events with of 1 GeV and 10 GeV without pile-up. Track candidates are reconstructed using the ACTS Combinatorial Kalman Filter from ACTS v29.1.0 in Athena 24.0.12 [259].

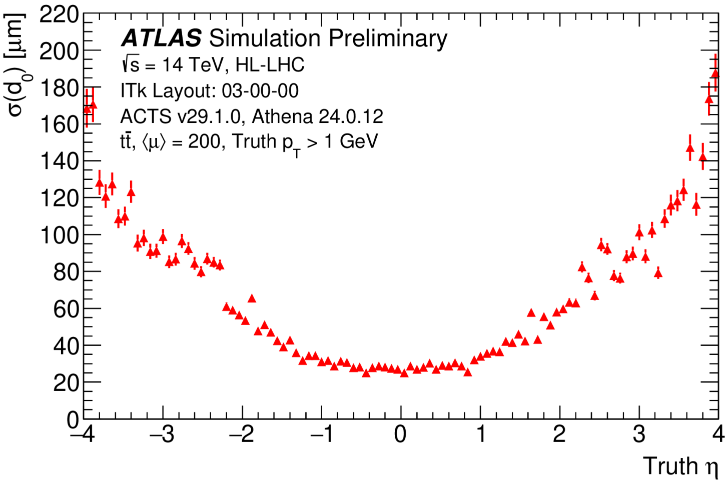

Figure 10.6: Resolution of the reconstructed transverse impact parameter $\sigma(d_0)$ as a function of the pseudo-rapidity η of the associated truth particle using the ITk Layout 03-00-00 for $t\bar{t}$ events at $\langle\mu\rangle = 200$. Track candidates are reconstructed using the ACTS Combinatorial Kalman Filter from ACTS v29.1.0 in Athena 24.0.12 [259].

10.2 ACTS CPU Improvements and Performance

A continuous optimization effort has enhanced various components of the track reconstruction code in both ACTS and the ATLAS software. Transitioning to ACTS requires modifications to the ATLAS Event Data Model (EDM) [233], including adopting the ACTS track representation and ensuring compatibility with the ATLAS xAOD infrastructure. These CPU improvements focus primarily on the EDM and the CKF module used in track finding, while preserving the physics performance shown in the previous section.

Figure 10.7 illustrates the progressive reduction in single-thread CPU time needed to reconstruct the same set of $t\bar{t}$ events at $\langle\mu\rangle = 200$, as improvements were incrementally applied to the ACTS-based ITk track reconstruction within the ATLAS software. Throughout the evaluation period, the default non-ACTS ITk track reconstruction software remained unchanged, serving as a consistent reference. The performance gains are based on the CPU time spent specifically on track finding, measured in the same Athena release for both ACTS-based and non-ACTS configurations. The labels along the horizontal axis denote improvements implemented chronologically and described below:

1. **Ready for Optimization:** Initial fully functional version of the ACTS-based ITk track reconstruction in Athena 24.0.24 (ACTS v32.0.2), deployed on 15 February 2024, performing six times slower than the non-ACTS ITk track finding.
2. **Branching Elimination:** Configured the CKF to consider only a single branch and produce one track candidate per input seed.
3. **Bi-directional Track Finding:** Enabled seed segment extension both inward (toward the interaction point) and outward.
4. **EDM Optimization (Seed Containers):** Improved storage and access of seed containers.
5. **EDM Optimization (Track Containers):** Enhanced usage of the internal representation of track containers.
6. **Branch Stoppers:** Introduced early branch-aborting conditions to terminate track finding when a candidate is not expected to lead to a good track.
7. **EDM Optimization (Navigation):** Simplified navigation between track states and measurements.
8. **Seed Fitting Disabled:** Removed seed parameter refinement using the Kalman filter, shown to have minimal impact on tracking performance.
9. **Measurement Selector Optimization:** Improved selection and calibration of measurements used in the CKF.
10. **Stepper Optimization:** Faster implementation of the propagation stepping code.
11. **Handling of Outliers:** Introduced a dedicated compatibility criterion to reduce the number of outliers allowed per track and stop track finding earlier. Outliers are defined as measurements with low compatibility with the predicted trajectory based on a χ^2 criterion.
12. **Avoid Unnecessary Extrapolation:** Avoided unnecessary extrapolation at the end

of track finding when it has already been performed.

13. **Improved Mapping to Geometry:** Enhanced mapping of detector elements and measurements to tracking geometry surfaces.

The combined optimization efforts have reduced the CPU requirements for ACTS-based ITk track finding by a factor of 5.4 when using Athena 25.0.16 (ACTS v36.2.1). This optimization brings the average CKF CPU time to only 8.5% slower than the default non-ACTS counterparts. The optimization process remains ongoing, with a focus on refining algorithmic implementation and configuration.

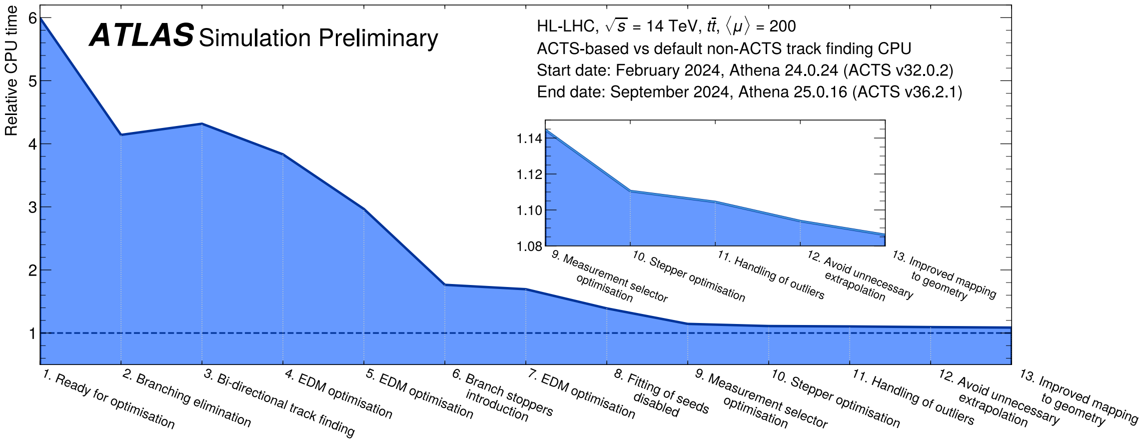

Figure 10.7: Incremental reduction in CPU time required to reconstruct $t\bar{t}$ events at $\langle\mu\rangle = 200$ as successive improvements are implemented in the ACTS-based ITk track reconstruction within the ATLAS software framework, Athena. The CPU time shown accounts exclusively to the track-finding step and is presented relative to the current non-ACTS counterparts. A zoomed view of the last five data points is also included. The timeline begins on 15 February 2024, using Athena 24.0.24 (ACTS v32.0.2). Improvements are shown chronologically along the horizontal axis. The final data point corresponds to the CPU time recorded on 10 September 2024 with Athena 25.0.16 (ACTS v36.2.1).

10.3 ACTS-based Fast Tracking Performance

An ACTS-based track reconstruction workflow based on the Fast Tracking configuration described in Section 7.3.2 has been fully integrated into ACTS with the goal of delivering excellent physics performance while staying within the CPU resource constraints of the HL-LHC. Its performance has been evaluated and compared to existing configurations.

Figure 10.8 presents the total execution time required to reconstruct $t\bar{t}$ events at $\langle\mu\rangle = 200$, comparing the non-ACTS tracking chain in both the default and Fast Tracking configurations with the ACTS-based tracking chain in the Fast Tracking configuration. The measurements are shown separately for the combined Seeding and Track Finding steps, as well as for the Ambiguity Solving step. The figure highlights

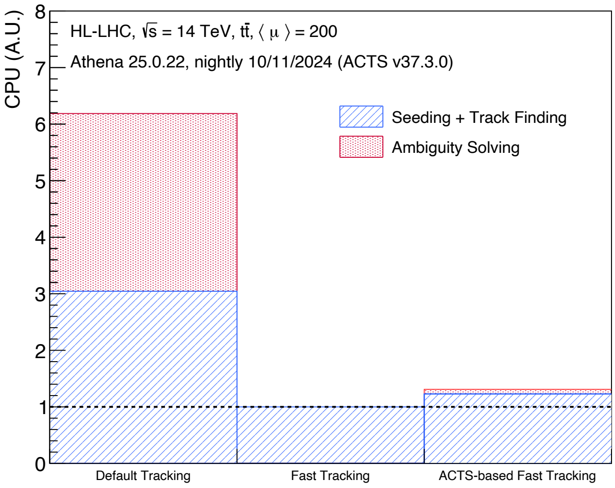

Figure 10.8: Total execution wall-time (in arbitrary units) required to reconstruct $t\bar{t}$ events at $\langle\mu\rangle = 200$ using Athena 25.0.22 (ACTS v37.3.0). The comparison includes the non-ACTS tracking chain with both the default and Fast Tracking configurations, alongside the ACTS-based tracking chain in the Fast Tracking configuration. Execution times are presented separately for the Seeding and Track Finding algorithms combined, as well as for the Ambiguity Solving algorithm.

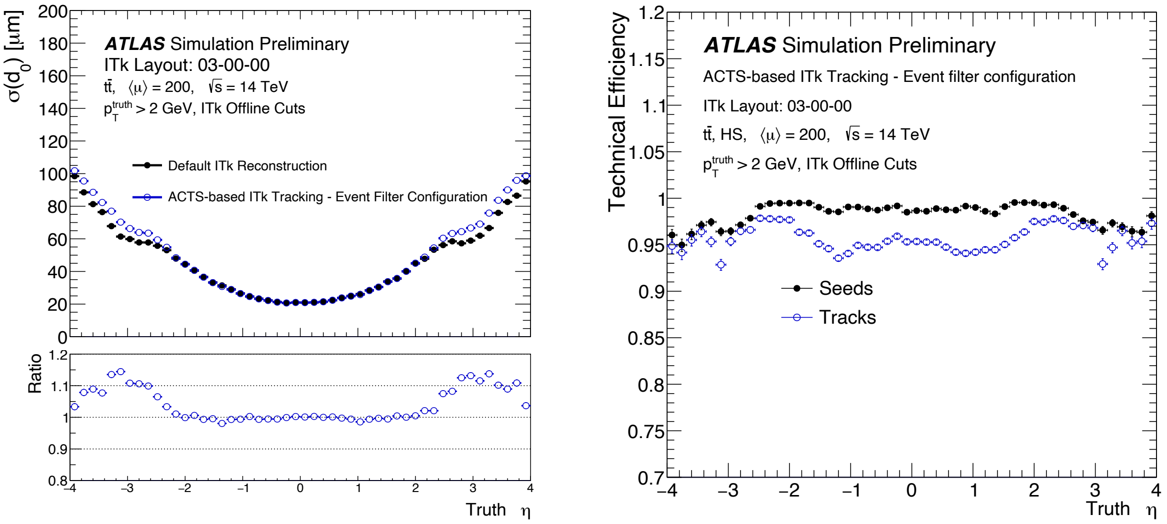

(a) **(b)**

Figure 10.9: Track parameter resolution for transverse impact parameter d_0 as a function of the true pseudorapidity for tracks comparing the ACTS-based ITk track reconstruction with Fast Tracking configuration, referred to as Event Filter configuration in the plot, and the default non-ACTS ITk track reconstruction software (a). Seeding and tracking technical efficiency as a function of the true pseudorapidity using the ACTS-based ITk track reconstruction with Fast Tracking configuration (b).

that, for the default reconstruction, most of the execution time is spent in the ambiguity solving step, specifically in the track fitting process performed during ambiguity resolution. As outlined in Section 7.3.2, the non-ACTS Fast Tracking configuration introduces assumptions during the track finding step to reduce the number of tracks. Additionally, cluster calibration allows for a more accurate estimation of track parameters, eliminating the need for track fitting in the ambiguity solving step. This approach demonstrates a significant speed-up, achieving approximately six times faster execution than the default tracking configuration. In contrast, the ACTS-based Fast Tracking configuration performs track fitting within the CKF step. It achieves comparable performance, being only 1.25 times slower than the non-ACTS Fast Tracking prototype. The non-ACTS Fast Tracking configuration removes the ambiguity-solving step entirely. However, ideally, you still want a module that resolves ambiguities within dense jet cores. This processing time was also represented in the plot for ACTS-based measurements.

Figure 10.9a compares the transverse impact parameter resolution between the ACTS-based ITk track reconstruction with the Fast Tracking configuration and the default non-ACTS ITk track reconstruction. Figure 10.9b illustrates the technical efficiency for seeds and tracks in the ACTS-based Fast Tracking configuration, which can be compared to the plots in Chapter 8. These results are very promising for tracking performance, showing significant potential for both physics and CPU optimization. While ongoing improvements are anticipated, these initial results demonstrate the viability of the Fast Tracking approach.

10.4 Discussion

This chapter has presented the current performance of ACTS-based tracking for Phase-II reconstruction, showing comparable physics and CPU performance with the existing Athena-based algorithms. A fully ACTS-based ITk reconstruction chain is implemented in ACTS framework, with seeding and clustering algorithms performing identically to their Athena counterparts. The ACTS CKF exhibits robust tracking efficiency and resolution, with ongoing optimization efforts to reduce CPU consumption. A dedicated CPU improvement campaign has resulted in a factor of 5.4 reduction in computational cost for ACTS-based ITk track finding, achieving similar performance to the default non-ACTS reconstruction. Additionally, the integration of the ACTS-based Fast Tracking configuration has shown promising results, achieving comparable execution times while maintaining excellent tracking performance. These results confirm that ACTS is an efficient solution for Phase-II track reconstruction and continued optimization efforts will further improve its performance.

Part IV

Conclusions

“Tem o certo. Tem o errado. E tem todo o resto.”
Cazuza

11

Conclusions

Following the discovery of the Higgs boson, one of the central objectives of the LHC has been to precisely measure its properties and probe for potential signs of new physics beyond the Standard Model (BSM). Among these efforts, the study of Higgs boson pair production (HH) provides a direct means to access the Higgs self-coupling, a crucial parameter in understanding electroweak symmetry breaking (EWSB). While searches have predominantly focused on gluon-gluon fusion (ggF) and vector boson fusion (VBF) due to their higher cross-sections, the associated production of Higgs pairs with top quarks ($t\bar{t}HH$) also offers a unique probe of the quartic top-Higgs coupling.

This thesis presents the first ATLAS search for $t\bar{t}HH$ production, a rare and experimentally challenging process that offers unique access to the quartic top-Higgs interaction. This work precedes the ATLAS publication on this production mode and the author of this dissertation has strongly contributed to make it possible. Using the full Run 2 and partial Run 3 dataset, corresponding to an integrated luminosity of 140 and 59 fb^{-1}, respectively, an upper limit on the signal strength was established, with an observed (expected) limit of 30.8 (24.6) times the SM prediction at 95% confidence level. No significant excess above the SM expectation was observed. While $t\bar{t}HH$ has a lower production rate compared to other HH channels, it provides direct sensitivity to BSM effects through top-Higgs interactions. In the framework of Effective Field Theories (EFTs), this thesis explores potential deviations from the SM by interpreting the 1L channel in terms of limits on the top-Higgs quartic interaction, parameterised by $c_{t\bar{t}HH}$. The top-Higgs quartic modifier is constrained to be in the range $-4.77 < c_{t\bar{t}HH} < 4.32$ ($-4.04 < c_{t\bar{t}HH} < 3.58$ expected) at 95% CL, assuming the SM scenario.

The results obtained in this analysis are the first step towards a broader exploration of this process. This search is a milestone in extending our current knowledge on the high-flavour phase-space that is poorly described by MC. Despite the difficulty of this measurement, its long-term prospects of constraining EFTs are promising, especially in the context of the HL-LHC, where increased data and improved detector technology will significantly enhance sensitivity.

However, the expected sensitivity to HH production at the LHC remains limited even in the dominant ggF and VBF channels, with only hints of possible evidence expected in Run 3. Part III of this thesis presents improvements in track reconstruction, which will be important in enhancing HH searches at the HL-LHC, including $t\bar{t}HH$, by improving b-tagging, vertex reconstruction, and forward jet identification.

The expected tracking performance of the ITk detector for the HL-LHC phase was presented in Chapter 7 showing that the ITk design and ATLAS tracking software maintain high efficiency despite increased pile-up. The redundancy in high-precision silicon measurements enhances track seeding, ensuring robust efficiency and a low fake rate. Tracking efficiency is expected to match Run 3 levels, with a quasi-linear scaling with track multiplicity. The smaller pixel pitch in ITk ensures enhanced impact parameter resolution. Forward tracking in the extended region ($2.4 < |\eta| < 4.0$) meets the standard requirements for object reconstruction and identification. Finally, vertex reconstruction is expected to surpass Run 3 performance, exhibiting better position resolution and efficiency.

To meet the computational demands of HL-LHC tracking, this thesis also contributes to the development and optimization of tracking algorithms within the ACTS framework, designed for efficient and scalable reconstruction. Chapter 9 presented the development and optimisation of the main seeding algorithm for the ITk detector for Phase-II upgrade. A fully ACTS-based reconstruction chain for ITk tracking was implemented and demonstrated comparable or improved physics performance relative to the legacy Athena-based framework, as described in Chapter 10. Seeding and clustering algorithms are performing identically to their Athena counterparts. The CKF exhibits robust tracking efficiency and resolution, with ongoing optimization efforts to reduce CPU consumption. A dedicated CPU optimization campaign has significantly reduced computational costs while maintaining tracking efficiency and resolution. Finally, the integration of ACTS into the Fast Tracking configuration has further shown promising results, achieving about six times faster execution time relative to the nominal tracking configuration, while maintaining good physics performance. These results validate ACTS's suitability for Phase-II track reconstruction and future optimisations will further improve its performance.

Tracking at the HL-LHC will be critical not only for precision Higgs measurements but also for broader searches for new physics. The results presented here represent a strong foundation for the future of ATLAS tracking performance, ensuring that the experiment can meet its physics goals in the high-luminosity era. The next decade of data-taking and analysis will push the boundaries of our understanding, bringing us closer to answering some of the most fundamental questions in particle physics.

Bibliography

[1] ACTS Collaboration, "ACTS documentation," `https://acts.readthedocs.io/en/latest/index.html` (2024), accessed: 2024-09-23.

[2] ATLAS Collaboration, *"Expected Tracking Performance of the ATLAS Inner Tracker at the High-Luminosity LHC,"* (2024), arXiv:2412.15090 [hep-ex] .

[3] L. F. Falda Coelho, C. Allaire, F. Bouvet, N. Calace, H. Grasland, Salzburger A. Rousseau, D., S. N. Swatman, C. Varni, and B. Yeo, *"Seed finding in the acts software package: Algorithms and optimizations."* Connecting The Dots Workshop 2023 (CTD2023) (2024).

[4] ATLAS Collaboration, *"Probing the CP nature of the top–Higgs Yukawa coupling in $t\bar{t}H$ and tH events with $H{\rightarrow}b\bar{b}$ decays using the ATLAS detector at the LHC,"* Phys. Lett. B **849**, 138469 (2024), arXiv:2303.05974 [hep-ex] .

[5] ATLAS Collaboration, *"Observation of a new particle in the search for the Standard Model Higgs boson with the ATLAS detector at the LHC,"* Phys. Lett. B **716** (2012), 10.1016/j.physletb.2012.08.020.

[6] CMS Collaboration, *"Observation of a new boson at a mass of 125 GeV with the CMS experiment at the LHC,"* Phys. Lett. B **716** (2012), 10.1016/j.physletb.2012.08.021.

[7] F. Englert and R. Brout, *"Broken Symmetry and the Mass of Gauge Vector Mesons,"* Phys. Rev. Lett. **13**, 321–323 (1964).

[8] P. Higgs, *"Broken Symmetries and the Masses of Gauge Bosons,"* Phys. Rev. Lett. **13**, 508–509 (1964).

[9] P. Higgs, *"Broken symmetries, massless particles and gauge fields,"* Phys. Lett. **12**, 132–133 (1964).

[10] G. Guralnik, C. Hagen, and T. Kibble, *"Global Conservation Laws and Massless Particles,"* Phys. Rev. Lett. **13**, 585–587 (1964).

[11] P. Higgs, *"Spontaneous Symmetry Breakdown without Massless Bosons,"* Phys. Rev. **145**, 1156–1163 (1966).

[12] T. Kibble, *"Symmetry Breaking in Non-Abelian Gauge Theories,"* Phys. Rev. **155**, 1554–1561 (1967).

[13] G. Apollinari *et al.*, *High-Luminosity Large Hadron Collider (HL-LHC): Preliminary Design Report*, CERN Yellow Reports: Monographs (CERN, Geneva, 2015).

[14] ATLAS Collaboration, *ATLAS Phase-II Upgrade Scoping Document*, Tech. Rep. CERN-LHCC-2015-020. LHCC-G-166 (CERN, Geneva, 2015).

[15] D. Contardo *et al.*, *Technical Proposal for the Phase-II Upgrade of the CMS Detector*, Tech. Rep. CERN-LHCC-2015-010. LHCC-P-008. CMS-TDR-15-02 (CERN, Geneva, 2015).

[16] Xiaocong Ai *et al.*, *"A Common Tracking Software Project,"* (2021), 10.48550/ARXIV.2106.13593.

[17] Xiaocong Ai, *"Tracking with A Common Tracking Software,"* (2020), arXiv:2007.01239 [physics.ins-det] .

[18] C. Burgard, "TikZ diagram of the Standard Model of physics." `http://www.texample.net/tikz/examples/model-physics/`.

[19] S. Navas *et al.* (Particle Data Group), *"Review of Particle Physics,"* Phys. Rev. D **110**, 030001 (2024).

[20] E. Noether, *"Invariant variation problems,"* Transport Theory and Stat. Phys. **1**, 186–207 (1971).

[21] F. Halzen and A. Martin, *Quarks and leptons: an introductory course in modern particle physics* (Wiley, New York, NY, 1984).

[22] I. Aitchison and A. Hey, *Gauge theories in particle physics: a practical introduction; 3rd ed.*, Graduate student series in physics (IOP, Bristol, 2004).

[23] D. Griffiths, *Introduction to elementary particles; 2nd rev. version*, Physics textbook (Wiley, New York, NY, 2008).

[24] G. Kane, *Modern elementary particle physics: explaining and extending the standard model; 2nd ed.* (Cambridge University Press, Cambridge, 2017).

[25] P. Langacker, *The standard model and beyond; 2nd ed.*, High energy physics, cosmology and gravitation (CRC Press, 2017).

[26] G. Arnison and others (UA1 Collaboration), *"Experimental observation of isolated large transverse energy electrons with associated missing energy at* $\sqrt{s} = 540$ *GeV,"* Phys. Lett. B **122**, 103–116 (1983).

[27] G. Arnison and others (UA1 Collaboration), *"Observation of a massive neutral intermediate boson,"* Phys. Lett. B **126**, 398–410 (1983).

[28] J. Goldstone, A. Salam, and S. Weinberg, *"Broken Symmetries,"* Phys. Rev. **127**, 965–970 (1962).

[29] Ettore Majorana, *"Teoria simmetrica dell'elettrone e del positrone,"* Il Nuovo Cimento (1924-1942) **14**, 171–184 (1937).

[30] LHC Higgs Cross Section Working Group Collaboration, "Handbook of LHC Higgs Cross Sections: 4. Deciphering the Nature of the Higgs Sector," (2017), arXiv:1610.07922 [hep-ph] .

[31] Georges Aad *et al.* (ATLAS), *"Measurement of the Higgs boson mass with* $H \to \gamma\gamma$ *decays in 140* fb^{-1} *of* s*=13 TeV pp collisions with the ATLAS detector,"* Phys. Lett. B **847**, 138315 (2023), arXiv:2308.07216 [hep-ex] .

[32] Georges Aad *et al.* (ATLAS), *"Measurement of the Higgs boson mass in the* $H \to ZZ^* \to 4\ell$ *decay channel using 139* fb^{-1} *of* $\sqrt{s} = 13$ *TeV pp collisions recorded by the ATLAS detector at the LHC,"* Phys. Lett. B **843**, 137880 (2023), arXiv:2207.00320 [hep-ex] .

[33] *Combined measurement of the Higgs boson mass from the* $H \to \gamma\gamma$ *and* $H \to ZZ^* \to 4\ell$ *decay channels with the ATLAS detector using* $\sqrt{s} = 7$*, 8 and 13 TeV pp collision data*, Tech. Rep. (CERN, Geneva, 2023).

[34] *Combined measurements of Higgs boson production and decay using up to* 139 fb^{-1} *of proton-proton collision data at* $\sqrt{s} = 13$ *TeV collected with the ATLAS experiment*, Tech. Rep. (CERN, Geneva, 2021).

[35] LHC Higgs Cross Section Working Group, "LHC HXSWG interim recommendations to explore the coupling structure of a Higgs-like particle," (2012), arXiv:1209.0040 [hep-ph] .

[36] Georges Aad *et al.* (ATLAS), *"A detailed map of Higgs boson interactions by the ATLAS experiment ten years after the discovery,"* Nature **607**, 52–59 (2022), [Erratum: Nature 612, E24 (2022)], arXiv:2207.00092 [hep-ex] .

[37] CMS Collaboration, *"Constraints on the spin-parity and anomalous HVV couplings of the Higgs boson in proton collisions at 7 and 8 TeV,"* Phys. Rev. D **92**, 012004 (2015).

[38] CMS Collaboration, *"Combined search for anomalous pseudoscalar HVV couplings in* $VH(H \to b\bar{b})$ *production and* $H \to VV$ *decay,"* Phys. Lett. B **759**, 672 – 696 (2016).

[39] ATLAS Collaboration, *"Evidence for the spin-0 nature of the Higgs boson using ATLAS data,"* Phys. Lett. B **726**, 120–144 (2013), arXiv:1307.1432 [hep-ex] .

[40] ATLAS Collaboration, *"Study of the spin and parity of the Higgs boson in diboson decays with the ATLAS detector,"* Eur. Phys. J. C **75**, 476 (2015), [Erratum: Eur.Phys.J.C 76, 152 (2016)], arXiv:1506.05669 [hep-ex] .

[41] L. Evans and P. Bryant, *"LHC Machine,"* JINST **3**, S08001 (2008).

[42] S Myers and Emilio Picasso, *"The design, construction and commissioning of the CERN Large Electron Positron collider,"* Contemp. Phys. **31**, 387–403 (1990).

[43] Ewa Lopienska, *"The CERN accelerator complex, layout in 2022. Complexe des accélérateurs du CERN en janvier 2022,"* (2022), general Photo.

[44] ATLAS Collaboration, *"The ATLAS Experiment at the CERN Large Hadron Collider,"* JINST **3**, S08003 (2008).

[45] CMS Collaboration, *"The CMS experiment at the CERN LHC,"* JINST **3**, S08004 (2008).

[46] ATLAS Collaboration, "ATLAS Luminosity Public Results for Run 2," `https://twiki.cern.ch/twiki/bin/view/AtlasPublic/LuminosityPublicResultsRun2#Luminosity_summary_plots_for_201`.

[47] ATLAS Collaboration, "ATLAS Luminosity Public Results for Run 3," `https://twiki.cern.ch/twiki/bin/view/AtlasPublic/LuminosityPublicResultsRun3`.

[48] Donald H. Perkins, *Introduction to High Energy Physics*, 4th ed. (Cambridge University Press, 2000).

[49] ATLAS Collaboration, "ATLAS Luminosity Public Results for Run 1," `https://twiki.cern.ch/twiki/bin/view/AtlasPublic/LuminosityPublicResults#2010_pp_Collisions`.

[50] R. Alemany-Fernandez *et al.*, *"Operation and Configuration of the LHC in Run 1,"* (2013).

[51] R. Bruce *et al.*, *"LHC Run 2: Results and challenges," Proceedings, 57th ICFA Advanced Beam Dynamics Workshop on High-Intensity and High-Brightness Hadron Beams (HB2016): Malmö, Sweden, July 3-8, 2016*, , MOAM5P50 (2016).

[52] ATLAS Collaboration, *"Luminosity determination in pp collisions at* $\sqrt{s} = 13$ *TeV using the ATLAS detector at the LHC,"* (2019).

[53] ATLAS Collaboration, *Preliminary analysis of the luminosity calibration of the ATLAS 13.6 TeV data recorded in 2022*, Tech. Rep. (CERN, Geneva, 2023).

[54] *Preliminary analysis of the luminosity calibration for the ATLAS 13.6 TeV data recorded in 2023*, Tech. Rep. (CERN, Geneva, 2024).

[55] ATLAS Collaboration, *ATLAS detector and physics performance: Technical Design Report, 1*, Tech. Rep. CERN-LHCC-99-014 (CERN, Geneva, 1999).

[56] ATLAS Collaboration, *"The ATLAS experiment at the CERN Large Hadron Collider: a description of the detector configuration for Run 3,"* JINST **19**, P05063 (2024), arXiv:2305.16623 [physics.ins-det] .

[57] "How to draw diagrams in LaTeX with TikZ," `https://wiki.physik.uzh.ch/cms/latex:tikz`.

[58] ATLAS Collaboration, *ATLAS inner detector: Technical Design Report, 1*, Tech. Rep. CERN-LHCC-97-016 (CERN, Geneva, 1997).

[59] ATLAS Collaboration, *ATLAS inner detector: Technical Design Report, 2*, Tech. Rep. CERN-LHCC-97-017 (CERN, Geneva, 1997).

[60] ATLAS Collaboration, *"The ATLAS Inner Detector commissioning and calibration,"* Eur. Phys. J. **C70**, 787–821 (2010), arXiv:1004.5293 [physics.ins-det] .

[61] *Alignment of the ATLAS Inner Detector and its Performance in 2012*, Tech. Rep. ATLAS-CONF-2014-047 (CERN, Geneva, 2014).

[62] ATLAS Collaboration, *"ATLAS pixel detector electronics and sensors,"* JINST **3**, P07007–P07007 (2008).

[63] ATLAS Collaboration, *"Operation and performance of the ATLAS semiconductor tracker,"* JINST **9**, P08009 (2014), arXiv:1404.7473 [hep-ex] .

[64] ATLAS TRT Collaboration, in *Astroparticle, particle and space physics, detectors and medical physics applications. Proceedings, 8th Conference, ICATPP 2003, Como, Italy, October 6-10, 2003* (2003) pp. 497–501, arXiv:hep-ex/0311058 [hep-ex] .

[65] ATLAS Collaboration, *The upgraded Pixel detector and the commissioning of the Inner Detector tracking of the ATLAS experiment for Run-2 at the Large Hadron Collider*, Tech. Rep. ATL-PHYS-PROC-2016-104 (CERN, Geneva, 2016) 15 pages, EPS-HEP 2015 Proceedings.

[66] "ATLAS Collaboration", *"Study of the material of the ATLAS inner detector for Run 2 of the LHC,"* Journal of Instrumentation **12**, P12009–P12009 (2017).

[67] *Track Reconstruction Performance of the ATLAS Inner Detector at* $\sqrt{s} = 13$ *TeV*, Tech. Rep. (CERN, Geneva, 2015).

[68] "ATLAS Collaboration", *"Measurement of the photon identification efficiencies with the ATLAS detector using LHC Run 2 data collected in 2015 and 2016,"* The European Physical Journal C **79** (2019), 10.1140/epjc/s10052-019-6650-6.

[69] M.N. Agaras *et al.*, *"Laser calibration of the atlas tile calorimeter during lhc run 2,"* Journal of Instrumentation **18**, P06023 (2023).

[70] Bernd Stelzer, *The New Small Wheel Upgrade Project of the ATLAS Experiment*, Tech. Rep. (CERN, Geneva, 2016).

[71] T Kawamoto *et al.*, *New Small Wheel Technical Design Report*, Tech. Rep. (2013).

[72] A. Yamamoto *et al.*, *"The atlas central solenoid,"* Nuclear Instruments and Methods in Physics Research Section A: Accelerators, Spectrometers, Detectors and Associated Equipment **584**, 53 – 74 (2008).

[73] ATLAS Collaboration, *ATLAS barrel toroid: Technical Design Report*, Tech. Rep. (Geneva, 1997).

[74] ATLAS Collaboration, *ATLAS end-cap toroids: Technical Design Report*, Tech. Rep. (Geneva, 1997) electronic version not available.

[75] ATLAS TDAQ Collaboration, *"The ATLAS data acquisition and high level trigger system,"* JINST **11**, P06008–P06008 (2016).

[76] ATLAS Collaboration, *"Performance of the ATLAS Trigger System in 2015,"* Eur. Phys. J. **C77**, 317 (2017), arXiv:1611.09661 [hep-ex] .

[77] ATLAS Collaboration, *"The run-2 ATLAS trigger system,"* J. Phys. Conf. Ser. **762**, 012003 (2016).

[78] ATLAS Collaboration, "ATLAS experiment - Public results," `https://twiki.cern.ch/twiki/bin/view/AtlasPublic/ApprovedPlotsDAQ`, 2017.

[79] L Rossi and O Brüning, *High Luminosity Large Hadron Collider: A description for the European Strategy Preparatory Group*, Tech. Rep. (CERN, Geneva, 2012).

[80] ATLAS Collaboration, *Letter of Intent for the Phase-II Upgrade of the ATLAS Experiment*, Tech. Rep. (CERN, Geneva, 2012).

[81] CERN, "HL-LHC Project," (2024), accessed: 2024-09-23.

[82] ATLAS Collaboration, *"Technical Design Report for the Phase-II Upgrade of the ATLAS TDAQ System,"* (2017), 10.17181/CERN.2LBB.4IAL.

[83] ATLAS Collaboration, *ATLAS Liquid Argon Calorimeter Phase-II Upgrade: Technical Design Report*, Tech. Rep. (CERN, Geneva, 2017).

[84] R. Frederix, S. Frixione, V. Hirschi, F. Maltoni, O. Mattelaer, P. Torrielli, E. Vryonidou, and M. Zaro, *"Higgs pair production at the lhc with nlo and parton-shower effects,"* Physics Letters B **732**, 142–149 (2014).

[85] Biagio Di Micco *et al.*, *"Higgs boson pair production at colliders: status and perspectives. Higgs boson potential at colliders: Status and perspectives,"* Rev. Phys. **5**, 100045. 161 p (2019), arXiv:1910.00012 .

[86] M. Grazzini, G. Heinrich, S. Jones, S. Kallweit, M. Kerner, J. M. Lindert, and J. Mazzitelli, *"Higgs boson pair production at nnlo with top quark mass effects,"* Journal of High Energy Physics **2018** (2018), 10.1007/jhep05(2018)059.

[87] Frédéric A. Dreyer and Alexander Karlberg, *"Fully differential vector-boson fusion higgs pair production at next-to-next-to-leading order,"* Physical Review D **99** (2019), 10.1103/physrevd.99.074028.

[88] Frédéric A. Dreyer, Alexander Karlberg, Jean-Nicolas Lang, and Mathieu Pellen, *"Precise predictions for double-higgs production via vector-boson fusion,"* The European Physical Journal C **80** (2020), 10.1140/epjc/s10052-020-08610-7.

[89] Frédéric A. Dreyer and Alexander Karlberg, *"Vector-boson fusion higgs pair production at N3LO,"* Physical Review D **98** (2018), 10.1103/physrevd.98.114016.

[90] R. Frederix, S. Frixione, V. Hirschi, F. Maltoni, O. Mattelaer, P. Torrielli, E. Vryonidou, and M. Zaro, *"Higgs pair production at the lhc with NLO and parton-shower effects,"* Physics Letters B **732**, 142–149 (2014).

[91] ATLAS Collaboration, *"Combination of Searches for Higgs Boson Pair Production in pp Collisions at* $\sqrt{s}=13$ *TeV with the ATLAS Detector,"* Phys. Rev. Lett. **133**, 101801 (2024), arXiv:2406.09971 [hep-ex] .

[92] B. Grzadkowski, M. Iskrzyński, M. Misiak, and J. Rosiek, *"Dimension-six terms in the standard model lagrangian,"* Journal of High Energy Physics **2010** (2010), 10.1007/jhep10(2010)085.

[93] Lina Alasfar and Others, "Effective field theory descriptions of higgs boson pair production," (2024), arXiv:2304.01968 [hep-ph] .

[94] Gerhard Buchalla, Oscar Catà, and Claudius Krause, *"Complete electroweak chiral lagrangian with a light higgs at NLO,"* Nuclear Physics B **880**, 552–573 (2014).

[95] R. Alonso, M.B. Gavela, L. Merlo, S. Rigolin, and J. Yepes, *"The effective chiral lagrangian for a light dynamical "Higgs particle","* Physics Letters B **722**, 330–335 (2013).

[96] *HEFT interpretations of Higgs boson pair searches in $b\bar{b}\gamma\gamma$ and $b\bar{b}\tau\tau$ final states and of their combination in ATLAS*, Tech. Rep. (CERN, Geneva, 2022).

[97] ATLAS Collaboration, *HL-LHC prospects for the measurement of Higgs boson pair production in the $b\bar{b}b\bar{b}$ final state and combination with the $b\bar{b}\gamma\gamma$ and $b\bar{b}\tau^+\tau^-$ final states at the ATLAS experiment*, Tech. Rep. (CERN, Geneva, 2022).

[98] M. Kobayashi and T. Maskawa, *"CP-Violation in the Renormalizable Theory of Weak Interaction,"* Prog. Theor. Phys. **49**, 652–657 (1973).

[99] CDF Collaboration, *"Observation of Top Quark Production in $\overline{p}p$ Collisions with the Collider Detector at Fermilab,"* Phys. Rev. Lett. **74**, 2626–2631 (1995).

[100] D0 Collaboration, *"Observation of the Top Quark,"* Phys. Rev. Lett. **74**, 2632–2637 (1995).

[101] Michał Czakon, Paul Fiedler, and Alexander Mitov, *"Total top-quark pair-production cross section at hadron colliders through (α_s^4),"* Physical Review Letters **110** (2013), 10.1103/physrevlett.110.252004.

[102] *Measurement prospects of the pair production and self-coupling of the Higgs boson with the ATLAS experiment at the HL-LHC*, Tech. Rep. (CERN, Geneva, 2018).

[103] Carlos Bautista, Leonardo de Lima, Ricardo D'Elia Matheus, Eduardo Pontón, Leônidas A. Fernandes do Prado, and Aurore Savoy-Navarro, *"Probing the top-higgs sector with composite higgs models at present and future hadron colliders,"* Journal of High Energy Physics **2021** (2021), 10.1007/jhep03(2021)049.

[104] Fabio Maltoni, Davide Pagani, and Xiaoran Zhao, *"Constraining the higgs self-couplings at e+e- colliders,"* Journal of High Energy Physics **2018** (2018), 10.1007/jhep07(2018)087.

[105] Tao Liu, Kun-Feng Lyu, Jing Ren, and Hua Xing Zhu, *"Probing the quartic higgs boson self-interaction,"* Physical Review D **98** (2018), 10.1103/physrevd.98.093004.

[106] R. Gröber and M. Mühlleitner, *"Composite higgs boson pair production at the lhc,"* Journal of High Energy Physics **2011** (2011), 10.1007/jhep06(2011)020.

[107] Kaustubh Agashe, Roberto Contino, and Alex Pomarol, *"The minimal composite higgs model,"* Nuclear Physics B **719**, 165–187 (2005).

[108] Claudio O Dib, Rogerio Rosenfeld, and Alfonso Zerwekh, *"Double higgs production and quadratic divergence cancellation in little higgs models with t-parity,"* Journal of High Energy Physics **2006**, 074–074 (2006).

[109] Chuan-Ren Chen and Ian Low, *"Double take on new physics in double higgs boson production,"* Physical Review D **90** (2014), 10.1103/physrevd.90.013018.

[110] ATLAS Collaboration, *"Software performance of the ATLAS track reconstruction for LHC Run 3,"* Computing and Software for Big Science **8** (2024), 10.1007/s41781-023-00111-y.

[111] ATLAS Collaboration, *"ATLAS pixel detector electronics and sensors,"* JINST **3**, P07007 (2008).

[112] ATLAS Collaboration, *"Performance of the ATLAS track reconstruction algorithms in dense environments in LHC Run 2,"* The European Physical Journal C **77** (2017), 10.1140/epjc/s10052-017-5225-7.

[113] "ATLAS Collaboration", *"Electron reconstruction and identification in the ATLAS experiment using the 2015 and 2016 LHC proton–proton collision data at* $\sqrt{s} = 13$ *TeV,"* The European Physical Journal C **79** (2019), 10.1140/epjc/s10052-019-7140-6.

[114] *Electron efficiency measurements with the ATLAS detector using the 2015 LHC proton-proton collision data*, Tech. Rep. ATLAS-CONF-2016-024 (CERN, Geneva, 2016).

[115] W Lampl, S Laplace, D Lelas, P Loch, H Ma, S Menke, S Rajagopalan, D Rousseau, S Snyder, and G Unal, *Calorimeter Clustering Algorithms: Description and Performance*, Tech. Rep. (CERN, Geneva, 2008).

[116] ATLAS Collaboration, "Electron efficiency measurements with the ATLAS detector using the 2012 LHC proton–proton collision data," ATLAS-CONF-2014-032 (2014).

[117] ATLAS Collaboration, *"Electron and photon performance measurements with the ATLAS detector using the 2015–2017 LHC proton-proton collision data,"* Journal of Instrumentation **14**, P12006 (2019).

[118] A. Hoecker *et al.*, *"TMVA - Toolkit for Multivariate Data Analysis,"* (2007), arXiv:physics/0703039 [physics.data-an] .

[119] ATLAS Collaboration, *"Muon reconstruction performance of the ATLAS detector in proton–proton collision data at* $\sqrt{s} = 13$ *TeV,"* EPJ C **76** (2016), 10.1140/epjc/s10052-016-4120-y.

[120] ATLAS Collaboration (ATLAS), *"Muon reconstruction and identification efficiency in ATLAS using the full Run 2 pp collision data set at* $\sqrt{s} = 13$ *TeV,"* Eur. Phys. J., C **81**, 578 (2021), arXiv:2012.00578 .

[121] ATLAS Collaboration, *"Jet reconstruction and performance using particle flow with the ATLAS detector,"* The European Physical Journal C **77** (2017), 10.1140/epjc/s10052-017-5031-2.

[122] Matteo Cacciari, Gavin P Salam, and Gregory Soyez, *"The anti-ktjet clustering algorithm,"* Journal of High Energy Physics **2008**, 063–063 (2008).

[123] ATLAS Collaboration, *"Jet energy scale and resolution measured in proton–proton collisions at $\sqrt{s} = 13$ TeV with the ATLAS detector,"* Eur. Phys. J. C **81**, 689 (2021), arXiv:2007.02645 [hep-ex] .

[124] S Catani, Yu L Dokshitzer, Michael H Seymour, and Bryan R Webber, *"Longitudinally-invariant $k_\perp$-clustering algorithms for hadron-hadron collisions,"* Nucl. Phys. B **406**, 187–224 (1993).

[125] ATLAS Collaboration, *"Jet energy scale measurements and their systematic uncertainties in proton-proton collisions at $\sqrt{s} = 13$ TeV with the ATLAS detector,"* Physical Review D **96** (2017), 10.1103/physrevd.96.072002.

[126] ATLAS Collaboration (ATLAS), *"Jet energy scale and resolution measured in proton–proton collisions at $\sqrt{s} = 13$ TeV with the ATLAS detector,"* Eur. Phys. J. C **81**, 689 (2021), arXiv:2007.02645 .

[127] ATLAS Collaboration (ATLAS), *"Jet energy scale measurements and their systematic uncertainties in proton-proton collisions at $\sqrt{s} = 13$ TeV with the ATLAS detector."* Phys. Rev. D **96**, 072002 (2017), arXiv:1703.09665 .

[128] Izaak Neutelings, "B tagging jets," `https://tikz.net/jet_btag/`, visited on 09/22/2024.

[129] *Optimisation and performance studies of the ATLAS b-tagging algorithms for the 2017-18 LHC run*, Tech. Rep. (CERN, Geneva, 2017).

[130] *Identification of Jets Containing b-Hadrons with Recurrent Neural Networks at the ATLAS Experiment*, Tech. Rep. (CERN, Geneva, 2017).

[131] *Secondary vertex finding for jet flavour identification with the ATLAS detector*, Tech. Rep. (CERN, Geneva, 2017).

[132] ATLAS Collaboration, *Topological b-hadron decay reconstruction and identification of b-jets with the JetFitter package in the ATLAS experiment at the LHC*, Tech. Rep. (CERN, Geneva, 2018).

[133] ATLAS Collaboration (ATLAS), *"ATLAS b-jet identification performance and efficiency measurement with $t\bar{t}$ events in pp collisions at $\sqrt{s} = 13$ TeV,"* Eur. Phys. J. C **79**, 970 (2019), arXiv:1907.05120 .

[134] *Deep Sets based Neural Networks for Impact Parameter Flavour Tagging in ATLAS*, Tech. Rep. (CERN, Geneva, 2020).

[135] *Graph Neural Network Jet Flavour Tagging with the ATLAS Detector*, Tech. Rep. (CERN, Geneva, 2022).

[136] Shaked Brody, Uri Alon, and Eran Yahav, "How attentive are graph attention networks?" (2022), arXiv:2105.14491 [cs.LG] .

[137] Ashish Vaswani, Noam Shazeer, Niki Parmar, Jakob Uszkoreit, Llion Jones, Aidan N. Gomez, Lukasz Kaiser, and Illia Polosukhin, "Attention is all you need," (2023), arXiv:1706.03762 [cs.CL] .

[138] *Transformer Neural Networks for Identifying Boosted Higgs Bosons decaying into $b\bar{b}$ and $c\bar{c}$ in ATLAS*, Tech. Rep. (CERN, Geneva, 2023).

[139] ATLAS Colaboration, *"Evidence for the $h \to b\bar{b}$ decay with the atlas detector,"* Journal of High Energy Physics **2017** (2017), 10.1007/jhep12(2017)024.

[140] *Performance of missing transverse momentum reconstruction for the ATLAS detector in the first proton-proton collisions at at $\sqrt{s}$= 13 TeV*, Tech. Rep. ATL-PHYS-PUB-2015-027 (CERN, Geneva, 2015).

[141] ATLAS Collaboration (ATLAS), *"Performance of missing transverse momentum reconstruction with the ATLAS detector using proton-proton collisions at $\sqrt{s}$ = 13 TeV,"* Eur. Phys. J. C **78**, 903 (2018), arXiv:1802.08168 .

[142] ATLAS Collaborations, *Recommendations of the Physics Objects and Analysis Harmonisation Study Groups 2014*, Tech. Rep. (CERN, Geneva, 2014).

[143] ATLAS Collaboration, "Luminosity determination in pp collisions at $\sqrt{s}$ = 13 TeV using the ATLAS detector at the LHC," ATLAS-CONF-2019-021 (2019).

[144] J. Alwall *et al.*, *"The automated computation of tree-level and next-to-leading order differential cross sections, and their matching to parton shower simulations,"* JHEP **07**, 079 (2014), arXiv:1405.0301 [hep-ph] .

[145] Stefano Frixione, Giovanni Ridolfi, and Paolo Nason, *"A positive-weight next-to-leading-order Monte Carlo for heavy flavour hadroproduction,"* JHEP **09**, 126 (2007), arXiv:0707.3088 [hep-ph] .

[146] Paolo Nason, *"A new method for combining NLO QCD with shower Monte Carlo algorithms,"* JHEP **11**, 040 (2004), arXiv:hep-ph/0409146 .

[147] Stefano Frixione, Paolo Nason, and Carlo Oleari, *"Matching NLO QCD computations with parton shower simulations: the POWHEG method,"* JHEP **11**, 070 (2007), arXiv:0709.2092 [hep-ph] .

[148] Simone Alioli, Paolo Nason, Carlo Oleari, and Emanuele Re, *"A general framework for implementing NLO calculations in shower Monte Carlo programs: the POWHEG BOX,"* JHEP **06**, 043 (2010), arXiv:1002.2581 [hep-ph] .

[149] Enrico Bothmann *et al.*, *"Event generation with Sherpa 2.2,"* SciPost Phys. **7**, 034 (2019), arXiv:1905.09127 [hep-ph] .

[150] NNPDF Collaboration, Richard D. Ball, *et al.*, *"Parton distributions for the LHC run II,"* JHEP **04**, 040 (2015), arXiv:1410.8849 [hep-ph] .

[151] Torbjörn Sjöstrand, Stefan Ask, Jesper R. Christiansen, Richard Corke, Nishita Desai, Philip Ilten, Stephen Mrenna, Stefan Prestel, Christine O. Rasmussen, and Peter Z. Skands, *"An introduction to PYTHIA 8.2,"* Comput. Phys. Commun. **191**, 159 (2015), arXiv:1410.3012 [hep-ph] .

[152] M. Bähr *et al.*, *"Herwig++ physics and manual,"* Eur. Phys. J. C **58**, 639 (2008), arXiv:0803.0883 [hep-ph] .

[153] Johannes Bellm *et al.*, *"Herwig 7.0/Herwig++ 3.0 release note,"* Eur. Phys. J. C **76**, 196 (2016), arXiv:1512.01178 [hep-ph] .

[154] *ATLAS Pythia 8 tunes to 7 TeV data*, Tech. Rep. (CERN, Geneva, 2014).

[155] P. Artoisenet *et al.*, *"Automatic spin-entangled decays of heavy resonances in Monte Carlo simulations,"* JHEP **2013** (2013), 10.1007/jhep03(2013)015.

[156] P. Artoisenet *et al.*, *"Automatic spin-entangled decays of heavy resonances in Monte Carlo simulations,"* JHEP **2013** (2013), 10.1007/jhep03(2013)015.

[157] ATLAS Collaboration, *"The ATLAS Simulation Infrastructure,"* EPJ C **70**, 823–874 (2010).

[158] S. Agostinelli *et al.*, *"GEANT4 – a simulation toolkit,"* Nucl. Instrum. Meth. A **506**, 250 (2003).

[159] ATLAS Collaboration, *The simulation principle and performance of the ATLAS fast calorimeter simulation FastCaloSim*, Tech. Rep. ATL-PHYS-PUB-2010-013 (CERN, Geneva, 2010).

[160] ATLAS Collaboration, "Studies on top-quark Monte Carlo modelling for Top2016," ATL-PHYS-PUB-2016-020 (2016).

[161] M. Beneke, P. Falgari, S. Klein, and C. Schwinn, *"Hadronic top-quark pair production with NNLL threshold resummation,"* Nucl. Phys. B **855**, 695–741 (2012), arXiv:1109.1536 [hep-ph] .

[162] Matteo Cacciari, Michal Czakon, Michelangelo Mangano, Alexander Mitov, and Paolo Nason, *"Top-pair production at hadron colliders with next-to-next-to-leading logarithmic soft-gluon resummation,"* Phys. Lett. B **710**, 612–622 (2012), arXiv:1111.5869 [hep-ph] .

[163] Peter Bärnreuther, Michal Czakon, and Alexander Mitov, *"Percent-Level-Precision Physics at the Tevatron: Next-to-Next-to-Leading Order QCD Corrections to $q\bar{q} \to t\bar{t} + X$,"* Phys. Rev. Lett. **109**, 132001 (2012), arXiv:1204.5201 [hep-ph] .

[164] Michal Czakon and Alexander Mitov, *"NNLO corrections to top-pair production at hadron colliders: the all-fermionic scattering channels,"* JHEP **12**, 054 (2012), arXiv:1207.0236 [hep-ph] .

[165] Michal Czakon and Alexander Mitov, *"NNLO corrections to top pair production at hadron colliders: the quark-gluon reaction,"* JHEP **01**, 080 (2013), arXiv:1210.6832 [hep-ph] .

[166] Michal Czakon, Paul Fiedler, and Alexander Mitov, *"Total Top-Quark Pair-Production Cross Section at Hadron Colliders Through* $O(\alpha_S^4)$*,"* Phys. Rev. Lett. **110**, 252004 (2013), arXiv:1303.6254 [hep-ph] .

[167] Michal Czakon and Alexander Mitov, *"Top++: A program for the calculation of the top-pair cross-section at hadron colliders,"* Comput. Phys. Commun. **185**, 2930 (2014), arXiv:1112.5675 [hep-ph] .

[168] Judith Katzy and Lars Ferencz, *Studies of Monte Carlo predictions for the* $t\bar{t}b\bar{b}$ *process*, Tech. Rep. (CERN, Geneva, 2021).

[169] Fabio Cascioli, Philipp Maierhöfer, Niccolo Moretti, Stefano Pozzorini, and Frank Siegert, *"NLO matching for* $t\bar{t}b\bar{b}$ *production with massive b-quarks,"* Phys. Lett. B **734**, 210–214 (2014), arXiv:1309.5912 [hep-ph] .

[170] Emanuele Re, *"Single-top* Wt*-channel production matched with parton showers using the POWHEG method,"* Eur. Phys. J. C **71**, 1547 (2011), arXiv:1009.2450 [hep-ph] .

[171] Stefano Frixione, Eric Laenen, Patrick Motylinski, Chris White, and Bryan R. Webber, *"Single-top hadroproduction in association with a* W *boson,"* JHEP **07**, 029 (2008), arXiv:0805.3067 [hep-ph] .

[172] Rikkert Frederix, Emanuele Re, and Paolo Torrielli, *"Single-top* t*-channel hadroproduction in the four-flavour scheme with POWHEG and aMC@NLO,"* JHEP **09**, 130 (2012), arXiv:1207.5391 [hep-ph] .

[173] Simone Alioli, Paolo Nason, Carlo Oleari, and Emanuele Re, *"NLO single-top production matched with shower in POWHEG:* s*- and* t*-channel contributions,"* JHEP **09**, 111 (2009), arXiv:0907.4076 [hep-ph] .

[174] J. Alwall, R. Frederix, S. Frixione, V. Hirschi, F. Maltoni, O. Mattelaer, H. S. Shao, T. Stelzer, P. Torrielli, and M. Zaro, *"The automated computation of tree-level and next-to-leading order differential cross sections, and their matching to parton shower simulations,"* JHEP **07**, 079 (2014), arXiv:1405.0301 [hep-ph] .

[175] NNPDF Collaboration, Richard D. Ball, *et al.*, *"Parton distributions with LHC data,"* Nucl. Phys. B **867**, 244 (2013), arXiv:1207.1303 [hep-ph] .

[176] Rikkert Frederix, Davide Pagani, and Marco Zaro, *"Large NLO corrections in $t\bar{t}W^{\pm}$ and $t\bar{t}t\bar{t}$ hadroproduction from supposedly subleading EW contributions,"* JHEP **02**, 031 (2018), arXiv:1711.02116 [hep-ph] .

[177] Stefano Frixione, Eric Laenen, Patrick Motylinski, and Bryan R. Webber, *"Angular correlations of lepton pairs from vector boson and top quark decays in Monte Carlo simulations,"* JHEP **04**, 081 (2007), arXiv:hep-ph/0702198 .

[178] Pierre Artoisenet, Rikkert Frederix, Olivier Mattelaer, and Robbert Rietkerk, *"Automatic spin-entangled decays of heavy resonances in Monte Carlo simulations,"* JHEP **03**, 015 (2013), arXiv:1212.3460 [hep-ph] .

[179] D. J. Lange, *"The EvtGen particle decay simulation package,"* *Proceedings, 7th International Conference on B physics at hadron machines (BEAUTY 2000)*, Nucl. Instrum. Meth. A **462**, 152 (2001).

[180] L. A. Harland-Lang, A. D. Martin, P. Motylinski, and R. S. Thorne, *"Parton distributions in the LHC era: MMHT 2014 PDFs,"* Eur. Phys. J. C **75**, 204 (2015), arXiv:1412.3989 [hep-ph] .

[181] Steffen Schumann and Frank Krauss, *"A parton shower algorithm based on Catani–Seymour dipole factorisation,"* JHEP **03**, 038 (2008), arXiv:0709.1027 [hep-ph] .

[182] Stefan Höche, Frank Krauss, Marek Schönherr, and Frank Siegert, *"A critical appraisal of NLO+PS matching methods,"* JHEP **09**, 049 (2012), arXiv:1111.1220 [hep-ph] .

[183] Stefan Höche, Frank Krauss, Marek Schönherr, and Frank Siegert, *"QCD matrix elements + parton showers. The NLO case,"* JHEP **04**, 027 (2013), arXiv:1207.5030 [hep-ph] .

[184] S. Catani, F. Krauss, B. R. Webber, and R. Kuhn, *"QCD Matrix Elements + Parton Showers,"* JHEP **11**, 063 (2001), arXiv:hep-ph/0109231 .

[185] Stefan Höche, Frank Krauss, Steffen Schumann, and Frank Siegert, *"QCD matrix elements and truncated showers,"* JHEP **05**, 053 (2009), arXiv:0903.1219 [hep-ph] .

[186] Fabio Cascioli, Philipp Maierhöfer, and Stefano Pozzorini, *"Scattering Amplitudes with Open Loops,"* Phys. Rev. Lett. **108**, 111601 (2012), arXiv:1111.5206 [hep-ph] .

[187] Ansgar Denner, Stefan Dittmaier, and Lars Hofer, *"COLLIER: A fortran-based complex one-loop library in extended regularizations,"* Comput. Phys. Commun. **212**, 220–238 (2017), arXiv:1604.06792 [hep-ph] .

[188] Federico Buccioni, Jean-Nicolas Lang, Jonas M. Lindert, Philipp Maierhöfer, Stefano Pozzorini, Hantian Zhang, and Max F. Zoller, *"OpenLoops 2,"* Eur. Phys. J. C **79**, 866 (2019), arXiv:1907.13071 [hep-ph] .

[189] Jon Butterworth *et al.*, *"PDF4LHC recommendations for LHC Run II,"* J. Phys. G **43**, 023001 (2016), arXiv:1510.03865 [hep-ph] .

[190] Tanju Gleisberg and Stefan Höche, *"Comix, a new matrix element generator,"* JHEP **12**, 039 (2008), arXiv:0808.3674 [hep-ph] .

[191] Charalampos Anastasiou, Lance Dixon, Kirill Melnikov, and Frank Petriello, *"High-precision QCD at hadron colliders: Electroweak gauge boson rapidity distributions at next-to-next-to leading order,"* Phys. Rev. D **69**, 094008 (2004), arXiv:hep-ph/0312266 .

[192] Rustem Ospanov, Rhys Thomas Roberts, and Terry Richard Wyatt, *Tagging non-prompt electrons and muons*, Tech. Rep. (CERN, Geneva, 2016).

[193] CMS Collaboration, *"Measurement of the $t\bar{t}$ production cross section in the all-jet final state in pp collisions at $\sqrt{s} = 7$ TeV,"* JHEP **05**, 065 (2013), arXiv:1302.0508 [hep-ex] .

[194] CMS Collaboration, *"Measurement of the cross section for $t\bar{t}$ production with additional jets and b jets in pp collisions at $\sqrt{s} = 13$ TeV,"* JHEP **07**, 125 (2020), arXiv:2003.06467 [hep-ex] .

[195] ATLAS Collaboration, *"Measurements of inclusive and differential fiducial cross-sections of $t\bar{t}$ production with additional heavy-flavour jets in proton–proton collisions at $\sqrt{s} = 13$ TeV with the ATLAS detector,"* JHEP **04**, 046 (2019), arXiv:1811.12113 [hep-ex] .

[196] Tomáš Ježo, Jonas M. Lindert, Niccolo Moretti, and Stefano Pozzorini, *"New nlops predictions for $t\bar{t} + b$-jet production at the lhc,"* The European Physical Journal C **78** (2018), 10.1140/epjc/s10052-018-5956-0.

[197] ATLAS Colaboration, *"Search for new phenomena in events with same-charge leptons and b-jets in pp collisions at $\sqrt{s} = 13$ TeV with the ATLAS detector,"* Journal of High Energy Physics **2018** (2018), 10.1007/jhep12(2018)039.

[198] ATLAS Collaboration (ATLAS), *"Observation of four-top-quark production in the multilepton final state with the ATLAS detector,"* Eur. Phys. J. C **83**, 496 (2023), arXiv:2303.15061 .

[199] ATLAS Collaboration, *Analysis of $t\bar{t}H$ and $t\bar{t}W$ production in multilepton final states with the ATLAS detector*, Tech. Rep. (CERN, Geneva, 2019).

[200] ATLAS Collaboration, *"Measurement of the total and differential cross-sections of $t\bar{t}W$ production in pp collisions at $\sqrt{s}$ = 13 TeV with the ATLAS detector,"* Journal of High Energy Physics **2024** (2024), 10.1007/jhep05(2024)131.

[201] Erik Gerwick, Tilman Plehn, Steffen Schumann, and Peter Schichtel, *"Scaling Patterns for QCD Jets,"* JHEP **10**, 162 (2012), arXiv:1208.3676 [hep-ph] .

[202] "Salt framework," `https://ftag-salt.docs.cern.ch/`.

[203] ATLAS Collaboration, *"Luminosity determination in pp collisions at $\sqrt{s}$ = 13 TeV using the ATLAS detector at the LHC,"* Eur. Phys. J. C **83**, 982 (2023), arXiv:2212.09379 [hep-ex] .

[204] G. Avoni *et al.*, *"The new LUCID-2 detector for luminosity measurement and monitoring in ATLAS,"* JINST **13**, P07017 (2018).

[205] ATLAS Collaboration, *"Measurement of the inelastic proton-proton cross section at $\sqrt{s} = 13$ TeV with the ATLAS detector at the LHC,"* Phys. Rev. Lett. **117**, 182002 (2016).

[206] ATLAS Collaboration, *"Performance of pile-up mitigation techniques for jets in pp collisions at $\sqrt{s}$ = 8 TeV using the ATLAS detector,"* EPJ C **76** (2016), 10.1140/epjc/s10052-016-4395-z.

[207] ATLAS Collaboration, *"Determination of jet calibration and energy resolution in proton–proton collisions at $\sqrt{s}$ = 8 TeV using the ATLAS detector,"* Eur. Phys. J. C **80**, 1104 (2020), arXiv:1910.04482 [hep-ex] .

[208] ATLAS Collaboration, *"Performance of missing transverse momentum reconstruction with the ATLAS detector using proton–proton collisions at $\sqrt{s}$ = 13 TeV,"* Eur. Phys. J. C **78**, 903 (2018), arXiv:1802.08168 [hep-ex] .

[209] ATLAS Collaboration, "$E_{\mathrm{T}}^{\mathrm{miss}}$ performance in the ATLAS detector using 2015–2016 LHC *pp* collisions," ATLAS-CONF-2018-023 (2018).

[210] ATLAS Collaboration, "Measurement of the production cross-section of a single top quark in association with a Z boson in proton–proton collisions at 13 TeV with the ATLAS detector," ATLAS-CONF-2017-052 (2017).

[211] Federico Demartin, Benedikt Maier, Fabio Maltoni, Kentarou Mawatari, and Marco Zaro, *"twh associated production at the LHC,"* EPJC **77** (2017), 10.1140/epjc/s10052-017-4601-7, arXiv:1607.05862 [hep-ph] .

[212] ATLAS Collaboration, *"Measurement of $W^{\pm}Z$ production cross sections and gauge boson polarisation in pp collisions at $\sqrt{s}$ = 13 TeV with the ATLAS detector,"* Eur. Phys. J. C **79**, 535 (2019), arXiv:1902.05759 [hep-ex] .

[213] D. de Florian and al. (LHC Higgs Cross Section Working Group), *Handbook of LHC Higgs Cross Sections: 4. Deciphering the Nature of the Higgs Sector*, CERN Yellow Reports: Monographs (2016).

[214] ATLAS Collaboration, *"Evidence for $t\bar{t}t\bar{t}$ production in the multilepton final state in proton–proton collisions at $\sqrt{s} = 13$ TeV with the ATLAS detector,"* The European Physical Journal C **80** (2020), 10.1140/epjc/s10052-020-08509-3.

[215] Alexander L. Read, *"Presentation of search results: the CL_S technique,"* J. Phys. G **28**, 2693 (2002).

[216] Noemi Calace, "Jet Substructure Techniques for the Search of Diboson Resonances at the LHC and Performance Evaluation of the ATLAS Phase-II Inner Tracker Layouts," (2018), presented 20 Jun 2018.

[217] *Technical Design Report for the ATLAS Inner Tracker Strip Detector*, Tech. Rep. (CERN, Geneva, 2017).

[218] *Technical Design Report for the ATLAS Inner Tracker Pixel Detector*, Tech. Rep. (CERN, Geneva, 2017).

[219] Claudia Gemme (ATLAS Collaboration), *The ATLAS Tracker Detector for HL-LHC*, Tech. Rep. (CERN, Geneva, 2020).

[220] *Expected tracking and related performance with the updated ATLAS Inner Tracker layout at the High-Luminosity LHC*, Tech. Rep. (CERN, Geneva, 2021).

[221] *Measurement prospects for VBF $H \rightarrow WW^{(*)} \rightarrow e\nu\mu\nu$ production with 3 ab^{-1} of HL-LHC pp-collisions*, Tech. Rep. (CERN, Geneva, 2016).

[222] ATLAS Collaboration, *ATLAS Phase-II Upgrade Scoping Document*, Tech. Rep. (CERN, Geneva, 2015).

[223] *Expected b-tagging performance with the upgraded ATLAS Inner Tracker detector at the High-Luminosity LHC*, Tech. Rep. (CERN, Geneva, 2020).

[224] *"Performance of b-jet identification in the ATLAS experiment,"* Journal of Instrumentation **11**, P04008–P04008 (2016).

[225] *Secondary vertex finding for jet flavour identification with the ATLAS detector*, Tech. Rep. (CERN, Geneva, 2017).

[226] *Optimisation and performance studies of the ATLAS b-tagging algorithms for the 2017-18 LHC run*, Tech. Rep. (CERN, Geneva, 2017).

[227] *Reconstruction, Energy Calibration, and Identification of Hadronically Decaying Tau Leptons in the ATLAS Experiment for Run-2 of the LHC*, Tech. Rep. (CERN, Geneva, 2015).

[228] *Development of ATLAS Primary Vertex Reconstruction for LHC Run 3*, Tech. Rep. (CERN, Geneva, 2019).

[229] *"Reconstruction of primary vertices at the ATLAS experiment in Run 1 proton–proton collisions at the LHC. Reconstruction of primary vertices at the ATLAS experiment in Run 1 proton-proton collisions at the LHC,"* Eur. Phys. J. C **77**, 332. 52 p (2016), arXiv:1611.10235 .

[230] P Calafiura, J Catmore, D Costanzo, and A Di Girolamo, *ATLAS HL-LHC Computing Conceptual Design Report*, Tech. Rep. (CERN, Geneva, 2020).

[231] ATLAS Collaboration, "ATLAS computing model projections for Phase-2," `https://twiki.cern.ch/twiki/bin/view/AtlasPublic/ComputingandSoftwarePublicResults` (2024), accessed: 2024-09-23.

[232] *Fast Track Reconstruction for HL-LHC*, Tech. Rep. (CERN, Geneva, 2019).

[233] Andrew Buckley, Till Eifert, Markus Elsing, Dag Ingemar Gillberg, Karsten Koeneke, Attila Krasznahorkay, Edward Moyse, Marcin Nowak, Scott Snyder, and Peter van Gemmeren (TheATLAScollaboration), *Implementation of the ATLAS Run 2 event data model*, Tech. Rep. 7 (CERN, Geneva, 2015).

[234] P F Åkesson, T Atkinson, M J Costa, M Elsing, S Fleischmann, A N Gaponenko, W Liebig, E Moyse, A Salzburger, and M Siebel, *ATLAS Tracking Event Data Model*, Tech. Rep. (CERN, Geneva, 2006).

[235] Paul Gessinger-Befurt, "Development and improvement of track reconstruction software and search for disappearing tracks with the ATLAS experiment," (2021).

[236] Azriel Rosenfeld and John L. Pfaltz, *"Sequential operations in digital picture processing,"* J. ACM **13**, 471–494 (1966).

[237] The ATLAS collaboration, *"A neural network clustering algorithm for the atlas silicon pixel detector,"* Journal of Instrumentation **9**, P09009 (2014).

[238] Andreas Salzburger, "Track Simulation and Reconstruction in the ATLAS experiment," (2008).

[239] R. Frühwirth *et al.*, *"Pattern recognition and reconstruction," Particle Physics Reference Library: Volume 2: Detectors for Particles and Radiation*, , 555–612 (2020).

[240] Christian Bierlich *et al.*, *"A comprehensive guide to the physics and usage of PYTHIA 8.3,"* SciPost Phys. Codebases , 8 (2022), arXiv:2203.11601 [hep-ph] .

[241] ATLAS Collaboration, *"The ATLAS Simulation Infrastructure,"* Eur. Phys. J. C **70**, 823 (2010), arXiv:1005.4568 [physics.ins-det] .

[242] Bandieramonte, Marilena, Bianchi, Riccardo Maria, Boudreau, Joseph, Dell´Acqua, Andrea, and Tsulaia, Vakhtang, *"The geomodel tool suite for detector description,"* EPJ Web Conf. **251**, 03007 (2021).

[243] ATLAS Collaboration, "ATLAS HL-LHC Computing Conceptual Design Report," (2020).

[244] *Clustering and Tracking in Dense Environments with the ATLAS Inner Tracker for the High-Luminosity LHC*, Tech. Rep. (CERN, Geneva, 2023).

[245] T. Cornelissen, M. Elsing, I. Gavrilenko, W. Liebig, E. Moyse, and A. Salzburger, *"The new ATLAS track reconstruction (NEWT),"* J. Phys. Conf. Ser. **119**, 032014 (2008).

[246] Irina Ene, Louis-Guillaume Gagnon, and Heather Gray, *ATLAS Run 3 charged particle track seed finding performance*, Tech. Rep. (CERN, Geneva, 2023).

[247] A. Adare *et al.*, "An upgrade proposal from the PHENIX collaboration," (2015), arXiv:1501.06197 [nucl-ex] .

[248] J. Osborn, "Requirements, status, and plans for track reconstruction at the sphenix experiment," (2020), arXiv:2007.00771 [physics.ins-det] .

[249] The CEPC Study Group, "CEPC conceptual design report: Volume 1 - accelerator," (2018), arXiv:1809.00285 [physics.acc-ph] .

[250] The CEPC Study Group, "CEPC conceptual design report: Volume 2 - physics & detector," (2018), arXiv:1811.10545 [hep-ex] .

[251] M. Achasov *et al.*, "STCF conceptual design report: Volume 1 – physics & detector," (2023), arXiv:2303.15790 [hep-ex] .

[252] C. Ahdida *et al.* (NA60+), *Letter of Intent: the NA60+ experiment*, Tech. Rep. (CERN, 2022) arXiv:2212.14452 [nucl-ex] .

[253] M. Tanabashi et al. (Particle Data Group), *"Passage of Particles Through Matter,"* Phys. Rev. D 98 **0300001**, 2–17 (2018).

[254] G.R. Lynch and O.I Dahl, *"Nucl. Instrum. Methods B58,"* Phys. Rev. D 98 **6**, 2–17 (1991).

[255] ATLAS Collaboration, *"Performance of the ATLAS Silicon Pattern Recognition Algorithm in Data and Simulation at* $\sqrt{s}$ = *7 TeV,"* https://cds.cern.ch/record/1281363 , 2–17 (Jul 2010).

[256] "Inside out - track seeding and finding," `https://atlassoftwaredocs.web.cern.ch/trackingTutorial/tracksf/`, accessed: 2022-08-16.

[257] T. Sjöstrand *et al.*, *"An Introduction to PYTHIA 8.2,"* Comput. Phys. Commun. **191**, 159–177 (2015), arXiv:1410.3012 [hep-ph] .

[258] K Edmonds *et al.*, *The Fast ATLAS Track Simulation (FATRAS)*, Tech. Rep. (CERN, Geneva, 2008).

[259] ATLAS Project, "Status of the ACTS Integration for Phase-II ATLAS Track Re-construction," (2023).

[260] Jannicke Andree Pearkes, "Higgs Pair Production Searches with the ATLAS Experiment at the LHC and the HL-LHC," (2022).

[261] Bastian Schlag, "Advanced Algorithms and Software for Primary Vertex Reconstruction and Search for Flavor-Violating Supersymmetry with the ATLAS Experiment," (2022).

[262] Petar Bokan, "Pair production of Higgs bosons in the final state with bottom quarks and τ leptons in the ATLAS experiment: Search results using LHC Run 2 data and prospect studies at the HL-LHC," (2020).

[263] Giulia Di Gregorio, "Search for the Higgs boson produced in association with a vector boson and decaying into a pair of b-quarks using large-R jets with the ATLAS detector," (2020).

[264] Nicole Michelle Hartman, "A Search for Non-Resonant $HH \to 4b$ at $\sqrt{s} = 13$ TeV with the ATLAS detector – or – $2b$, and then another $2b$... now that's the thesis question." (2022).

[265] Meng-Ju Tsai, "Studies of Four-Top-Quark Production in Proton-Proton Collisions at the LHC With The Same-Sign Dilepton and Multilepton Final States," (2024).

[266] Emanuel Gouveia, "Probing the CP nature of the Higgs coupling to top quarks with the ATLAS experiment at the LHC," (2021).

[267] Luisa Carvalho, "Measurements of Higgs boson properties in associated production with top quarks with the ATLAS detector," (2023).

[268] Luis Falda Coelho, "Study of the CP nature of the top-higgs coupling in $t\bar{t}h$ events at the lhc," (2020).